For New Technology Network

NTN®

TECHNICAL REVIEW

No. 78

Special Issue;
Products for Industrial Machinery and Elemental Technologies

October 2010

ISSN 0915-0528 OSAKA, JAPAN

NTN®

TECHNICAL REVIEW

No.78

Special Issue:
Products for industrial machinery and elemental technologies

NTN corporation

NTN TECHNICAL REVIEW No.78

CONTENTS

[Preface]

An introduction to this special edition on products for industrial machinery and elemental technologies

Yoshikazu FUKUMURA
Managing Director

Concerns about global warming and other environmental problems have been growing rapidly. Global responses to these concerns are increasing. In the automotive field, this means increasing fuel efficiency and converting to electric power. The industrial machinery field has seen the development of equipment that uses natural energy sources, such as wind and solar power.

In these changing times, harmonious existence with the global environment is also a focus for **NTN**. Using advanced technological abilities that we have so far developed, we are developing green products based on the concepts of low torque, long life and reduced size and weight to conserve resources and energy.

At **NTN**, we have published this journal to correspond with the holding of the 25th Japan International Machine Tool Fair It features **NTN**'s cutting-edge technology and new products for industrial machinery, in addition to fundamental concepts and ideas, This fair, also known as JIMTOF 2010, has the theme of "Mono-Zukuri Innovation" and is being held from October 28 to November 2, 2010.

We start our journal with an introduction entitled, "New manufacturing technologies and tribology," contributed by Takashi Nakamura, who is an authority in the field of tribology and Vice-President of the Nagoya Institute of Technology. This is followed by discussions about fundamental bearing technology for industrial machinery, including machine tools, tribology, ceramics and sensor technologies, as well as our recent developments with new technology and products. We also describe three products we developed that received awards this year, including the Commendation for Science and Technology by the Minister of Education, Culture, Sports, Science and Technology and an award from the Japanese Society of Tribologists.

At JIMTOF 2010, **NTN** is exhibiting with the theme, "**NTN**: Supporting Evolving Manufacturing (manufacturing that is good for the environment)." We are presenting new technology and products related to industrial machinery and elemental technology. Even before now, we had brought to market the Ultage Series, which responds to industrial machinery market needs, including high precision, high speed, energy conservation and contribution to a better environment. This year at JIMTOF 2010, in addition to pioneering technology for industrial machinery precision bearings, we are also making a presentation about ultra-precision inspection and measurement technology. This merges our **NTN-SNR** sensor technology with unique products developed for production technology.

In the two years starting with fiscal 2009, we have sought to realize becoming a strong corporation that does not depend on scale in our new "**NTN** 2010 for the Next Step" medium-term management plan. This includes our corporate philosophy, "For New Technology Network: We shall contribute to international society through creating new technologies and developing new products." We are also following the fundamental principle of "technological leadership." By promoting the development of new technology and products, we will continue contributing to the sustainable advancement of society.

New Machining Technologies and Tribology

Takashi NAKAMURA
Professor, Vice President, Nagoya Institute of Technology (NIT), D. Eng.

Some machining technologies are necessary for manufacturing real products, and the continuous pursuit of superior machining technologies is required to sustain and expand manufacturing industries in Japan. New machining processes promoted by the author and others are introduced in this paper, and the significance of these technologies and their relevance to tribology are explained.

1. Introduction

Following the April 6, 2010 commencement ceremony of state-run Nagoya Institute of Technology (NIT), a seminar of Japan's business leaders was held. During this seminar, Yasunobu Suzuki, **NTN**'s Chairman, presented a speech titled "'Dream' and 'Ki (spiritual energy)'—Let us have a pluralistic picture of the world". This speech covered topics ranging from his student days at NIT's Department of Metal Engineering to those in his career at **NTN** (**Fig. 1**). He emphasized the values of intellectual power, physical power and will power, the necessity to study history and establish 'kata (one's own style)', and the importance of viewing the world based on a wide sense of values. The attending freshmen and their parents ardently listened to the speech. The author was also a member of the audience and was deeply impressed by the speech. Beginning in 2005, NIT, in marking the 100th anniversary of its foundation, has been honoring "individuals who have been committed to the cultivation of human resources and shown significant achievements in the development of education and research" with an NIT honorary degree. The first person honored by NIT was Colin L. Powell, an ex. US Secretary of State, who presented a special lecture at NIT's 100th anniversary. The second person who received the honorary degree was Fujio Cho, the-then vice chairman of Toyota Motor Corp. At the 2010 seminar of Japan's top business leaders, NIT awarded Yasunobu Suzuki, **NTN** Chairman, with NIT's 7th honorary degree (**Fig. 2**). We hope he will continue providing precious advice to encourage further development of NIT.

Fig.1 Chairman Yasunobu Suzuki making his speech at the seminar of business leaders at NIT

Fig.2 Commencement ceremony
(left : Nagoya Institute of Technology President Minoru Takahashi
right : **NTN** Chairman Yasunobu Suzuki)

This spring (2010), another enthusiastic graduate from my laboratory joined **NTN**. The author has long been supported by **NTN** in various aspects. In particular, my joint researcher Fumihiro Itoigawa, Associate Professor at NIT, was heavily supported by **NTN** while preparing his doctoral thesis "Research into precision of steel balls for precision equipment[1)]". **NTN** provided a guided tour through its ball production facility and gave useful recommendations about possible test methods. NIT is grateful for this support. In this paper, lapping techniques for steel balls will be described as well as new machining technology and their affect on tribology. Production of high precision steel balls is only possible with a fundamental understanding of engineering and a great deal of manufacturing experience and expertise. Mass production of steel balls with a high precision level is otherwise impossible. Although it may produce a highly accurate spherical surface, even the most advanced 5-axis ultra high-precision machine tool cannot manufacture such high-quality steel balls. Therefore, in order for the new machining technology described herein to be used properly, the technology needs to be supported by the fundamental principles of engineering and satisfy the latest machining requirements.

Incidentally, before drafting this paper, the author checked past contributions to **NTN** Technical Reviews on **NTN**'s website. When seeing a portrait of Yoshiji Kimura[2)], an ex-president of Kagawa University, the author recalled his cheerful high-pitched laugh and his comment,"Mr. Nakamura! You wish to be a contributor to **NTN**'s review?" At that moment the author felt honored to contribute to this issue of the **NTN** Technical Review. Being impressed by Mr. Kimura's unique insight in the paper "Introduction to Tribology"[3)] coauthored with the late Heihachiro Okabe (a former leading tribology scientist in Japan), the author hopes this paper is as insightful to the readers.

2. Techniques for lapping steel balls

During my student days at the university, I was taught that the machining principles that govern machining accuracy are the "maternal principle" and the "generating principle". "Maternal principle" refers to a fact that the operating accuracy of a machine tool (also known as the "mother machine") is directly transferred to the product made by the machine—a "child" can never be superior to his/her "mother". Nowadays it is no longer the norm for a mother alone to take every responsibility. However, at that time I felt this principle was interesting as education theory and discussed this concept in a separate paper related to social education. In reality, the precision of machines has been improving from year to year, and this trend is said to result from the "generating principle". Several machining processes are currently available which are based on the "generating principle". One of the typical machining techniques is lapping of steel balls which is described below. Note, however, that the term "generation machining" refers to gear generation using a hob cutter, pinion cutter or grinding operation for special shaped work-pieces using an NC-controlled machine tool. For this reason, in the remainder of this paper I will call processes such as lapping a Suriawase process. Thanks to recent advances in measuring techniques for machine tools, it is increasingly common for operational errors and thermal deformation are measured in advance and the necessary adjustments are simultaneously performed during the machining operation. This practice also may be regarded as a Suriawase process. Speaking of Suriawase, recently a number of commentators say that Japanese auto companies manufacture cars with internal combustion engines based on Suriawase technology. Any manufacturer can produce EV's simply by purchasing the components and then assembling them similar to the production of personal computers—"the future of Japan seems gloomy". It is true that some people accept this "opinion". This practice is a very maternal production system, and does not promote the progress of technologies.

Is lapping of steel balls—a time-honored machining process—based on the "all things belong to sphere" principle? To answer this question, I have researched into existing manufacturing techniques for making balls. **Fig. 3** schematically illustrates a situation where a steel ball is held between lapping plates. Depending on the lapping technique used, a cutout slot is formed at the bottom of circular arc slot, or a V-sectioned slot is formed[4)]. Now, let me recall a scene at an **NTN** production site that has a US-made steel ball lapping machine that was manufactured year ago. Though

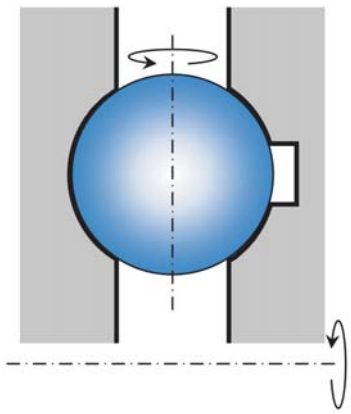

Fig.3 Lapping of a Steel Ball

unsure that this machine is still operational today, previously this machine was producing ultra high-precision steel balls at their maximum possible dimensional accuracy. Thus, it is apparent that the maternal principle does not apply to the lapping process on this machine. As many **NTN** employees know, steel balls are processed on this machine in a particular sequence. Two lapping plates are butted together along their lateral axis with the plates having concentrically formed circular arc-shaped slots. Each steel ball blank is loaded into the lapping machine through the stationary lapping plate, and is subjected to a lapping motion for one revolution, and then delivered into a stocker with a large capacity. The steel ball is allowed to sit in the stocker, and is then loaded into the lapping machine again. The repetition of reloading/unloading cycle has two important functions. First, this technique helps the axis of rotation of each ball change randomly. As determined experimentally, rolling elements turning at high speeds in angular contact ball bearings or thrust roller bearings do not readily change their axis of rotation. In other words, if a ball is lapped without changing its axis of rotation, the finished ball will be egg-shaped rather than spherical. This is the purpose of the reloading/unloading cycle on a lapping machine: to ensure the area being ground is random. Second, the wear rate between the lapping plates and the grinding rate of the steel ball are adjusted so that the optimal shape conformity between the circular arc groove and steel ball coincides with the time length of steel ball final finishing. When shape-conformity is not good, the shape of final balls tends to be polygonal (or tetrahedral in many cases). When the lapping operation for steel balls is allowed to continue with machining parameter values unchanged, circularity improves over time but begins to worsen after a certain point. Therefore, the lapping time must be controlled precisely for steel balls to be finished to a target accuracy. To this end, intuition, experience and tribological technology are important. The lapping compound and oil used during this process affect the circularity of the steel balls. A Manager at **NTN**'s Kuwana Works once commented, "For best machining accuracy, we even consider the weather of the day". In other words, highly accurate steel balls with good circularity are manufactured by lapping under the optimal work environment and conditions rather than following the "all things belong to sphere" principle. After careful consideration, this idea makes sense because we have never heard that "operating a ball bearing in clean conditions for a prolonged period helps produce highly accurate balls". In his doctoral thesis, Fumihiro Itoigawa, Associate Professor at NIT, attempted to clarify the manufacturing process for bearing balls. At the same time, he proposed a specific measure for further improving the accuracy and efficiency of the process. His proposal was to provide add a cutout slot at the bottom of circular arc slot on one lapping plate as shown in **Fig. 3**. With this arrangement, the three-lobed component of circularity error would be positively inhibited. However, due to the limitation in the measuring technique and no manufacturing plant to try this suggestion, it has yet to be verified that this arrangement would help produce ultrahigh-precision steel balls. Presently, three approaches have been proposed to the Manager of **NTN** Kuwana Works. First, add an in-process measuring operation (likely very difficult) for the slot profiles and the steel diameter to the lapping machine. Second, add an in-process measuring operation for the grain size distribution of the lapping compound. Third, adjust the lapping plate forcing load based on the data obtained from steps 1 and 2. Essentially the contact mode between the lapping plates and the steel ball is elastic Hertzian contact. Since the lapping plate forcing load causes the pure sliding position to shift, it may be possible to control the profile of the slot on the lapping plate. Any of these approaches poses a difficult engineering challenge and requires a lot of experimental research. Nevertheless, these concepts all have the potential to help create higher precision steel balls.

3. Suction removal of loose material

Any metal cutting or grinding operation inevitably creates loose material. In fact most of the energy consumed to machine a work-piece is removing the loose material from the machine tool during the turning operation. To avoid any adverse effects on machining accuracy from the heat generated by cutting or grinding, loose material should be removed from the working area as promptly as possible. However, on certain unattended automated production lines airborne loose material can cause problems during its operation. Loose material can get trapped in gaps between jigs and tools, leading to a greater dimensional mounting error or blocking the sliding motion of the tool. In order to completely eliminate these problems, we have created a prototype of a suction tool that removes loose material (illustrated in **Fig. 4**) that helps improve the milling operation shown in **Fig. 5**[5]. Loose material created by the machining process hits a cover enclosing the cutting face of the tool and is then drawn into the opening in the center of tool. Use of this new suction type ball end mill will lead to a cleaner machined surface free of loose material

as shown in **Fig. 5**. In contrast, when a conventional end mill is used to finish a cavity die shown in **Fig. 5**, loose material can bounce off the work-piece surface, interfere with the tool edge, and produce a lower quality finished surface. To avoid this type of defect at the final finish step in a time-consuming die machining process, this chip suction type milling tool would be useful. Though various engineering challenges still remain, prototypes have been built of suction type tools for a face mill and drill and tap, and tests are being run on these tools. Various manufacturers, whose specialties include cutting tools and tool holders, machine tools and chip disposers, are likely to support these efforts. During this academic year, NIT has studied a “debris-free grinding” technique where loose material from grinding is collected on the grinding wheel side of the machine. This technique, when fully commercialized, should be good news for various machine component manufactures, in particular, bearing manufacturers.

4. Laser lap welding

One technique used to weld together two thermoplastic resin members with heat generated by a laser beam is called “laser lap welding”. Although the word “lapping” means to finish a work-piece by lap grinding, the term “laser lap welding” is derived from the word “overlap”. Since in this type of process, a laser beam is directed onto a prospective weld between two overlapped members as shown in **Fig. 6**, at least one member has to be able to transmit the laser beam. Another lap welding technique available is called “ultrasonic welding” where a prospective weld is heated by friction from ultrasonic vibration. Both techniques are unique in that only the interface at the prospective weld area is heated and the influence of heat on other areas is limited. In an ordinary laser lap welding process, one resin member is made of light-absorbing material as shown in the left side of **Fig. 6** or the interface at the prospective weld is coated with a light-absorbing material. We have attempted to determine optimal welding conditions by measuring the surface roughness of the two members (which has always been a subject of interest in the tribological engineering field)[6]. As a result, an unexpected effect was found and a unique welding operation similar to the one shown in **Fig. 7** is now possible. More specifically, when a particular rough surface area on a transparent material absorbs laser beam, the surface

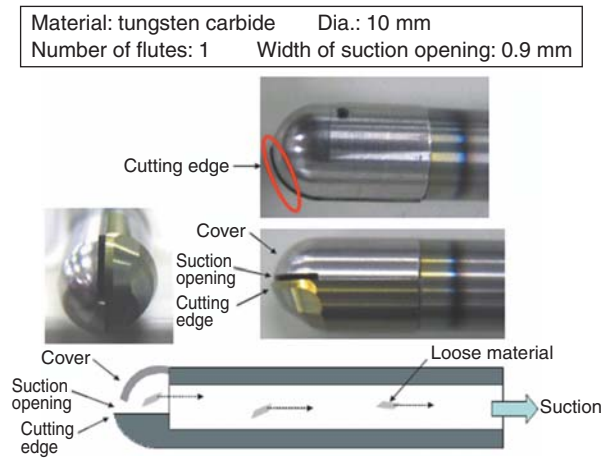

Fig.4 Suction type ball end mill

Fig.5 Finishing of cavity-type die with suction type tool

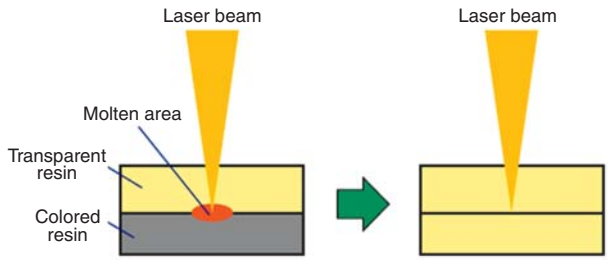

Fig.6 Conventional laser lap welding vs. laser lap welding technique for joining resin members

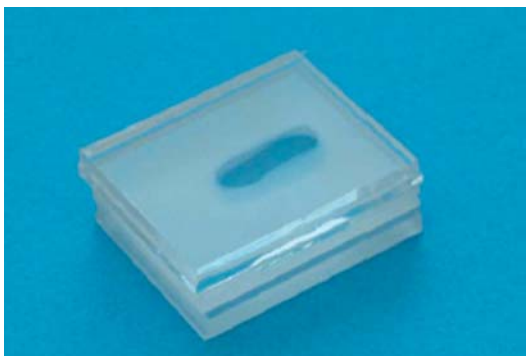

Fig.7 Simultaneous welding of three transparent resin (PMMA) layers

becomes molten and the transparent members begin to weld together. Then the resultant weld becomes transparent and, as a result, heat generation in the weld stops and the welding process automatically ends. This technique can be conveniently used for an application where a plurality of resin members are piled up as demonstrated by **Fig. 7** where completion of welding begins with the layer nearest to the laser beam emitter (although for human eyes welding of the overlapping members appears to take place simultaneously). This technique can be applied to a welding process for a plurality of overlapped thermoplastic members each having a unique melting point. Though useful only for thermoplastic transparent resin materials, this technique is promising for 'Monozukuri" as tribologists are conscious about the usefulness of "surface roughness".

5. Electro-discharge machining for C-FRP material

We have been investigating the material removal mechanism of work-pieces subjected to an electro-discharge machining technique that is often used to machine metal dies. It has been said that in an electro-discharge machining process, thermal energy from an electric discharge melts metal material and causes vaporized machining liquid to splash the molten metal. However, there have been reports denying this claim, based on the observation of machining marks and measurements of machining efficiency. We have prepared a work environment that simulates the actual electro-discharge machining process, developed an instrument that can directly monitor the area being machined, and have recorded pictures of the electro-discharge machining operation using a high-speed video camera. The images captured are amazing: immediately after the electric discharge, a bubble made of vaporized machining liquid expands, and then red-hot metal debris flying from the discharge point collides with the inner wall of the bubble and is stopped[7]. In other words, there occurs a collision state when the molten metal spontaneously splashes and the machining liquid contains the discharge point in ultra high-pressure atmosphere for a period of time. This is a very important finding that will help clarify the operating principle of the electro-discharge machining process (we are still investigating detailed mechanism for this process). Textbooks for production engineering classify the cutting process and the grinding process into "removal machining", to which electro-discharge machining belongs too. From a tribologists' viewpoint, removal machining may be regarded as one positive application of wear phenomenon. When we have succeeded in clarifying the working principle of the electro-discharge machining process, we will reach a better understanding of the corrosion wear phenomenon on electric contacts, as well as the ability to propose appropriate measures for preventing corrosion wear of electric contacts. That is, machining and tribology involve common considerations in direct association with each other such as the wear of machining tools but also in understanding the details of machining and tribology. Though the author is not sure if it is good situation—several researchers (including the author) are deeply involved in an interdisciplinary region between these two academic fields.

Furthermore, the suggestion that the electro-discharge machining process could be used to machine a material not attempted before, we have attempted to apply electro-discharge machining technique to C-FRP, a material that is being used more frequently in recent years. At an early stage of research, the technique was unsuccessful—an occurrence-avoidance cycle of short-circuit simply recurred, while the C-FRP work-pieces, consisting of electrically conductive carbon fibers bonded with resin, were not properly machined by the electro-discharge process. Shin-ya Hayakawa, Assistant Professor, and his undergraduate students attempted to determine the optimal machining conditions, thereby machining work-pieces like the one shown in **Fig. 8** with the wire electro-discharge machining process[8]. Though the machining speed is still low, the resultant cross-sectional shape is very clear-cut and the cut faces are free from fluffing. I believe this technique will be useful as a machining technique for certain portions of work-pieces made of C-FRP, a material that will likely be used increasingly on transportation equipment for lighter designs.

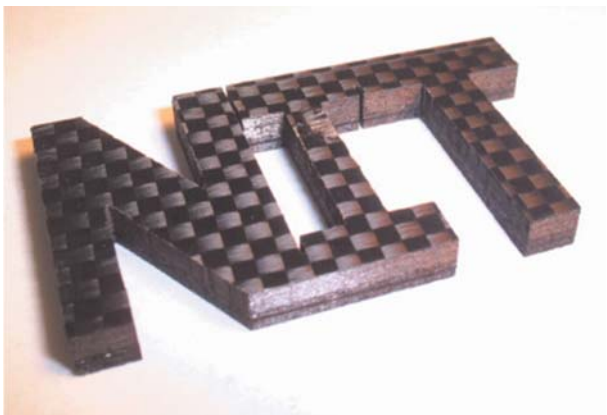

Fig.8 C-FRP material trimmed by wire-electrical discharge machine

6. Break-in process

The feed mechanisms of machine tools have long been manually finished by the '*suriawase*' technique with a scraper ('*suriawase*' in this context means "manual finishing by manual scraping"). Based on the '*suriawase*' principle previously described in Sec. 2, this unique technique gives critical areas in machine tools a higher degree of precision than possible with machining. At the same time, delicate uneven surface patterns formed by scraper finishing helps achieve a higher degree of sliding quality needed for machine tools. As higher speeds are increasingly needed for machine tools, linear rolling bearings are frequently used since they feature lower frictional resistance in wide range of speeds. However, feed mechanisms of machine tools may need to withstand heavy loads and minute load variations and feature highly effective vibration dampening performance. **Fig. 9** graphically plots the sliding characteristics of sliding guide ways reproduced by an experimental rig developed in our laboratory[9].

The graph in **Fig. 9** displays the measurements of the coefficient of friction with a wide speed range with three lubricating oils specially developed for use on slide ways. These characteristic curves appear to differ from ordinary Stribeck curves. The values for the coefficient of friction tend to be smaller in the lower speed region where boundary lubrication occurs (usually the coefficient of friction should remain relatively constant in this speed region). With a certain type of lubricating oil, the coefficient drops below 0.005. The "boundary lubrication region" (i.e. boundary film lubrication region) corresponds to a state where the boundary oil film adsorbed by the slide way surface governs its friction. These specially formulated sliding lubricants form a rigid high-viscosity oil film which mitigates solid contact, leading to the above-mentioned characteristics. These dynamic sliding characteristics are ideal so that the table can be stopped correctly at a specific position with an accuracy of 0.1 μm needed for high efficiency machine tools.

Is it possible to meet the sliding characteristics shown in **Fig. 9** simply by scraping and using a special sliding lubricant? The answer to this question: impossible. In our test, these characteristics were only achieved after break-in operation for more than 20 hours. I have been told that after assembly, machine tools require break-in operation for more than two full days. The author believes that this practice is the ultimate example of the "suriawase process". Next, let us consider what is occurring during the break-in operation of the slide way surfaces. It is said that in an ordinary break-in operation, the high points on the contact surfaces are worn away so that flat working faces are formed. However, the scraping process (having been performed prior to break-in operation) already resulted in 20 bare spots per square inch (class A standard), and fairly smooth working faces. The author thinks that during the break-in operation of a slide way surface having undergone the scraping process, corners of very small individual working faces still have ultra-small peaks. **Fig. 10** graphically illustrates a comparison between the oil pressure on the working faces (drops are provided on both ends of each working face) of the slide way lubricated with a special lubricant, with consideration of the elastic deformation of working faces[10].

This chart corresponds to a situation where the upper working faces shift to the left relative to the lower stationary working faces. Oil pressure occurs at the inlet side of the working faces and the elastic deformation that occurs on each working face allows the oil pressure to be maintained to the midpoint on the working face. Consequently, the working faces support loading without developing solid contact. For this test,

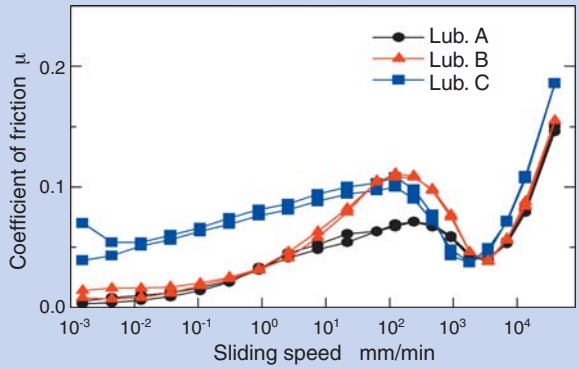

Fig.9 Stribeck curve of sliding lubricant

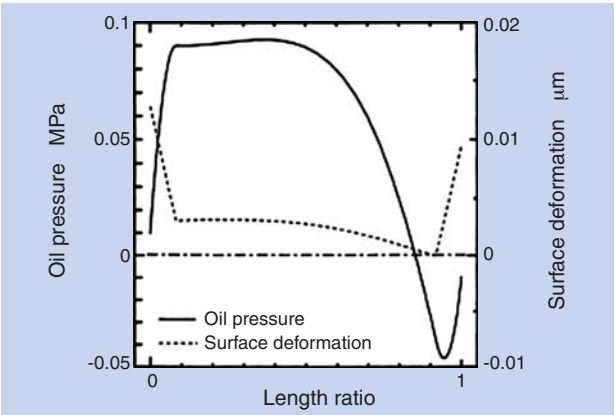

Fig.10 Elastic deformation and oil film pressure of contact surface with droop
(Sliding velocity: 0.10 ms, initial oil film thickness: 1.3 mm)

we have made calculations using oil with ordinary lubricant viscosity. However, when a special sliding lubricant is used and a highly viscous film of adsorbed oil is formed on a sliding guide surface, a greater oil pressure occurs between working faces, thereby allowing the sliding guide surface to develop a higher load bearing capacity[11].

To sum up, a slide way having undergone scraping exhibits an ideal surface quality thanks to the tribological wear process. In other words, this approach helps optimize the boundary film lubrication mode, known as a labyrinth in the field of tribology, according to the intended application by using a lubricant containing an appropriate additive.

7. Conclusion

This paper has presented the author's latest knowledge regarding techniques for machining bearing components. The topics covered include the lapping of steel balls, the suction removal of loose material, the laser lap welding process, the electro-discharge machining process for C-FRP, and the 'suriawase' technique for finishing slide ways. Capable of understanding calculated precision, maternal principle-based machining processes are suitable for mass-production but do not allow for an improvement in precision and performance. 'Suriawase' is a technique used to achieve a higher degree of precision through interactions between materials and tools and necessitates unique techniques and experience that cannot be easily expressed in the form of mathematic formulas or tabulations. The author strongly believes that manufacturers in Japan should remain committed to the creation of products with improved performance through a succession of techniques and experience from previous generations and continue to explore these techniques and experiences. Tribology is an academic field that involves interactions between two surfaces moving in different directions and has many things in common with the 'suriawase' process. Being a specialist in tribology, **NTN** CORP. has been active as a leading bearing manufacturer around the world and has a very dependable presence in Japan.

References

1) F. Itokawa, Research Related to the Precision of Steel Balls used in Precision Machinery—Precision Evaluation Methods, and Analyses of Steel Ball Lapping Processes and Ball Bearing Motion Errors (Doctoral thesis), Nagoya Institute of Technology (1993).
2) Y. Kimura, Industry-University Partnerships in R&D of Machine Elements, NTN Technical Review No. 76 (2008) 2-9.
3) Y. Kimura and H. Okabe, Introduction to Tribology, Yokendo, Ltd. (1982).
4) F. Itokawa et al., Steel Ball Lapping using Laps with V-shape Grooves, Transactions of the Japan Society of Mechanical Engineers, Series C, Vol. 59, No. 562 (1993) 304-310.
5) T. Nakamura et al., The Present Status of Environmentally Friendly Machining and its Future, Journal of Japanese Society of Tribologists, Vol. 53, No. 1 (2008) 21-26.
6) M. Yamakawa et al., Study on Laser Welding of Transparent Thermoplastic Resin Plates, Transactions of the Japan Society of Mechanical Engineers, Series C, Vol. 74, No. 744 (2008) 149-153.
7) S. Hayakawa et al., Observation of Bubble Expansion and Flying Debris in Parallel Flat Gap Space in Electrical Discharge Machining, International Journal of Electrical Machining, No. 14 (2009) 29-35.
8) T. Ito et al., Test Applications of Electric Discharge Machining of Carbon Fiber-Reinforced Polymer (CFRP), 2010 Japan Society for Precision Engineering Spring Meeting Academic Lecture Proceedings, CD-ROM (2010) 577-578.
9) T. Norihisa et al., Development of Friction Test Apparatus for Slide-Guide Way of Machine Tool, Journal of Japanese Society of Tribologists, Vol. 52, No. 9 (2007) 45-52.
10) T. Nakamura et al., Isoviscous-EHL Mechanism of Parallel Slide-Way with Oil Groove, Journal of Japanese Society of Tribologists, Vol. 44, No. 4, pp. 42-48 (1999).
T. Norihisa et al., Study on Velocity-Dependent Property of Friction in Boundary Lubrication under Low Contacting Pressure Condition (Part 2)—Consideration into Mechanism of Velocity-Dependent Property of Friction Lubricated with Oil Containing Alkyl Acid Phosphate, Journal of Japanese Society of Tribologists, Vol. 53, No. 10 (2008) 51-58.
11) W.C. Oliver and G.M. Pharr: An improved technique for determining hardness and elastic modules using load and displacement sensing indentation experiments, J. Mater. Res., Vol.7 No.6, 64, 1992

<Author's profile>

Takashi Nakamura
Professor, Vice President, Nagoya Institute of Technology (NIT), D. Eng.

1975 Graduates from Industrial Mechanical Engineering Dep., College of Engineering, NIT
1977 Completes master's course at Mechanical Engineering Dep., NIT
1980 Completes doctoral course for mechanical engineering at Nagoya University
1980 Assistant at Nagoya University
1982 D. Eng. (Nagoya University)
1983 Instructor at NIT
1987 Assistant professor at NIT
2000 Professor at NIT
2005 Professor at Graduate School, NIT
2010 Vice President, NIT

[Technical Article]

Technical Trend of Machine Tool Bearings

Hiroshi TAKO*
Yasutsugu TANAKA**

For machine tool bearings, high- speed, high rigidity and high accuracy are important. Recently, reducing environmental impacts and costs have also become important.
This paper gives an overview of technical trends for machine tool bearings and explains current machine tools.

1. Introduction

Machining efficiency and machining quality are two criteria historically common to the machine tool industry. Current economic times call for additional criteria, those being reduced machining cost and a decrease on environmental impacts. To address these challenges, bearing manufacturers are committed to the development of improved materials and the optimization of bearing internal design. As a result, the performance of main spindles and feed systems will improve due to higher speeds, higher rigidity, improved lubrication, and better overall accuracy.

This paper will present the recent engineering trends of machine tool bearings and introduce products **NTN** has developed to meet these requirements.

2. Recent engineering trends of machine tools and machine tool bearings

Though there are signs of recovery from the 2008 global recession, worldwide demand in the machine tool market remains sluggish. China, whose manufacturing output was largest in the world in 2009, is rapidly improving their machine tool industry and will soon equal the technology of Japanese and European machine tool industry.

Due to the slow recovery and the increased impact of the Chinese market, machine tool development in Japan has been divided in two directions. The first being high-end machines featuring improved machining efficiency and accuracy as well as the capability of processing larger parts. The second option is for lower-cost general purpose machines accomplished through utilization of common components, lower machining accuracy, and limited part size capability. **NTN** has designed machine tool bearings for both the high-end and general purpose markets.

NTN has been developing machine tool bearings focusing on attaining both high speed performance and higher rigidity (two conflicting requirements), as well as higher accuracy and eco-friendliness. In this context, **NTN** has been developing unique machine tool bearings to support further sophistication of functionality for 5-axis machine tools and CNC turning centers.

As for the increased interest in general purpose machine tools, **NTN** has been helping reduce both the cost and size of main spindles by developing various technology, including grease-lubricated bearings that do not need an additional lubricating oil supply system.

3. Engineering trend of NTN's machine tool bearings

Fig. 1 illustrates engineering improvements in **NTN**'s precision bearings for machine tools.

3.1 Engineering trend of NTN's angular contact ball bearings

In the 1980s, need for high-speed main spindles began, resulting in the development of high-speed angular contact ball bearings. **NTN**'s efforts in

* Industrial Business HQ. Industrial Engineering Dept.
** Industrial Business HQ.

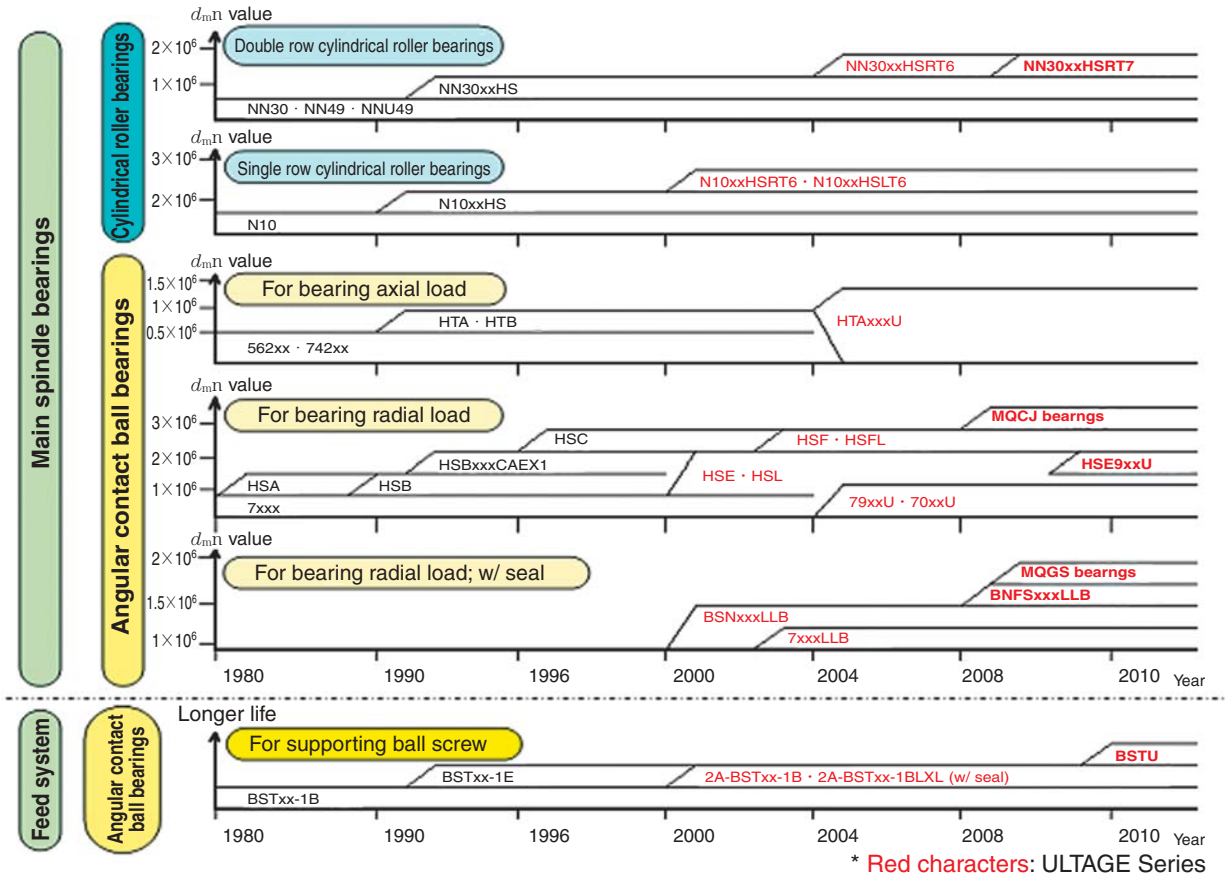

Fig. 1 Development history of precision bearings for machine tool

developing high speed angular contact ball bearings began with HSA bearings that are similar to standard types but feature smaller diameter rolling elements. Around 1990, **NTN** developed "**HSB bearings**" that were improved HSA bearings featuring limited heat generation, as well as "**HSBxxxCAEX1 bearings**" that are capable of even higher speed. In 2000, **NTN** released "**ULTAGE Series high-speed angular contact ball bearings**—also known as HSE Bearings" that utilize bearing rings made from special bearing steel featuring excellent wear resistance and anti-seizure quality. Thanks to use of special bearing steel, HSE bearings are capable of greater mounted preload compared with conventional bearings. Thus, they feature both high-speed performance and greater rigidity, helping greatly enhance functionality of the machine tool main spindles they support.

Furthermore, **NTN** marketed "**HSF bearings**" in 2002. Compared with the HSE bearings, the diameter of their rolling elements is much smaller. **NTN** developed this new series of bearing products as air-oil lubricated constant preload bearings for ultra-high speed main spindles on machine tools such as die machining machines.

Main spindle bearings allowing for higher speed helped improve the efficiency of machining and the quality of machined surfaces. Recently, need for higher speeds with these bearings have decreased as the demands for die machining machines have been sluggish. Instead, there has been an increase in the needs for cost reduction and size reduction of machine tools.

To address this market trend, **NTN** has recently developed the **"New 9-Series High-Speed Angular Contact Ball Bearings (HSE9xxU)"** and **"Ball Screw Supporting Double Row Angular Contact Ball Bearings (BSTU)"**. These two product lines will be later described in further detail in Sec. 4 "Introduction to **NTN**'s Newly Developed Bearings".

3.2 Engineering trend of NTN's cylindrical roller bearings

Single-row cylindrical roller bearings are often used to support machine tool equipment main spindles. As a result of creating high-speed angular contact ball bearings for machine tools, it was now required to increase the speed capabilities of the supporting cylindrical roller bearings. To address this challenge, **NTN** developed the "**N10xxxHS bearings**" that feature a smaller roller diameter verses that of the

standard **NTN** single row cylindrical roller bearings. In 2000, **NTN** developed the ULTAGE Series "**N10xxHSRT6 Bearings**" that incorporate a PEEK resin cage which allow an even higher speed when used with main spindle bearings. In 2004, a similar modification was made to double-row cylindrical roller bearings NN30xx often used to support turning center main spindles. This resulted in the high-speed double row cylindrical roller bearings "**NN30xxxHSRT6 bearings**" that incorporate PEEK resin cage.

3.3. NTN's technology for improving bearing accuracy

There are JIS accuracy classes, equivalent to those specified in a corresponding ISO standard. Machine tool main spindles often use bearings of JIS accuracy class 4. Applications that need particularly high bearing accuracy employ bearing of JIS accuracy class 2.

As stated previously, there are additional needs in the machine tool bearing market including: bearing users who want both high accuracy and low cost, bearings of special accuracy, or those satisfying both JIS accuracy class 2 in terms of running accuracy and JIS accuracy class 4 in terms of dimensional accuracy. To meet these needs, **NTN** added a unique line of products whose accuracy class is categorized into "P42" as standard bearings to the "**Sealed Standard Angular Contact Ball Bearings 7xxCD/ADLLB Bearings**" series products that were developed for use on rotary tools.

Main spindles attaining much higher accuracy employ unique bearings whose NRRO (Non-Repetitive RunOut) has been decreased by limiting variation in the diameter of rolling elements and regulating bearing ring roundness.

NTN offers angular contact ball bearings in two levels of NRRO—0.3 mm or smaller, and 0.1 mm or smaller. These angular contact ball bearings are used in main spindles of high-precision machining and turning equipment.

3.4 NTN's eco-friendly bearing technology

Around 2000, machine tool manufacturers started their efforts reducing environmental impacts, lowering power consumption, and improving work environments.

On the basis of its ULTAGE Series bearings, **NTN** has established new lines of eco-friendly bearing products illustrated in **Fig. 2**: the "**HSL bearings**" that are based on the HSE bearings, the "**HSFL bearings**" that derive from the HSF bearings, and the "**N10xxHSLT6 bearings**" that are essentially improved N10xxHSRT bearings. These eco-friendly bearings are unique in that lubricating oil is fed through a special nozzle into the bearing, thus helping reduce consumption of compressed air and oil 50% to 75% compared with those of conventional bearings. At the same time, noise level of the bearing is reduced by limiting the flow of compressed air interfering with

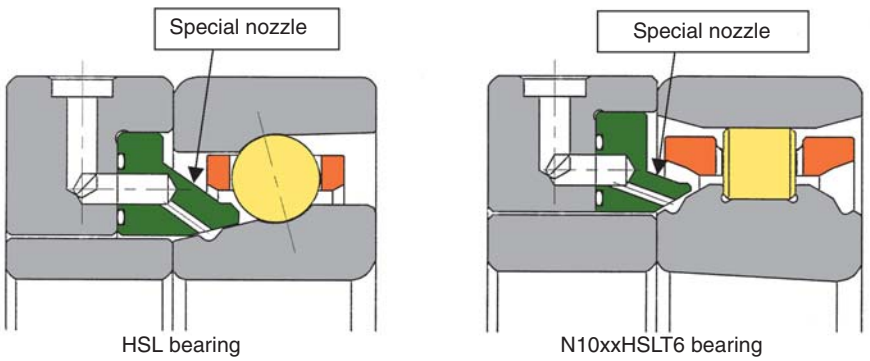

Fig. 2 Eco-friendly air-oil lubricated bearing

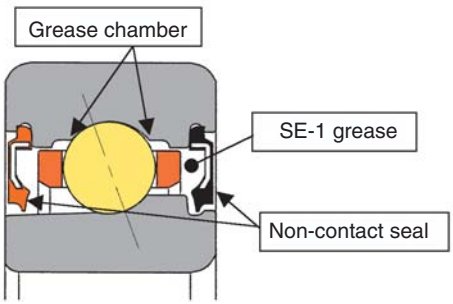

Fig. 3 BNS bearing

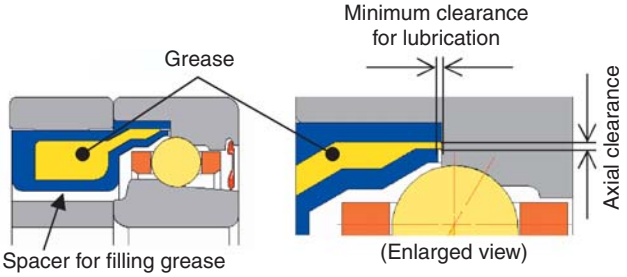

Fig. 4 MQGS lubrication bearing

the rolling elements, thereby these air-oil lubricated, eco-friendly machine tool bearings contribute to reduction in consumption of energy and resources as well as improved work environments.

Use of grease-lubricated bearings can also contribute to reduction in consumption of compressed air, oil, and electricity. Since 2000, **NTN** has been developing the "**BNS/BNFS bearing**" products shown in **Fig. 3.** These bearings feature grease chambers on the outer ring rolling surfaces, a non-contact seal, and high-speed long-life grease "SE-1", all of which contribute to the improved reliability of grease-lubricated machine tool bearings.

Thanks to these improvements, higher speed is also now possible with grease-lubricated bearings. In other words, air-oil lubricated bearings typically used in higher speed machine tool applications can be replaced with grease-lubricated bearings.

NTN made another innovation in 2008—the "MQGS Lubrication Bearings (d_{mn}: 1.9×10^6)", schematically illustrated in **Fig. 4**. This bearing design features a unique spacer that delivers a minimum amount of base oil to the outer ring rolling surface in order to help extend grease life and improve the high-speed capability of the bearing.

4. NTN's newly developed machine tool bearings

4.1 New 9 series high speed angular contact roller bearings

As shown in **Fig. 5**, the cross-sectional area of 9 series angular contact ball bearings (often used in the European market) is smaller compared with 0 series angular contact ball bearings (commonly used in Japan). As a result, the same size spindle can be used in a more compact housing, or alternately, a larger, more rigid spindle can be used in an equivalent sized housing.

One disadvantage is that the load capacity of the 9 series bearings are smaller compared with the 0 series bearings due to their smaller cross-sectional area.

To address this drawback, **NTN** has developed the "**HSE9xxU bearings**" that feature the high-speed performance of the HSE9 series bearings. Optimal specifications for bearing internal design have led to 50% increase in dynamic load rating and 20% increase in axial load rating relative to conventional similar bearing products.

Thanks to this engineering development, it is now possible to design compact, high-speed, high-rigidity main spindles employing 9 series angular contact ball bearings.

Detailed information about the **high-speed angular contact bearings—9 series HSE9xxU** bearings will be provided in a separate article within this technical review.

4.2 Ball screw supporting bearings

In the Asian machine tool industry, ball screw supports employ duplex angular contact ball bearings. In the same application, European machine tool industries use double-row angular contact ball bearings whose outer rings have mounting holes. The advantages of this bearing type include a simpler mounting procedure, a decreased number of parts since the bearing can be mounted directly to the bearing housing, and no need to match bearing pairs.

To its ULTAGE series of bearing product, **NTN** has added the "**double row angular contact ball bearings BSTU for supporting ball screws**" schematically illustrated in **Fig. 6.** This bearing type is essentially double-row angular contact ball bearing with the outer ring having mounting holes mentioned above, except that the BSTU bearing has a uniquely shaped seal. Features of this bearing include high-load capacity, low contact pressure and low torque, as well as long-life grease.

Detailed information about the **double-row angular contact ball bearings BSTU bearings** will be provided in a separate article within this technical review.

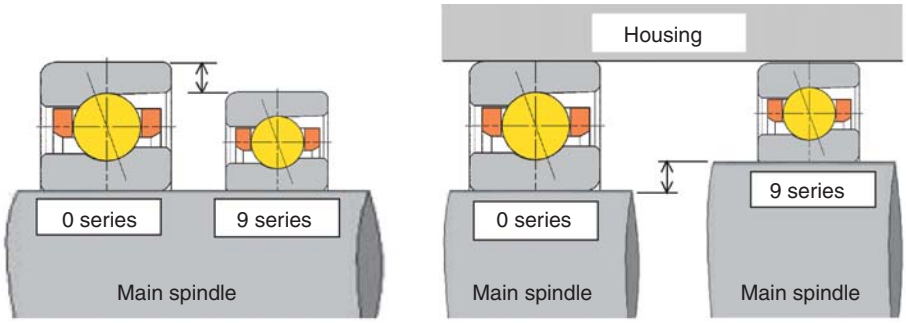

Fig. 5 High-speed angular contact bearings new 9 series

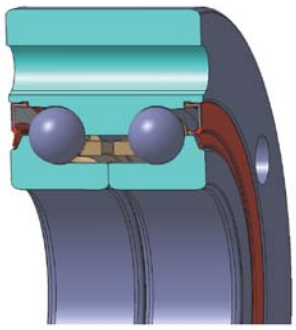

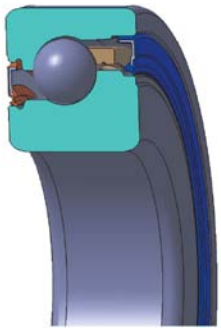

Fig.6 BSTU bearing　　BST Bearing (Current)

5. Conclusion

With its unique ULTAGE series of bearings, **NTN** has been helping machine tool manufacturers satisfy the ever demanding engineering needs for their machine tool products.

Machine tool manufacturers have experienced a dramatic change in engineering trends for machine tools—from higher functionality to reduction in cost and size. We believe that the most challenging needs in the machine tool industry may vary as the market demands will vary. Typical examples of engineering challenges include eco-friendly technology, higher functionality, and cost reduction.

In order to address the ever changing engineering trends in bearing industry and to contribute to the engineering development of machine tools, **NTN** will continue to be committed to the development and improvement of its bearing technology.

Photo of authors

Hiroshi TAKO

Industrial Business HQ.
Industrial Engineering Dept.

Yasutsugu TANAKA

Industrial Business HQ.

Application of Ceramics to NU-Type Cylindrical Roller Bearings for Machine Tool Main Spindles

Masatsugu MORI*
Takuji KOBAYASHI*

Ultra-high-speed operation of an air-oil lubricated NU-type cylindrical roller bearing has been made possible by using a ceramic inner ring. A maximum speed of up to 35,000 min^{-1} is possible ($d_m n$ value of 3.25 million, inner ring bore of 70 mm). Devising the outer ring rib structure to streamline lubricant drainage resolves the occurrence of high and broad temperature rises around the mid-speed range, which is typical of conventional NU-type cylindrical roller bearings, as well as rapid temperature rises at high shaft speeds. The developed bearing will allow the practical application of NU-type cylindrical roller bearings to machine tools that require high bearing stiffness over a wide range of operation speeds. The cage made of PEEK is guided on the air-oil nozzle outside surfaces, while rollers made of steel can be used even at 35,000 min^{-1} and control the inner ring temperature below 70˚C.

1. Introduction

Bearings used to support main spindles on machine tools need to be capable of higher speed and greater rigidity. This is true since any main spindle that turns together with a tool or work piece mounted onto it is one of the critical machine tool components that directly affects machining efficiency and accuracy of the machine tool, and the bearings that support the main spindle are the most critical machine elements on the machine tool [1]. Other mechanical characteristics any main spindle bearing needs to satisfy include higher bearing accuracy, lower vibration, and lower noise. Rolling bearings are most often used to support main spindles because they satisfy various requirements, including cost-effectiveness and maintainability of balance compared with hydrodynamic (static or dynamic pressure) bearings and magnetic bearings.

Typical rolling bearing types used to support machine tool main spindles are angular contact ball bearings, cylindrical roller bearings, and tapered roller bearings. In particular, cylindrical roller bearings are preferred as non-locating bearings because they boast higher load capacity and greater rigidity in the radial direction, and their inner and outer rings are capable of moving in the axial direction relative to the main spindle. Since requirements appear to be increasing for higher speed with the fixed position preload bearing system (which features greater rigidity) for rolling bearings on machine tool main spindles, capability for much higher speed will be needed for rear-position (that is, free-side) single row cylindrical roller bearings.

To address this challenge, we attempted to use ceramic inner rings (this topic will be described in detail later) to prevent occurrence of excessive preload that will pose a direct obstacle against achievement of higher main spindle bearing speed. In a previous **NTN** Technical Review [2], we already reported our experience in developing the N-type cylindrical roller bearings series having ceramic inner ring (featuring double rib inner ring)—this cylindrical roller bearing type, lubricated with an air-oil lubrication system, achieved ultrahigh-speed bearing operation as fast as $d_m n$ (bearing pitch diameter mm × inner ring running speed min^{-1}) value = 3.25×10^6. This speed level is equivalent to that obtained from not-yet-mounted ultrahigh-speed constant-pressure preloaded angular contact ball bearings [3]. However, the N-type is uniquely structured in that its ceramic inner ring is tightly fitted with steel spacer rings also serving as ribs: therefore, a simpler-structured ceramic inner ring has been needed to simplify formation and mounting of inner ring.

To address this challenge, we have developed NU-type cylindrical roller bearings (featuring double-rib outer ring) that have ceramic rings lacking spacer rings, and achieved ultrahigh-speed bearing operation as fast as $d_m n$ value = 3.25×10^6 with air-oil lubrication. This article reports the performance of our new engineering development.

*Elemental Technology R&D Center

Use of ceramic materials in elements of rolling bearings has long been proposed [4]. In the technical field of machine tools, there have been an increasing number of cases [6] where ceramic rolling elements are used in angular contact ball bearings in order to inhibit adverse effects of gyro-moment [5] that poses problems in particular with machine tool main spindles running at higher speeds. However, there have been a limited number of applications of ceramic materials to cylindrical roller bearings for machine tools. In addition to the information already presented in **NTN** Technical Review (No. 76) [2], we want to provide additional information in this Technical Review in order to demonstrate that by utilizing benefits of ceramic materials, cylindrical roller bearings can offer high-speed performance comparable to that of constant-pressure preload angular contact ball bearings.

2. Structure, and elemental technologies for high-speed operation

Fig. 1 shows a cross-sectional view of the **NTN**'s newly developed NU-type cylindrical roller bearing.

The structure of the NU-type cylindrical roller bearing in **Fig. 1** is characterized as follows: the inner ring is made of silicon nitride (Si_3N_4), which is a structural ceramic material; the cage is made of PEEK (polyether ether ketone); the bore surface of the cage rides on the outer circumferential surface of the air-oil nozzle spacer; the rollers and outer ring are made of common bearing steel (SUJ2); the outer ring is fitted with oil drain spacers that doubles as ribs, and lubricating oil is drained via the gaps (marked with a red circle) between the outer ring and oil drain spacer/rig.

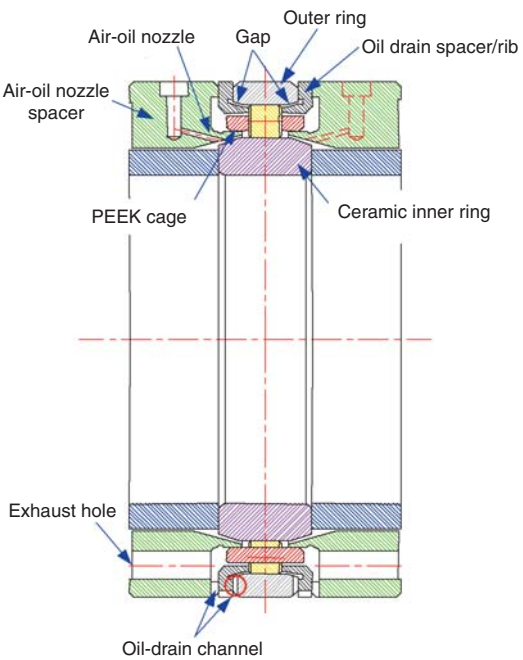

Fig.1 Developed NU-type cylindrical roller bearing

One characteristic that any machine tool main spindle bearing needs to satisfy is avoidance of excessive preload. On a cylindrical roller bearing, the inner ring and outer ring freely move relative to each other in the axial direction, so no axial preload occurs. On the other hand, a problem can occur in the radial direction: the inner ring expands owing to heat buildup and greater centrifugal force resulting in particular from high-speed bearing operation, leading to over-preload radially; heat buildup increases between the rollers and raceway surface; the resultant rapid temperature rise can potentially lead to bearing failure. In machine tool main spindles, jacket cooling is typically provided on the outer surface side of outer ring, which is a stationary body, in order to prevent heat generation on the main spindle system from adversely affecting the entire machine tool. Temperature on the inner ring side can readily rise because of heat generation on the bearing and built-in motor, as well as a structure that does not readily release heat; consequently, a steep heat gradient occurs across the inner ring and outer ring, and preload on the bearing at higher speed can be excessively large. Therefore, problem-free high-speed operation of bearing is possible through reduction of heat generation inside the bearing and thermal expansion of the bearing.

Based on the above-mentioned assumption, the elemental technologies for the elements inside the bearing that allow higher speed operation will now be described. First, the physical properties of ceramic material (silicon nitride) are compared with those of steel for the inner ring as summarized in **Table 1**. Low linear expansion coefficient of the ceramic material (30% of that of the steel material) very much helps inhibit the thermal expansion of the inner ring. Though the physical density of this ceramic material is as low as 40% that of the steel material, the modulus of longitudinal elasticity with the ceramic material is 150% as great as the steel material, and, at the same time, difference in Poisson's ratio between these two materials is very small. Consequently, the centrifugal expansion on the inner ring is limited to approximately

Table 1 Properties of Si_3N_4 and steel

	Si_3N_4	Steel
Linear expansion coefficient 1/K	3.2×10^{-6}	11×10^{-6}
Density kg/m^3	3.2×10^{3}	7.8×10^{3}
Modulus of longitudinal elasticity GPa	314	211
Poisson's ratio	0.26	0.3

30%. More specifically, compared with the steel inner ring, increase in preload is reduced with the ceramic inner ring, and heat generation inside the bearing is more efficiently prevented.

As previously reported in **NTN** Technical Review 76[2], it is important with a cage riding system that lubricating oil of controlled temperature is always supplied to the cage lands, and is promptly drained away to prevent the lubricating oil (which has become very hot from shear heat generation) from remaining on the guide surface. This arrangement helps inhibit heat buildup in the bearing. As shown in **Fig. 1**, the lubricating oil ejected from the air-oil nozzle together with compressed air hits the ramp of the rotating inner ring, then rises along the ramp by surface tension and centrifugal force working on it, and lubricates the rollers and raceway surface. At the same time, driven by compressed air, the lubricating oil passes the cage riding clearance from the inside of the bearing and is drained away. In other words, fresh lubricating oil is always supplied into the cage lands and then promptly drained away from the bearing.

Another unique arrangement has been incorporated into the oil-drain structure in the outer ring side. When the bearing is running at a higher speed in particular, the fresh lubricating oil supplied into the bearing tends to remain in the vicinity of the bore of outer ring because of the centrifugal force working on it. An excessive amount of lubricating oil remaining in and around the bore of outer ring will lead to increase in stir resistance and, as a result, heat generation inside the bearing. Compared with the N-type bearings, this tendency is more apparent with the NU-type cylindrical roller bearings whose outer ring include ribs. Therefore, for trouble-free high speed bearing operation, the oil-drain structure on the outer ring side needs to incorporate a special solution.

For the purpose of comparison, the N-type cylindrical roller bearing presented in **NTN** Technical Review 76 [2] is illustrated in **Fig. 2**.

The structure of this bearing is characterized in that its ceramic inner ring is fitted with spacer rings on both ends. The ceramic inner ring is interference-fit onto the shaft while the ring spacers are slip-fit onto the shaft. To be able to replace the steel inner ring on the N-type cylindrical roller bearing with a ceramic inner ring, it is necessary to use a ring with integrated ribs or fitted with separate ribs. Compared with the NU-type bearing in **Fig. 1**, either ceramic inner ring variant described above complicates the inner ring design – this “ceramic-based solution” poses a drawback of significantly increased machining costs, as ceramic material machining cost is much higher compared with steel. To the advantage of the N-type bearings, the

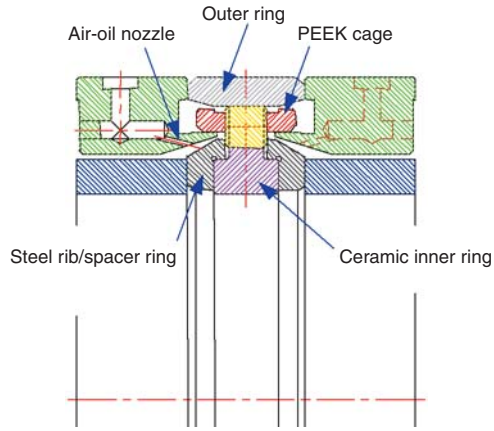

Fig.2 N-type cylindrical roller bearing with a ceramic inner ring

outer ring does not have a rib—lubricating oil thrown to the outer ring side by centrifugal force therefore does not tend to remain in the bearing. Note that the cage riding system and material of the cage in the N-type bearings are essentially identical to those of the **NTN**’s newly developed NU-type bearings shown in **Fig. 1**.

3. Oil-draining capability and high-speed running performance of NU-type cylindrical roller bearings

Considering the oil-draining performance of the NU-type cylindrical roller bearings mentioned in Sec. 2, we have developed various bearing prototypes. In this section, we will describe the result of our investigation into temperature-dependent characteristics of these prototypes being run at various speeds. These prototypes are essentially NU-type cylindrical roller bearings, categorized into “standard oil-drain structure variant, “oil-drain groove variant”, and “oil-drain hole variant”—their structures are schematically illustrated in **Figs. 3**, **4** and **5**, respectively.

In the standard oil-drain structure variant shown in **Fig. 3**,, the inner ring is made of steel (SUJ2) while the rollers are made of ceramic material. The outer ring rib is independent of the outer ring, the PEEK cage is the nozzle outer surface riding type shown in **Figs. 1** and **2**: however, the oil-drain structure on the outer ring side is the standard type.

The oil-drain groove variant in **Fig. 4** is unique in that a separate outer ring rib is provided, wherein the fresh lubricating oil flows through the gaps on both ends of rollers and the gap between the outer ring and rib toward the outer surface side of outer ring, and the heated lubricating oil is drained away from the bearing through the groove formed on the outer surface of outer ring.

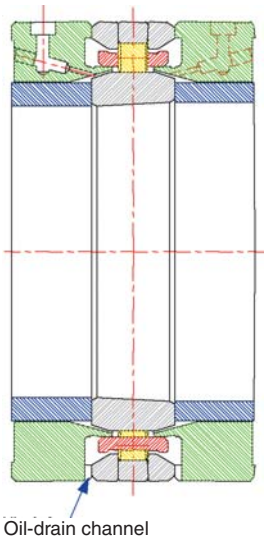

Fig.3 Standard structure NU-type cylindrical roller bearing

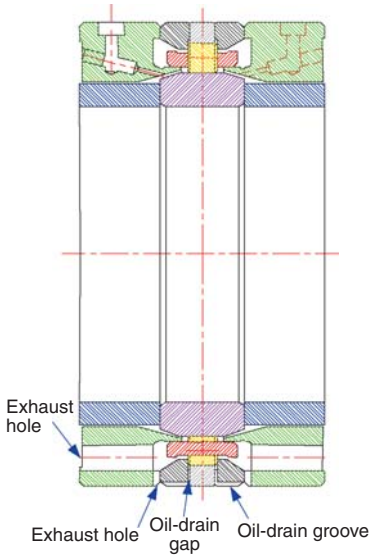

Fig.4 Oil-drain groove structure NU-type cylindrical roller bearing

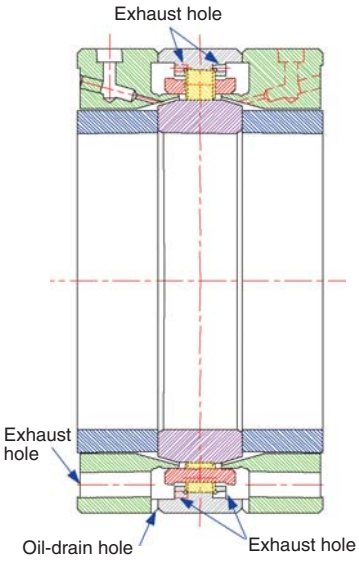

Fig.5 Oil-drain hole structure NU-type cylindrical roller bearing

On the oil-drain hole variant in **Fig. 5**, outer ring ribs on both sides each have six equally spaced oil-drain holes toward their outer circumference in order to direct the heated lubricating oil to the outside of bearing, wherein the phases of both outer ring ribs are shifted with each other so that the locations of the oil-drain holes on one outer ring rib are not directly opposite to the oil-drain holes on the other outer ring rib.

Note that the oil-drain groove variant (**Fig. 4**) and oil-drain hole variant (**Fig. 5**) both have inner rings and rollers made of ceramic material, and the PEEK cage is riding on the outer circumferential surface of the air-oil nozzle.

Major technical data of these test cylindrical roller bearings and test conditions are summarized in **Table 2**, while the cross-sectional view of the spindle test rig used throughout our present development work is illustrated in **Fig. 6**. The test result obtained from the NU-type cylindrical roller bearings of **Figs. 3** through **5** is illustrated graphically in **Fig. 7**.

From the graphs in **Fig. 7**, it should be understood that apparent temperature peaks occur at around 10,000 min^{-1} with all designs – the “standard oil-drain structure variant”, “oil-drain groove variant”, and “oil-drain hole variant”. This is the major reason why the NU-type bearings have not yet been used as air-oil lubricated cylindrical roll bearings for machine tools. Therefore, the challenges for the present development work were to increase the maximum allowable bearing speed, as well as providing a bearing that can maintain its rigidity in a wider speed range without developing heat buildup – all in an economically viable design. The original objective of our development work for prototypes of the oil-drain groove variant and the oil-drain hole variant was to improve oil-draining performance at higher bearing speeds. Though the maximum allowable bearing speed with the oil-drain groove variant reached 35,000 min^{-1}, the temperature peak in the medium speed range at around 10,000 min^{-1} still persists with either variant. Note that the test for standard oil-drain structure variant and oil-drain

Table 2 Test bearings (**Figs. 3**～**5**) and conditions associated with **Fig. 7**

Standard oil-drain structure variant	Cross-sectional plan	**Fig. 3**
	Size	ϕ70×ϕ110×20
	Pitch diameter	93mm
	Inner ring	SUJ2 (tapered hole: 1/12 bore diameter)
	Outer ring	SUJ2
	Rollers	Si_3N_4, ϕ7×7, 22 pcs.
	Cage	PEEK+CF30%, Nozzle outer surface riding
Oil-drain groove variant	Cross-sectional plan	**Fig. 4**
	Size	ϕ70×ϕ110×20
	Pitch diameter	93mm
	Inner ring	Si_3N_4 (cylindrical bore)
	Outer ring	SUJ2
	Rollers	Si_3N_4, ϕ7×7, 22 pcs.
	Cage	PEEK+CF30%, Nozzle outer surface riding
Oil-drain hole variant	Cross-sectional plan	**Fig. 5**
	Size	ϕ70×ϕ110×20
	Pitch diameter	93mm
	Inner ring	Si_3N_4 (cylindrical bore)
	Outer ring	SUJ2
	Rollers	Si_3N_4, ϕ7×7, 22 pcs.
	Cage	PEEK+CF30%, Nozzle outer surface riding
Test conditions	Initial radial clearance -3 – -4 mm Bearing lubrication Air-oil ISO VG32 Oil is supplied from both sides of bearing. 0.01cm^3 / 10 min×2 Jacket cooling temperature Room temperature ±1˚C	

hole variant was suspended because of sudden temperature rise.

To be able to find a solution, we first assumed the cause for this temperature peak was poor oil-draining performance, and attempted to verify this assumption. **Fig. 8** includes two sets of data obtained from two cases of bearing operation shown in **Fig. 4**—one case corresponds with a scenario where a sufficient amount of air-oil mixture was supplied to the bearing prior to operation, while in the other scenario, no air-oil mixture was supplied to the bearing prior to operation.

In the two cases in **Fig. 8**, the test bearings were quickly accelerated to 13,000 min^{-1} while being lubricated with an oil-air flow rate of 0.01 cm^3/10 min × 2. In the scenario in **Fig. 8 (a)**, air-oil mixture was supplied to the test bearing for 90 minutes prior to the test operation, while in the scenario in **Fig. 8 (b)**, no air-oil mixture was supplied to the test bearing prior to start of the test operation. When comparing the data in the scenario **(a)** with that of the scenario **(b)**, the heat rise on the inner ring with the scenario a is approximately as much as 30˚C higher and that on the outer ring is approximately as much as 15˚C higher. From these findings, we suspect the cause of the temperature peak at the medium speed range is “residual heated lubricating oil” remaining in the bearing. Therefore, an oil-drain structure boasting positively efficient oil-draining capability in both high-speed and medium-speed ranges is needed. Also, since such temperature peaks do not occur with the N-type bearings, we feel we should consider oil-draining behavior at around the outer ring rib, and

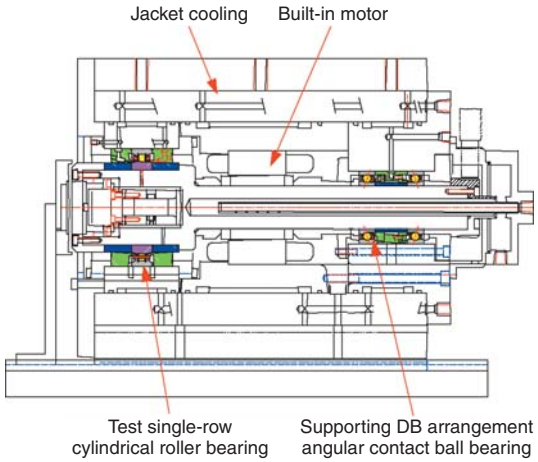

Fig.6 Section view of spindle test rig

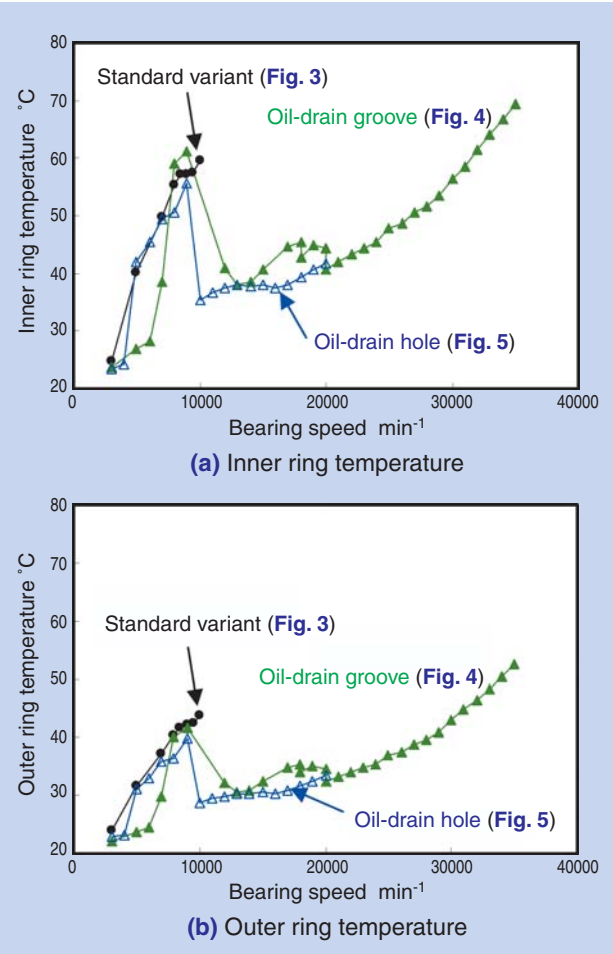

Fig.7 Inner and outer ring temperatures vs. rotational speed

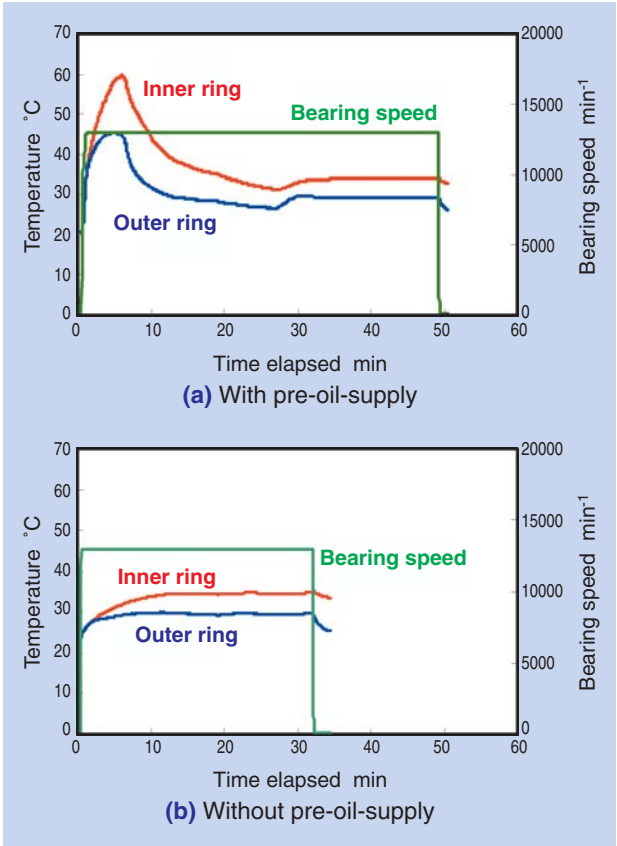

Fig.8 Pre-oil-supply and temperature rise

believe that this approach will lead to improved oil-draining capability on the outer ring side of the bearing running at a higher speed.

Starting with these findings, we have further continued with review and prototyping activities and have finally reached the current cylindrical roller bearing structure (NU-type) shown in **Fig. 1**. The test conditions associated with these activities are summarized in **Table 3**. Test results from the NU-type bearing and those from the N-type bearing in **Fig. 2** [2] are shown in **Fig. 9**. **Fig. 9 (a)** shows the test data from bearing samples with ceramic rollers, while **Fig. 9 (b)** gives the test data from bearing samples with steel rollers.

As is shown in **Fig. 9 (a)**, the samples of the newly developed NU-type as well as those of the N-type do not show a temperature peak in the medium speed range at around 10,000 min^{-1}, and exhibit smooth temperature rise curves up to the targeted maximum running speed of 35,000 min^{-1} ($d_m n$ value=3.25×10^6). Compared with the N-type, the inner ring temperature on the NU-type at 35,000 min^{-1} is 2˚C lower. Also, as apparent from the test data of the NU-type samples in the data in **Fig. 9 (b)**, there is no temperature peak at around 10,000 min^{-1}, and the temperature slowly increases up to 35,000 min^{-1}. The inner ring temperature at 35,000 min^{-1} reads 70˚C which is 4˚C lower compared with the N-type—a very favorable achievement.

From these findings, it has been verified that the bearing configuration illustrated in **Fig. 1** (NU-type), which comprises the ceramic inner ring (no spacer rings), the cage riding on outside surface of air-oil nozzle, and the outer ring having oil-drain gaps, does not exhibit the temperature peak in the medium speed range, and can be run up to ultrahigh-speed range without developing sudden temperature rise. With a variant of this bearing configuration that uses steel rollers rather than ceramic, the inner ring temperature at 35,000 min^{-1} is limited to 70˚C, which is the maximum allowable temperature for commercially acceptable bearing operation. Compared with the N-type in **Fig. 2** [2], the NU-type has the simpler-shaped ceramic inner ring as well as steel rollers, allowing this bearing to be offered at a commercially acceptable price.

By the way, it is apparent that use of the ceramic inner ring has helped achieve problem-free high-speed operation of the bearing. However, use of ceramic material in a bearing leads to additional benefits. When a bearing having a steel inner ring is run at a higher speed, bearing fit to the shaft can get loose owing to expansion of inner ring bore resulting from heat and centrifugal force occurring from bearing operation: to prevent loosening of the bearing relative

Table 3 Test bearings (**Figs. 1** and **2**) and conditions associated with **Fig. 9**

Newly developed NU type	Cross-sectional plan **Fig. 1** Size ϕ70×ϕ110×20 Pitch diameter 93mm Inner ring Si_3N_4 (w/o steel spacer rings) Outer ring SUJ2 Rollers Steel or Si_3N_4, dia. ϕ7×7mm, 22 pcs. Cage PEEK+CF30%, Nozzle outer surface riding Fit between shaft and inner ring 5 μm, interference-fit
N-type with ceramic inner ring	Cross-sectional plan **Fig. 2** Size ϕ70×ϕ110×20 Pitch diameter 93mm Inner ring Si_3N_4 (w/ steel spacer rings) Outer ring SUJ2 Rollers Steel or Si_3N_4, dia. ϕ7×7mm, 22 pcs. Cage PEEK+CF30%, Nozzle outer surface riding Fit between shaft and inner ring 2 μm, interference-fit
Test conditions	Initial radial clearance 0–3 mm Bearing lubrication Air-oil ISO VG32 Oil is supplied from both sides of bearing. NU type 0.01cm^3/10min×2 (Si_3N_4 rollers) 0.01cm^3/6min×2 (steel rollers) N type 0.01cm^3/10min×2 (Si_3N_4 rollers)) 0.01cm^3/5min×2 (steel rollers) Jacket cooling temperature Room temperature ±1˚C

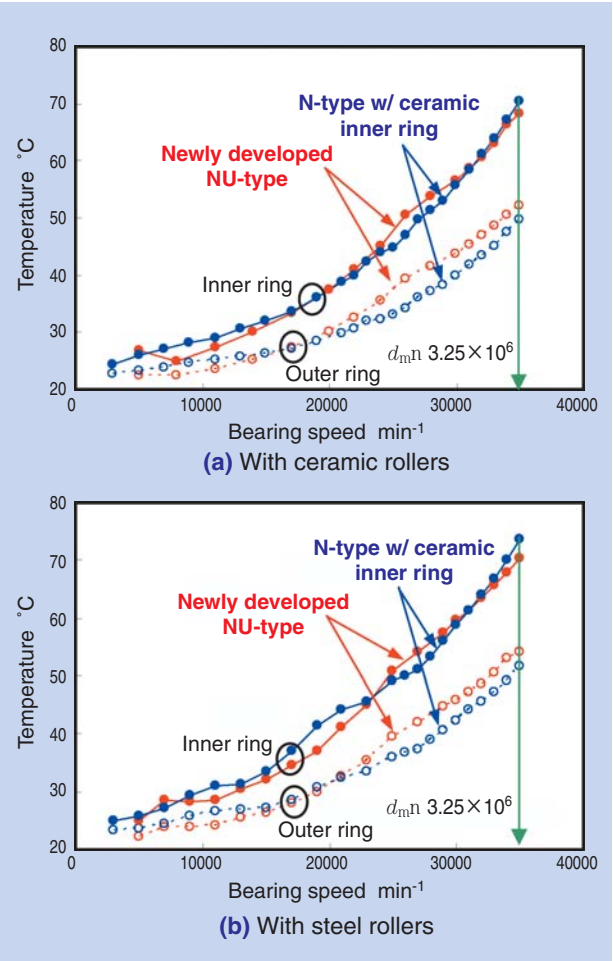

Fig.9 Inner and outer ring temperatures vs. rotational speed

to the shaft, a rolling bearing of bore diameter 50 to 100 mm which is often used to support a machine tool main spindle is interference-fitted over the main spindle with interference allowance of 30 μm or greater: consequently, there will be difficulty when mounting the bearing by press-fitting. In contrast, use of a ceramic inner ring, whose expansion from heat and centrifugal force is small, will help the bearing to be interference-fitted over the shaft with interference allowance of 5 μm or smaller, leading to much easier bearing mounting work.

Furthermore, the greater modulus of longitudinal elasticity of ceramic material helps enhance the rigidity of bearing. This topic is discussed in the following section.

4. Improvement in bearing rigidity by use of ceramic material

Remember that in Section 1 in this article, we briefly stated that any cylindrical roller bearing for machine tool main spindle needs to be capable of not only higher speed, but also greater rigidity. Through calculation, we have verified the effect of use of ceramic material in improving bearing rigidity. Here we will describe this effect in detail.

The internal clearance of a cylindrical roller bearing of bore diameter 70 mm was selected as zero: then, combining steel or ceramic inner ring with steel or ceramic rollers, we have prepared various cylindrical bearing samples. To simulate operation of the bearing sample on an actual machine tool, the maximum radial load applied to the bearing has been set to 7 kN.

The relation between radial load and displacement of the bearing center is graphically plotted in **Fig. 10**. The result of bearing rigidity in the 3 to 7 kN region that features good linearity within the radial load vs. bearing center displacement, as summarized in **Table 4**. Improvement in rigidity with the sample using ceramic material only for the inner ring is 7%, and that with the sample using a ceramic material only for the rollers is 19%. Use of ceramic rollers leads to greater improvement in bearing rigidity, since roller-to-inner ring rigidity and roller-to-outer ring rigidity are simultaneously improved. Use of ceramic material for inner ring alone results in relatively small effect in improving bearing rigidity: however, this arrangement greatly contributes to improvement in high-speed performance of the bearing.

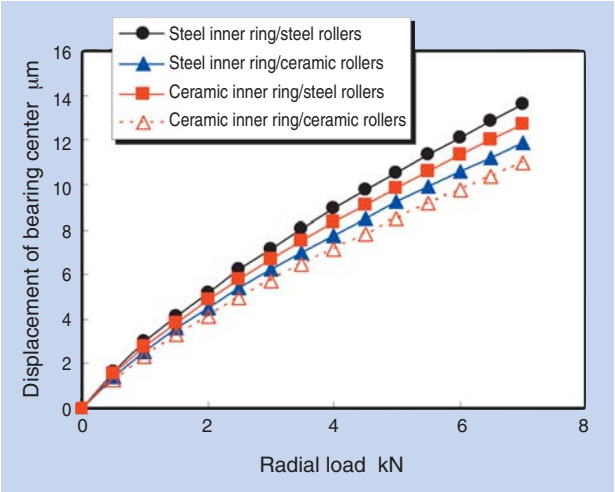

Fig.10 Radial load vs. calculated bearing deflection

Table 4 Bearing stiffness improvement due to ceramic elements

Inner ring/rollers	Rigidity N/m	Increase %
Steel/steel	6.23×10^8	0
Si_3N_4/steel	6.64×10^8	+7
Steel/Si_3N_4	7.43×10^8	+19
Si_3N_4/Si_3N_4	8.09×10^8	+30

5. Verification of mechanical strength of ceramic inner ring

When ceramic material is used for a bearing inner ring it is necessary to prove that the inner ring has sufficient mechanical strength against hoop stress occurring from both heat generation and centrifugal expansion. In the axisymmetric deformation mode, no shear stress occurs; therefore, the major stresses involved are circumferential hoop stress, axial stress, and radial stress, wherein on a thin-walled cylinder subjected to internal pressure and centrifugal force, the stress with the greatest impact is hoop stress.

Fig. 11 illustrates the hydraulic loading test rig we have used to test the mechanical strength of the ceramic inner ring. The test piece used is the same inner ring used in the NU-type cylindrical roller bearing in **Fig. 1**. High-pressure hydraulic oil supplied from an outside hydraulic pump is uniformly distributed within the bore of inner ring, and either an inner ring alone or an inner ring in a bearing assembly (complete with rollers and outer ring) can be tested. The test result is illustrated in **Fig. 12**, with the hydraulic pressure applied to the bore surface of the inner ring on the X-axis, and the corresponding hoop stress occurring on the bore surface of inner ring on the Y-axis. The inner ring has developed fracture at a hoop stress of 500

MPa when tested alone, and at a hoop stress of 640 MPa when tested in the bearing assembly. These hoop stress values are approximately three times and four times greater than maximum commercially allowable hoop stress (160 MPa) for inner ring in typical cylindrical roller bearings for machine tool main spindles. When assembled together with the rest of the bearing, a compressive stress is applied to the inner ring in a direction which helps the compressive stress overcomes the hoop stress; therefore the inner ring in this configuration can withstand a greater internal pressure than the inner ring alone can withstand.

Thus, we have proven functionality and mechanical strength of our newly developed NU-type cylindrical roller bearing, as illustrated in **Fig. 1**. Typical photographic views of this bearing type are given in **Fig. 13**.

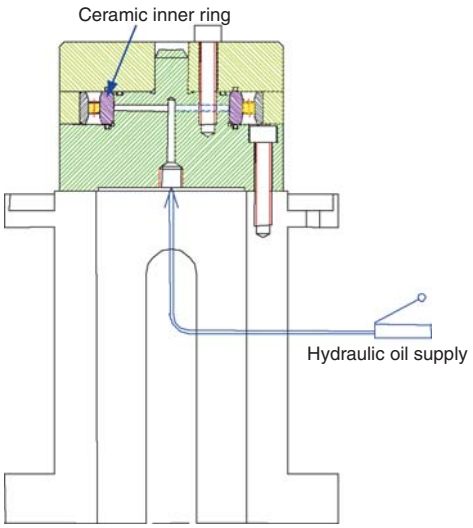

Fig.11 Hydraulic loading test rig

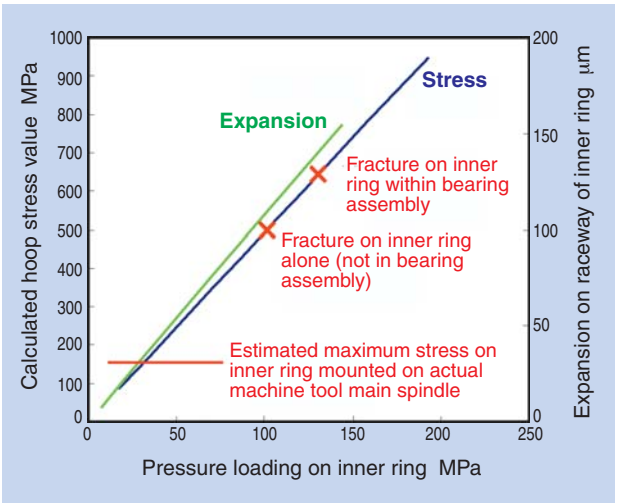

Fig.12 Inner loading pressure vs. hoop stress and inner ring expansion

6. Conclusion

To enhance high-speed capability of its NU-type cylindrical roller bearing for machine tool main spindle, **NTN** has introduced the following elemental technologies:

(1) Ceramic (silicon nitride) inner ring
(2) Cage riding on the outer surface of the air-oil nozzle
(3) Oil drain structure with separate outer ring rib

Ceramic materials boast a low linear expansion coefficient, low density and high modulus of longitudinal elasticity. Thanks to these features, the ceramic inner ring can resist over-preload that can result from expansion of the inner ring while the bearing is running at a greater speed. This improvement helps mitigate heat buildup within the bearing, which is the biggest obstacle to problem-free

(a) Bearing body

(b) Bearing and air-oil nozzle spacers

Fig.13 Developed NU-type cylindrical roller bearing

high speed operation of bearings.

Incidentally, stagnant lubricating oil within a bearing can lead to higher bearing temperatures, due to shear heat generation of lubricating oil. In addressing this problem, we have improved the guide surface on the cage to promote draining of oil from the slide way on cage, and at the same time, introduced a draining structure independent of the outer ring rib in order to promote draining of oil from an area around the outer ring rib.

By adoption of the above-mentioned elemental technologies, **NTN** has successfully developed an improved variant of NU–type cylindrical roller bearing that boasts ultrahigh-speed range, that is, dmn value=3.25×10^6 (bore diameter 70 mm, bearing speed 35,000 min^{-1}). At the same time, we have analyzed the mechanical strength of the ceramic inner ring, and have determined that this inner ring has mechanical strength sufficient for commercial use of the new NU-type bearing.

Higher functionality and improved reliability of bearings directly contribute to better performance of machine tools, and pose not-yet-solved challenges for bearing manufacturers. **NTN** will remain committed to further sophistication of its bearing technologies.

References

1) Japan Machine Tool Builders' Association Technical Committee, Design Theory of Machine Tools (Applications)—Basic Knowledge for Mather Machine Design (1998) 93.
2) M. Mori and T. Kobayashi, Development of High-Speed Cylindrical Roller Bearings for Machine Tools, NTN Technical Review No. 76 (2008) 80-87.
3) NTN, Precision Rolling Bearings Cat. No. 2260/E (2008) 160.
4) K. Rokkaku and K. Nishida, Outline of Ceramic Antifriction Bearings, Journal of the Japan Society for Precision Engineering, Vol. 54, No. 7 (1988) 1240-1244.
5) Japan Society of Mechanical Engineers, editors, Advanced Machine Tool Technologies—Methods for High Speed, High Precision and Multifunctionality, 2nd edition, Kogyo Chosakai Publishing Co., Ltd. (1989) 104.
6) Japan Machine Tool Builders' Association, Machine Tool Design Technology Expert Committee, Design Theory of Machine Tools (Applications)—Basic Knowledge for Mather Machine Design, (1998) 99-100.

Photo of authors

Masatsugu MORI
Elemental Technology R&D Center

Takuji KOBAYASHI
Elemental Technology R&D Center

[Technical Paper]

Evaluation of Scratched Contact Fatigue Life with Artificial Dent of Carbonitrided SUJ2 Steel Whose Surface Nitrogen Content is Controlled Note)

Chikara OHKI*

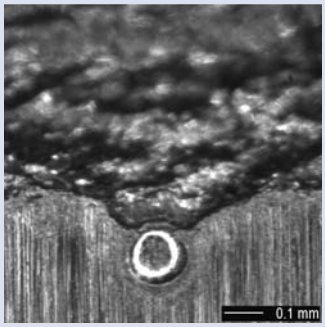

Scratched contact life performance is very important for rolling bearings, but there is no research about the relationship between nitrogen concentration and scratched contact life. In consideration of this situation, the scratched contact life of SUJ2 (SAE52100 equivalent), which had nitrogen concentration accurately controlled, was investigated in this research. To avoid unexpected accidents occurring due to additive contamination to lubrication oil, artificial dents were added to the inner rings of ball bearings using a Rockwell indenter (196N), and these were used for the scratched contact life test. The Weibull slope of the test results from this operation condition was sharper than that of test results from a general test method (i.e., bearing rolling contact fatigue life test in contaminated lubrication condition). Therefore, it is thought that the test method in this research is suitable for collecting quantitative data. A significant test result appeared that when the surface nitrogen concentration is over 0.05 mass %, the scratched contact life is superior to that of normal SUJ2 with a reliability of 99%. Moreover, experimental results revealed that, when the surface nitrogen concentration is 0.4 mass %, the life can be longer than that of 0.1 mass % nitrogen concentration. The sample that had surface nitrogen concentration of 0.4 mass % demonstrated L_{50} life that was 4 times as long as normal SUJ2.

1. Introduction

The effectiveness of carbonitriding in improving scratched contact fatigue life[1] of rolling bearing has been already reported by Kurabe, et al., and recently by Dommarco, et al.[2), 3)] Recently, it has been reported that the life of rolling bearings in contaminated lubrication environments (here-after referred to as “scratched contact life”) is critical for bearing life in automotive transmissions, automotive hubs and reducers. With lubricating oil contaminated with foreign matter of higher hardness, it has been verified that carbonitriding is effective in extending the scratched contact life of rolling bearings[4), 5)]. Note that there is no life data for SUJ2 material whose nitrogen concentration has been strictly controlled[6), 7)].

NTN has attempted to establish data on the scratched contact life of SUJ2 material whose nitrogen concentration was strictly controlled. Test pieces each having artificial dents were used for this life test. **NTN** used a Rockwell indenter to form artificial dents on the raceway surface of bearing inner rings. This test is to be called the “scratched contact fatigue life test”. For comparison, **NTN** has also performed life test under contaminated lubrication environments[4), 5)].

2. Test Method

The test bearing used was a deep groove ball bearing (bearing number: 6202, 30 mm ID, 62 mm OD, 16 mm W, nine rolling elements). To avoid the adverse effect of bidirectional crack possibly occurring on the raceway surface[8)], ceramic balls were used as rolling elements (dia. 9.525 mm (3/8 inch)). The base material used for the inner ring and outer ring subjected to our scratched contact fatigue life test belongs to a same lot per JIS-SUJ2 whose chemical composition is summarized in **Table 1**. The inner ring and outer ring have been heat-treated in a batch heat treatment furnace (capacity 120 L). The furnace atmosphere during the carbonitriding process for these work pieces was analyzed by the following techniques: CO and CO_2 partial pressures were measured by non-dispersive infrared absorption method, H_2 partial pressure by thermal conductometry, and NH_3 partial pressure by gas

*Elemental Technology R&D Center

NOTE) This technical paper has been developed by adding new information to and modifying existing information in “Tetsu-to-Hagane (Iron and Steel)”, vol. 95 (2009), pp. 695-703.

chromatography. Applying the Ohki' method, **NTN** has controlled nitrogen concentration distribution in steel by controlling undecomposed NH_3 partial pressure, H_2 partial pressure, carbon activity and processing duration[6), 7)]. Because the life of outer rings, on which no dent is formed, is unconditionally longer than that of inner rings, the outer ring has been subjected to ordinary hardening/tempering rather than carbonitriding. **Table 2** summarizes heat treatment conditions and grinding allowances applied. The experimental numbers for the respective tests are described by using alphanumerical notations such as those indicating the surface nitrogen concentration of completed specimens having undergone grinding processes as listed in **Table 2**.

Each test piece has been heated to the temperature listed in **Table 2**, and hardened by oil quenching, and then subjected to tempering for 2 hours at 180˚C. N0 and N0C mean non-carbonitrided specimens. The suffix "C" means a specimen intended for test under contaminated lubrication. N005 is intended for a case with low nitrogen concentration, while N01 and N04 are intended for specimens whose nitrogen concentration remains at a certain level even after grinding. After heat treatment, two test pieces have been taken, at random, from a group of test pieces associated with a given experimental number. Then, for each test piece, the carbon and nitrogen concentration distribution profiles at the midpoint of bottom of the groove within inner ring raceway surface have been investigated by line analysis using an Electron Probe Micro Analyzer (EPMA). The resultant data are graphically illustrated in **Fig. 1**. For any given experimental number, no dispersion in data points has been found in both carbon distribution and nitrogen distribution; the nitrogen distribution profile matches closely with the estimated nitrogen profile plotted in **Fig. 1**. Note that carbon (or, nitrogen) concentration values obtained from EPMA are each a sum of concentration of carbon (or nitrogen) dissolved in solid Fe and concentration of carbon (or nitrogen) within deposited matter.

Table 1 Chemical composition of JIS-SUJ2 used (mass %)

C	Si	Mn	P	S	Ni	Cr	Mo	Cu	O (ppm)
0.99	0.26	0.44	0.012	0.006	0.08	1.46	0.03	0.15	9

Table 2 Heat treatment conditions and grinding allowances (N0C for the test under contaminated lubrication)

Notation of each specimen	Inner ring				Outer ring
	N0, N0C	N005	N01	N04	
Partial pressure of NH_3 (Pa)	—	30	213	←	—
Partial pressure of H_2 (kPa)	33.4	36.5	42.5	←	33.4
Flow rate of RX gases measured at 25˚C and 1 atm (L/min)	11.5	←	←	←	11.5
Treating temperature (˚C)	850	852	852	←	850
Duration (s)	3000	8000	5300	←	3000
Carbon activity a_C	0.70	0.95	←	←	0.70
Machining allowance (μm)	100	110	130	50	100
Surface nitrogen concentration after grinding (mass %)	0	0.05	0.1	0.4	0

By line analysis with EPMA, **NTN** has determined nitrogen concentration distribution profiles at the middle of the bottom groove on the inner ring raceway surface after grinding. **NTN** has taken measurements on two data points for each experimental number. The results are graphically plotted in **Fig. 2**. The nitrogen concentration distribution profiles generated from actual concentration measurements match well with those developed by subtracting the grinding allowances summarized in **Table 2** from the nitrogen concentration distribution profiles shown in **Fig.1**. Three types of nitrogen concentration profiles were obtained from heat-treated parts. However, **NTN** has prepared four types of steel specimens featuring unique nitrogen concentration distribution profiles by varying the grinding allowance. By applying x-ray diffraction technique, **NTN** has determined values for residual stress and the amount of retained austenite at a depth of 50 μm from the outermost surface at the middle of the groove surface on specimens not yet tested. The resultant data are graphically plotted in **Table. 3**. The residual stress mode occurring in the

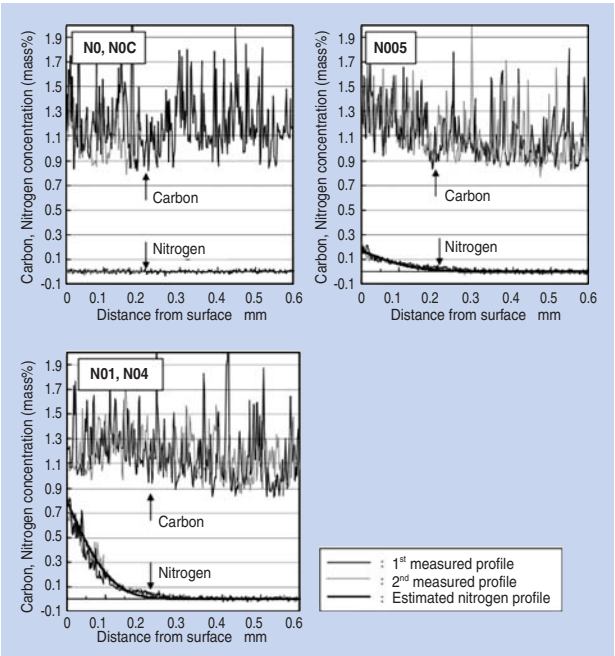

Fig. 1 Carbon & Nitrogen concentration distribution profiles before grinding

entire test is “compression” regardless of the heat treatment conditions applied. There is no large variation in the quantitative values of residual stress. The amount of retained austenite is greater with specimens of greater nitrogen concentration, and is greatest with specimen N04, and lowest with non-carbonitrided specimen N0.

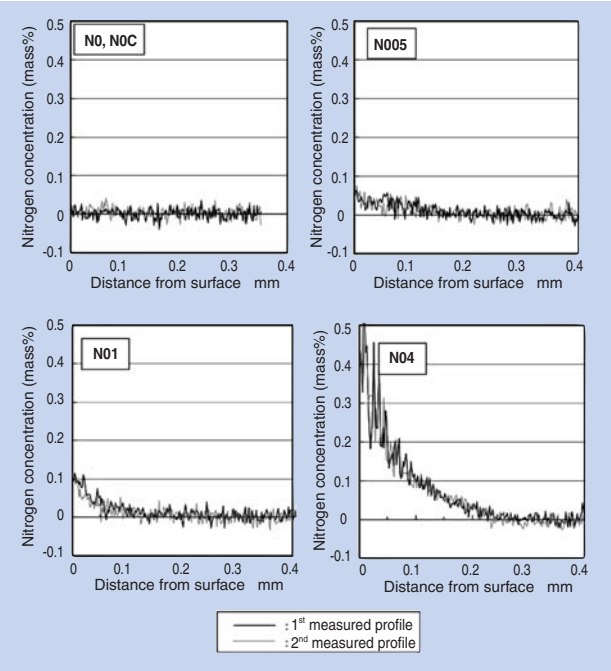

Fig. 2 Nitrogen concentration distribution profiles after grinding

Table 3 Characteristics measured by X-ray diffraction

Notation	Residual atress (MPa)	Retained austenite (%)
N0, N0C	-53	8.5
N005	-92	15.3
N01	-75	15.8
N04	-119	23.3

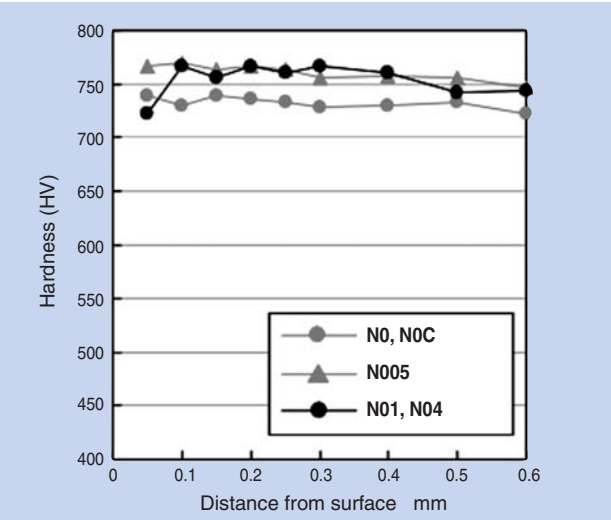

Fig. 3 Hardness distribution profiles on heat-treated specimens before grinding

Fig. 3 shows hardness distribution profiles with specimens having undergone heat treatment. At the distances from the surface, which correspond with the outermost surface after grinding, the hardness distribution profiles with specimens N005 and N01 are situated somewhat higher than that of specimens N0 and N04. However, the difference is small: not greater than 50 HV. Judging from these findings, we believe that there are two major characteristics that mark uniqueness of each experimental number (specimen notation), that is, nitrogen concentration and retained austenite in steel.

2.2 Life test method

The subject tested was an inner ring of a deep groove ball bearing. The artificial dents were formed by forcing a cone-shaped diamond Rockwell hardness indenter (conical indenter with cone angle of 120 degrees, whose tip has a spherical face of curvature 0.2 mm) onto the midpoint of the groove with a force of 196 N. **NTN** has analyzed the profile of the dent with a 3D surface profile analyzer, and have verified that the profile of ridge around dent on each specimen is nearly symmetrical in both axial and circumferential directions, with respect to the center of dent. **Fig. 4** shows typical dent profiles on specimens. The number of dents formed per inner ring specimen is 30 (equally spaced at 12-degrees intervals).

As shown in **Fig. 5**, the life test rig used is capable of applying a load evenly to two test bearings. The test bearings are lubricated with an oil bath system. The test conditions applied are summarized in **Table 4**. To be able to detect occurrence of flaking, a vibrometer was used. While the vibration acceleration test was set to approximately 1.5 m/s^2 (frequency range: 3 Hz to 5 kHz, effective value), the test rig was adjusted so that the test was terminated when the vibrometer detected the increase of vibration acceleration at 6 m/s^2. **NTN** has found that when the vibration acceleration reaches approximately 6 m/s^2, one of the dents formed on the inner ring develops significant flaking. To eliminate the adverse effects of instrument error between test rigs, **NTN** has used only one life test rig for the life test with all the specimens.

For comparison, **NTN** has subjected a non-carbonitrided bearing (N0C) to a life test under a much commonly applied contaminated lubrication environment[4), 5)] (here-after referred to as “contaminated lubrication test”). The bearing material type life test rig, applied radial load, inner ring running speed and lubrication system for this test were same as those for the scratched contact fatigue life test.

Other test conditions were virtually same as those of the scratched contact fatigue life test. However, this test is unique in that no artificial dents were made on the inner ring, while a predetermined amount of hard foreign matter (shape: spherical, amount: 0.4 g/L, hardness: 800HV, grain size: 108 to 180 mm) was mixed into lubricating oil.

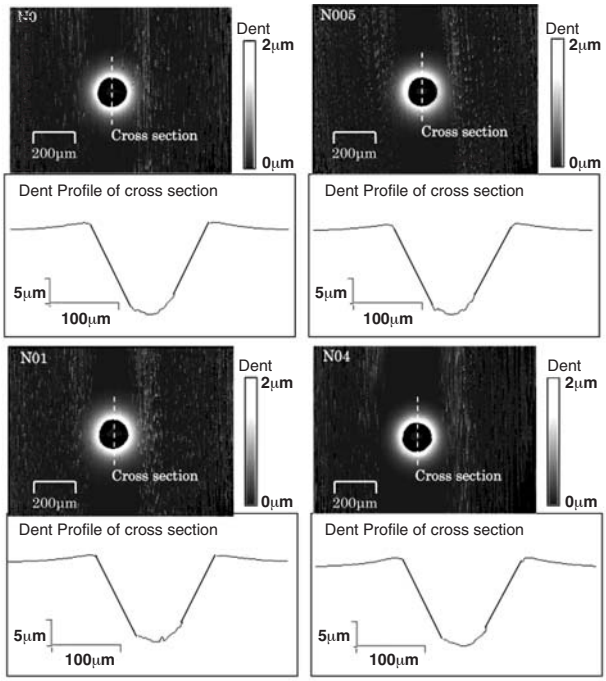

Fig. 4 Examples of dent's shape

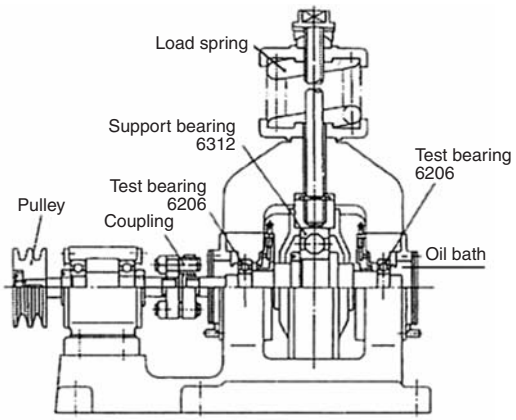

Fig. 5 Schematic drawing of rolling contact fatigue life tester for ball bearing

Table 4 Test conditions of scratched contact life testing

Radial load (kN)	4.9
Radial internal clearance (μm)	20
Maximum contact stress of flat surface (GPa)	3.04
Rotating speed of inner ring (min^{-1})	3150
Lubricant	Turbine oil (Dynamic Viscosity at 40˚C :58.6mm^2/s)

3. Test result

3.1 Facts about flaking and dents

In the scratched contact fatigue life test, flaking has occurred on the inner ring of all the test bearings, while no failure has occurred on the rolling elements and outer rings on these bearings. Major flaking has occurred only on one of 30 dents formed on the inner ring. **Fig. 6** provides examples of starting point flaking. Similar views were also found on other test bearing specimens. Flaking started at the ridge around the dent rather than within the dent and propagated along the direction of shifting load. This mode is identical to the flaking mode [9] found on the conventional test method [4), 5)].

Fig. 7 shows typical views of flaked areas resulting from the contaminated lubrication test. It will be apparent from these photos that flaking starts at the ridge around dent and propagates along the direction

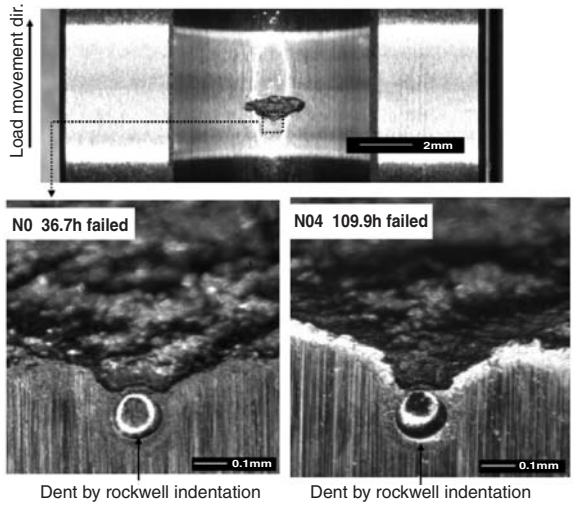

Fig. 6 Examples of flaking area with artifical dent

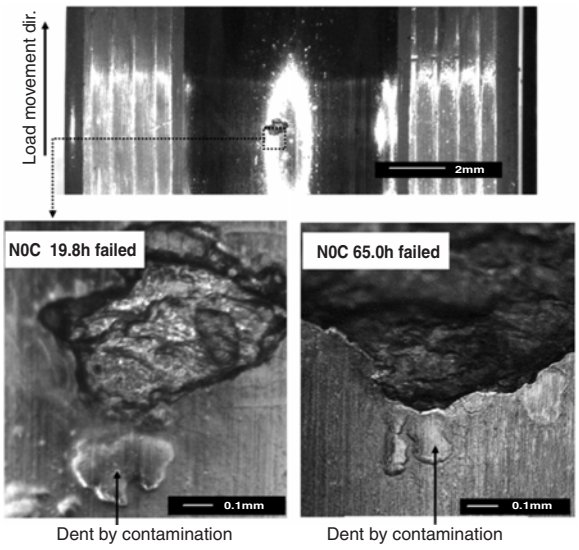

Fig. 7 Examples of flaking area under contaminated lubrication condition

of shifting load. Similar flaking took place on other test bearing types. **Fig. 8** shows views of dents distributed on the inner ring raceway surface having undergone the test (areas around these dents did not develop flaking). On a certain N0C specimen, the inner ring raceway developed flaking as early as 14.7 h, and the quantity of dents formed on this raceway surface is more than double the quantity of dents formed on the inner ring raceway surface of another N0C specimen in which flaking occurred at 65.0 h. It should be understood that the tendency of dent occurrence greatly varies in this test even when test conditions remain unchanged.

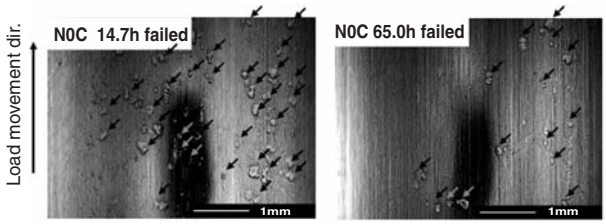

Arrows mark dents formed by contaminants.

Fig. 8 Appearance of inner ring raceway surface after contaminated lubrication test

3.2 Weibull distributions

Table 5 summarizes data obtained from the test. In this test, **NTN** has determined scratched contact fatigue life by assuming that bearing life, according to classical theory of Lundberg-Palmgren[10], follows 2-parameter Weibull distribution function.

Table 6 summarizes the results of the scratch contact life test on bearing specimens determined from Weibull distributions. **Fig. 9** graphically provides the Weibull distributions for non-carbonitrided specimens (N0C) with contaminated lubrication compared with those from the scratched contact fatigue life test. The Weibull slope for the former specimen type is much gentler because dispersion in the life values with the former specimens is great. This seems to be because in the contaminated lubrication life test, the quantity of foreign matters biting into the raceway surface can vary greatly depending on the state of distribution of hard foreign matter in the oil bath as well as the start timing for bearing operation. As a result of the scratched contact fatigue life test, the Weibull slope is steeper and better life data has been obtained. We believe this is because there are no uncertain factors such as the quantity of foreign matters biting into the raceway surface since dents are intentionally formed on the raceway surface and there is little dispersion in the quantity of resultant artificial dents (in other words, variation in vulnerable volume where fatigue typically develops).

Fig. 10 shows Weibull distributions that represent bearing life which is dependant on the variation in surface nitrogen concentration. Each test session has resulted in the least variation in life data and steeper slope. We believe this test method is useful for predicting the life of a bearing mounted on an actual machine. The L_{50} life data in **Table 6** shows that the life is 57.7 h for specimen N0 (no-carbonitrided); 117.3 h for specimen N005 (surface nitrogen concentration of approx. 0.05mass%); 121.3 h for specimen N01 (surface nitrogen concentration of approx. 0.1mass%); and 218.0 h for specimen N04 (surface nitrogen concentration of approx. 0.4mass%). In other words, the longest L_{50} life of these specimens is approximately four times as long compared with the shortest L_{50} life. Greater surface nitrogen

Table 5 Results of scratched contact life test

N0C		N0		N005		N01		N04	
Cumulative life (%)	Failure time (h)	Cumulative life (%)	Failure time (h)	Cumulative life (%)	Failure time (h)	Cumulative life (%)	Failure time (h)	Cumulative life (%)	Failure time (h)
15.9	14.1	5.6	36.7	10.9	66.6	5.6	78.4	8.3	109.9
38.6	14.7	13.7	42.5	26.5	95.3	13.7	87.1	20.2	150.4
61.4	19.8	21.8	44.4	42.2	119.6	21.8	100.9	32.1	200.7
84.1	65.0	29.8	47.0	57.8	123.6	29.8	101.9	44.0	235.6
—	—	37.9	50.1	73.5	130.7	37.9	105.8	56.0	241.7
—	—	46.0	55.3	89.1	168.2	46.0	111.6	67.9	244.2
—	—	54.0	58.5	—	—	54.0	121.2	79.8	244.2
—	—	62.1	62.9	—	—	62.1	122.3	91.7	319.2
—	—	70.2	63.0	—	—	70.2	130.5	—	—
—	—	78.2	70.1	—	—	78.2	146.3	—	—
—	—	86.3	71.6	—	—	86.3	146.4	—	—
—	—	94.4	85.7	—	—	94.4	195.0	—	—

Table 6 Test results from Weibull distributions

	N0C	N0	N005	N01	N04
L_{10} life※ (h)	8.0	38.6	67.6	81.7	124.9
L_{50} life※ (h)	24.3	57.7	117.3	121.3	218.0
Weibull slope※	1.70	4.68	3.42	4.77	3.38

※Calculation value from 2 parameter Weibull distribution.

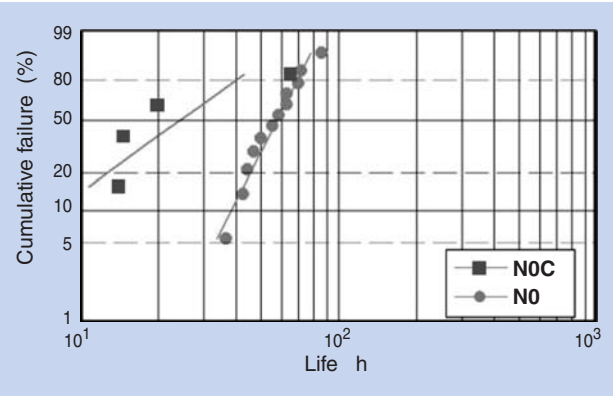

Fig. 9 Difference in Weibull distributions dependent on test method used

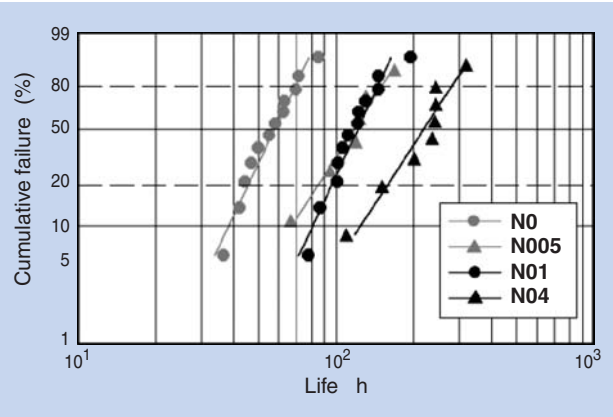

Fig. 10 Difference in Weibull distributions dependent on variation in nitrogen concentration distribution

concentration leads to longer bearing life. Note, that there is a difference in surface nitrogen concentration between N005 and N01. The Weibull distributions obtained from these two specimen types are virtually identical. This topic will be discussed later in Sec. 4.

3.3 t-test for significant differences

Experimentally developed Weibull distributions can be used to compare bearing life[4, 5, 11]. However, if the number of test bearing specimens is low, the resultant Weibull distributions are less reliable, making this comparison practice not always relevant. If this is the case, it would be necessary to make comparisons based on significant differences by applying statistical data processing techniques. However, there have been few researches about the t-test for significant differences with Weibull distributions. In researching t-test technique for this significant difference in Weibull distributions, Johnson has adopted a statistical approach, and Fujita has applied a technique to use random numbers developed by a computer[12, 13]. However, these approaches are not yet regarded as fully established techniques. To address this issue, **NTN** has attempted to assess the life test results obtained in the present research, by t-testing for significant differences with normal distributions. When comparing two populations when normal distributions and variances of the distributions are unknown, it will be possible to assume a population standard deviation common to both populations and then test the significant differences of population averages based on t-distributions[14]. Weibull distribution coincides with normal distributions when its gradient is 3.26[10].

The Weibull gradient in the contaminated lubrication test is 1.7, and approximation to normal distribution will result in greater error (skewness: 1.9, kurtosis: 3.8). The Weibull gradients observed in the scratched contact fatigue life fall in a range of 3.38 to 4.77, and neat to 3.26 (max. skewness: 1.1, max. kurtosis: 1.8). The Weibull distributions appear to fairly match the standard distributions. **Table 7** summarizes data resulting from fair approximation to standard distributions, wherein the data for each specimen consist of average life, standard deviation and the sum of squares. When Weibull distributions fairly approximate (match) normal distributions, the average life of any specimen matches a value virtually the same as L_{50} life obtained from the Weibull distributions for that specimen. For this reason, we believe that the magnitude of errors resulting from approximation to normal distributions is small.

Table 8 summarizes the results of the t-test. There appears to be a noteworthy difference, when the level of significance is 1%, between the population mean of N0 (specimen not undergone carbonitriding) and that of N005 or N01 (specimen having undergone carbonitriding). Our carbonitriding technique apparently helps realize longer life for specimens subjected to scratched contact fatigue life test. **NTN** has learned that there is no sizeable difference, when

Table 7 Approximations to normal distribution

	N0	N005	N01	N04
Average life (h)	57.3	117.3	120.6	218.2
Standard deviation	14.2	34.3	31.5	64.4
Sum of squares	2211.9	5869.8	10903.7	29040.0

Table 8 Resulta of t -test

Objects	Standard deviation of population	t_0	$t(\phi,0.1)$	$t(\phi,0.01)$
N0 and N005	22.475	5.339	1.746	2.921**
N0 and N01	24.416	6.350	1.725	2.845**
N005 and N01	32.378	0.204	1.746	2.921
N01 and N04	47.107	4.539	1.734	2.878**

**Significant difference is present when level of significance is 1%.

the level of significance is 10%, between the population mean of N005 and that of N01. There is a considerable difference between the population mean of N04 (whose surface nitrogen concentration is as high as approximately 0.4mss%) and that of N01, when the level of significance is 1%. From the findings obtained in our scratched contact fatigue life test, we can judge that our carbonitriding technique positively help extend life of SUJ2 material used as bearing components and this effect will be enhanced with higher nitrogen concentration in carbonitrided case layer.

4. Discussion

From the findings obtained in our scratched contact fatigue life test, **NTN** has determined that our carbonitriding technique applied to SUJ2 (typical bearing steel material) positively helps extend the life of bearing components made from SUJ2 material. This life-extending effect is more apparent when the nitrogen concentration is higher in the carbonitrided case of a bearing component made of SUJ2. The next section describes the reasons for why our carbonitriding technique helps extend the service life of bearing components made from SUJ2.

A report about scratched contact life of bearing steel material, states that a smaller gradient of the inside face of dent (dent depth divided by dent diameter) means a longer scratched contact fatigue life of the bearing component in question[15]. However, since the variation of the shapes of dents is small, as previously shown in **Fig. 4**, the gentle slope inside the scratch-derived dents does not account for the longer life of carbonitrided bearing components in the present scratched contact life test.

Other reports show that greater stress concentration will occur as the fatigue on the ridge around dents progresses. The scratched contact fatigue life of the material in question will be shorter if the value obtained by dividing the curvature radius on the ridge around the dent is divided by the dent radius is smaller[11] and/or if the angle at apex of ridge is smaller[16] (acute angle). The shapes of ridges (downstream in the shift direction of load) around dents before and after scratched contact fatigue life test are illustrated in **Figs. 11** and **12**. Note that the inner raceway surface on the dent-free specimen was taken at the Y-axis origin, and the intersection point of the ramp of ridge around dent and the Y-axis is taken at the X-axis origin.

Fig. 11 shows that before the test, the shapes of apex of the ridge around the dents on the carbonitrided specimens (N005, N01, N04) are more obtuse and their curvature radii are greater compared with the shapes on similar areas on the non-carbonitrided specimens (N0). Retained austenite seems to trigger generation of work-induced martensite, which leads to a greater work hardening coefficient. The carbonitrided specimens feature greater amounts of retained austenite. There is research that investigates the relation between physical properties of steel materials and the shapes of dents (indentations) formed on specimens made of these steels[17]. According to this research, the apexes of ridges around dents on steel are duller with greater work hardening coefficients. Thus, the results obtained from our scratched contact fatigue life test appear to be relevant. However, in comparison with pre-test data in **Fig. 11**, the post-test data in **Fig. 12** indicate that the heights around the apexes of ridges around dents decreased to those as low as nearly half the original heights. The shapes near the apexes of the ridge around the dents maintain their shape regardless of the material and elapsed test time. According to previous researches, the shapes of the ridge around the dents in rolling contact mode varies greatly in the earlier stages of fatigue life (until

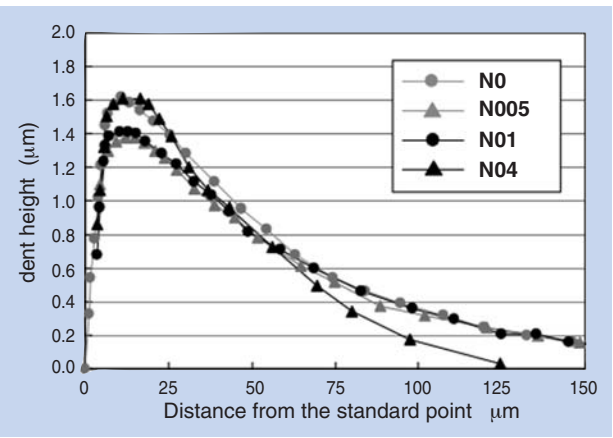

Fig. 11 Shapes around dents before rolling contact fatigue

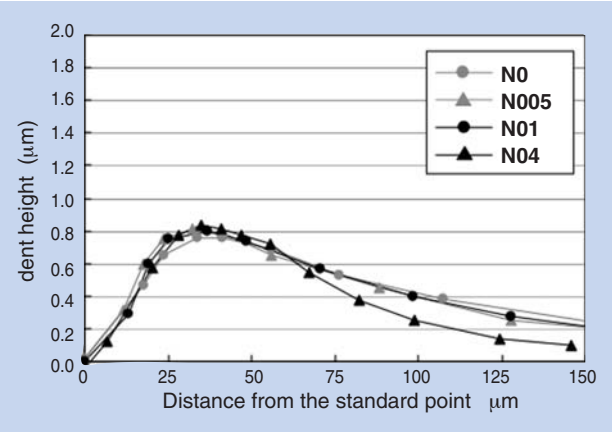

Fig. 12 Shapes around dents after rolling contact fatigue

approximately 1/8 flaking life, and does not change greatly afterwards[18]. It is estimated that while fatigue progresses, stress concentration remains virtually unchanged regardless of the steel type. Thus, we think that the true cause of longer life by carbonitriding is not caused by the shapes of ridges around dents, but from the enrichment in retained austenite.

We believe that since our carbonitriding technique[6), 7)] does not lead to decarburizing, the sum of carbon and nitrogen concentration in carbonitrided case increases by the concentration of interstitial nitrogen portion. For this reason, we currently think that solid-solution strengthening[19)] caused by carbonitriding may contribute to longer fatigue life of steel specimens. However, Weibull distribution obtained from specimen N005 whose surface nitrogen concentration stands at approximately 0.05mas% is nearly identical to that of specimen N01 whose surface nitrogen concentration is as high as approximately 0.1mss%. Therfore, surface nitrogen concentration alone cannot explain longer rolling fatigue life. To address this issue, we have attempted to determine, using a market-available thermodynamics phase equilibration state calculation software package, the interrelation between nitrogen concentrations in steel and the concentration of nitrogen dissolved (here-after referred to nitrogen concentration in solid) in austenite (here-after referred to "γ-Fe"). SUJ2 contains chemical compounds C, Si, Mn and Cr. To simplify calculation, Si and Mn have been excluded from the calculation, and the equilibrated state for 1mass% C-1.5mass% Cr-Fe system including addition of nitrogen has been analyzed. The test temperature has been set to 850˚C, which is same as the carbonitriding temperature. On a commercial production basis, steel work pieces are heated, and then hardened. Therefore, the concentration of nitrogen dissolved in martensite should be determined, but this calculation is very difficult. At the same time, because the hardening mode in the present research is oil quenching, we thought that nitrogen concentration in martensite did not greatly differ from that in γ-Fe at 850˚C. Furthermore, though nitrogen is present, other than as CrN, in the form of element that substitutes carbon in cementite ($(Cr,Fe)_3(C,N)$), the amount of this nitrogen portion is very small, and we have ignored this portion in the calculation. **Table 9** summarizes the calculation results of nitrogen concentration in γ-Fe at 850˚C. When total nitrogen concentration is 0.05mass%N, two phases (γ-Fe + cementite) are present in γ-Fe at 850˚C. When the total Ni concentration falls in a range of 0.1 to 0.3mass%N, three phases (γ-Fe + cementite + CrN) exist. With the total Ni concentration range of 0.4 to 0.6mass%,

Table 9 Calculation results of nitrogen concentration in γ-Fe at 850˚C (1mass%C-N-1.5mass%Cr-Fe)

Total nitrogen concentration (mass%)	Mass of CrN per steel 1g (g)	Nitrogen concentration in γ-Fe※ (mass%)	Phase at 850˚C
0.05	0	0.050	γ-Fe※+cementite
0.1	0.001	0.077	γ-Fe※ +cementite+CrN
0.2	0.005	0.092	
0.3	0.009	0.115	
0.4	0.012	0.154	γ-Fe※+CrN
0.5	0.014	0.211	
0.6	0,015	0.286	

※ Austenite-Fe

only two phases (γ-Fe + CrN) remain. When the total nitrogen concentration stands at 0.05mass%N, CrN phase does not occur, thereby the resultant nitrogen concentration in γ-Fe remains equivalent to the total nitrogen concentration. In contrast, when total nitrogen concentration is 0.1mass%N, CrN phase occurs, and the nitrogen concentration in γ-Fe increases to approximately 0.077mas%. Also, when total nitrogen concentration reaches 0.4mass%N, CrN phase occurs too. Owing to higher total nitrogen concentration, nitrogen concentration in γ-Fe increases to approximately 0.154mass% (this is twice as high as with a case where the total Ni concentration stands at 0.1mass%N). The reason why the mean life of N005 does not differ from that of N01 seems that the total Ni concentrations on these steels are virtually the same. From these findings, **NTN** believes that scratched contact fatigue life of carbonitrided bearing steel will be longer with higher total dissolved nitrogen concentrations.

5. Conclusion

We have attempted to obtain life data and better repeatability of the fatigue life of deep groove ball bearings made of SUJ2 steel whose surface nitrogen concentration is accurately controlled. For this purpose, we intentionally formed dents on the raceway surface of the inner ring and then subjected the inner rings to scratched contact fatigue life tests. The results obtained from the test are summarized below:

1) The Weibull distributions of any specimens obtained from our test feature smaller scattering and steep Weibull slopes as compared with the conventional life test under contaminated lubrication with hard foreign matters. **NTN** believes that this is because of the elimination of the

uncertain factor of biting of foreign matters into the raceway surface. Our test method is suitable for obtaining life data of good repeatability, and will make a useful test method for predicting bearing life on actual machinery.

2) The L_{50} lives, determined from the Weibull distributions, are 57.7 hours with specimens not undergoing carbonitriding; 117.3 hours, 121.3 hours and 218.0 hours with specimens whose surface nitrogen concentrations are 0.05mass%, 0.1mass% and 0.4mass%, respectively. The longest life is approximately four times as long as the shortest life. In other words, higher surface nitrogen concentration means longer life.
3) The Weibull distributions were approximated to normal distributions, whose significant differences were tested with the t-test method. Previously, Weibull distributions obtained from conventional contaminated lubrication life test could not be approximated to normal distributions because of gentle Weibull slopes. In contrast, our test method has revealed that the mean life of carbonitrided specimens is, when the level of significance is 1%, longer than that of non-carbonitrided specimens. The mean life of specimens featuring higher surface nitrogen concentration, such as 0.4mass%, is, when level of significance is 1%, longer than those of specimens with surface nitrogen concentration 0.05mass% or 0.1mass%.
4) As a result of the calculation with thermodynamic phase equilibration diagram, the life of carbonitrided steel material appears to be higher with higher concentration of nitrogen dissolved in solid Fe.

References

1) N. Mitamura, J. Jpn. Soc. Tribol., Vol. 53 (2008), 641.
2) H. Kurabe, T. Araki, Tetsu-to-Hagané, Vol. 53 (1967), 1305.
3) R. C. Dommarco, K. J. Kozaczek, P. C. Bstias, G. T. Hahn, C. A. Rubin, Wear, 257 (2004), 1081.
4) K. Maeda, Kougyou Kanetsu, Vol. 38 (2001), 2.
5) C. Ohki, SAE Technical Paper Series (2004), 2004-01-0634.
6) C. Ohki, Tetsu-to-Hagané, Vol. 93 (2007), 220.
7) C. Ohki, Tetsu-to-Hagané, Vol. 94 (2008), 42.
8) Y. Fujii , K. Maeda, Wear, Vol. 252 (2002), 787.
9) T. Sada, T. Mikami, J. Jpn. Soc. Tribol., Vol. 49 (2004), 948.
10) S. Shimizu, Introduction to Reliability Design for Mechanical Engineering, Suurikougakusha-Sha Co., Ltd., Tokyo (2006) 34.
11) Y. Murakami, Machine Design, Vol. 39.
12) L. G. Johnson, The Statistical Treatment of Fatigue Experiments, Elsevier Publishing Company, St. Louis, (1964), 3.
13) T. Fujita, Proceedings of Tribology Conference, Japanese Society of Tribologists, Aichi (2008), 439.
14) S. Moriguchi, Statistical Methods, Newly Revised Edition, Japan Standards Association, Tokyo (1989) 121.
15) A. Lubrecht, C. H. Venner, S. Lane, B. Jacobson, E. Ioannides, Proceedings of the Japan International Tribology Conference, Aichi (1990), 185.
16) C. Ooki, Proceedings of Tribology Conference, Japanese Society of Tribologists, Tokyo (2000) 169.
17) S. Maki, J. Mater. Test. Res. Assoc. Jpn., Vol. 39 (1994) 127.
18) H. Kakishima, E. Kimoto , A. Korenaga, T. Yoshioka, Proceedings of Tribology Conference, Japanese Society of Tribologists, Tokyo (1997) 443.
19) M. Kato, Introduction to the Theory of Dislocations, Shokabo Publishing Co., Ltd., Tokyo (1999) 179.

Photo of author

Chikara OHKI
Elemental Technology
R&D Center

[Technical Paper]

Plasma Nitriding Treatment of High Alloy Steel for Bearing Components

Kazuhiro YAGITA*
Chikara OHKI*

Bearings for special purposes, including aerospace engines, should have a very high reliability in consideration of safety. In addition, they need to have extended maintenance intervals in consideration of economics. In order to achieve these, it is necessary to prevent the unexpected failure of bearings caused by surface damage from exposure to contaminated lubricant. A countermeasure to contaminated lubricant is to provide a hardened layer to bearing races to reduce the effect of contamination. One method of surface modification is low-temperature nitriding as a kind of surface hardening. In particular, plasma-nitriding (ion-nitriding) is a treatment that does not use ammonia and has few environmental impacts, while being relatively suitable for high alloy steel. This report describes examples of plasma-nitriding applications.

1. Introduction

Bearings used under high-temperature and high-speed conditions are required to satisfy a high degree of reliability; therefore, these bearings use materials with cleanliness that is much better than ordinary bearing steel. These highly clean steel materials are resistant against internally propogated flaking that often begins at non-metallic inclusions within steel, resulting in longer life.

Unfortunately, bearings are not always lubricated with clean oil, and operating conditions for bearings with contaminated lubrication may be very severe. In such severe operating conditions, contamination will dent bearing races before internally propagated flaking occurs, and the resulting indentations can provide propagation points for flaking. In this demanding situation, bearing life is shorter than under internally propagated flaking mode and can vary depending on a variety of factors including quantity of contamination, and the size and hardness of foreign contaminants.

When a bearing fails due to foreign contamination, the failure usually occurs suddenly and unexpectedly. This failure mode is particularly critical for safety in aerospace engine bearings since engine trouble during flight can require an emergency landing. Also, for economic reasons, longer bearing life under contaminated lubrication and extended bearing replacement intervals are needed.

To make bearings more resistant against failure caused by foreign contamination in lubricating oil, various techniques are available, including improved heat treatment techniques[1)–3)]. One example of is a surface hardening process for forming a hardened layer on bearing raceway surfaces. Plasma nitriding, also referred to as ion nitriding, is a variation of a low-temperature nitriding process.that, thanks to the sputtering effect[4)], can realize nitriding relatively easily on high alloy steels for which gas nitriding would be difficult. **NTN** has been using M50[5)] or M50NiL[6)] (**Table 1**) for bearings used under high-temperature and high-speed conditions, and the plasma nitriding process is suitable for these high alloy steels.

Depending on process conditions, low-temperature nitriding process can cause a chemical compound layer (also known as white layer) to occur on the surface of steel or cause precipitates (**Fig. 1)** to occur in grain boundary. These phenomena can adversely affect the rolling fatigue life of the bearing. Any nitriding technique applied to bearing components must not develop a chemical compound layer or intergranular precipitates. At the same time, a certain degree of nitrided case depth needs to be achieved such that the surface of bearing components withstands the adverse effects caused by

*Elemental Technology R&D Center

contaminants in lubricating oil. This technical paper describes our experience in applying a plasma nitriding technique to M50 and M50NiL which satisfies the above-mentioned requirements.

Table 1 Chemical compositions of M50 and M50NiL

	C	Si	Mn	Ni	Cr	Mo	V
M50	0.80	0.2	0.3	0.1	4.0	4.3	1.0
M50NiL	0.13	0.2	0.2	3.4	4.1	4.3	1.2

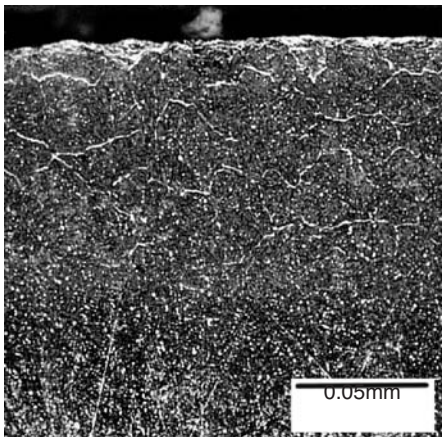

Fig. 1 Typical intergranular precipitates (etched in nital)

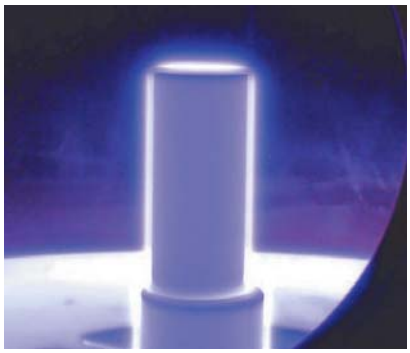

Fig. 2 Appearance of glow discharge

2. Plasma heat treatment

This section contains an overview of plasma heat treatment. Various plasma heat treatment machines are currently available. In the basic arrangement common to these machines, a vacuum pump evacuates the interior of the machine, and a DC voltage is applied to a work-piece using the work-piece as a cathode and the inside wall of the machine as an anode. The work-piece is subjected to nitriding and/or carburizing through application of DC voltage.

When a DC voltage is applied to electrodes under reduced atmospheric pressure, glow discharge occurs across the electrodes (**Fig. 2**). During glow discharge, electrons are released from the cathode toward the anode. These electrons collide with gas molecules introduced into the machine, converting the gas molecules into ions. The resulting ions are accelerated toward the cathode(that is, the work-piece), penetrating into the workpiece surface when they collide with the surface[7].

One outstanding advantage of plasma heat treatment is the lower environmental impact it poses compared with heat treatment with a controlled atmosphere furnace. For example, nitriding with a controlled atmosphere furnace often uses ammonia gas. In contrast, using a plasma nitriding technique, a steel material can be nitrided with nitrogen and hydrogen. Also, with plasma nitriding, the intended work-piece alone is heated without heating the entire interior of the furnace—a practice necessary for a controlled atmosphere furnace.

Fig.3 shows schematics of typical plasma heat treatment equipment configurations. With cold-wall or hot-wall configurations where a bias voltage is applied to a work-piece, a clean surface is exposed on the work-piece through sputtering where ions collide with the work-piece. Consequently, the surface of a

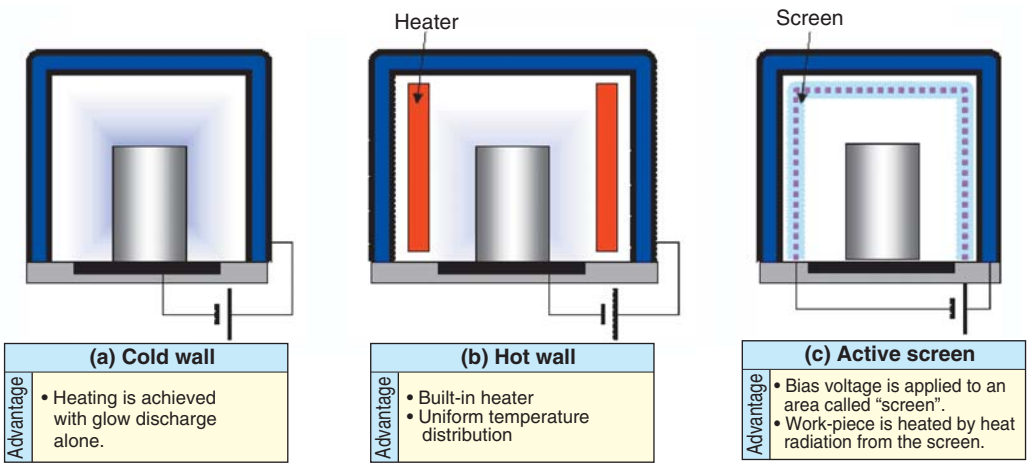

Fig. 3 Schematic diagram of plasma heat treating equipment

material is nitrided in a short time even if the material type needs a longer time for nitriding with a gas nitriding or vacuum nitriding process. However, conventional plasma heat treatment techniques have disadvantages such as poor surface smoothness resulting from sputtering. To address this problem, a unique configuration known as the “active screen” method has been developed, wherein a bias voltage is not applied to the work-piece.

In the test performed for this paper, we have used a cold wall type plasma heat treatment equipment, as well as a radiation thermometer to help control the temperature of the plasma heat treatment equipment.

3. Typical applications of plasma nitriding

3.1 Intergranular precipitates

As mentioned previously, formation of a chemical compound layer on the work piece surface, and intergranular precipitates are challenges associated with low temperature nitriding. These problems can provide a propagation points for flaking or fracture, and can very often adversely affect the rolling fatigue life of a bearing. This section provides information about the occurrence of intergranular precipitates.

Prior to nitriding, specimens were subjected to conventional heat treatment such as hardening and tempering, and then M50 specimens (immersion quenched) and M50NiL specimens (carburized) were subjected to Ar sputtering, and were allowed to stand at 480˚C for 30 hours; during this course, a gas mixture (N_2:H_2:CH_4=79:80:1, volume ratio) was introduced into the furnace in order to nitride the specimens. The CH_4 was added to the gas mixture to prevent minor decreases in nitrogen concentration around the surface of specimens during low-temperature nitriding[8), 9)].

We have analyzed the carbon and nitrogen concentration distribution profiles on the nitrided specimens with Electron Probe Micro Analyzer (EPMA), and measured cross-sectional hardness profiles on each specimen using a Vickers hardness tester (**Fig. 4**). Nitrogen has penetrated to a depth of approximately 0.1 mm with M50 specimens, and approximately 0.2 mm with M50NiL specimens. As shown in the photos of microstructures in **Fig. 5**, etching with nital caused white precipitates to become visible along the grain boundary. Intergranular precipitates occurred to a depth of approximately 0.05 mm with M50 specimens, and approximately 0.2 mm with M50NiL specimens. The analysis has revealed that these intergranular precipitates consist of iron nitrides, in particular, Fe_3N.

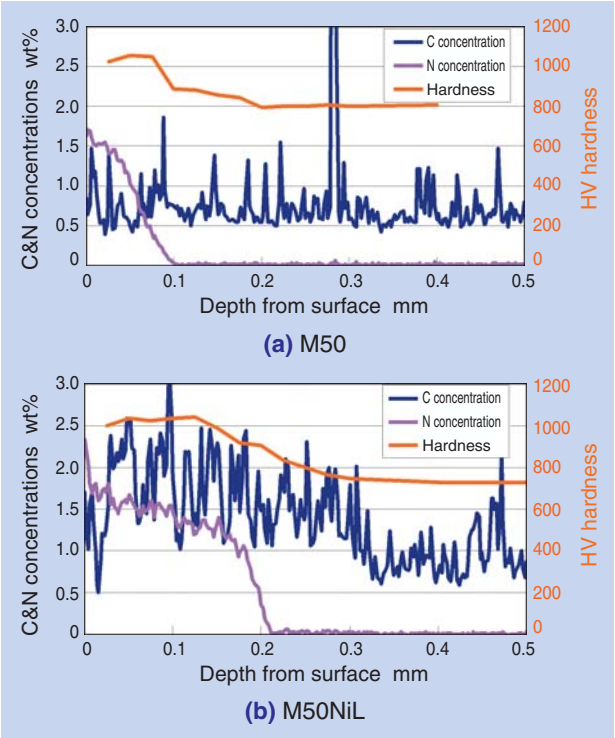

Fig. 4 Depth profiles of carbon, nitrogen content and hardness of plasma nitrided specimen

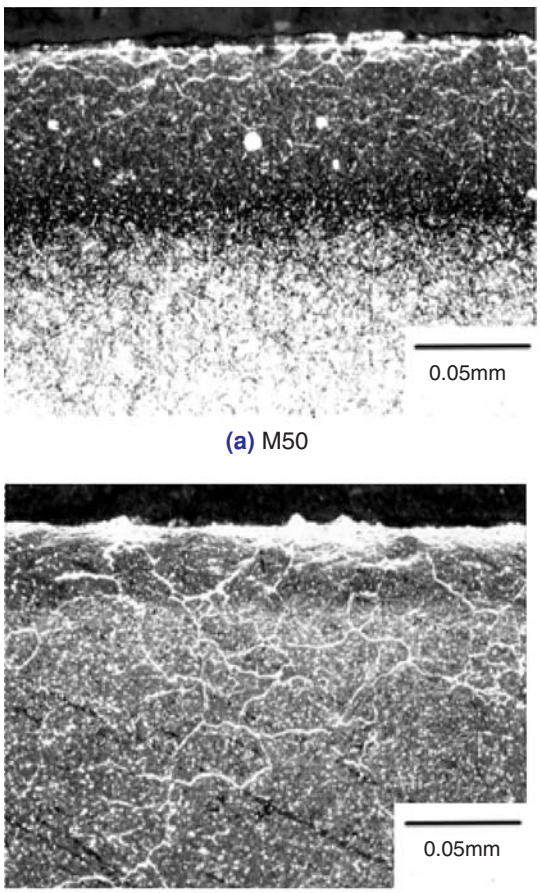

Fig. 5 Microstructures of plasma nitrided specimen (etched in nital)

3.2 Inhibition formation of intergranular precipitates

We have subjected to M50 and M50NiL specimens to plasma nitriding test, and have learned that while intergranular precipitates tend to occur in steel materials with higher nitrogen concentration, intergranular precipitates may or may not occur at a given nitrogen concentration.

From the findings in Sec. 3.1, we suspected that carbon concentration governs occurrence of intergranular precipitates, and reinterpreted the test results by considering not only nitrogen concentration but also carbon concentration. Consequently, it has become apparent that, as illustrated in **Fig. 6**, intergranular precipitation occurs only when the sum of carbon concentration and nitrogen concentration in base steel materials is higher than approximately 1.7wt%. Note that the higher concentration data resulting from precipitates contained in the areas for analysis have been excluded from analysis. From these findings, we have learned that for better plasma nitriding results, we need to remain aware not only of nitrogen concentration alone but also of the sum of carbon concentration and nitrogen concentration.

We have also learned that when the plasma nitriding duration is set longer in order to achieve a necessary nitrided case depth, nitrogen concentration around the surface layer will become higher and intergranular precipitates occur before much nitrogen is diffused into the steel specimens (this state is known as “diffusion controlled” mode).

To summarize, intergranular precipitation will not occur when nitrogen is allowed to penetrate only a shallow depth below the surface for a short duration by plasma nitriding; However, a problem will occur when plasma nitriding is applied to steel specimens for a longer duration in order to obtain a sufficiently deep nitrided case. That is, though nitrogen atoms will quickly penetrate the steel material, nitrogen atoms will be very slowly diffused in the steel material, and nitrogen atoms of higher concentration will remain around the surface of the steel material, thereby causing intergranular precipitates to occur in this region. Thus, it will be difficult to achieve a sufficiently deep nitrided case while inhibiting occurrence of intergranular precipitation by plasma nitriding alone.

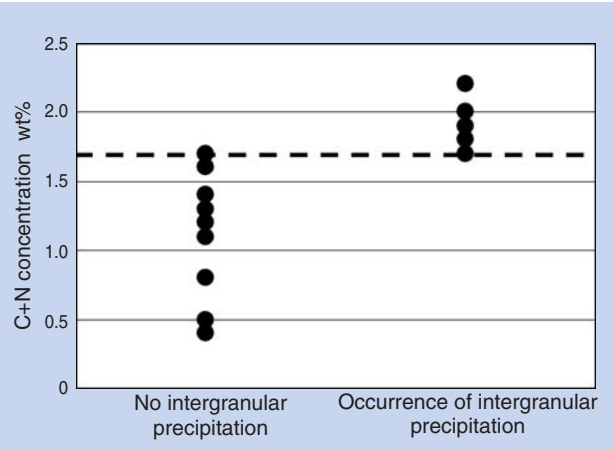

Fig. 6 Relationship between sum of carbon and nitrogen content and occurrence of intergranular precipitates

3.3 Discussion of dispersion treatment conditions

When plasma nitriding process alone is applied to M50 and M50NiL specimens, it is difficult to achieve a nitrided case depth sufficient for bearing components without causing intergranular precipitates to occur. Therefore, we have attempted to achieve a sufficient nitrided case depth without triggering intergranular precipitation by performing a diffusing process after plasma nitriding.

Generally, completing a diffusion process at a higher temperature and for a longer duration is effective to increase the diffusion depth of any element diffused into steel material. We have tried various diffusion process conditions, and learned that if the diffusion process is performed for a prolonged time after plasma nitriding, the core hardness of the base steel material will decrease even though the diffusion process temperature is lower than the tempering temperature. When the core hardness of the base steel material deteriorates even though a sufficient nitrided case depth is achieved, the material cannot be used for bearing components. Therefore, we have to establish diffusion process conditions that do not lead to a decrease in the core hardness of base steel material while maintaining a satisfactorily large nitrided case depth.

Using M50 and M50LiN specimens, we have attempted to determine the relationship between the temperature and duration of the diffusion process and deterioration in core hardness of the base steel material (**Fig. 7**) as well as determine the nitrided case depth.The triangular region illustrated in **Fig. 8** defines relevant diffusion process conditions. The sub-section below describes the result of combining plasma nitriding processes and relevant diffusion processes.

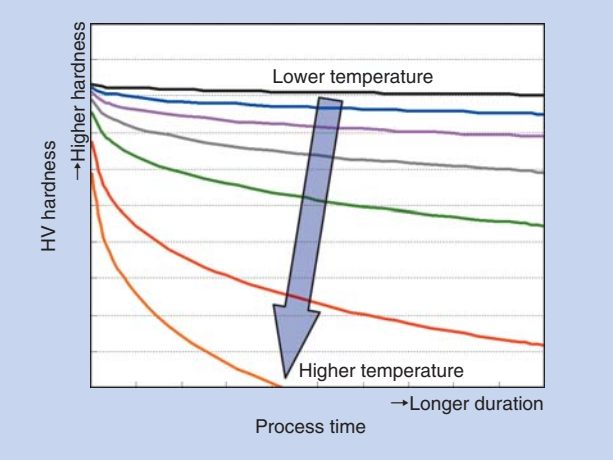

Fig. 7 Relationships among treatment temperature, time and matrix hardness

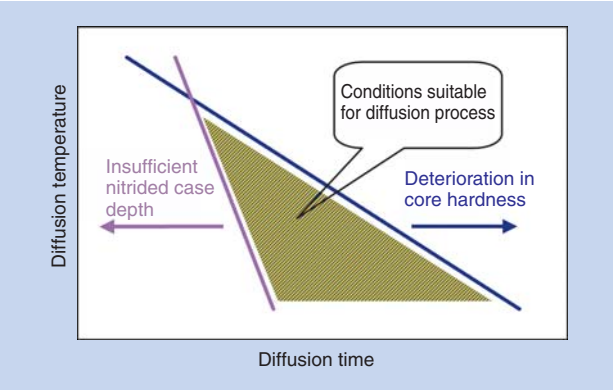

Fig. 8 Schematic diagram of diffusion treatment condition

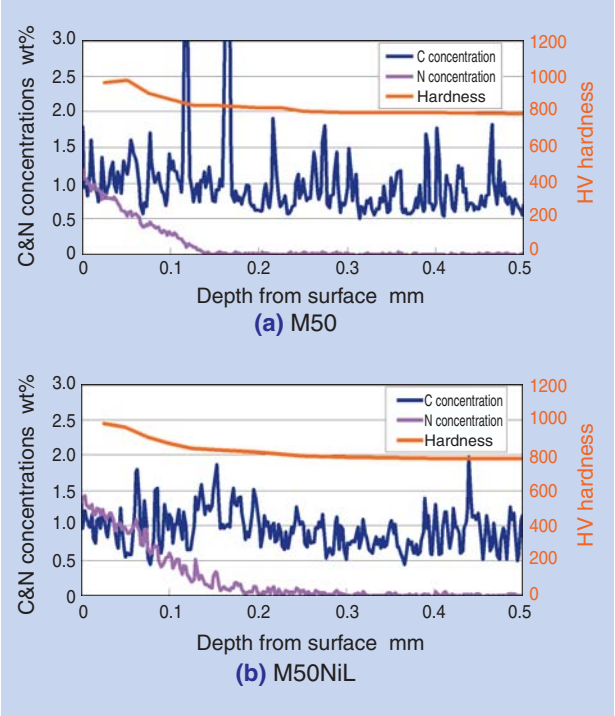

Fig. 9 Carbon and nitrogen concentration and hardness profiles of plasma nitrided specimen, after diffusion treatment

3.4 Example of treatment involving diffusion process

Prior to plasma nitriding, specimens were subjected to conventional heat treatment. M50 specimens (immersion quenched) and M50NiL specimens (carburized) were subjected to Ar sputtering in plasma heat treatment equipment, and were then allowed to stand at 430˚C for 10 hours. During this process, gas mixture (N_2:H_2=1:1, volume ratio) was introduced into the equipment to plasma-nitride the specimens. The nitrided specimens were allowed to cool to room temperature in the furnace, and then removed from the equipment and loaded into a constant temperature diffusion chamber where they were kept at 430˚C for 160 hours.

Fig. 9 shows carbon and nitrogen concentration profiles and cross-sectional hardness profiles of specimens having undergone the diffusion process. **Fig. 10** provides photos of microstructures of plasma nitrided specimens having undergone natal etching. Nitrogen has penetrated to a depth of approximately 0.15mm in M50 specimens, and approximately 0.2

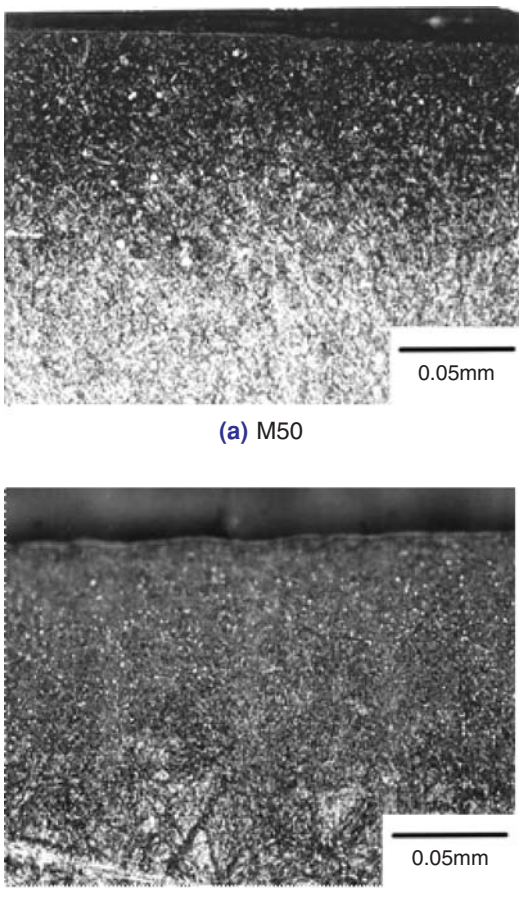

Fig. 10 Microstructures of plasma nitrided specimen, after diffusion treatment (etched in nital)

mm in M50NiL specimens. The sum of carbon and nitrogen concentration on nearly the entire nitrided region is less than 1.7wt% with the exception of locations with high concentration due to detection of precepitates.

We have compared the test results in Sec. 3.4 with those in Sec. 3.1 (**Fig. 4**), find that increase in hardness is limited in the nitrided area due to the reduced amount of nitrogen atoms; notwithstanding, the surface hardness of this area exceeds 900 Hv and the microstructure in this area does not exhibit intergranular precipitation. We believe that our process, consisting of the plasma nitriding and diffusion techniques described in this paper is suitable for treating bearing components subjected to rolling fatigue load.

3.5 Procedure for applying plasma nitriding technique to bearing components

Fig. 11 shows a process flow that appears to be relevant for applying plasma nitriding to bearing components made of M50 or M50NiL based on the findings mentioned previously. Among the steps in **Fig. 11**, those framed in red are processes that are added to apply plasma nitriding. The steps necessary for this procedure are described below:

- Treat the work-pieces in a conventional heat treatment process, and then rough-grind the work-pieces. Be sure to keep grinding allowance for finish grinding.
- Using plasma heat treatment equipment, subject the work-pieces to Ar sputtering and plasma nitriding.
- To achieve a necessary case nitrided depth, perform a diffusion process under relevant conditions.
- Finish-grind the work-pieces, then treat the work-pieces in a manner identical to those that are not subjected to plasma nitriding.

Note that the diffusion process need not be executed in plasma heat treatment equipment, and may be performed as necessary in a vacuum furnace or atmosphere furnace.

Finish grinding is performed after diffusion process in order to correct changes in surface roughness resulting from plasmas nitriding or possible changes (though very small) in shape or dimensions of the work-pieces.

As a result of these process steps, a sufficiently deep nitrided case is formed on bearing component while occurrence of intergranular precipitates is inhibited and the hardness of steel material is maintained at a same level that is obtained by heat-treating M50 or M50NiL with conventional heat treatment process.

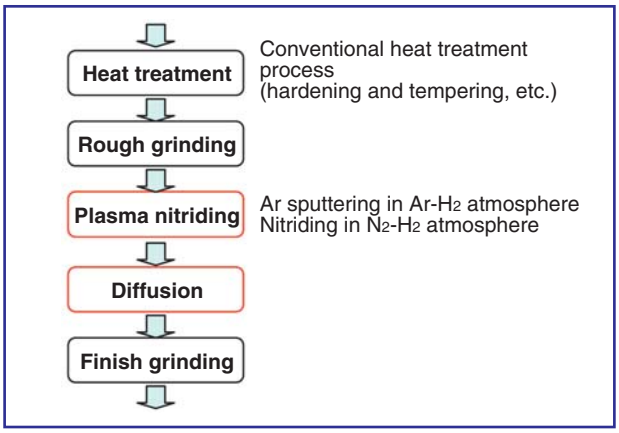

Fig. 11 Process flow for producing plasma nitrided components

4. Verification of effect of plasma nitriding

To determine the degree of surface damage resistance provided by plasma nitrided steel material, we have adopted a double roller rolling fatigue test. **Fig. 12** illustrates the test rig used, and **Table 2** summarizes the test conditions applied. The driving cylinder is driven by an electric motor, while the driven cylinder is driven by the driving cylinder. The driving cylinder, featuring a rough-textured outer surface, is made of SUJ2. This cylinder was allowed to cause peeling damage on the smooth-textured outer surface of driven cylinder made of M50 or M50NiL.We have assessed the severity of the peeling damage and evaluated the effectiveness of plasma nitriding through comparison peeling damage severity between

Fig. 12 Schematic diagram of double roller test

Table 2 Conditions of double roller rolling test

Driving cylinder	Dia. 40×L12, secondary curvature R60, Ra-0.5 μm, standard heat-treated product made of SUJ2
Driven cylinder	Dia. 40×L12, no secondary curvature, Ra = 0.02 μm
Running speed	2000min^{-1}
Max. contact pressure	2.3GPa
Number of loading cycles	4.8×10^5 cycles (4 hrs.)
Ambient temperature	Ordinary temperature
Lubricating oil	Additive-free turbine oil VG46
Lubrication system	Lubricating felt pad

driven cylinder specimens having undergone conventional heat treatment only and driven cylinder specimens that were plasma nitrided and then subjected to diffusion process under the process conditions mentioned in Sec. 3.4 before being finish-ground.

Fig. 13 shows some examples peeling damage appearance on driven cylinders made of M50. With both M50 and M50Nil materials, peeling damage has occurred on the outer surface of non-plasma nitrided driven cylinder. In contrast, no peeling damage has occurred on the outer surface of driven cylinders that were plasma nitrided and then subjected to a diffusion process. To summarize, plasma nitriding apparently improves surface damage resistance of the steel bearing components.

Next, we manufactured 6202 bearing specimens with M50NiL material (this material is used for bearing ring on aero-engine) subjected to plasma nitriding, and diffusion processes prior to finish grinding.We then evaluated the life of these speciments under contaminated lubrication. For the bearing life test, we have formed, with a load of 20 kgf, 30 equally spaced Rockwell indentations at the bottom of the raceway groove in the inner ring raceway surface of each test specimen in order to simulate the indentations that are caused by foreign contamination in lubricating oil. For comparison purposes, we have also prepared non-plasma nitrided inner ring specimens made of M50NiL (carburized) that have been heat-treated with conventional process only, and have formed Rockwell indentations in a manner identical to that mentioned above. Using the test rig in **Fig. 14** and applying the test conditions in **Table 3**, we have tested the rolling fatigue life of 6202 bearing samples having incorporated these inner rings.

The test results are graphically plotted in **Fig. 15**. From this chart, it is apparent that the plasma nitrided specimens feature longer life and are much more resistant against damage caused by contaminated lubrication.

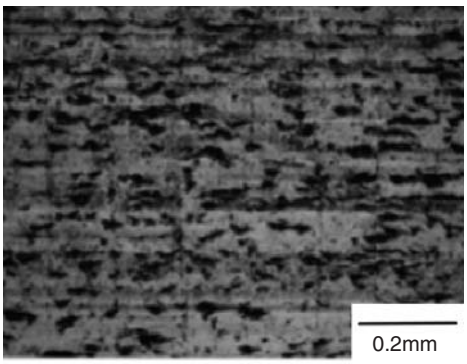

(a) M50

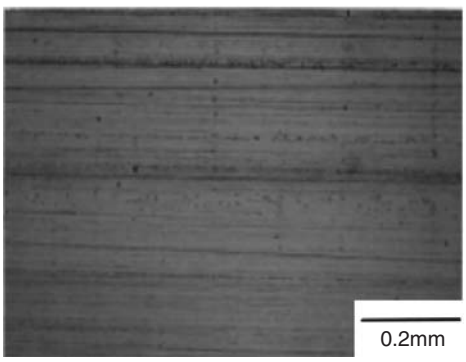

(b) M50 (plasma nitriding + diffusion)

Fig. 13 View of peeling damage

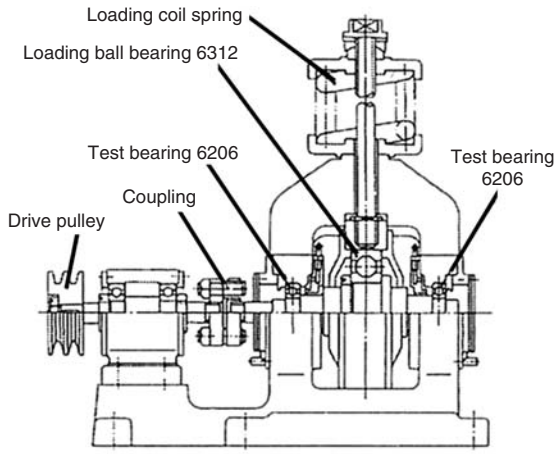

Fig. 14 Schematic of rolling contact fatigue life test rig for ball bearings

Table 3 Test conditions of rolling contact fatigue life test

Bearing	6206C3
Radial load	6.86kN
Max. contact pressure (inner ring)	3.44GPa
Max. contact pressure (outer ring)	3.56GPa
Running speed	3000min^{-1}
Lubricating oil	Circulating lubrication with VG56

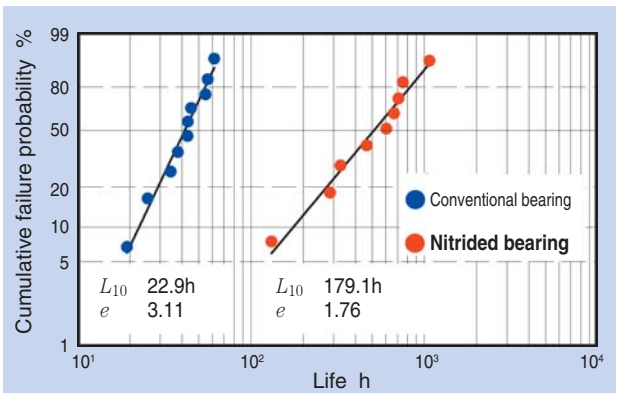

Fig. 15 Test results of rolling contact fatigue life test

5. Conclusion

We have attempted to determine optimal conditions for plasma nitriding M50 and M50NiL materials used for bearing components subjected to high-temperature and high-speed conditions, and have attained the following findings:

1) When the sum of carbon concentration and nitrogen concentration in a steel material exceeds 1.7wt%, intergranular precipitates can more readily occur, which adversely affect the quality of bearing components in question.
2) Nitriding alone cannot achieve a sufficiently deep nitrided case while inhibiting the occurrence of intergranular precipitates;a diffusion process needs to be added.
3) Even when the diffusion temperature is below the tempering temperature, diffusion process with prolonged duration will cause the hardness of the base steel material to decrease; Therefore, the work-pieces need to be subjected to diffusion process under relevant process conditions that help realize a sufficiently deep nitrided case while not causing a decrease in hardness of the base steel material.
4) Peeling damage resistance of steel material is improved through plasma nitriding and diffusion processes.
5) The hardness of the outermost surface and surface layer is improved on M50 and M50Nil specimens having undergone appropriate plasma nitriding and diffusion processes. Compared with M50 and M50NiL specimens not undergone plasma nitriding, these plasma nitrided specimens boast improved damage resistance and rolling surface with indentations exhibit longer life.

References

1) H. Kurabe and T. Araki, Rolling Fatigue Characteristics of Carburized or Carbonitrided 1% Cr Steel at Elevated Temperatures, Vol. 53, No. 11 (1967) 1305.
2) K. Maeda, H. Nakashima, N. Tsushima, Proc. of the Int. Tribology Conf. Yokohama, JAST (1995) 1387.
3) C. Ooki, K. Maeda and H. Nakashima, Improving Rolling Contact Fatigue Life of Bearing Steels Through Grain Refinement, NTN Technical Review No. 71 (2003) 2-7.
4) K. Nishiguchi, Y. Takahashi, M. Tanaka, Pre-Prints of the National Meeting of JWS, 51 (1992) 334.
5) For example, Aerospace Material Specifications (AMS) 6491.
6) For example, Aerospace Material Specifications (AMS) 6278
7) Example when processing nitride, J. Walkowicz, Surf. Coat. Technol. (2003) 174-175, 1211
8) M. Lovonyak, Proc. of the 17th IFHTSE Congress (2008) 1 (2009) 61.
9) Kaoru Ikenaga, Proc. of the 17th IFHTSE Congress (2008) 2 (2009) 685.

Photo of authors

Kazuhiro YAGITA
Elemental Technology
R&D Center

Chikara OHKI
Elemental Technology
R&D Center

Improve Productivity for Warm Ring Rolling Process of Bearing Race

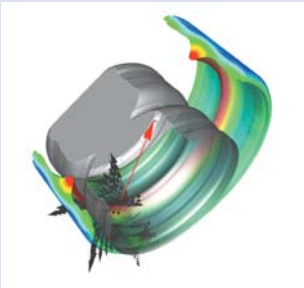

NTN-SNR Eric PELLETIER*
Pierre EHINGER*

NTN-SNR improved the accuracy of numerical simulations for the warm ring rolling process in order to achieve productivity improvement and scrap reduction. Since 1960, **NTN-SNR** has applied the warm ring rolling process, and has been able to realize the improvement of forming tool life and the reduction of cycle time for manufacturing and machine adjustment through the improvement of numerical simulation technology.

1. Preface

Machine component manufacturers across the globe have long faced the challenge of improving productivity in order to reduce production costs. To this end, **NTN-SNR** has been applying a warm ring rolling process to the production of its bearing raceways, eliminating the need for a turning process. In order to further improve the effectiveness of the warm ring rolling process, **NTN-SNR** has been optimizing a numerical simulation technique that aids in the warm ring rolling process. In this article, we report our efforts toward improving our warm roll-forging technique, taking the outer ring of a double-row angular contact ball bearing as a typical work piece.

2. Structure and features of warm roll-forging system

Fig. 1 schematically illustrates difference between a conventional roll-forging technique and **NTN-SNR**'s unique warm roll-forging technique.

In the conventional roll-forging technique, the rotating roll-forming tool is forced to the bore surface of the work piece blank to form the blank into its intended cross-sectional shape and enlarge the blank to its target diameter while reducing the blank wall thickness.

NTN-SNR's warm roll-forging system is very unique in that a work piece blank is placed in two outer circumferential profile regulating dies, whereupon the spirally-moving roll-forming tool is forced against the bore surface of the blank to form the blank into its intended cross-sectional shape and enlarge the blank to its target diameter.

As schematically illustrated in **Fig. 2**, the outer circumferential profile of a work piece blank is regulated with the outer dies (1) and (2), ensuring that the profile of the roll-forming tool is accurately transferred to the work piece blank. In summary, **NTN-SNR**'s unique roll-forging technique produces high-precision ring-shaped bearing components through a rolling process that forms the bore and outer circumferential surfaces without the need for any turning operation.

Fig. 3 offers a diagram showing the spiral trajectory of the roll-forming tool that is a unique feature of the **NTN-SNR** process. By this spiral motion, a work piece blank is formed to its intended shape and dimensions, simultaneously reducing its wall thickness and enlarging its diameter.

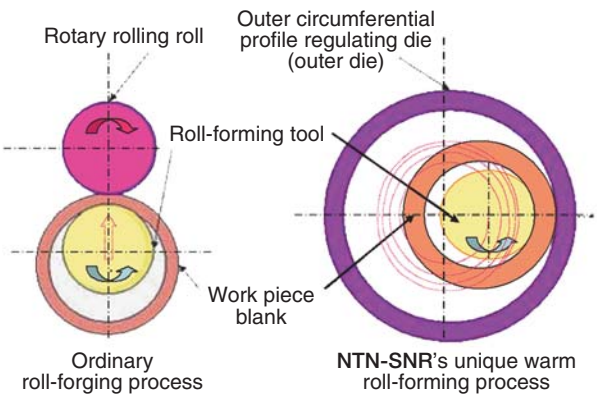

Fig. 1 Comparison of rolling process

*NTN-SNR ROULEMENTS Production Engineering R&D

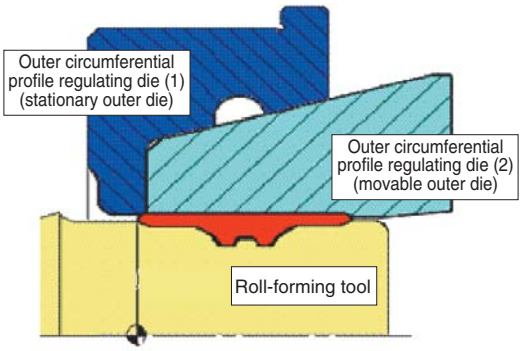

Fig. 2 Fixed die and roll forming tool

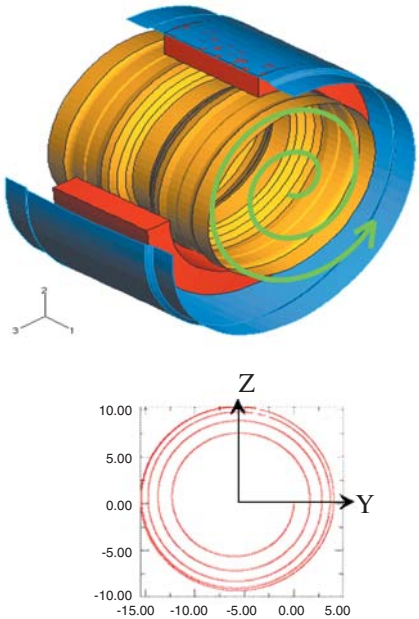

Fig. 3 Spiral trajectory for roll forming tool

3. Feature of the NTN-SNR warm-rolling machine, and NTN-SNR's commitments to improvement in productivity

A view of **NTN-SNR**'s unique warm-rolling machine is shown in **Fig. 4**. This machine operates as described below:

1) The roll-forming tool drive causes the roll-forming tool to turn.
2) The roll-forming tool spiral motion drive, rack mechanism actuator, and roll-forming tool push-in drive are linked with each other through gearing to cause the roll-forming tool to follow a spiral trajectory.
3) As indicated in **Fig. 2**, the outer die (1) is stationary, while the outer die (2) is movable. By operation of the outer die (2), a work piece blank is loaded into the space between the outer rollers and the roll-forming tool; once the work piece has been formed it is removed from the warm-rolling system, again by the movable outer die (2).

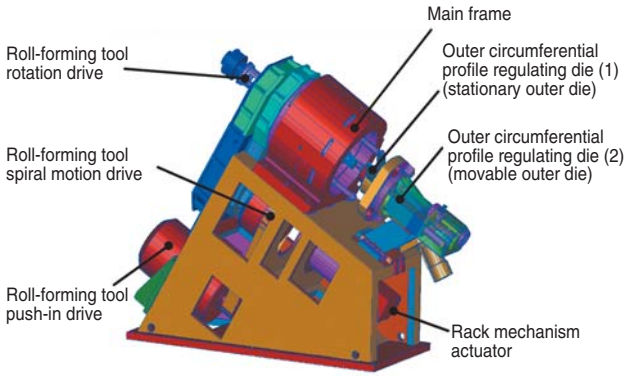

Fig. 4 View of warm-rolling machine

The main frame of the machine supports the roll-forming tool. Its inclined angle allows the formed products to be automatically delivered by gravity. In other words, its simple construction removes the need for a product delivery mechanism.

Instead of the previous hydraulic drive, the new model of the machine is actuated by an NC system. Consequently, operation of all the mechanisms within the machine is now centrally controlled to inhibit variation in motion that can occur from variations in mechanical components. Furthermore, by fully utilizing position information from the NC controller, simulation accuracy has been improved, resulting in the reduction of rolling cycle time.

3.1 Numerical simulation

To reduce machining cycle time, extend tool life, and decrease setup time for its warm-rolling machine, **NTN-SNR** has been developing a numerical simulation tool that helps optimize operation of its warm roll-forging process and roll-forming tool.

3.1.1 Temperature analysis

An example of the results of temperature analysis on various areas of the warm-rolling machine during the warm roll-forging process is given below.

Fig. 5 illustrates the temperature distribution on a work piece blank during warm roll-forging; **Fig. 6** shows the temperature distribution on the outer dies; and **Fig. 7** provides the temperature distribution on the roll-forming tool. **Fig. 8** provides a comparison between the values resulting from numerical simulation and empirically measured values by plotting the time elapsed and temperatures occurring

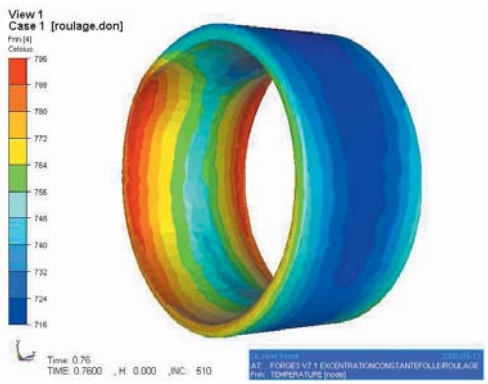

Fig. 5 Temperature of blank during rolling

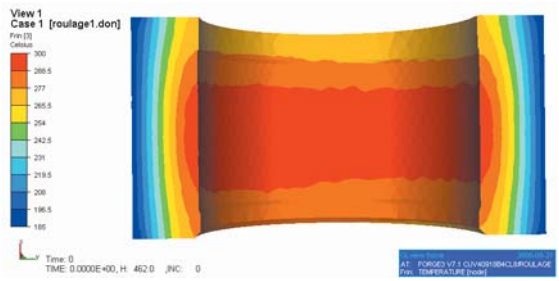

Fig. 6 Temperature of outer die during rolling

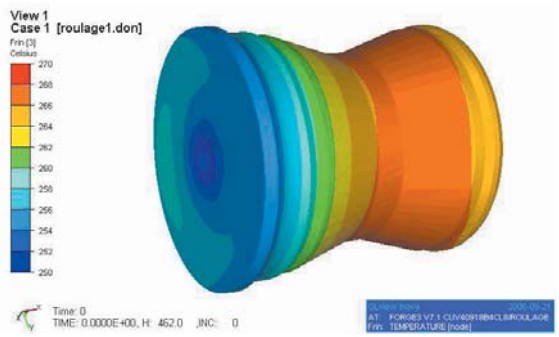

Fig. 7 Temperature of roll-forming tool during rolling

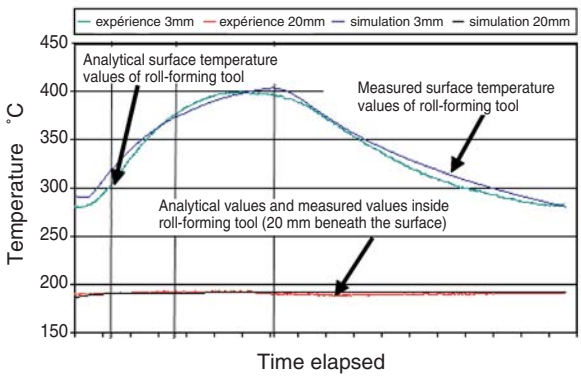

Fig. 8 Relation between time and temperature during rolling

on the roll-forming tool during warm roll-forging operation.

From this diagram, it can be seen that the result of numerical simulation closely matches the measured values for temperatures of the roll-forming tool, both at its outer surface and within the tool (20 mm beneath the surface). In other words, the numerical simulation tool developed by **NTN-SNR** exhibits a very high degree of accuracy.

3.1.2 Analysis for stress and deformation

Fig. 9 offers an example of the results of analysis on stresses occurring on the roll-forming tool during warm roll-forging, while **Fig. 10** illustrates the results of deformation analysis in the same situation.

Fig. 11 illustrates the relation between run time of the above-mentioned machine and load applied to the roll-forming tool in the machine during warm roll-forging. Differences in various data sets between the pre-operation analytical values and the actual values obtained from the machine during operation were fed back to the simulation system. Then, reanalysis was

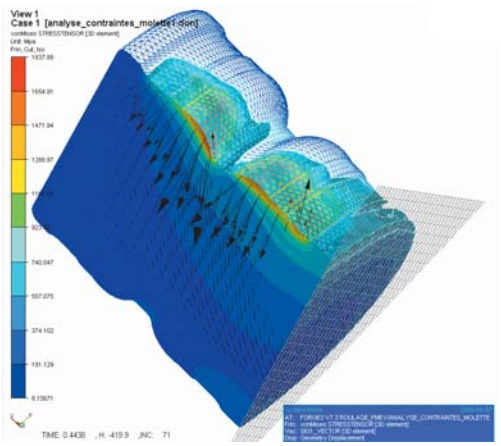

Fig. 9 Stress distribution on roll-forming tool during rolling

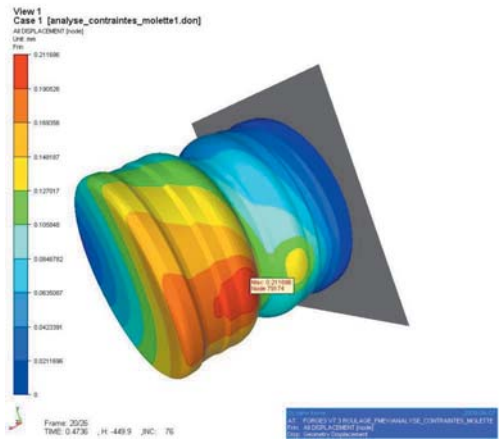

Fig. 10 Deformation distribution on roll-forming tool during rolling

performed using the newly-fed data: It was found that, in terms of the peak load acting on the roll-forming tool, the analytical values (post-operation) closely match the measured values. This means that our simulation method fairly accurately represents the timing and magnitude of the peak load applied to the roll-forming tool during roll-forming operation.

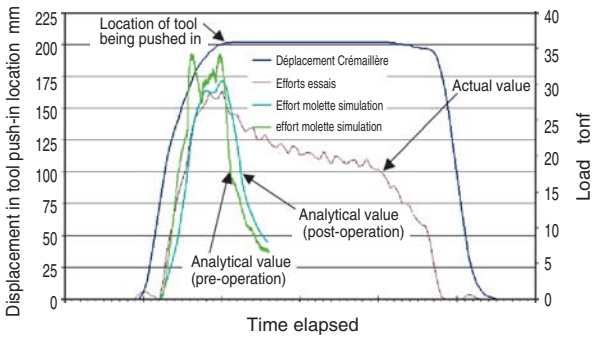

Fig. 11 Load applied to roll-forming tool during rolling

4. Conclusion

Through improvement of its numerical simulation technique for warm ring rolling process, **NTN-SNR** has been endeavoring to optimize process conditions, while always remaining careful not to deteriorate the effective life of the roll-forming tool.

By our efforts, we have achieved approximately 20% reduction in cycle time, compared with the previous technique, as shown in **Fig. 12**.

NTN-SNR will remain committed to developing new technologies targeting improved productivity, reduced scrap production, and simplified processes. Further improvement in its forging technology is to be capable of forming more complicated, medium-sized ring-shaped bearing components. In doing so, **NTN-SNR** will remain fully conscious of the conservation of the global environment.

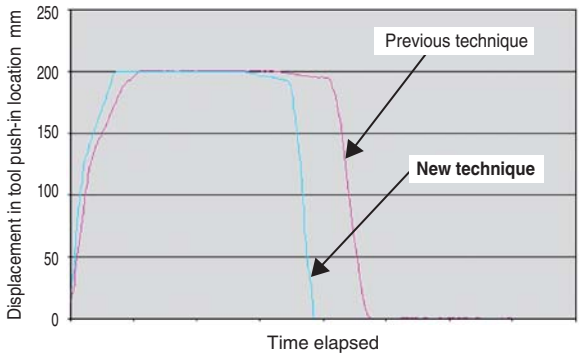

Fig. 12 Cycle time

Photo of authors

Eric PELLETIER

NTN-SNR ROULEMENTS
Production Engineering R&D

Pierre EHINGER

NTN-SNR ROULEMENTS
Production Engineering R&D

Air Oil Lubrication Bearings with Re-lubricating Hole on the Outer Ring for Machine Tool

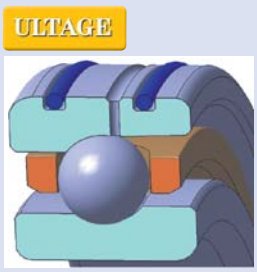

Futoshi KOSUGI*
Kouji NISHINO*

The best design specification was established for angular contact ball bearings with outer ring re-lubricating holes for machine tool main spindles. In this report, we introduce the features and the test data for these air oil lubrication bearings with outer ring re-lubricating holes for machine tools.

1. Introduction

Air-oil lubrication systems are often used to lubricate machine tool main spindle bearings, wherein the lubricating oil is traditionally fed into the interior of each bearing through a ring spacer having re-lubricating holes. There are also some present-day European machine tools featuring machine tool bearings where oil penetrates more directly into the bearing interior through outer ring re-lubricating holes. Lubricant oil flow in this manner will lead to various benefits including improved lubrication efficiency and eliminating the need of a separate ring spacer component. This article describes **NTN**'s unique version of "air-oil lubricated machine tool main spindle bearings with outer ring re-lubricating holes" including the basic design concept and performance test results.

2. Bearing design details – machine tool bearing design with outer ring re-lubricating holes

Fig. 1 illustrates the comparison between **NTN**'s new design concept and the traditional bearing/spacer system used now. The traditional system requires oil to flow through the separate spacer.

The **NTN** design also includes an O-ring on each side of the outer ring to prevent oil leakage out the sides, while oil is fed into the bearing via the circumferential oil groove and holes.

3. Basic advantage for the bearing to have an outer ring with re-lubricating holes

We checked heat and noise generation between NTN's new design idea with the traditional bearing / spacer system.

Fig. 2 schematically illustrates the test rig (main spindle type test rig) for this test. **Table 1** summarizes the test conditions.

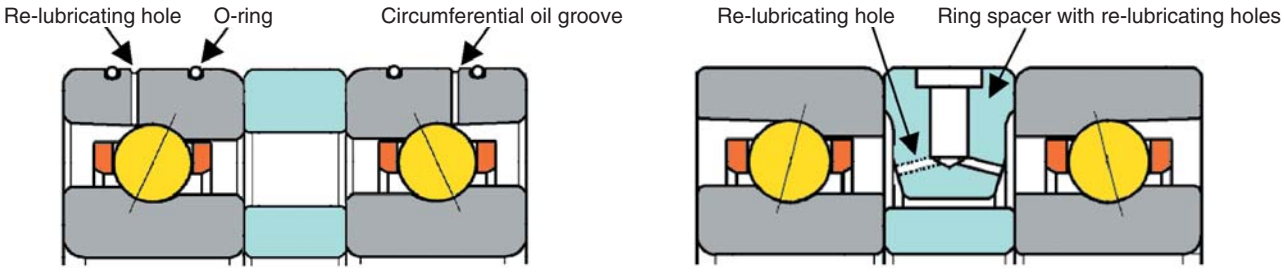

Fig. 1 Design of bearing

*Industrial Business HQ. Industrial Engineering Dept.

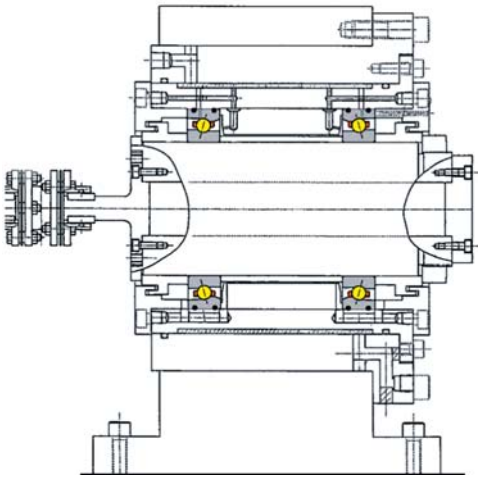

Fig. 2 Test spindle

Table 1 Test conditions

Test bearing	ϕ100×ϕ150×24
Materials	Bearing ring: special bearing steel Rolling elements: ceramic material
Contact angle	25°
Type of preload	Fixed position preload (preload on mounted bearing: 98 N)
Oil feed rate	0.03 mL/10min
Lubrication system	Air-oil
Lubricating oil	VG32
Number of relubricating holes	One/bearing
Jacket cooling	Yes

Fig. 3 provides outer ring temperature data for speeds up to up to 13,000 min^{-1} using fixed position preload bearing samples. Notice that the temperature increase profile using the traditional standard bearing / ring spacer system (oil hole bore dia. 1.2 mm, air flow rate 40 NL/min) was virtually same as the bearing sample using outer ring re-lubrication holes (bore dia. 0.8 mm, air flow rate 25 NL/min).

The data shown in **Fig. 3** shows the temperature rise results while running at 13,000 min^{-1}, but varying the oil and air flow rate. **Fig. 4** gives temperature rise result after fixing the air flow rate at 15 NL/min, but the lubrication injection intervals at 0.03 mL/shot were varied. When the re-lubrication interval was set at 1 shot per minute for the bearing with outer ring re-lubricating holes, over-lubrication occurred and the bearing temperature actually rose significantly (heat buildup). When re-lubrication intervals were reduced to once every 25 minutes, the traditional bearing / ring spacer system exhibited only minor heat rise. We believe that, even though the total oil flow rate into bearing is decreased, the standard bearing / ring spacer system becomes under-lubricated as it is readily affected by an “air-curtain” effect created by

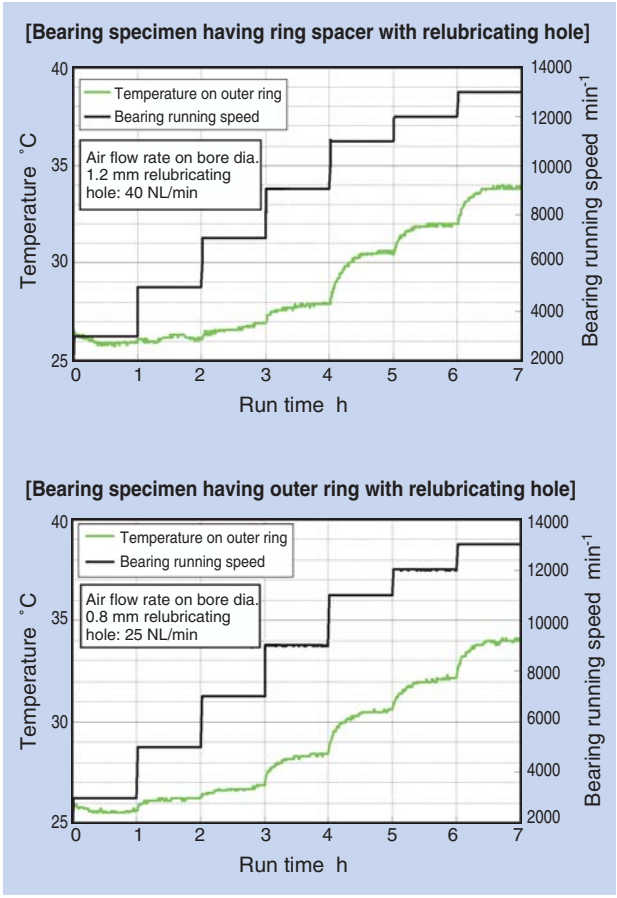

Fig. 3 Bearing temperature

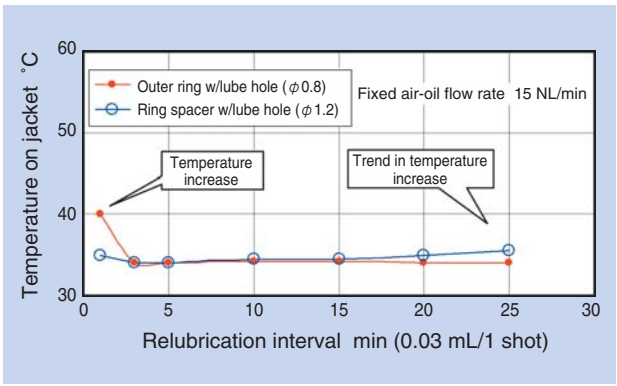

Fig. 4 Amount of oil and bearing temperature

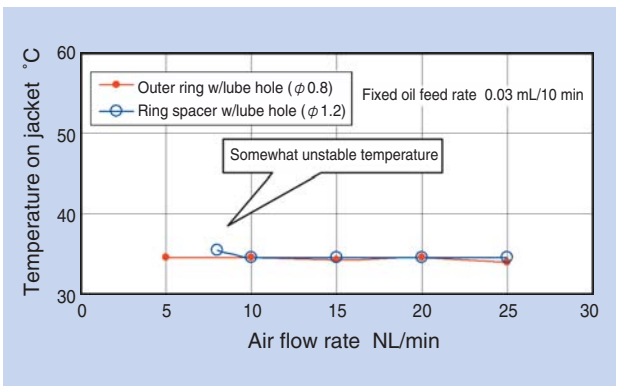

Fig. 5 Volume of air flow and bearing temperature

the high speed movement of rolling elements around the bearing center.

Fig. 5 is a graphic that illustrates test results when the oil flow rate was fixed at 0.03 mL/10 min and the air flow rate was varied. When the air flow rate is reduced, temperature fluctuation occurs with the bearing / ring spacer system. This phenomenon seems to be the result of an “air-curtain” effect that keeps lubricating oil flow from remaining smooth, and the bearing becomes under-lubricated.

From these results, we can see that the oil and air flow rates for a non-traditional bearing that uses an outer ring with re-lubricating holes (bore dia. 0.8 mm) can be reduced, and this bearing type can operate with an air flow rate of 10 - 20 NL/min and oil feed rate ranging from 0.03 mL/5 min to 0.03 mL/25 min.

Fig. 6 is a graph showing the noise levels measured of bearing test samples. Bearings with both the non-traditional outer ring with re-lubricating hole system (bore diameter either 0.8 mm or 1.2 mm) and the traditional bearing / ring spacer system (spacer re-lubricating holes of bore dia. 1.2 mm) were compared. The traditional bearing with a ring spacer / re-lubricating hole (bore diameter 1.2 mm) exposed to an air flow rate of 40 NL/min had a noise level generally less than the non-traditional bearing with an outer ring re-lubricating hole (bore dia. 0.8 mm or 1.2 mm). However, when the air flow rate is reduced to 15 NL/min, the bearing with the non-traditional bearing using an outer ring re-lubricating hole running faster actually generated a lower noise level. These noise level differences seem to result of an air condition created when the air is injected through each re-lubricating hole configuration.

Fig. 7 shows measurement results and the relationships between the re-lubricating hole bore size, air pressure, and air flow rate. When the air pressure is constant, air flow rate is dependent on the re-lubricating hole diameter. Naturally, the smaller the hole, the lower the air flow rate with constant air pressure. Similarly, when the re-lubrication hole size is constant, a lower air flow rate results with a reduced air pressure.

Fig. 8 illustrates the relationship between the re-lubricating hole diameter and air flow velocity (air jet speed) for various air flow rates (calculated values are based on assumption of no loss).

When the re-lubricating hole diameter is constant, the air flow velocity becomes lower as the air flow rate becomes lower. When the air flow rate is constant, the air flow velocity becomes lower as the nozzle diameter becomes larger.

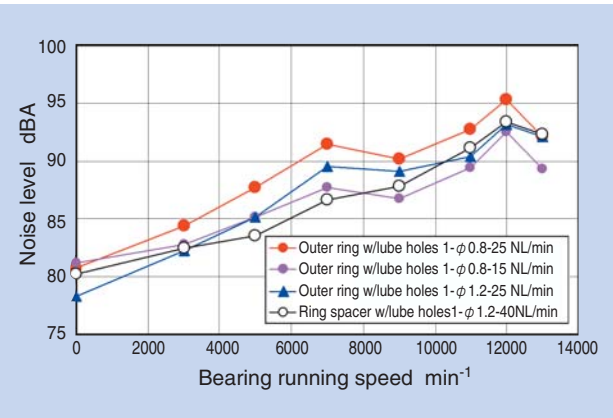

Fig. 6 Noise level

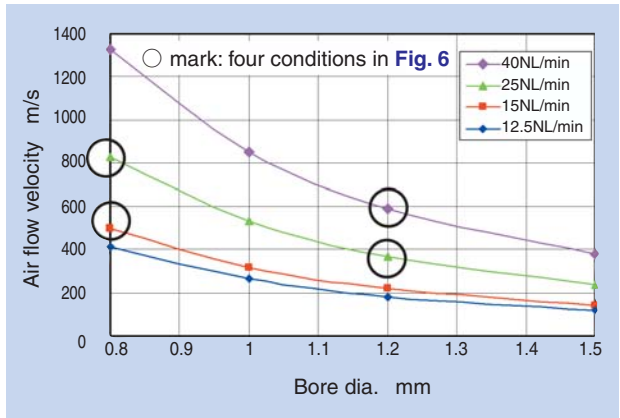

Fig. 8 Air flow velocity

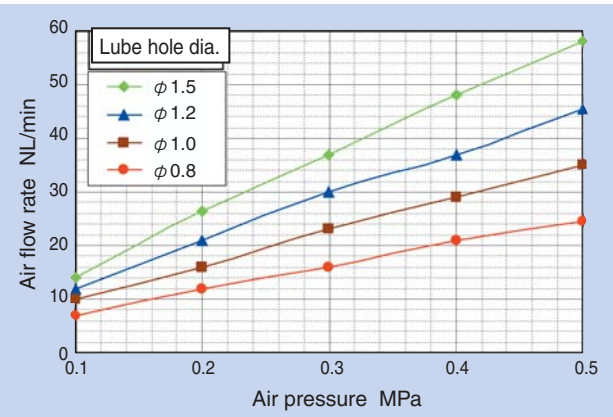

Fig. 7 Air flow volume

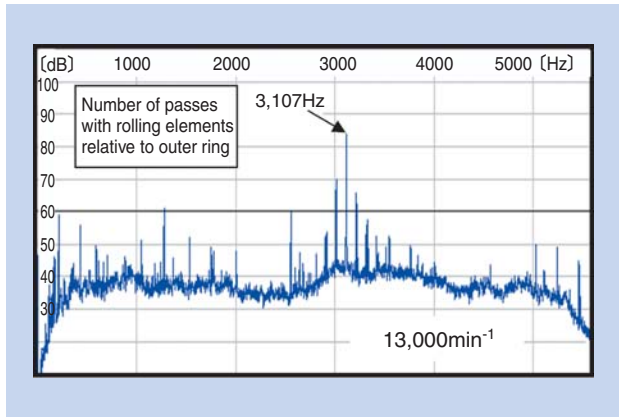

Fig. 9 Frequency of bearing noise

In the case of non-traditional bearings with outer ring re-lubricating holes, high-pressure air is injected through the re-lubricating holes and directly reaches the rolling elements. Also, the distance that the injected air travels is much shorter as compared to using the traditional bearing / spacer system. The reason why the noise level is greater with the non-traditional, outer ring-lubrication system to be that the injected high-pressure air reaches the rolling elements with less velocity loss causing the rolling elements to develop a whistling sound (**Fig. 9**). Information shown in **Fig. 6** shows that the noise level of the non-traditional bearing with outer ring re-lubricating holes (bore dia. 0.8 mm) and an air flow rate of 15 NL/min is lower when compared to the same bearing experiencing an air flow rate of 25 NL/min. The noise level is also lower when the re-lubricating hole bore diameter is 1.2 mm (25 NL/min). It is believed that this is due to the difference in air flow velocity. Air flow velocity in the traditional ring spacer system is limited to only 600 m/s. It seems that the "air curtain" effect helps reduce the air flow velocity before air reaches actually the rolling elements.

4. Improved bearing having outer ring with re-lubricating holes

Sec. 3 provides information showing that the noise level (whistling noise) of a bearing with the non-traditional outer ring re-lubricating system is less than than the traditional bearing / ring spacer system even with improved oil flow efficiency. It seems that a reduction in air flow rate and air flow velocity will reduce noise level.

Method of reducing air flow rate:

Lower the air supply pressure and use a smaller re-lubricating hole bore diameter

Method to decrease air flow velocity:

Reduced air flow rate and use a larger re-lubricating hole diameters

However, because a reduced air flow rate will affect lubrication oil capacity in the supply line tube to the nozzle[1], the flow rate needs to be at least 20 NL/min. In a real-life commercial operation it would probably be appropriate to set air pressure between 0.3 to 0.5 MPa: the re-lubricating hole bore diameter should be 1.2 to 1.5 mm to reduce the air flow velocity while maintaining an air flow supply rate of 20 NL/min. In our investigation, we adjusted the air flow velocity to 400 m/s or lower. We then investigated the nozzle parameters to satisfying all of the above-mentioned requirements.

As a result of our investigation, we have developed a special bearing specification capable of reducing air flow velocity, but maintaining air pressure at approximately 0.3 MPa and also supply a air flow rate of at least 20 NL/min: as illustrated in Fig. 10. The non-traditional outer ring design has two equally spaced re-lubricating holes measuring 1.5 mm diameter as well as a circumferential groove with a cross-sectional area equivalent to a 0.8 mm diameter re-lubricating hole.

Usually, when an outer ring is fed with an air pressure of 0.3 MPa and has two bore 1.5 mm diameter re-lubricating holes, the air flow rate per hole is about 40 NL/min, and the air flow velocity is around 400 m/s. Therefore, we decided to adopt a bearing specification that helps limit the supply air flow rate to approximately 20 NL/min relative to an air pressure of 0.3 MPa (see **Fig. 11**). We also used a smaller outer ring circumferential groove than usual to help control the air flow rate. Furthermore, using of a two-hole design helps cut the air flow rate in half and limit the air flow velocity to 400 m/s or lower.

Fig. 12 compares phase differences of re-lubricating holes on the housing and outer ring with air flow rates. The air flow rate reduction created by the circumferential groove is particularly apparent when

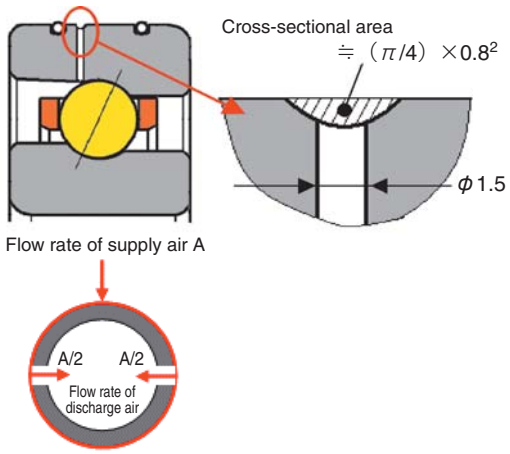

Fig. 10 Improved design

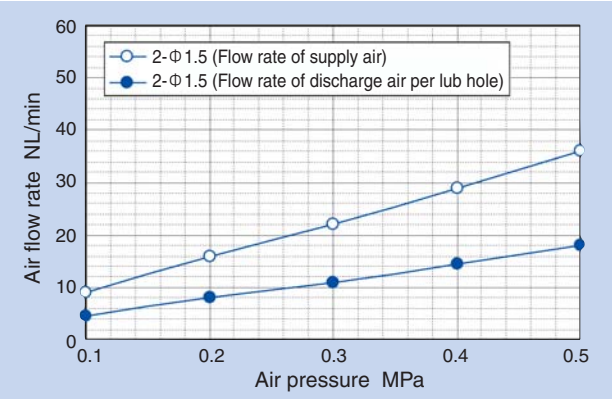

Fig. 11 Air flow volume

the hole diameter is 1.5 mm. When the two re-lube holes are more than 90 degrees apart, this apparently does not significantly affect the overall air flow rate. A maximum flow rate reduction per outer ring re-lubrication hole is achieved by using “axisymmetrically situating” (equally spaced) holes each with a 1.5 mm diameter and situating the housing relube holes exactly at the midpoint between the holes on the bearing outer ring.

Fig. 13 graphically illustrates the result of assessing our improved bearing design. Noise level of our new, non-traditional design outer ring hole system with the hole geometry and distribution mentioned above is lower compared to using a non-traditional bearing with outer ring oil holes a 0.8 mm diameter or a traditional bearing / spacer system.

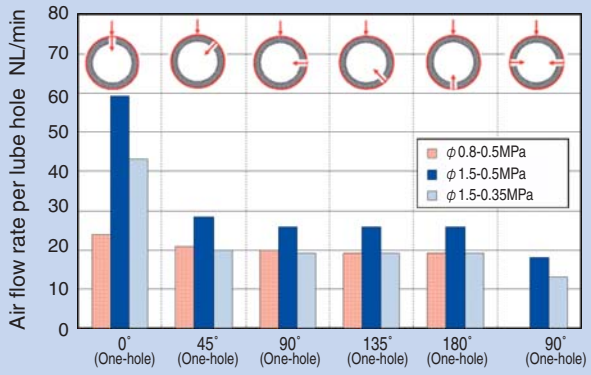

Fig. 12 Phase and air flow volume

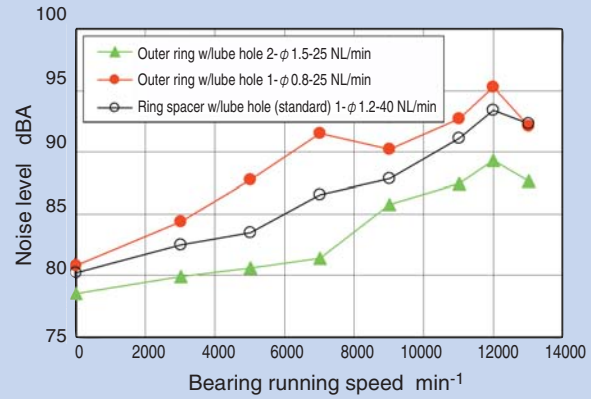

Fig. 13 Noise level

5. Conclusion

We have tested bearing samples designed with a non-traditional, outer ring re-lubricating hole system and evaluated the results to adjust the details to an optimal bearing design. Heat generation of our improved, non-traditional bearing design concept is equivalent to the traditional bearing / ring spacer system where oil is injection nozzle while its noise remains the same. Consequently, redesigning to incorporate a re-lubrication nozzle to the new design onto the ring spacer is needed, but allows the bearing system to be smaller by eliminating the ring spacer. This helps to create an overall more compact machine tool main spindle design that has increased tool rigidity when re-locating the bearing more towards the outer end of tool than when using a traditional bearing / spacer system. In addition, tests results prove that our improved, non-traditional bearing design using outer ring re-lubricating holes is reliably lubricated, and we learned that the air flow rate and oil consumption can be reduced compared to that of the traditional bearing system that uses a separate spacer / re-lubricating hole. At the same time, we have clarified that changing a re-lubricating hole bore diameter size affects bearing noise generation. We plan to continue our efforts to improve bearing lubricating systems and conditions to allow even greater machine tool main spindles speeds. It is encouraging to see how our lower-noise, air-oil lubricated bearing helps improve the functionality of machine tool main spindles.

References

1) Y. Akamatsu and M. Mori, Minimizing Lubricant Supply in an Air-Oil Lubrication System, NTN Technical Review No. 72 (2004) 12-19.

Photo of authors

Futoshi KOSUGI
Industrial Business HQ.
Industrial Engineering Dept.

Kouji NISHINO
Industrial Business HQ.
Industrial Engineering Dept.

High-speed Angular Contact Ball Bearings New 9 Series for Machine Tool

Futoshi KOSUGI*

Many 9 series angular contact ball bearings are used for the main spindles of machine tools in Europe. However, demand for them has risen also in Japan recently. We improved the current design and developed new 9 series high-performance angular contact ball bearings.

We introduce the features and the performance test data of these new 9 series high-speed angular contact ball bearings in this report.

1. Introduction

In order to shorten lead time by addition of process integration capability, an increasing number of machine tool models have recently been adopting unique main spindles whose angle can be varied during machining operation, and examples of such main spindles include milling main spindles on 5-axis machine tools and combined machine tools.

Main spindles on these machines swing to change their angle, and a sufficiently large space is needed on these machine tools to accommodate the motion of main spindles. Therefore, any main spindle in these machines needs to be compact in size, and the main spindle bearing also needs to be compact in size. For this reason, 9 series bearings are used because of their low cross-sectional heights and smaller width.

This article hereunder describes the features and performance of the **NTN**'s newly developed "high-speed angular contact ball bearing 9 series" products.

2. Advantages of 9 Series bearings

Fig. 1 provides information that helps clarify the advantages of 9 series bearings in comparison with 0 series bearings. Because of lower cross-sectional height, 9 series bearings have the following advantages over 0 series bearings:

- **When main spindle diameter (bearing bore diameter) is same with both series (Fig. 1a)** for a given main spindle diameter, a bearing product of smaller outside diameter may be used. Thus, a more compact gearbox design is possible, which leads to size reduction for main spindle.
- **When bearing outside diameter is same with both series (Fig. 1b)**

  In an application where there is limitation on the bearing outside diameter dimension, use of a 9 series bearing can lead to larger main spindle diameter. This feature will allow a main spindle design that provides greater shaft rigidity.

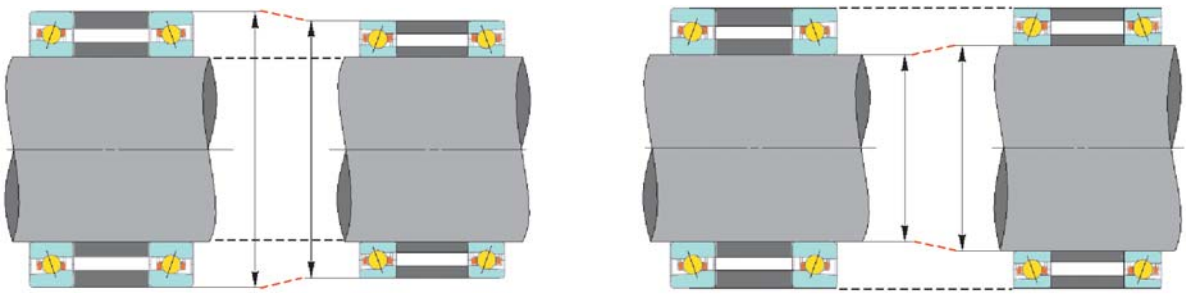

a) Comparison for same shaft diameter (bearing bore diameter) **b)** Comparison for same bearing outside diameter

Fig. 1 Feature of 9 series angular contact ball bearing

*Industrial Business HQ. Industrial Engineering Dept.

On the disadvantage side, having balls smaller than those of 0 series, 9 series bearings are inferior to 0 series bearings in terms of their radial load capacity and maximum allowable axial load. To eliminate this problem, **NTN** has developed 9 series bearing variants that boast greater load capacity.

3. Improved functions on New 9 Series products

3.1 Load rating and allowable axial load

Our newly developed high-speed angular contact ball bearing products—new 9 series—feature improved internal design that include rolling elements of increased diameter as shown in **Fig. 2**, thereby the load rating has been improved by a maximum of 50% and the allowable axial load has been increased by 20% (**Fig. 3**). Consequently, the new 9 series bearing products boast longer life and increased allowance against axial load that occurs during tool change process on machine tools; thus, these bearings will be used in a larger scope of applications.

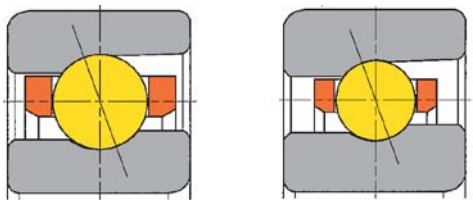

Fig. 2 Design of new product

Fig. 4 provides axial rigidity graph and radial rigidity graph with high-speed angular contact ball bearings (new design and old design), internal bore diameter 100 mm, with constant pressure preload (GN preload).

3.2 Result of operation test

The result of operation test with the high-speed angular contact ball bearings (new design and old design) is described below.

Fig. 5 schematically illustrates the construction of the test rig (main spindle type test rig) used for the test.

Fig. 6 summarizes a result of temperature rise test on the new and old bearing design variants with ceramic balls, air-oil lubricated, and with fixed position preload.

The pattern of heat rise on the outer ring of our new design, up to d_{mn} = 1.45×10^6 (12,000 min^{-1}) is identical to that of the old design. However, at higher speed range, the temperature with the new design is somewhat higher (1 to 2˚C). A possible cause is a larger ball size, which leads to greater PV value (contact surface pressure x slip velocity).

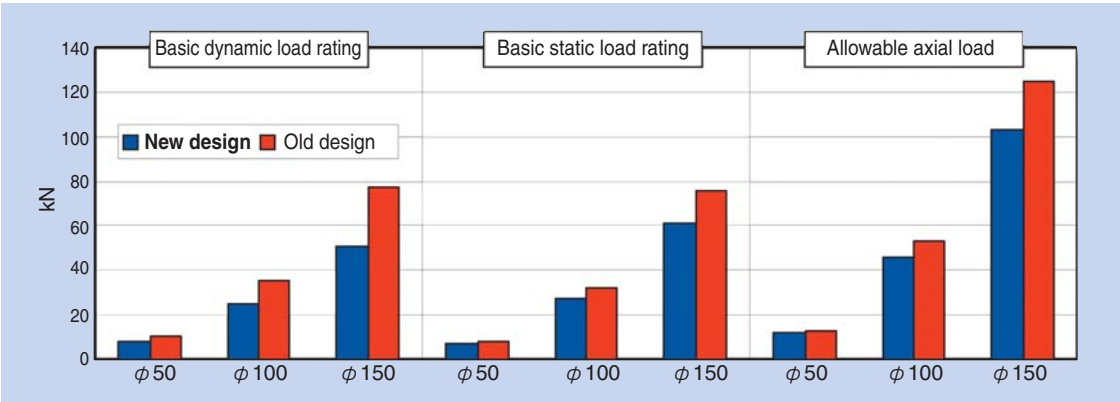

Fig. 3 Basic load ratings and allowable axial load (steel ball, contact angle 20˚)

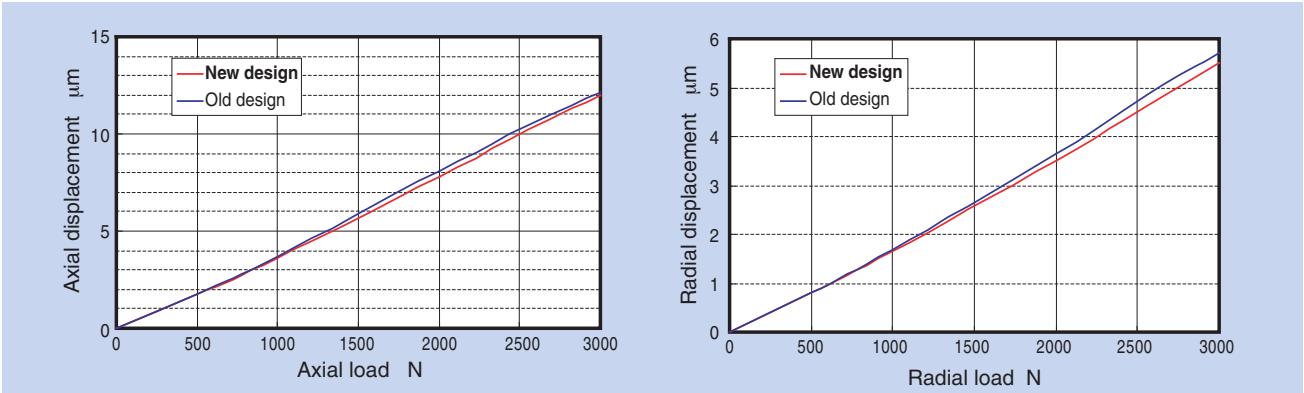

Fig. 4 Rigidity graph (bearing bore dia. 100 mm, constant pressure preload)

Fig. 7 graphically plots the variation in bearing preload in this test: the diagram shows that the new design helps reduce possible increase in preload by approximately 15% compared with the old design. To sum up, the temperature on outer ring on our new design is somewhat higher compared with the old design: nevertheless, our new design boasts improved anti-seizure property because temperature difference across its inner ring and outer ring is smaller, minimizing the increase in preload.

Fig. 8 illustrates test result with constant pressure preload type bearing specimens.

The temperature on the outer ring of our new design is higher by 1˚C compared with the old design: nevertheless, our new design is capable of stable operation up to ultrahigh-speed region of $d_m n = 2.40 \times 10^6$ (20,000 min^{-1}).

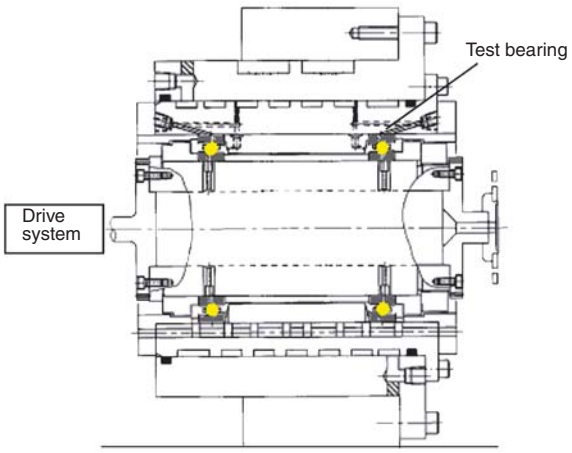

Fig. 5 Test spindle

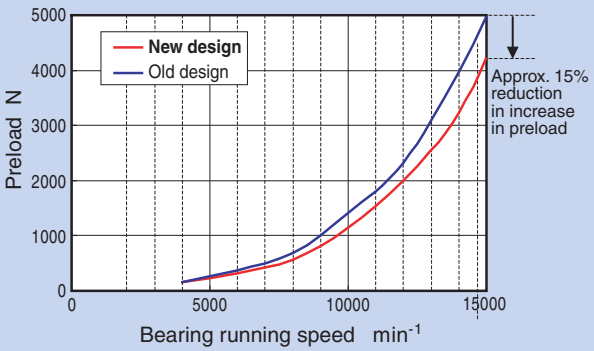

Fig. 7 Correlation between speed and preload

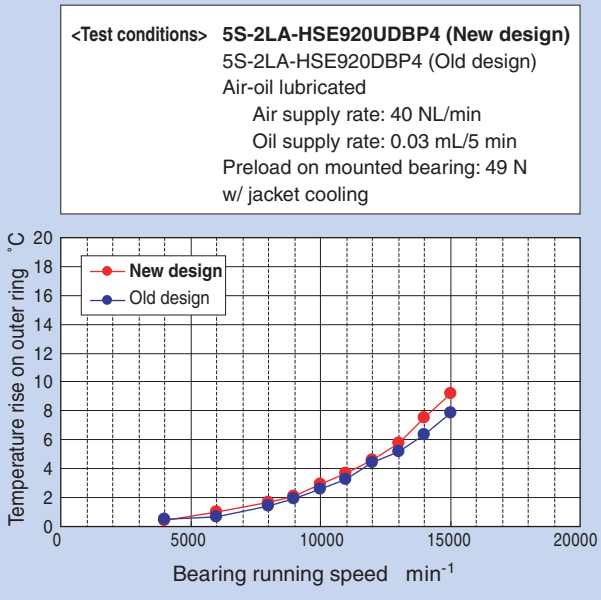

Fig. 6 Test results (Fixed position preload, Air-oil)

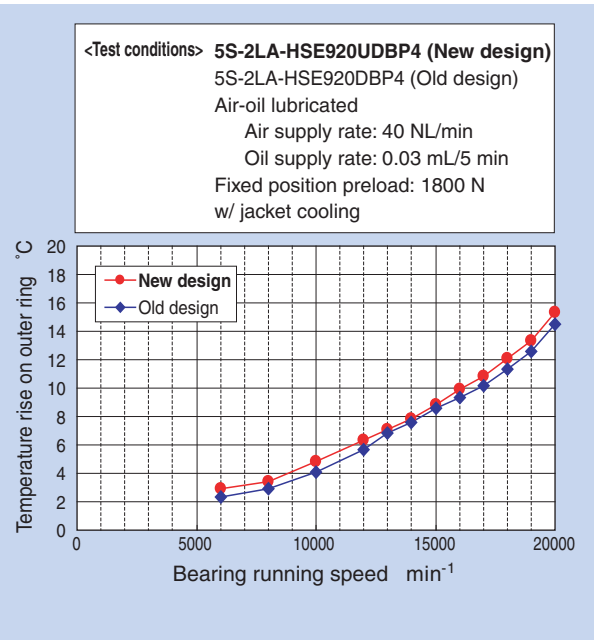

Fig. 8 Test results (Constant pressure preload, Air-oil)

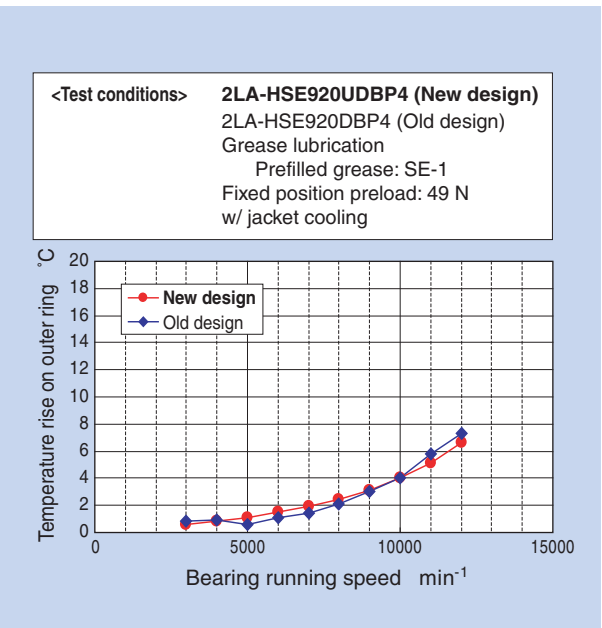

Fig. 9 Test results (Fixed position preload, Grease)

Fig. 9 summarizes test result with grease-lubricated specimens having steel balls, with fixed position preload setting. Even under these conditions, heat rise on the outer ring of the new bearing design remains low up to $d_{\mathrm{m}}n$ = 1.44×10^6 (12,000 min^{-1}).

4. Conclusion

Compared with old products, our newly developed high-speed angular contact ball bearing 9 series products boast greater radial load capacity and allowable axial load, and longer life and increased load capacity during tool change process on machine tools.

In terms of functions, the bearing temperature on our new design is 1 to 2˚C higher compared with old design. Nevertheless, the temperature gradient across the inner ring and outer ring on our new design is low and increase in preload in high-speed bearing operation is also low. Thus, our new design excels in anti-seizure property.

NTN will add its “high-speed angular contact ball bearing new 9 series” products, which boast compact size and enhanced functionality, to its ULTAGE Series line of products, and will actively market these novel products.

Photo of author

Futoshi KOSUGI

Industrial Business HQ
Industrial Engineering Dept.

Ball Screw Support Angular Contact Thrust Ball Bearing Unit "BSTU Series"

Hiroki TANIMURA*

ULTAGE

NTN had developed the BST series of single row angular ball bearings for ball screw support in the ULTAGE series. Now, **NTN** has developed the BSTU series of double row angular ball bearings for the ULTAGE series.

The BSTU series products have high basic load ratings (highest levels in the world as bearings for ball screw support), low torque, and high dust-proofing.

1. Introduction

NTN has been marketing ball screw support bearings—the ULTAGE Series “ball screw support single row angular contact thrust ball bearing unit (BST series)” products.

Recently, **NTN** has developed and commercialized a novel high load rating double row angular contact ball bearing unit and has added it to the ULTAGE series line of products.

Our single row BST series products are typically used in Asian markets: while our newly developed BSTU series of products, standard ball screw support angular contact thrust ball bearing products, are intended for the European market.

Our newly developed BSTU series high capacity double row angular contact ball bearings unit products boast a higher load bearing capacity—highest among ball screw support bearings in the world. At the same time, adoption of a novel seal helps realize lower running torque and positive dust-proofing performance.

NTN has named this new series **“BSTU (Ball screw Support angular contact Thrust ball bearing Unit) series”**.

2. Structure and advantages

Fig. 1 shows the structure of a BSTU series product.

The advantages of the BSTU series bearings are hereunder described.

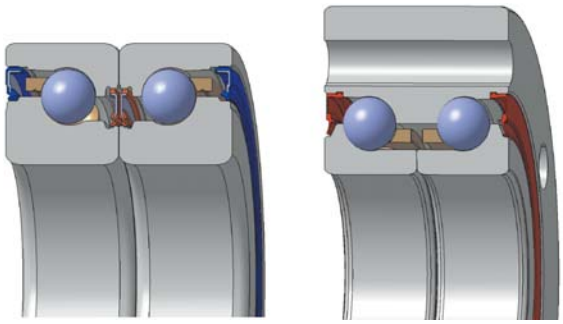

BST series
Single row (DB duplex)

BSTU series

Fig. 1 Design of BST and BSTU

2.1 Realization of higher load capacity

Through its unique design featuring the maximum possible number of larger steel balls, **NTN** has realized greater load capacity, as shown in **Figs. 2** and **3**. These load capacity values are highest among the world’s ball screw support bearings.

*Industrial Business HQ. Industrial Engineering Dept.

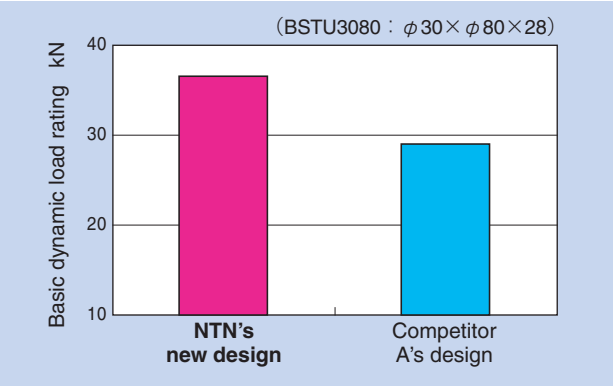

Fig. 2 Basic dynamic load rating (BSTU3080)

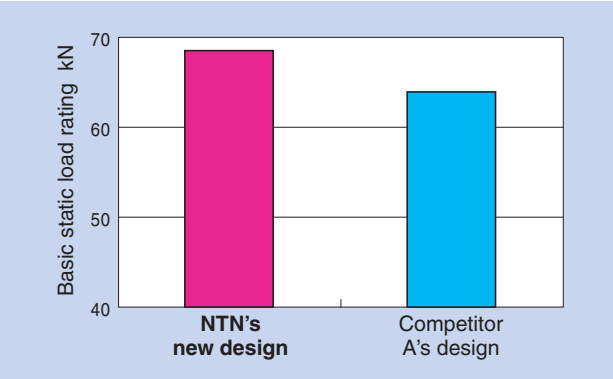

Fig. 3 Static load rating (BSTU3080)

2.2 Low torque and reliable dust-proofing performance

By adopting a novel seal lip shape shown in **Fig. 4** (light contact seal), we have achieved both reliable dust-proofing performance and lower running torque of the bearing.

A unique light-contact type main lip helps realize reliable dust-proofing performance and lower running torque of the bearing: the side lip positively prevents the grease in the bearing from flowing out.

This pre-greased bearing is an easy-to-handle, eco-friendly design—the user does not need to rinse and degrease the bearing and prefill grease into the bearing when assembling the bearing at the user's site.

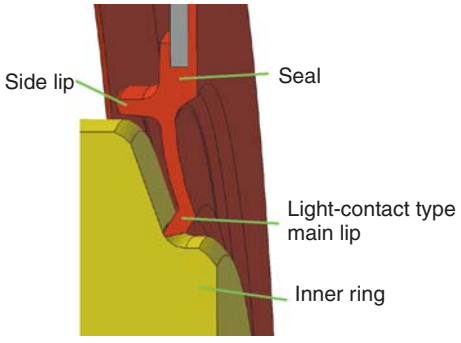

Fig. 4 Seal design

2.3 Longer life

Any ball screw support bearing is subjected to vibration during rapid traverse (the cutting tool approaches the work piece) and low speed rotation in machining, as well as during cutting operation. Therefore, the bearing has to satisfy very demanding requirements for its lubrication. To prevent possible disruption of oil film caused by vibration and shock, we have adopted urea-based grease as standard because of its excellent fretting resistance quality and grease life.

The performance of **NTN**'s standard urea-based grease "L588 " will be described later in Sec. 3.

2.4 Improved mountability

As shown in **Figs. 5** and **6**, the outer ring is provided with mounting bolt holes so that the bearing is easily mounted to the housing.

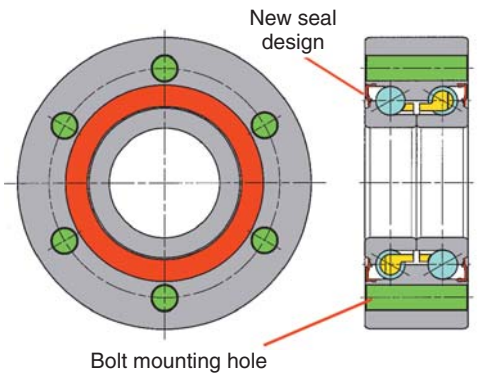

Fig. 5 Bearing design

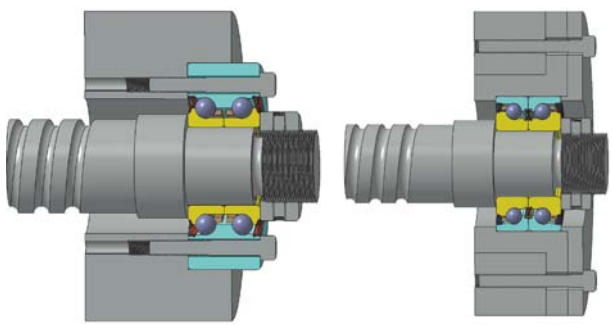

Fig. 6 Bearing assembly

2.5 Adoption as new standard series

The BSTU line of products feature bore diameter of 20 to 100 mm, and outside diameter of 68 to 200 mm.

The bearing designation system of this new series is described to the right.

[Example of bearing designation]

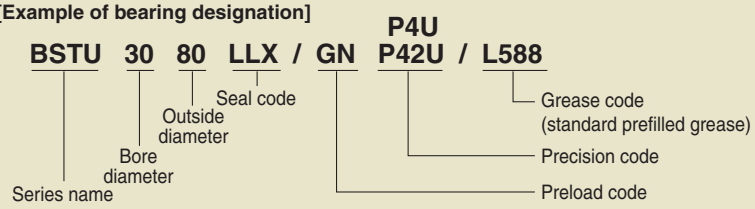

3. Assessment of performance

The results of performance test on the BSTU series bearings are described below.

3.1 Temperature characteristics

The test bearings were run, simulating typical run patterns for machine tool bearings. Consequently, as shown in Fig. 7, the NTN's BSTU series bearings boast excellent temperature characteristics (limited temperature rise) thanks to adoption of the "new light-contact type seal". We believe that owing to positively limited temperature rise, the BSTU series bearings least contribute to thermal elongation of the ball screw, and is capable of high-speed operation on machine tools.

<Test conditions for temperature rise test>

Bearing number: BSTU3080LLX/GNP4U/L588
Running speed: 1,000–5,000 min^{-1}
Preload: 2,700 N
Lubrication system: Grease lubrication
(Amount of prefill: 1.6 gr, 25% the bearing space)

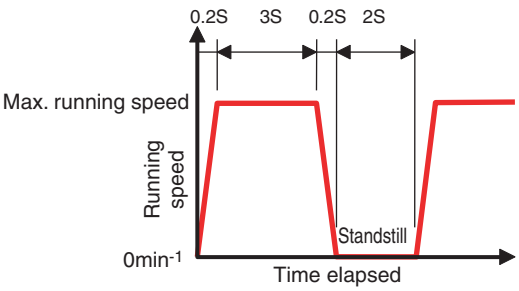

Run pattern for temperature rise test

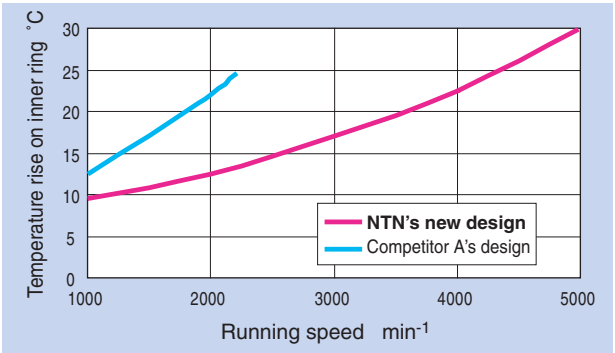

Fig. 7 Test results of temperature rise

3.2 Torque characteristics

Fig. 8 provides information about running torque occurring on the test bearings running in one direction only. Regardless of running speed, the BSTU test bearings boast stably low running torque.

<Test conditions for torque characteristics test>

Bearing number: BSTU3080LLX/GNP4U/L588
Preload: 2,700 N
Lubrication system: Grease lubrication
(Amount of prefill: 1.6 gr, 25% the bearing space)

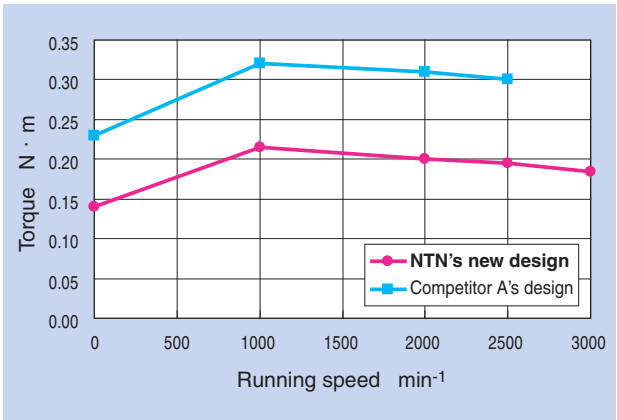

Fig. 8 Test results of rotational torque

3.3 Limiting speed

Because of limited temperature rise and stably low torque, the BSTU bearings are capable of operation at higher speed range (**Fig. 9**).

Bearing number: BSTU3080LLX/GNP4U/L588
Lubrication system: Grease lubrication
(Amount of prefill: 1.6 gr, 25% the bearing space)

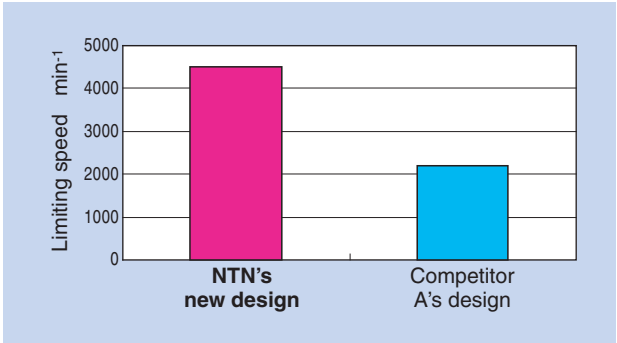

Fig. 9 Limiting speed

3.4 Grease characteristics

The BSTU bearings adopt urea-based grease "L588" that boasts excellent fretting resistance quality and grease life. **Fig. 11** shows the results of fretting corrosion test. In this test, a stationary ball is forced to a plate as shown in **Fig. 10**, and the plate is horizontally reciprocated to develop reciprocating friction, thereby the characteristics of the grease are evaluated based on the depth of resultant wear.

Compared with lithium grease, the **NTN**'s standard urea-based grease "L588" boasts excellent fretting corrosion resistance quality, and is suitable for ball screw support bearings that are subjected to inching motion and oscillating motion.

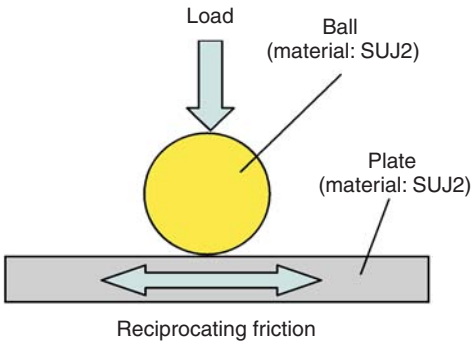

Fig. 10 Test method of fretting corrosion

<Test conditions for fretting corrosion test>

Load: 98 N
Max. contact pressure: 2,560 MPa
Number of load applications: 8.6 (x10^5 cycles)
Test duration: 8 h
Sliding cycles: 30 Hz, amplitude: 0.47 mm
Ambient conditions: Room temperature, atmosphere

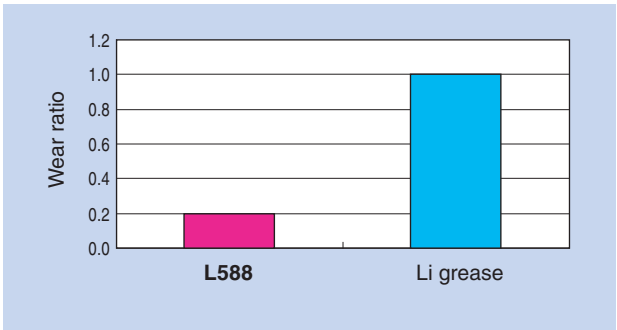

Fig. 11 Test results of fretting corrosion

3.5 Dust-proofing characteristics

On machine tools, chips and coolant can reach an area around the ball screw. Therefore, the ball screw support bearing needs to be resistant against ingress of dust.

Fig. 12 exhibits the result of dust-proofing test on our newly developed ball screw support bearing. Thanks to excellent dust-proofing feature of the novel light-contact type seal, there is no ingress of foreign matters into the bearing.

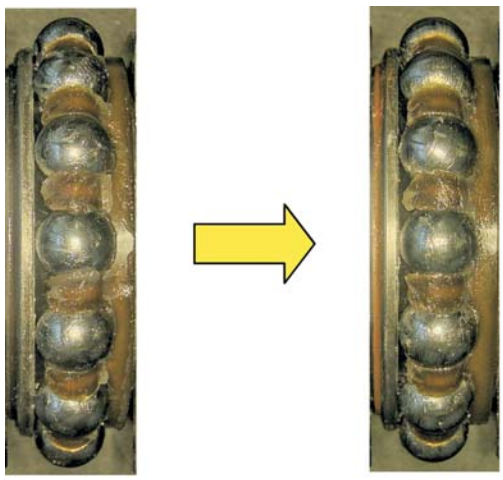

Fig. 12 Results of dust test

<Test conditions for dust-proofing test>

Bearing number: BSTU3080LLX/GNP4U/L588
Running speed: 2,200 min^{-1}
Lubrication system: Lubrication with prefilled grease
Dust: Grain size 5 to 75 μm
(Ingredients: SiO_2, Fe_2O_3, Al_3O_3, etc.)
Hue of dust: Brown
Test duration: 1 hr.

4. Conclusion

NTN's newly commercialized ball screw support bearing "BSTU series" products boast higher load capacity and lower torque, which mark the world's best performance levels, as well as improved dust-proofing quality, longer life and easier mounting procedure. To be able to help realize the eco-friendly society, bearing manufactures have to realize engineering innovations to satisfy various requirements on various areas in machine tools. In this context, our BSTU products provide solutions to needs for longer bearing life and lower energy consumption.

To be able to cope with various market needs, **NTN** will remain committed to development efforts for next-generation bearings through continued improvements and challenges for higher functionality.

Photo of author

Hiroki TANIMURA

Industrial Business HQ
Industrial Engineering Dept.

Ultra Small Grinding Sludge Briquetting Machine

Akira NISHIYAMA*
Michio TANAKA*
Yuuki HONMA*

We had already established an economical recycling technology that separates the steel and grinding lubricant in grinding sludge and had developed a grinding sludge briquetting machine.

This time, we developed the PRG-III model ultra-small grinding sludge briquetting machine for small plants that produce low volumes of grinding sludge.

1. Introduction

Since acquisition of ISO 14001 certification in 1998, **NTN** has been making efforts in mitigating its environmental impacts in order to help realize the recycling-oriented society. In business year 2000, **NTN** developed an economically justifiable technique to separate grinding sludge, occurring from its bearing manufacturing process, into metal and coolant. Also a machine tailored for this purpose (that is, grinding sludge briquetting machine) would need to be designed and created. Thus **NTN** has successfully established a recycling technology (**Fig. 1**) for reusing recovered metal sludge and coolant as useful resources.

Consequently, **NTN** has achieved not only great cost reduction in treating its grinding sludge but also “zero emission” (no grinding sludge is disposed outside **NTN**’s site).

In marketing this technology, **NTN** has been supplying two types of grinding sludge briquetting machines to cope with varying volume of grinding sludge occurring in the users of **NTN** briquetters: these types are model PRG-I whose compression

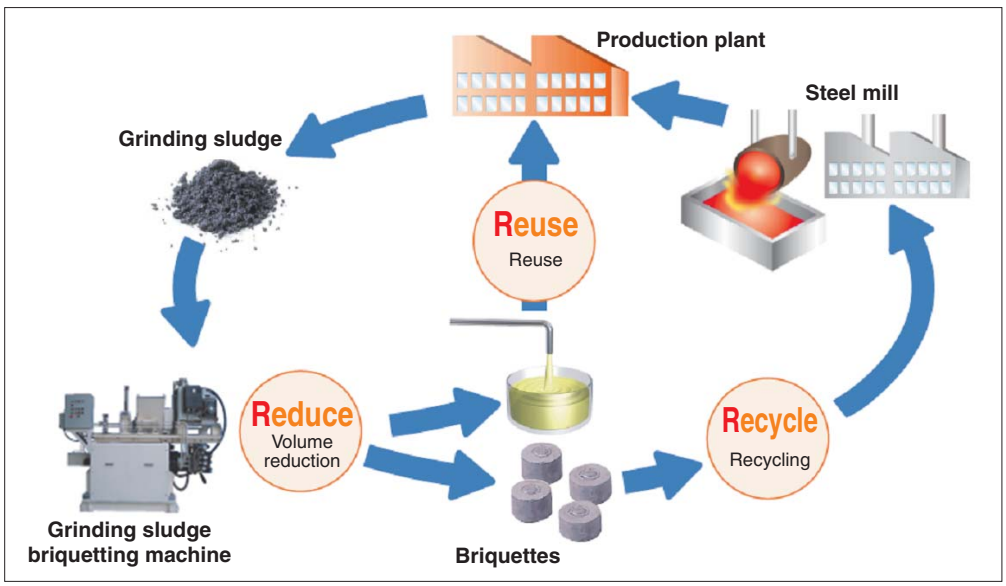

Fig. 1 Grinding sludge recycle system

*Production Engineering R&D Center

power is rated at 1,000 kN (processing capacity: 30 t/month) and model PRG-IIL whose compression power is rated at 520 kN (processing capacity: 20 t/month). From these marketing efforts, **NTN** has learned that certain large-scale manufacturers would prefer to dispose of the grinding sludge generated by the smaller machining lines on-site.

To address this trend, **NTN** has developed, based on its so-far accumulated grinding sludge briquetting technique, a novel super-compact grinding sludge briquetting machine for small-scaled production sites—this new development is **NTN**'s model PRG-III that requires a smaller floor space.

2. Concept of Model PRG-III

Fig. 2 illustrates percentage proportions of number of manufacturers in terms of grinding sludge emissions particularly in the fields of automotive components, bearings, and steel products.

This diagram shows that monthly grinding sludge emission is not greater than 5 tons with 46% manufacturers. In other words, grinding sludge emissions are relatively low with many manufacturers, and these companies want a grinding sludge disposing equipment that needs a smaller floor space.

In addition, we have learned that because physical properties (in particular, water content) of grinding sludge are unique to each manufacturer and can vary every day, the grinding sludge briquetting machine has to be capable of adjusting compression conditions according to the physical properties of the intended grinding sludge.

From these findings, we have established the following concept for our novel supercompact grinding sludge briquetting machine model PRG-III:

(1) Automatic setup of compression conditions
Knowledge based setup, and optimization for compression conditions

(2) Compact
Floor space: 40% as small compared with PRG-I
Machine weight: 40% as low, compared with PRG-I
Capacity for treating grinding sludge: 5 tons per month

(3) User-friendly
Improved operability and maintainability

(4) Eco-friendly
Reduction in electricity consumption

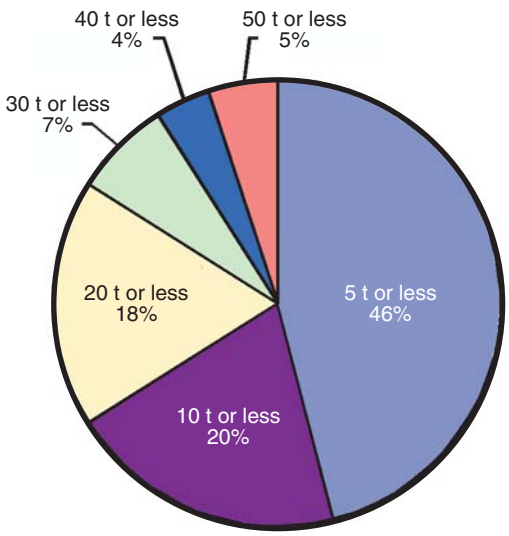

Fig. 2 Breakdown of manufacturers in percentages by monthly grinding sludge emission

3. Specification and advantages

An appearance of our newly developed supercompact grinding sludge briquetting machine model PRG-III is shown in **Fig. 3**, and a result of comparison of its specification with those of the conventional models PRG-I and PRG-II L is summarized in **Table 1**.

Fig. 4 below shows appearances of briquettes obtained from the models PRG-I and PRG-III.

The major advantages of the machine are :

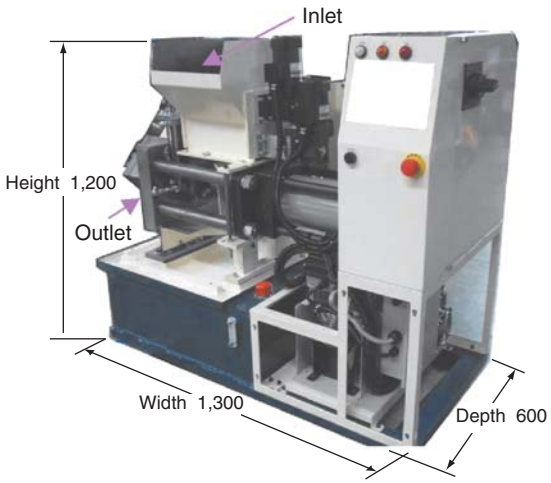

Fig. 3 View of PRG-Ⅲ

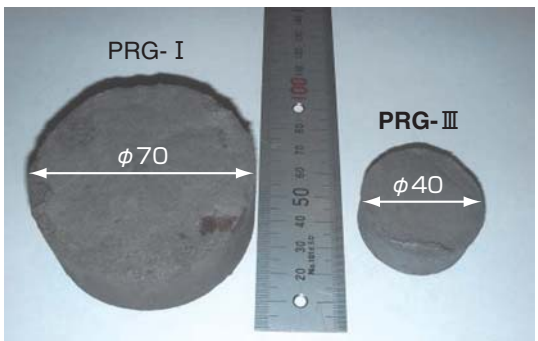

Fig. 4 Briquets of PRG-Ⅰ & PRG-Ⅲ

Table 1 Grinding sludge briquetting machine type and main specification

Major characteristics	PRG-Ⅰ	PRG-ⅡL	**(New) PRG-Ⅲ**
Capacity (water-soluble sludge)	max. 80kg/h (30 t/month)	max. 50kg/h (20 t/month)	max. 13kg/h (5 t/month)
Dehydrating performance in %	90wt%	90wt%	90wt%
Compression force	max. 1000kN	max. 520kN	max. 300kN
Briquette size	ϕ70	ϕ60	ϕ40
Approx. dimensions W×H×D	2510×2200×850	2220×1950×620	1300×1200×600
(Benchmark) Floor space needed	2.1m^2	1.4m^2	0.8m^2 (40%, compared with PRG-I)
Machine weight	2500kg	1800kg	800kg

(1) Adoption of automatic compression conditions setup system (knowledge based setup, and optimization for compression conditions)

For optimal briquetting of various grinding sludge types, each having a unique water content, compression conditions (compressing force, and compressing velocity), need to be set up according to the water content of sludge. To address this challenge, we have developed a unique solution—that detects compressing force and compressing velocity during briquetting cycle. The water content is then estimated based on the resultant measurements, thereby optimal compression conditions (compressing force and compressing velocity) are automatically adjusted. Consequently, we have achieved stable briquette formation.

(2) Space saving (compact design)

The machine adopts a rack that integrally consists of a main base, a hydraulic oil tank, a compact compressing mechanism and a compact feeder. Thus, the machine needs a smaller floor space measuring 1,300 mm in width and 600 mm in depth (40% as small, compared with conventional PRG-I).

Also, the machine boasts light weight as summarized in **Table 1** (40% as low, compared with conventional PRG-I).

(3) User-friendly (improved operability and maintainability)

Aiming at realization of user-friendly machine, we have achieved improved operability and maintainability. The typical improvements achieved are :

[1] The total height is limited to 1,200 mm to mitigate difficulties in feeding grinding sludge into the machine.

[2] A touch-panel type operator's control panel has been adopted to improve operator-friendliness of the machine.

[3] A database of briquetting conditions other than compression conditions has been established and the machine is equipped with this database: consequently, the operator can change over the processing conditions for handling a new grinding sludge type, by simply manipulating one push-button switch.

[4] This new machine type incorporates a unique monitor system that is capable of data management, including updating of production records, maintenance records, and fault occurrence log. The unit also contains an early warning system, alerting the user of necessary maintenance needed to the machine. The machine is also capable of real-time monitoring of its status at a remote site so that a fault on the machine is promptly corrected.

(4) Improved stability in forming briquettes, improved material loading and delivering

Adoption of the previously-mentioned automatic compression conditions setup system helps optimize the briquetting conditions.

To ensure more reliable sludge loading and briquettes discharging, we have incorporated the following features into the machine:

[1] To prevent stagnant sludge flow at the sludge loading port and feeding section (that is, bridging of sludge), a reversing cycle is provided for the stirring paddle unit in the sludge loading port as well as the sludge feed screw. At the same time, the motors for the stirring paddle unit in the sludge loading port and the sludge feed screw n can be arbitrarily changed so that the machine is capable of handling sludge types of various physical properties.

[2] To prevent failure in delivering briquettes, we have introduced a newly designed discharge section (**Fig. 5**) that obliquely delivers grinding sludge-derived briquettes in the direction same as that along the delivery chute. Also, we have adopted a

uniquely structured slide that positively prevents ingress of sludge and coolant so as to improve durability of the slide.

(5) Energy saving

The machine adopts an inverter-driven hydraulic pump as well as a novel pump control system that allows the hydraulic pump on the machine to run only when needle for actuating the hydraulic cylinder: as a result, power consumption has been reduced by 14% compared with conventional hydraulic pump control systems that require the hydraulic pump to run continuously.

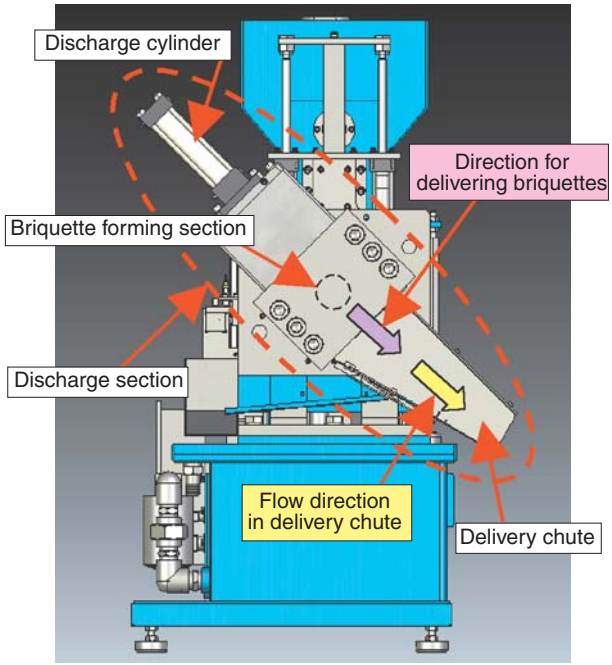

Fig.5 Discharge section in PRG-Ⅲ

4. Conclusion

So far, **NTN** has remained committed to development of recycling techniques typically intended for disposal of grinding sludge emitted from centralized coolant filtration equipment in large-scale manufacturing sites. **NTN** has recently developed the “super-compact grinding sludge briquetter model PRG-III” that incorporates a unique control system capable of optimizing compression conditions (compressing pressure and compressing velocity) in accordance with the water content of an intended grinding sludge type. We expect that this equipment will be conveniently used in disposing small lots of varying physical properties released from small-scale coolant filtration equipment, etc.

One additional application of our super-compact briquetter is solidification of various materials such as paper dust, cutting chips, dehydrated sludge, and tumbler sludge. To be able to solidify a diversity of materials, **NTN** will further continue R&D works for the equipment to help achieve mitigation of environmental impacts from manufacturing activities so as to realize the recycling-oriented society.

Photo of authors


Akira NISHIYAMA
Production Engineering R&D Center


Michio TANAKA
Production Engineering R&D Center


Yuuki HONMAI
Production Engineering R&D Center

Compact and Multifunction Controller for Parts Feeder

Kunihiko SUZUKI*

NTN parts feeders that automatically line up and supply parts are accepted by manufacturing in various fields, and are contributing to the improvement of automation and productivity in manufacturing processes. **NTN** developed a new series of controllers for parts feeders. Features of these controllers are that they are lightweight, compact and multifunction. Moreover, a special vibration sensor has been newly developed. This article introduces the features of these new small controllers for parts feeders.

1. Introduction

Vibratory parts feeders are commonly used in production lines of various industrial fields, which include car manufacturing, electric appliance manufacturing, food processing and semiconductor device manufacturing. Controllers that control vibration of these vibratory parts feeders have to be compact and light weight while being capable of supporting ever diversifying applications.

NTN has commercialized a new series of parts feeder controllers aiming at size reduction, lighter weight and multi-function capability. This report provides information about the advantages of these new controller products.

2. Overview of NTN's new Parts Feeder controllers

In 1996, **NTN** marketed a digital controller for parts feeders—the first in the bearing manufacturing industry in Japan. Its higher control accuracy and improved operation, not obtained from conventional analog controllers, was highly appreciated. This controller become the standard digital controller for parts feeder in the manufacturing industry in Japan. The controller models described in this document are **NTN**'s third generation parts feeder controllers, and boast both compact light-weight design and multi-function capability through incorporation of additional user-friendly functions thanks to unique digital control technology.

Fig. 1 provides comparison with the old controller model in appearance. The new model is shown in the right—its outside dimensions are much smaller though its control capacity is equivalent to that of the old model.

In **Table 1**, the technical data of our new controllers are compared with those of the old controller.

To accommodate an increased number of functions, the quantity of terminals including I/O signal terminals has doubled: therefore, a new compact terminal block has been designed, and at the same time, the entire control panel on the new controllers can be fully opened to provide a sufficiently large space for wiring work (see **Fig. 2**).

Furthermore, in addition to development of the new controllers, we have also developed a novel vibration sensor. Though compact in size, the new controllers are more immune to noise interference thanks to their improved circuitry: they allow for extension of lead wires using an ordinary terminal block or cable, etc.; thereby wiring work on the controller at the site is much easier.

3. Advantages of the new controllers

(1) Compact size, and light weight

In terms of the physical volume, the size of the new models—K-ECH45/K-ECJ45—are 60% of the size of the old model (see **Table 1** and **Fig. 3**).

The challenge to size reduction of the controller is how to reduce the surface area needed for heat radiation and interfacing arrangement.

*Precision Equipment Division Product Engineering Department

Fig. 1 Externals view (right side : new model)

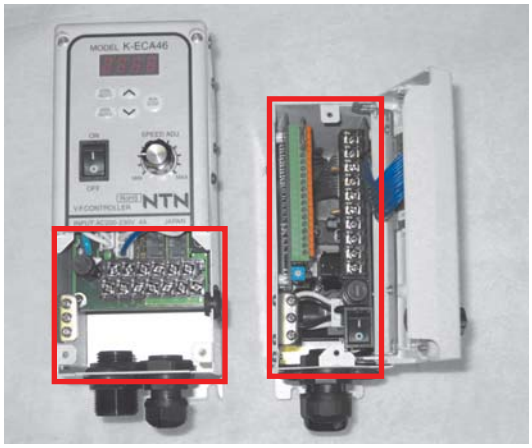

Fig. 2 Wiring enclosure (right side : new model)

Table 1 Comparison table of new and old model

Characteristics \ Model number		New model (low capacity)		New model (high capacity)		Old model		Features of new model
		K-ECF25	K-ECG25	K-ECH45	K-ECJ45	K-ECA49	K-ECA46	
External dimensions W×H×D[mm]		60×140×142		82×140×142		80×180×180		Compact size as small as approx. 60% the old controller of a same control capacity
Supply voltage		100/200V		100/200V		100V	200V	New model is capable of inputs of both 100 V and 200 V.
Control capacity		2A		4.5A		4A		
Allowable frequency range		30～500Hz		30～500Hz		30～250Hz		Can drive SMD feeder.
Functions	Multi-speed function	Panel + 3 stages		Panel + 3 stages		No		Internally includes three speed memories.
	Analog voltage command	Yes		Yes		No		Capable of speed change from outside device.
	Valve control function	Yes		Yes		No		Can be connected to three valves.
	No work-piece warning function	Yes		Yes		No		Capable of switching over between sensor 1 and sensor 2.
	Fault signal output	Yes		Yes		No		Fault signal is triggered when a fault occurs.
	Alarm signal output	Yes		Yes		No		Alarm signal is triggered when alarm situation occurs.
	Over-load protection function	Yes		Yes		Yes		
	F/V curve	18 sets		18 sets		2 sets		Greater selectable range for load protection curves.
	Constant voltage function	Yes		Yes		Yes		
	Constant amplitude function	No	Built-in	No	Built-in	Optional; externally provided		
	Resonance point tracking function	No	Built-in	No	Built-in	No		

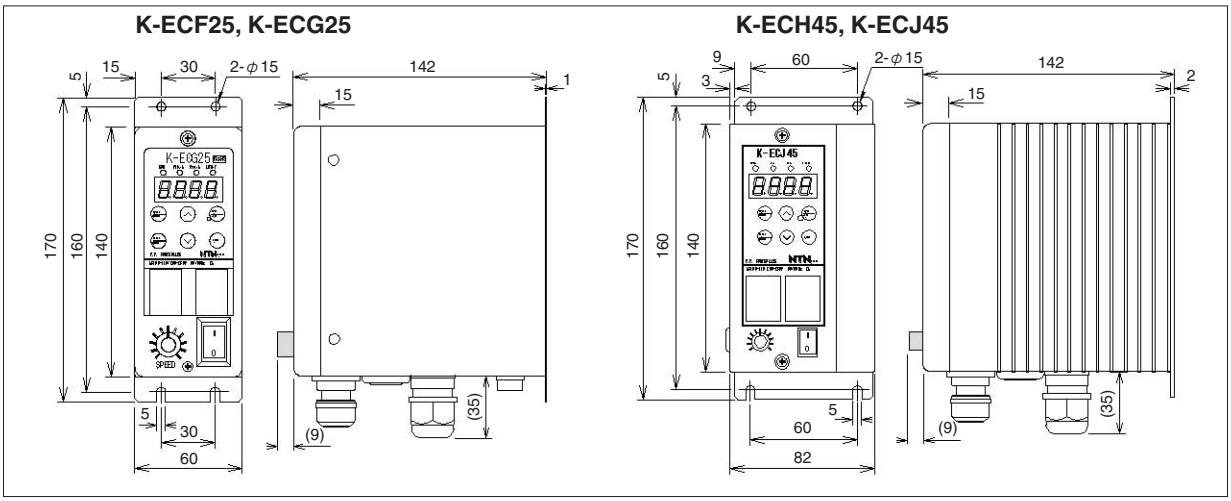

Fig. 3 New controller outline dimension

To be able to reduce heat radiation area, it is most important to mitigate heat generation from the built-in parts. The heat generation on the controller has been reduced by adoption of an appropriate FET and improvement in the drive circuit; thereby the surface area needed for heat radiation has been reduced by 20%.

Furthermore, the location for mounting the radiation fins on the new controllers is a side face instead of the rear face on the old controller; thereby a greater radiation area is available and the size of the radiation fins can be reduced by half. Note that the rated current greatly differs between the medium sized general-purpose vibrator and large-sized general-purpose vibrator. Previously, one controller model has been used regardless of necessary control capacity. In contrast, two differently sized controller types are now available—the larger size controller features greater control capacity. The smaller capacity controller (K-ECF25/K-ECG25) that is responsible for control of vibrators up to a medium size, boasts a reduced size—46% of the old model.

On the new controllers, the surface area is large enough for interfacing work, including wiring work is provided since the entire control panel can be fully opened (see **Fig. 2**). Now, the wiring space is as large as the front face of the controller: at the same time, the signal circuit employs a compact plug-in-type terminal block. Consequently, the new controllers boast an increased number of I/O points despite their smaller space requirement.

Furthermore, adoption of smaller radiation fins has led to a light-weight enclosure design that does not require greater mechanical strength: consequently, thinner wall thickness can be adopted, leading to 30% weight reduction with the entire controller.

(2) Multi-function capability

• Overload protection

The new controllers are capable of setting the rated current of the vibrator so that the vibrator connected to the controller is reliably protected against a possible overload. The level of current flowing to the electro-magnet in the vibrator can greatly vary depending on the dimension of gap between the magnet and the armature. Previously, incorrect setup of the controller could cause overcurrent to flow the electro-magnet. The **NTN**'s new controllers automatically regulate their output voltage in order to protect the electro-magnet. This feature has been available with the **NTN**'s old controller model: however, the new controllers feature improved detection accuracy and the lower limit of their allowable setting rage is 0.2 A instead of 0.5 A on the old model.

• Control for solenoid valve

When the parts feeder is a two-track (two-lane) type as shown in **Fig. 4**, a conventional parts feeder controller needs to control the solenoid valve for a relevant track (lane) in accordance with the current status detected by a work-piece presence sensor, by using a compact programmable logic controller (hereinafter referred to as "PLC"). This system poses a cost problem since an additional PLC, DC power supply, casing, etc. will be needed in order to control two air-supply solenoid valves. **NTN**'s new series of parts feeder controllers do not need additional control components in this control scenario because the new controller models each include a PLC controlling one-chip microcomputer that contains control functions needed for various parts feeder types. What the operator must do on our new parts feeder controller is to select an intended function and then set up timer duration. The user of the parts feeder controller does not need to a programming tool and software specific to an intended parts feeder. **NTN**'s parts feeder controllers are very easy to use.

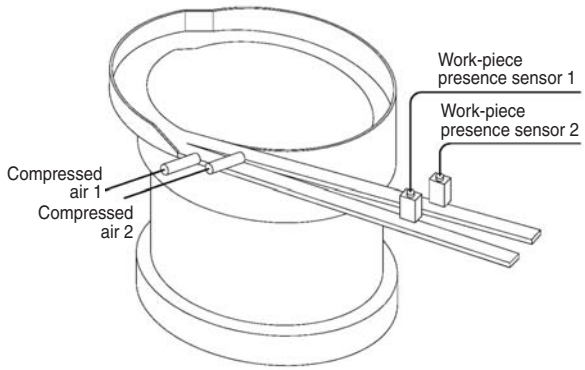

Fig. 4 Two tracks bowl feeder

• Switch-over between carrier frequencies

Our new parts feeder controller models adopt sinusoidal wave PWM* technique to drive parts feeders. To improve control accuracy for this technique, a higher carrier frequency for modulation is preferable: however, higher carrier frequency can trigger higher harmonic noise which can adversely affect measuring instrument involved. The controller models K-ECH45/K-ECJ45 permit the operator to select one of three carrier frequencies. This ability to change over carrier frequencies helps mitigate adverse effect of higher harmonic noise.

* PWM: Acronym for Pulse Width Modulation: one technique to generate AC waveform.

(3) Novel vibration sensor

We have also developed a novel vibration sensor. To detect vibration, piezoelectric elements are often used. In the aspects of electrical characteristics, piezoelectric elements feature much greater output impedance and this fact leads to more demanding requirements from the cables connected to the piezoelectric elements. Our newly developed sensor not only includes a built-in band-path filter that allows only signals of the necessary band to pass but also features lower output impedance to alleviate limitations on the cable to be connected to the vibration sensor. Consequently, when wanting to extend the cable for the vibration sensor, the user of vibration sensor can extend the line by using an ordinary cabtyre cable and terminal block without adopting a shielded cable. Use of a shielded cable was necessary for conventional vibration detection systems with piezoelectric elements. Wiring work is much simplified.

Fig. 5 shows an appearance of our novel vibration sensor. **Fig. 6** gives a view of cable extension with a length of ordinary cabtyre cable; this type of connection was difficult with the old controller model.

Fig. 6 Typical arrangement of cable extension for new vibration sensor

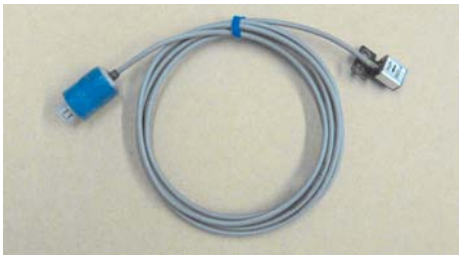

Fig. 5 Vibration sensor

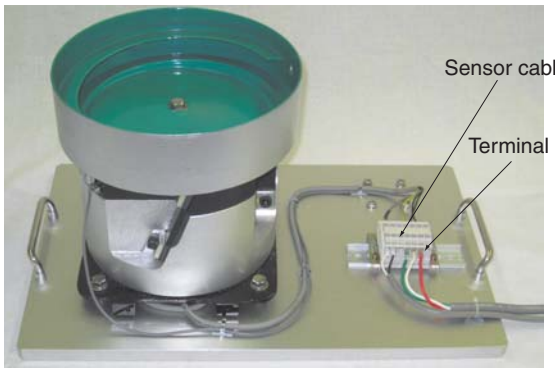

Fig. 6 Example of cable expansion for new type vibration sensor

(4) Constant amplitude operation mode

On our two new controller models, K-ECG25 and K-ECJ45, the magnitude of amplitude of vibration is adjusted with an amplitude dial to a target value. The controller automatically regulates its output voltage so that the signals from the vibration sensors are kept at constant level. Typical examples of control characteristics of our new controller obtained from this constant amplitude function and resonance point tracking function described below are shown in **Fig. 7**. Our new controllers are capable of automatic regulation of their output voltage so that they restore the amplitude on the parts feeder to the original level even when a load on parts feeder has increased (for

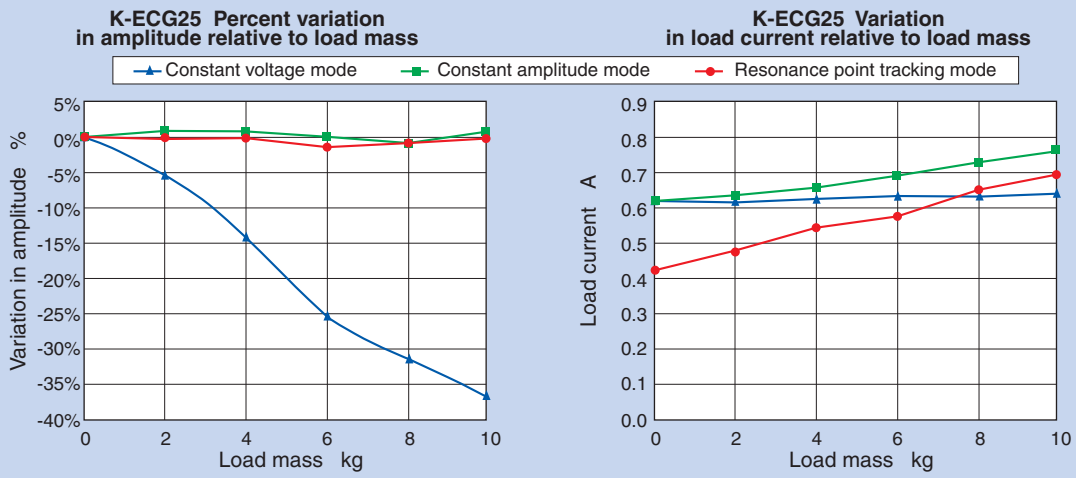

Suppose a load (work-pieces in the bowl) on the parts feeder is gradually increased. In the conventional constant voltage mode (no amplitude feedback is available), the amplitude will decrease; in contrast, in the constant amplitude run mode (amplitude feedback is available), change in amplitude is minimized because load current is increased as necessary. At the same time, it should be understood that in the resonance point tracking run mode (feedback of amplitude and resonance point is available), change in amplitude is mitigated and a load current necessary to achieve a given amplitude is low compared with the constant amplitude mode.

Fig. 7 Constant amplitude characteristic (typical example)

example when the work-pieces have been loaded into the parts feeder). The parts feeder can keep supplying work-pieces at constant vibration frequency. Previously, the constant amplitude function on our old controller model could be enabled only after manual adjustment with GAIN potentiometer. The new controller models are capable of automatic GAIN adjustment. New controller models help the user always select an optimal GAIN without relying on the judgement of an operator of the controller.

(5) Resonance point tracking run mode

The resonance point of a given parts feeder can vary depending on the factors including the quantity of work-pieces in its bowl. Our two new vibratory parts feeder controller models K-ECG25 and K-ECJ45 are capable of automatically tracking the resonance point of the parts feeder being controlled and accordingly control the vibration frequency of the parts feeder. A vibratory parts feeder utilizes resonance phenomenon to amplify vibration on it to line up and feed work-pieces to an assembling machine. For this reason, the parts feeder will operate at optimal efficiency when the vibration frequency matches the resonance point. This arrangement may not be advantageous in that vibration-feed operation at resonance frequency is vulnerable to outside disturbance and as a result stable vibration is not readily achieved. To address this problem, our old controller model was designed to run at a frequency where its vibration is stable, somewhat higher than the resonance point, even though the load current is higher than that in resonance point-matched mode. The new controller models are capable of resonance point tracking run mode where the controller detects occurrence of resonant state based on signals from vibration sensors, thereby the controller automatically regulates the vibration frequency so that the parts feeder is always locked to resonant state. Vibration on the feeder remains stable even when the vibration frequency coincides with the resonance point, thereby load current needed for the test parts feeder controlled by the new controller to generate a given amplitude is approximately 20% lower compared with the old controller, (percentage decrease in necessary current can vary depending on the model, settings and operating conditions, etc. of the vibrator).

To enable resonance point tracking function, a certain adjustment is necessary, however, the new controller models automatically achieve this adjustment thanks to their auto-calibration function. The operator does not need to waste time for this procedure. On the **NTN**'s new parts feeder controllers, once calibration work is complete, an intended run mode automatically starts and a corresponding mode indicator lamp will light up. The operator of our new controllers can easily execute the necessary setup and checkup procedures.

Since resonance point auto tracking function alone does not provide stable vibration frequency for the vibratory parts feeder, our new controllers in resonance point auto tracking mode unconditionally enable the constant resonance mode.

The resonance point tracking function is useful in particular in realizing high-speed feeding of work-pieces: however, this function may be less effective in terms of inching-speed work-piece feeding performance or reliability of the parts feeder depending on the settings on the vibrator and/or the type of work-pieces handled by the parts feeder.

With the new controllers, the "LIMIT" indicator lamp will light up when the parts feeder is running while being controlled by the constant amplitude function and if the control limit is reached. There may be cases where necessary amplitude is no longer achieved due to reasons including excessive fatigue on the leaf spring in the vibrator. The "LIMIT" indicator lamp will light up so that the user can maintain the parts feeder in question.

(6) Other functions

The new controller models are capable of handing various functions and signals, and examples of which include multi-speed capability, control of setup voltage (amplitude) with analog voltage, control dial lockup (inhibition of manipulation), no work-piece detection alarm, fault signal and alarm signal. A user of parts feeder can achieve a diversity of unique control functions by using one unit of the **NTN**'s parts feeder controller instead of developing a purpose-specific control circuit. Consequently, the user of our parts feeder controllers will enjoy benefits such as reduction in costs for production equipment and stock of maintenance parts.

(7) Costs

NTN has attempted to minimize cost increase over the old model though introducing more functions; thereby the users of **NTN**'s new parts feeder controllers can use a wider scope of control function at a price approximately comparable to that of the old model.

4. Conclusion

This paper has provided information about the advantages of **NTN**'s four multi-function, compact and light-weight controller models for parts feeders. **NTN** will include as an option to the lineup of parts feeder controllers a special step-up transformer unit that allows a 200 V rated parts feeder to be operated with a 100 V power supply.

Because of a diversity of possible applications, parts feeders need to be capable of handing a wide variety of work-piece types. **NTN**'s new parts feeder controllers satisfy most of these requirements, and cope with higher levels of users' needs. **NTN** will remain committed to development of novel parts feeder controller products that are accepted by more users as they help realize the best combination between characteristics of parts feeder proper, optimal tooling and appropriate control scheme.

Photo of author

Kunihiko SUZUKI

Precision Equipment Division
Product Engineering Department

NTN-SNR High Performance and Flexible Linear Modules Series AXDL

Ulrich GIMPEL*
Michael WILLE*

The AXDL linear modules series has been developed as a positioning module with high rigidity to meet high requirements for accuracy, zero maintenance and dynamics. A concept-oriented CAD design has resulted in an extremely flexible program to respond to various specifications, such as size and functions, from customers and innovative synchronous-belt clamping and complete sealing that ensure long service lives and high operating safety. AXDL modules can be combined with the complete AXC/AXLT series ranges by using a standardized system of connecting and fastening elements.

1. Foreword

Linear modules have been incorporated into various manufacturing machines for automobiles, photovoltaic generation systems, lumber processing, aircraft, packaging, and medical treatment systems since the 1980s. They are used as basic component parts for portal Cartesian coordinate robots including tip units and pick-and-place units of robots and are an indispensable technology for automation and transfer mechanisms. Depending on their applications, they are required to have high positioning accuracy or endurance under load. They are used in a variety of working environments ranging from outdoor locations to clean rooms. This article introduces AXDL linear modules developed by **NTN-SNR** to respond to diversifying market needs.

2. AXDL Series

2.1 Features of the AXDL series linear module

In an AXDL series linear module, a driving unit, a guide mechanism and a moving stage are joined to an aluminum frame with a unique structure. The most outstanding feature is its high general versatility that allows the optimum driving unit and guide mechanism to be combined to the frame freely.

The features of the AXDL series linear module are as follows:

1) Selection of a drive unit allowed

(1) Toothed-belt drive unit

Fig. 1 shows the appearance of an AXDL linear module equipped with a toothed-belt drive unit. The stage is fastened to the toothed belt, and is moved by the toothed belt motor-driven from the drive head. The toothed-belt drive unit is capable of being advanced at a high speed of 10 m/s as a result of combining it with the track roller parallel guide described later.

The AXDL series toothed belt drive module is characterized by the method of fixing the toothed belt that facilitates the replacement of belts. In common toothed belt drive units, toothed belts are often arranged at locations at which it is difficult to handle the inside of the unit, requiring many man-hours for belt replacement. For AXDL series products, a new fixing method has been developed, as shown in Figs. 2 and 3, in which the part on the cross-section of the stage through which the toothed belt is passed is formed as a space with a wedge-shaped cross-section, into which a wedge member is squeezed as if the toothed belt were to be inserted there. This fixing method allows the toothed belt to be fixed securely and replaced without removing component parts.

***SNR** Wälzlager GmbH Engineering Bielefeld

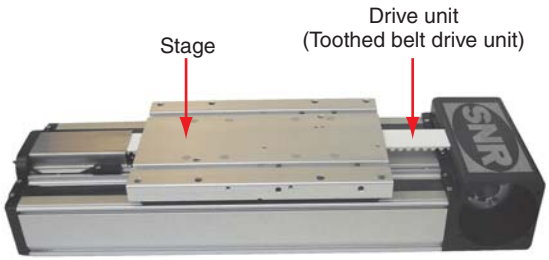

Fig. 1 AXDL240Z linear module with toothed-belt drive

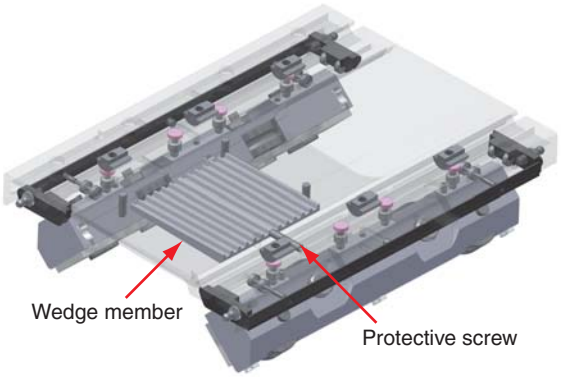

Fig. 2 Fixed unit of toothed belt

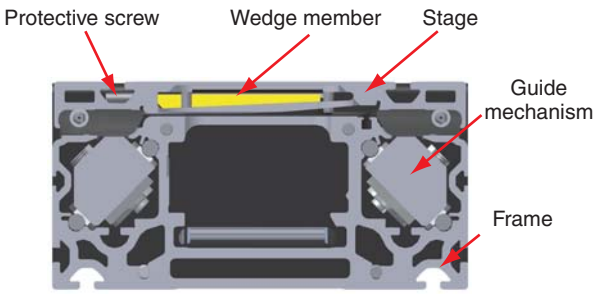

Fig. 3 Fixed method of toothed belt

(2) Ball screw drive unit

Fig. 4 shows the AXDL ball screw drive module.

In the AXDL module equipped with a ball screw drive unit, the type of feed screw and the accuracy class of ball screws can be selected depending on the performance required.

In the standard specification, rolled ball screws with the accuracy class of T7* are used, while ball screws of up to accuracy class T3** can be selected for high-accuracy positioning applications. In addition, trapezoidal screws can be selected for adjustment action application not requiring positioning accuracy.

When a ball screw drive unit is used for high-speed transfer applications, it is necessary to be careful not to exceed the allowable rotational speed of the ball screw. The allowable rotational speed is determined by the shaft diameter of the ball screw and the distance between the supports and must not be exceeded.

NTN-SNR developed a wire-driven ball screw floating support mechanism shown in **Fig. 5**, making it possible to handle a high-load condition through an improvement of the shape of the support unit. This mechanism is structured to allow a pair of support units with a coupling element to move axially as the ball screw nut moves. **Fig. 6** shows an example of action of a floating support equipped with a pair of support units. Applying support units makes it possible to reduce the support-to-support distance in comparison with a structure having a fixed support bearing only. Increasing the number of support units has made it possible to increase the allowable rotational speed as shown in **Fig. 7**.

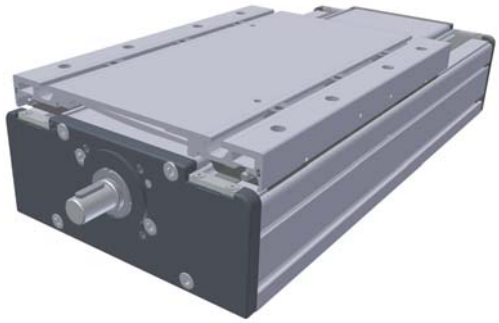

Fig. 4 AXDL240S: linear module with ball screw drive

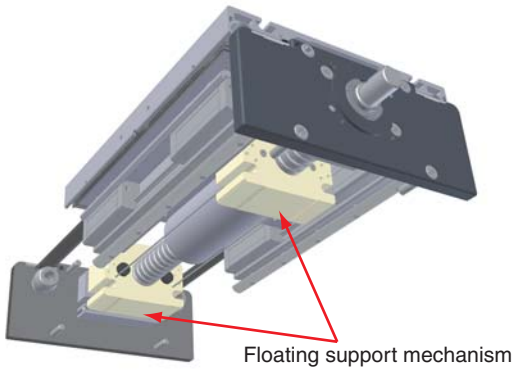

Fig. 5 Floating support system

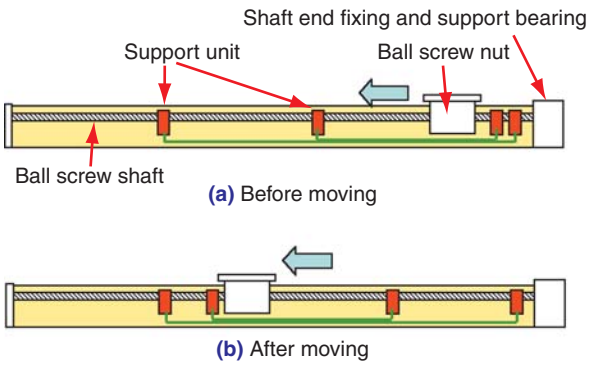

Fig. 6 Floating support （case of 2 support units）

*Class C7 in the JIS notation
** Class C3 in the JIS notation

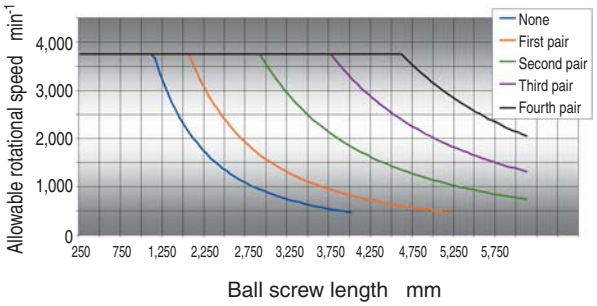

Fig. 7 Limiting rotation speeds

2) Selection of a guide mechanism

(1) Linear guide

Linear guide using a ball with a holder is applied. This guide mechanism has a high load capacity, having a higher rigidity, a higher accuracy, and a longer life than the track roller described later. **Fig. 8** shows a cross-sectional view combined with a linear guide perspective view.

(2) Track roller guide unit

Generally, the rated operating speed of a linear module using a linear guide is up to 5 m/s. With the AXDL series, however, combining the track roller guide mechanism with the toothed belt drive as shown in **Fig. 9** allows the system to reach a speed of 10 m/s.

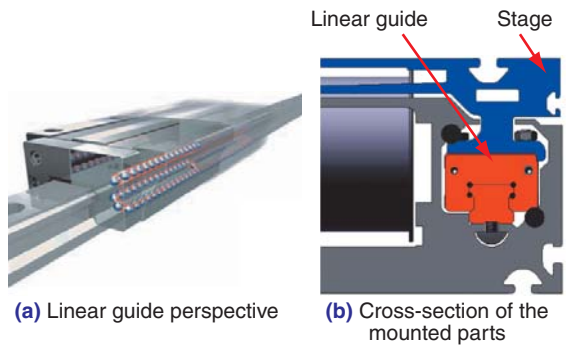

(a) Linear guide perspective

(b) Cross-section of the mounted parts

Fig. 8 Linear guide systems with ball chains.

(a) Example of mounting of a track roller guide

(b) Cross-section of mounting

Fig. 9 Track roller guide units

3) The latitude in selecting a drive motor is large.

Motor flanges, couplings, and reduction gears allowing the combination with a motor with the best drive characteristics.

2.2 Improvement of the design of the AXDL series products

The AXDL series products are born out of the incorporation of a variety of improved technologies into the existing AXC series. The points of improvement are shown below:

1) Optimization of the frame shape

Since the cross-sectional shape of the frame affects the rigidity of the unit, it is necessary to increase the moment of inertia of area in two directions shown in **Fig. 10** , Ix and Iy.

The frame is composed of extruded aluminum members. In manufacturing extruded parts, aluminum bars (billets) are extruded through a trimming die to form extruded parts with a desired cross-section. By induction-heating billets to about 500˚C in advance, adequate material liquidity associated with forming is obtained. The forming conditions are optimized so that stable drift velocity may be obtained even when the thickness varies locally in the same cross-section. The straightness of the AXDL 240Z product is optimized within the physical limits of the extrusion process by means of the finite element analysis so that it may be less than 0.5 mm/m (in conformity with DIN EN 12020-2).

The cross-sectional structure of the frame manufactured by the extrusion shown in **Fig. 11** exerts a significant effect on the rigidity of the linear module and that of the unit as a whole. Rigidity shows the amount of deformation of the unit due to load.This is an important element determining the function and durability of the unit.

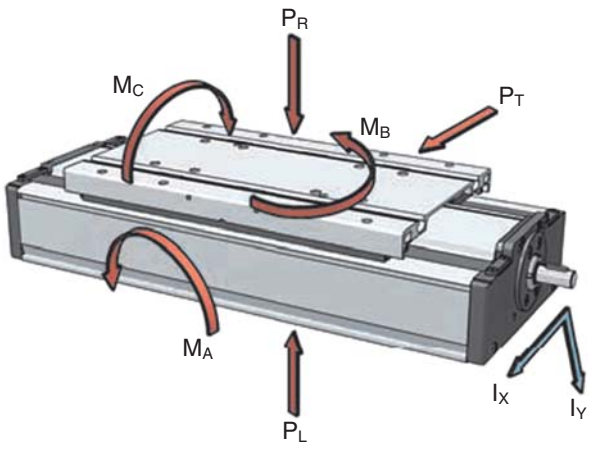

Fig. 10 Coordinate of linear module

Rigidity was measured on AXDL 240 double-row linear guide products (with a height of 25 mm), double-row track roller guide products (with a track diameter of 47 mm) and conventional AXC 120 single-row linear guide products according to the coordinate system shown in **Fig. 10** . The rigidity is denoted with the inclination angle produced by the moment load, converted into the displacement at 1 m ahead. The experimental results are shown from the moment load M_A (**Fig. 12**), M_B **Fig. 13**), and M_C (**Fig. 14**).

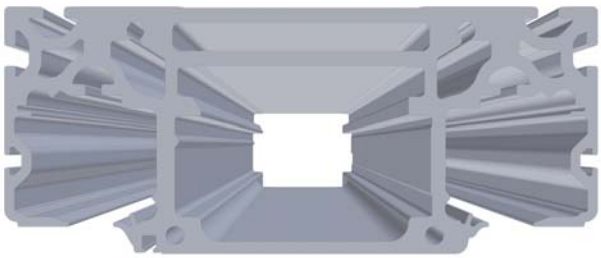

Fig. 11 Cross section structure of flame

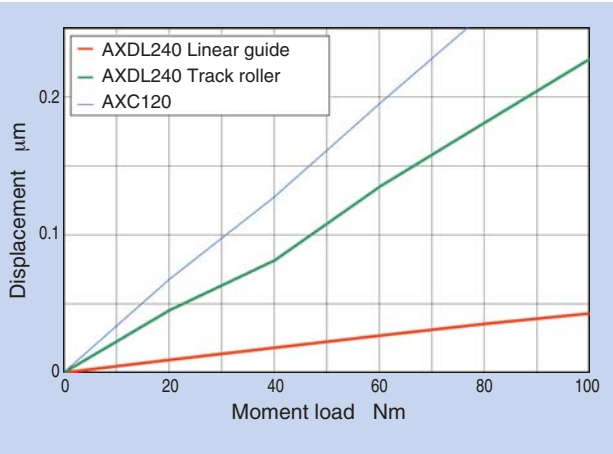

Fig. 12 Comparison of the rigidity in M_A direction

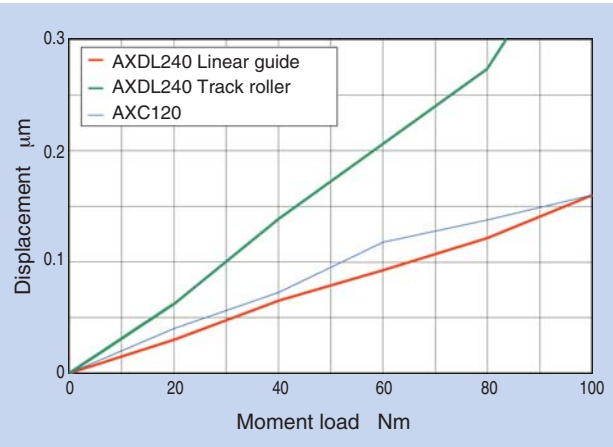

Fig. 13 Comparison of the rigidity in M_B direction

2) Optimization of rigidity of component members

Fig. 15 shows an example of the calculation of the effect on the device rigidity of different module component parts by means of finite element analysis, which was carried out in addition to the optimization of the frame cross-sectional shape in order to increase the rigidity of the unit as a whole. An analysis carried out on an imagined condition of combined component parts (the track roller guide and the stage in the case represented by **Fig. 15**) allows mutual effects of members on one another to be evaluated and the effect on the entire unit to be estimated.

3) Improvement of the method of joining the linear guide unit with the ball screw drive unit

When the linear guide unit is joined with the ball screw drive unit, it is important to prevent stress that will affect the durability of the entire unit from occurring. As shown in **Fig. 16** , **NTN-SNR** has improved the method of joining the nut holder of the ball screw with the linear guide unit. The structure is such that the joint with the linear guide unit is formed

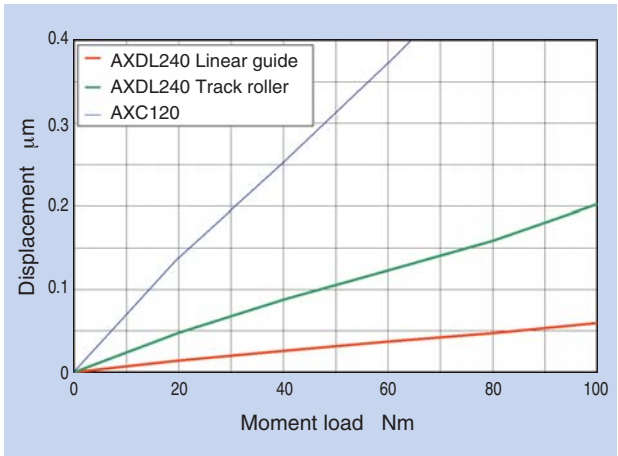

Fig. 14 Comparison of the rigidity in M_C direction

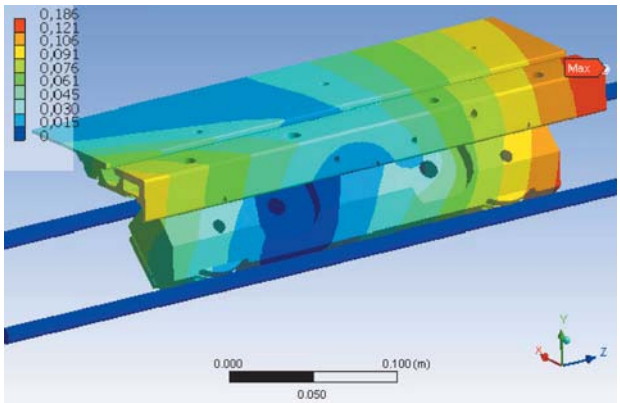

Fig. 15 FEM analysis result for AXDL

via the beam that projects only in the direction of the radius from the ball screw nut holder. This reduces the generation of stress due to the error in relative positions between the ball screw and the linear guide unit. This improvement also eliminates the adjustment during the assembly process and thereby preventing the occurrence of defects in assembling.

4) Improvement of dust-tightness by means of optimization of the seal structure

The dust-tightness of the unit is important from the viewpoint of improving the durability and reducing maintenance work. As shown in **Fig. 17**, a seal strip and a side strip, both made of polyamide (PA), are provided to improve the dust-tightness.

5) Increased ease of assembling to the unit

Fig. 18 shows the structure of the drive head of the toothed belt drive unit. For AXDL series products, the ease of assembling is improved by assembling the motor drive shaft into the drive head. This makes it possible to secure the compactness of the unit even with a large diameter pulley incorporated into the assembly, providing the following advantages:

⇒ Restraining the installation height of the system

⇒ Securing a large effective stroke length as compared with the total length of the system

3. Example of application of the AXDL series product

Fig. 19 shows an example of application of the AXDL series product to a two-shaft screw driving robot for automobile production systems.

Using the AXDL series product with a parallel-arranged two-row guide mechanism in this application has made it possible to accommodate a large angular moment (M_C). In a quest to prevent vibration associated with the movement of the shaft, the rigidity of each module has been increased.

Y axis: Servo-motor-driven AXDL 160 toothed belt module equipped with a planetary reduction gear

Z axis: AXDL 110 ball screw drive module equipped with a motor-mounting flange and a coupling to connect with a servo motor

The Z-axis is equipped with an electric driver to screw the valve cover to the cylinder head of an automobile engine.

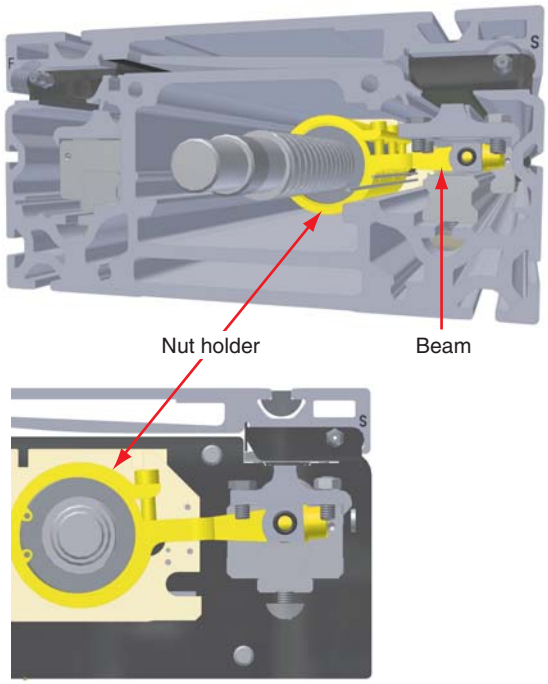

Fig. 16 Connecting between ball screw and guide system

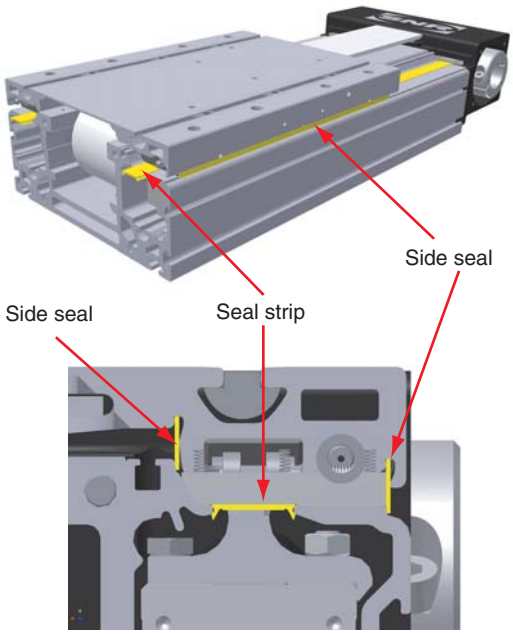

Fig. 17 Sealing design

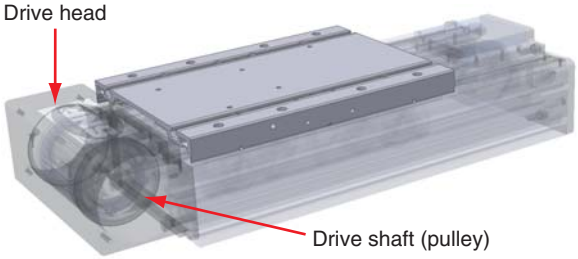

Fig. 18 Structure of motor drive head

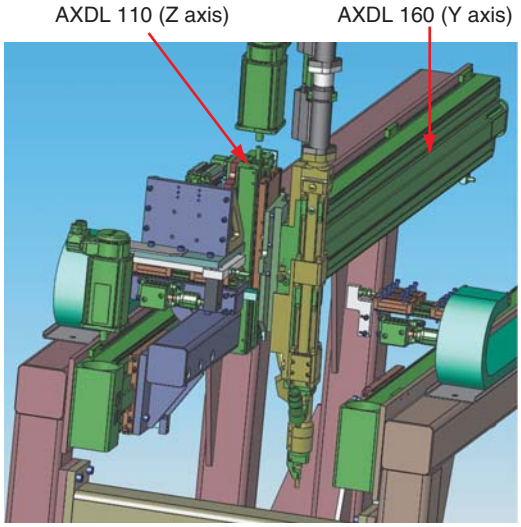

Fig. 19 Example of application : Screw-driving unit for automotive parts

4. Conclusion

The high-rigidity AXDL series linear module has been developed to meet strict requirements for accuracy, freedom from maintenance, and motion responsiveness. The unification of design concepts has made it possible to combine a drive unit and a guide mechanism, both suitable to a particular application, to flexibly meet diversified customer needs varying in terms of the size and function. Added to this have been technologies of ball screw support schemes, methods of fixing toothed belts, and perfect sealing of internal component parts to achieve a long service life and high stability of operation. Furthermore, the connection and fixing brackets for the AXDL series products are standardized to allow the AXDL series products to be used in combination with all conventional AXC and AXLT series products.

Photo of authors

Ulrich GIMPEL
NTN Wälzlager GmbH
Engineering Bielefeld

Michael WILLE
NTN Wälzlager GmbH
Engineering Bielefeld

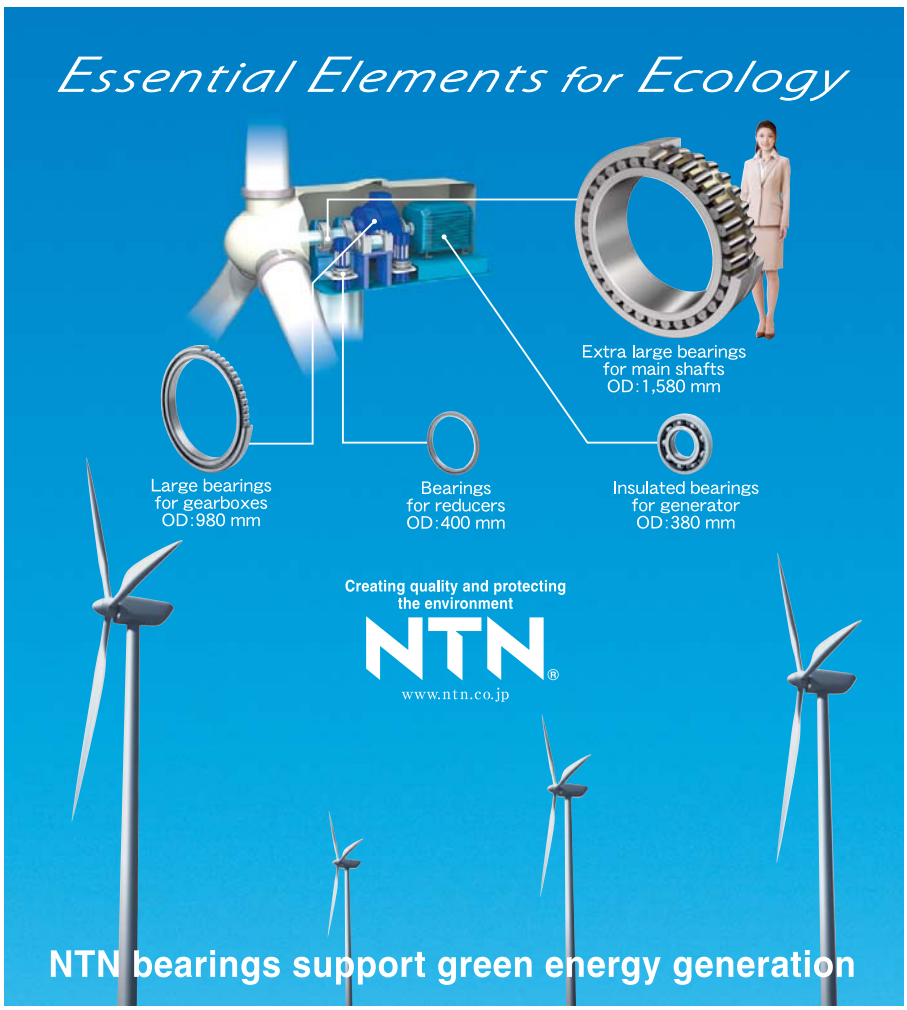
Essential Elements for Ecology
Extra large bearings
for main shafts
OD:1,580 mm
Large bearings
for gearboxes
OD:980 mm
Bearings
for reducers
OD:400 mm
Insulated bearings
for generator
OD:380 mm
Creating quality and protecting
the environment
NTN
www.ntn.co.jp
NTN bearings support green energy generation

High Resolution Sensor Bearing with an Index Signal

NTN Hiroyoshi ITO*
Toru TAKAHASHI**

NTN-SNR Pascal DESBIOLLES***
Cyril PETERSCHMITT***
Shintarou UENO***

This bearing with a rotation sensor is used for the purpose of speed control and rotational direction detection of servomotors used in, for example, battery forklifts. The sensor outputs two phase A and B signals. **NTN** and **NTN-SNR** have now newly developed a high-resolution rotational sensor bearing with an index signal output.

1. Foreword

NTN has added to its lineup “rotation sensor-equipped bearings” that combine a shaft and a rotation sensor into a unit as products that supports electrical control of industrial machines such as rotation control of servo motors [1), 2)]. Using a sensor IC (MPS40S) [3)] made by **NTN-SNR ROULEMENTS**, a member of the **NTN** group, **NTN** has developed, jointly with **NTN-SNR**, a “bearing equipped with a home position signal output type high-resolution rotation sensor” that allows the home position signal (phase Z) to be outputted. Thanks to the Hall elements installed inside, the **NTN-SNR**’s sensor IC is capable of increasing the rotation detection capability by up to 40 times and of outputting the home position signal. In addition, this newly developed product has adopted a connector-based connection system to improve the ease of mounting it to devices, with the power and signal output wires separate from the main body.

2. Construction

Fig. 1 shows the construction of the newly developed product.

(1) Inner ring side: a press-fitted magnetic encoder
(2) Outer ring side: A type C spring fastens the sensor case, and the substrate fastened to the sensor case is equipped with a sensor IC and a connector. **Fig. 2** shows how the sensor IC is mounted. A QFN28 package is used to achieve compact implementation.

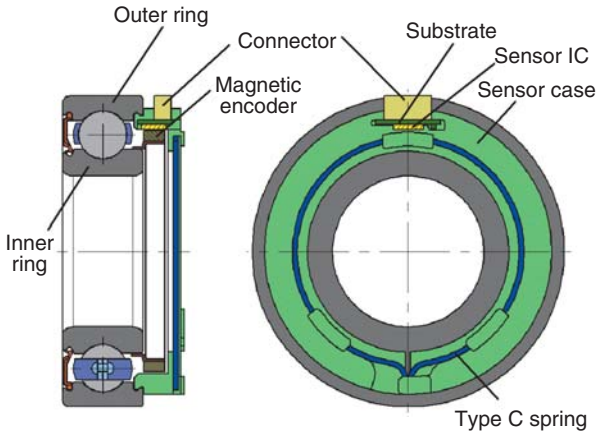

Fig. 1 Structure

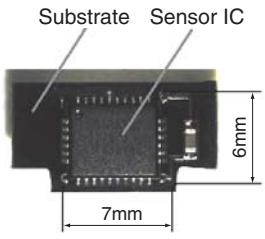

Fig. 2 Sensor IC soldered with circuit board

3. Features

The features of the newly developed product and of the sensor IC used in the product are described below.

*Industrial Business HQ. Industrial Engineering Dept. **New Product Development R&D Center Mechatronics Research Dept.
***NTN-SNR ROULEMENTS New Product and Mechatronics R&D

3.1 Features of the newly developed product

The newly developed product has the following features:

(1) Capable of detecting rotation without contact and free from the possibility of performance deterioration due to wear;
(2) A rotational angle resolution of 0.14˚ is achieved on the 6206 size bearing because the capability of outputting a rotation signal is up to 40 times that of the current product;
(3) Capable of detecting the rotational speed and direction by means of the signal output in phases A and B;
(4) Capable of detecting the home position by means of phase Z signal output (For example, this is applied to the detection of a motor shaft, the position of the steering, and the like.); and
(5) Ease of mounting the bearing as a result of the adoption of a connector-based connection system.

Table 1 shows the comparison of specifications between the newly developed size 6206 product and the current one.

Table 1 Specifications of 6206 size

	Newly developed product	Current product
Number of output pulses from phases A and B	2,560 pulses/rotation	64 pulses/rotation
Resolution	0.14 degrees/pulse	5.625 degrees/pulse
Home position signal	Allowed	—
How to connect signals	Connector-based connection	Wiring-based connection

3.2 Features of the sensor IC

Several Hall elements are installed in a line in the sensor IC (MPS40S). Signals from these Hall elements are combined with a specially designed multiplication circuit; this allows the magnetic pattern in the magnetic encoder to be divided up to 40 times internally to increase resolution. The major features of this IC are shown below and the specifications in **Table 2**.

(1) A single IC package is capable of outputting signals from phases A, B, and Z, with the assembling of a sensor made easy;
(2) The adoption of an ultra-small IC package allows assembling to be performed in a small space;
(3) A decrease in the magnetism in the encoder can be detected;
(4) Equipped with a self-diagnosing function that monitors the state of the sensor IC and encoder and if an abnormality (an extreme abnormality of the magnetization pitch, for example) occurs, the function provides notification that an error occurred.
(5) The width of the magnetic pole, number of multiplication, and form of signal output can be specified by programming;
(6) With the phase difference between phase A and phase B signals being accurate, an increase in the resolution can be achieved by means of quadruplication processing.

Table 2 Specification of sensor IC

Required magnetic flux density	±5 mT or more
Power supply voltage	5V±10%
Current consumption	40 mA max
Compatible width of magnetic pole (that can be specified)	1.15–3 mm
Maximum frequency of input magnetic field	5kHz
Number of multiplication (that can be specified)	1x, 2x, 4x, 8x, 16x, 32x, 5x, 10x, 20x, 40x
Signal output	Phase A, Phase B, Phase Z
Output form (that can be specified)	5 V TTL level or open drain
Package	TSSOP20 or QFN28
Acquired certification	AEC-Q100※

※Certification standard for the stress test for automotive integrated circuits

4. Characteristics of the output waveform

Fig. 3 shows the comparison of the rotation signal output waveform between the current product and the newly developed one in terms of the magnetic pole of the magnetic encoder. The current product outputs a signal of a single pulse per pair of N-S magnetic poles (64 pulses per rotation), while the newly developed product outputs a signal of 40 pulses (2560 pulses per rotation). The rotation signal shown in **Fig. 3** denotes phase A signal only, for both the current and the newly developed product. In reality, rotation signals from two phases are outputted; that is, phase A signal and phase B signal having a 90-degree phase difference from phase A (a phase difference equal to a quarter pulse). The rotation signal from the newly developed product is multiplied 40 times inside the sensor IC compared to the rotation signal from the current product. **Fig. 4** shows how to generate the home position signal by using a magnetic encoder. The magnetization pattern of the magnetic encoder is composed of double row tracks layed out in the axial direction. Of the two tracks, the track that is magnetized in equal pitches is called the HR track and the one magnetized in uneven pitches is called the RP track. They have the following roles:

HR track: For outputting signals from phases A and B

RP track: For outputting signals from the home position (phase Z)

The portion in the RP track near the position at which the home position signal is detected is magnetized so that the magnetic phase differs from other positions. The home position signal is outputted when the magnetic force of the RP track exceeds the threshold value at the position at which the polarity of the HR track changes (the zero crossing position).

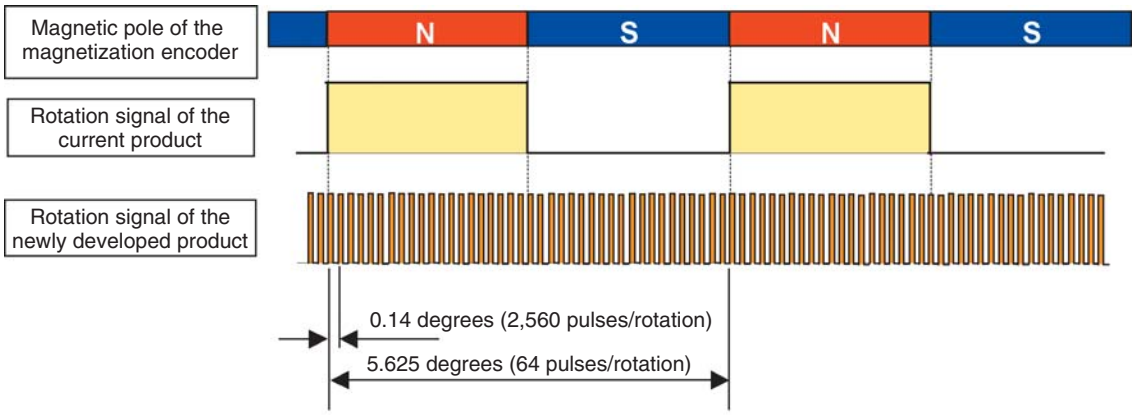

Fig. 3 Comparison of output form of current product and newly developed product

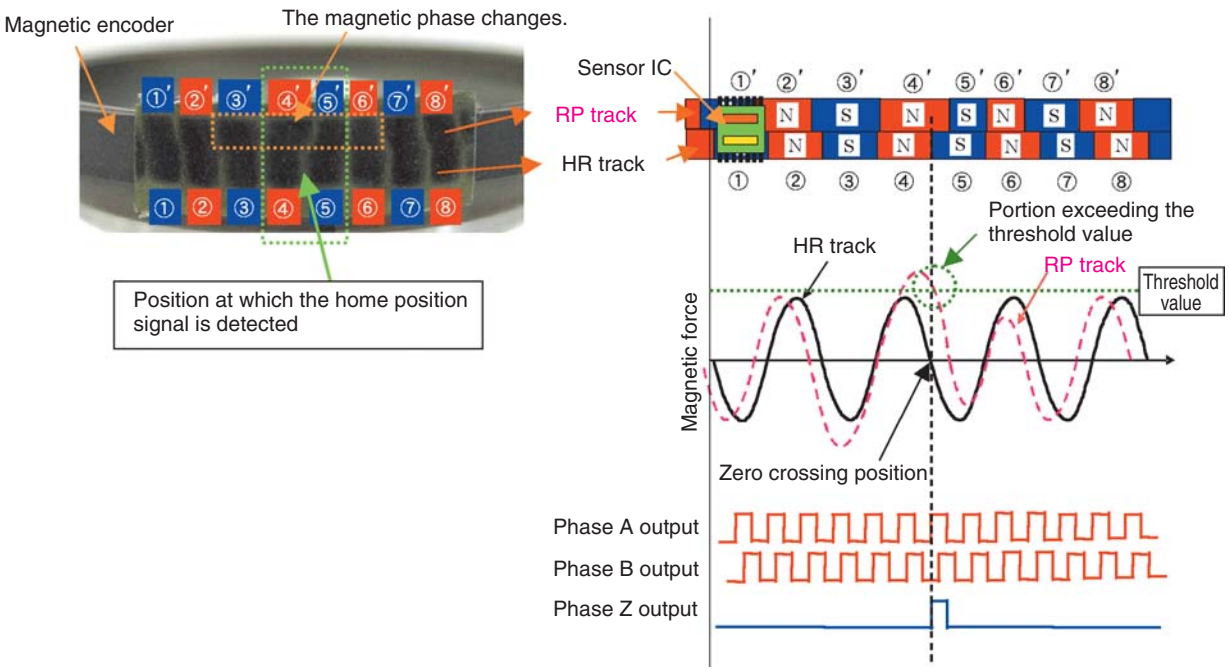

Fig. 4 Generation of output wave form of index signal

5. Important specifications of different parts

Tables 3 to **5** show important standard specifications of the newly developed product.

(1) The specification for the bearing is selected considering the use of the bearing in supporting the motor;

(2) Adoption of a magnetic encoder magnetized in double tracks; and

(3) Two of the core wires of the five-core connector are assigned to each of the ground connections and one to each of phases A, B, and Z signal outputs.

Table 3 Specification of bearing

Bearing size	6206 (ϕ30×ϕ62×16)
Radial internal clearance	C3 (0.013–0.028 mm)
Sealed-in grease	Motor-use long life grease
Seal	Contact type rubber seal
Cage	Ribbon steel sheet cage
Allowable rotational speed	4687min^{-1} ※
Working temperature range	-40 to +120˚C

※Limit imposed by the sensor response frequency (5 kHz)

Table 4 Specification of magnetic encoder

Rubber material	NBR
Magnetic material	Ferrite
Number of magnetized poles	64 N poles and as many S poles
Direction of magnetization	Radial direction (Double tracks)
Surface flux density	17 mT or more (at a gap of 0.5 mm)

Table 5 Specification of connector

Number of terminals	5
Applicable wire size	AWG26

6. Evaluation tests

The evaluation tests described in Subsections 6.1 to 6.4 were conducted to measure the accuracy of sensor output. The accuracy of sensor output is evaluated by means of the adjoining pitch error, duty ratio, and phase difference defined below. (See **Fig. 5**.) The specified range to be used as an evaluation standard was determined by taking into consideration error factors arising from the measuring system (such as accuracy in fabricating an encoder) and installation errors. If an error exceeds this range, an abnormality is suspected.

(1) Adjoining pitch error (%)
$|(T_n - T_{n+1})|/T_n \times 100$: Maximum in a single rotation
Specified range: 10% or less

(2) Duty ratio (%)
$T_p/T_n \times 100$:: Maximum in a single rotation
Specified range: 35 to 65%

(3) Phase difference (degrees)
$T_{AB}/T_n \times 360$: Maximum in a single rotation
Specified range: 45 to 135 degrees

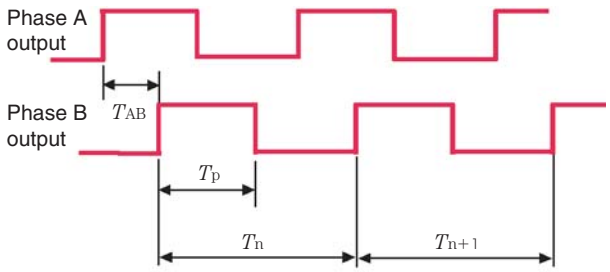

Fig. 5 Definition of sensor output accuracy

6.1 High temperature shelf test (at 120˚C)

Output accuracies of sensors that underwent a high temperature atmosphere condition of 120˚C for 0, 300, 600, and 1,000 hours were measured at room temperature. **Fig. 6** shows the test results. The initial sensor output accuracy was maintained after each of the different shelf test hours.

6.2 Low temperature shelf test (at -40˚C)

Output accuracies of sensors that underwent a low temperature atmosphere condition of -40˚C for 0, 300, 600, and 1,000 hours were measured at room temperature. **Fig. 7** shows the test results. The initial sensor output accuracy was maintained after each of the different shelf test hours.

6.3 Thermal shock test

(-40˚C×60 minutes⇔Room temperature×10 minutes⇔120˚C×60 minutes)

The thermal shock test was conducted between -40˚C and 120˚C, and output accuracies of sensors that underwent 0, 100, 600, and 800 cycles were measured at room temperature. **Fig. 8** shows the test results. The initial sensor output accuracy was maintained after each of the different numbers of cycles.

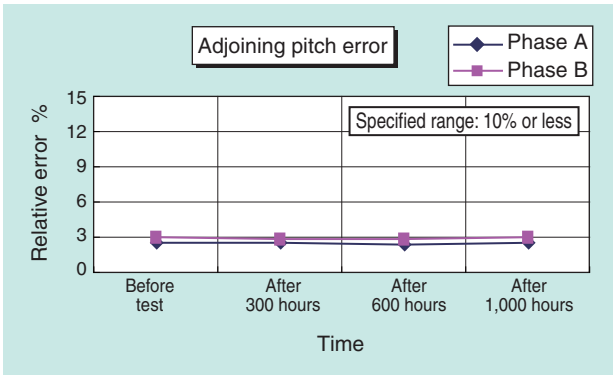

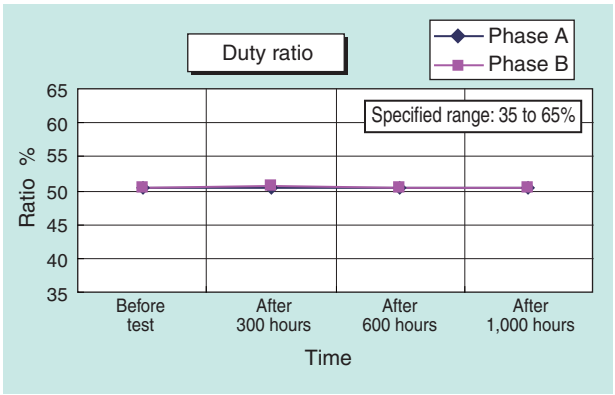

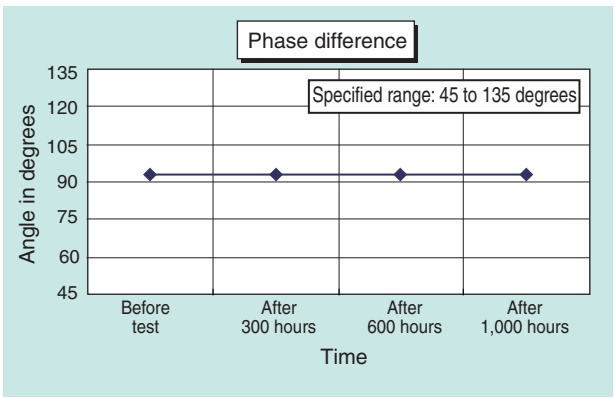

Fig. 6 Result of high temperature environment test

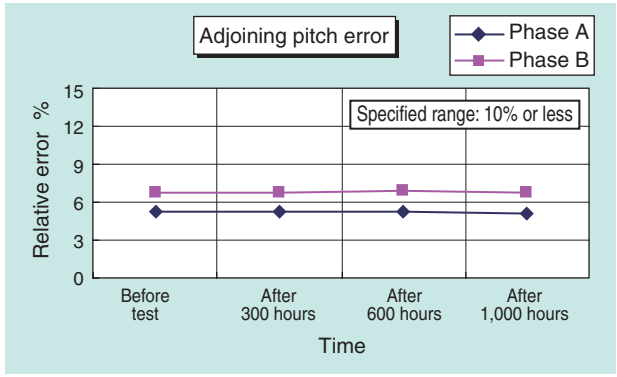

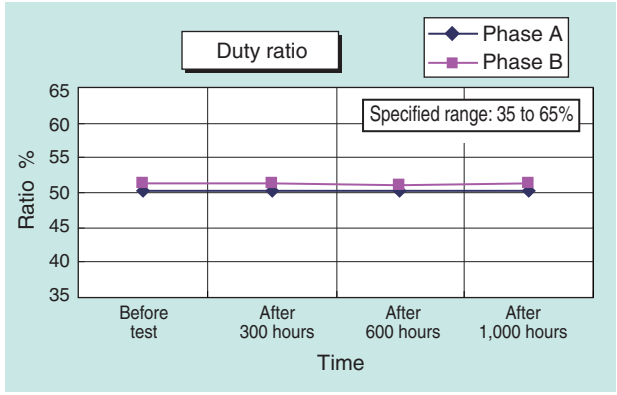

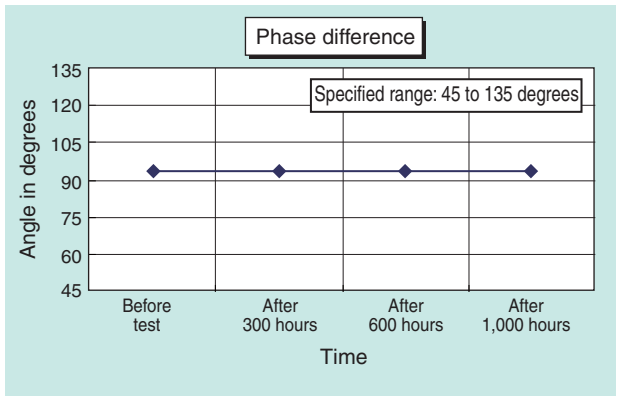

Fig. 7 Result of low temperature environment test

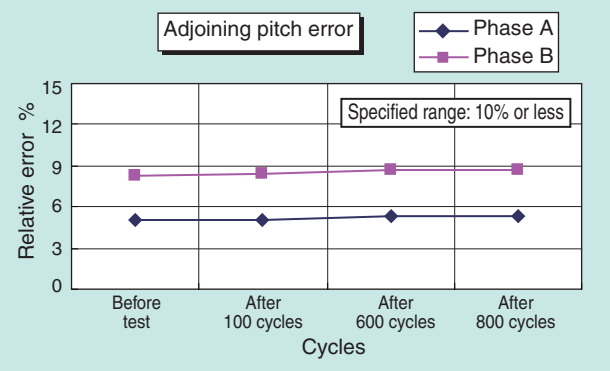

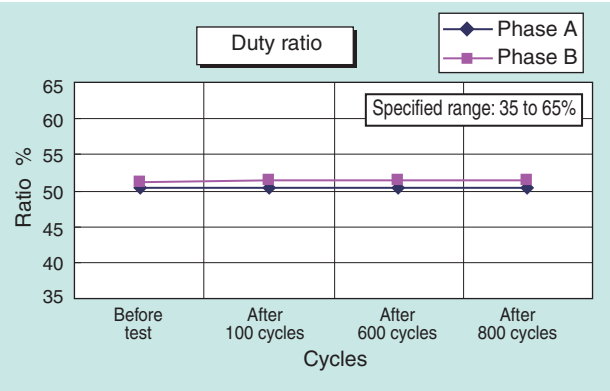

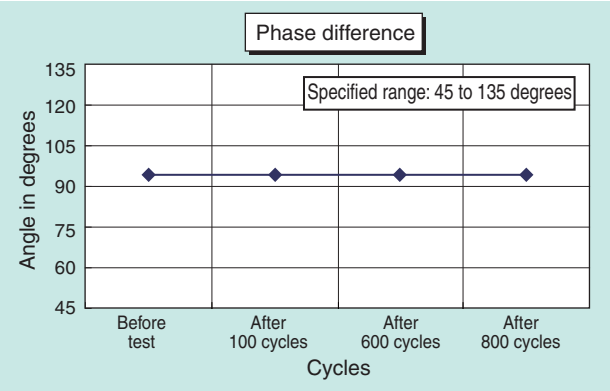

Fig. 8 Result of heat shock test

6.4 Vibration test

Sensor output accuracies were measured at room temperature before and after undergoing vibration under the conditions shown in **Table 6** and **Fig. 9**. A cycle of frequencies varying continuously from 5 Hz to 200 Hz in 15 min was repeated. **Fig. 10** shows how the vibration test was performed and **Fig. 11** shows the test results. The initial sensor output accuracy was maintained after 24-hour (96 cycles) vibration.

Table 6 Condition of vibration test

Frequency (Hz)	5	38.62	200
Acceleration (G)	0.5	30	30
Amplitude (mm)	10	10	0.37
Vibration condition (one cycle)	The frequency is varied gradually from 5 to 200 and then down to 5 Hz in 15 minutes.		
Direction of vibration	Axial direction		
Test duration	24 hours (96 cycles)		

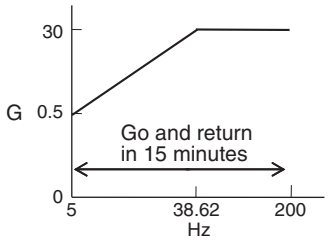

Fig. 9 Relation between vibratory acceleration and frequency

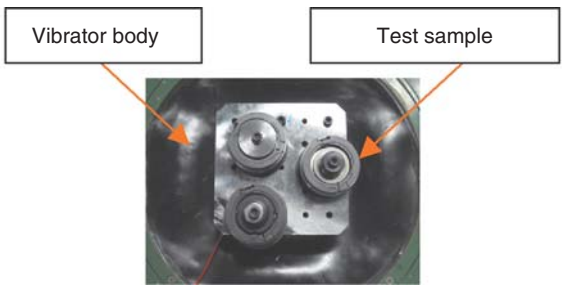

Fig. 10 Condition of vibration test

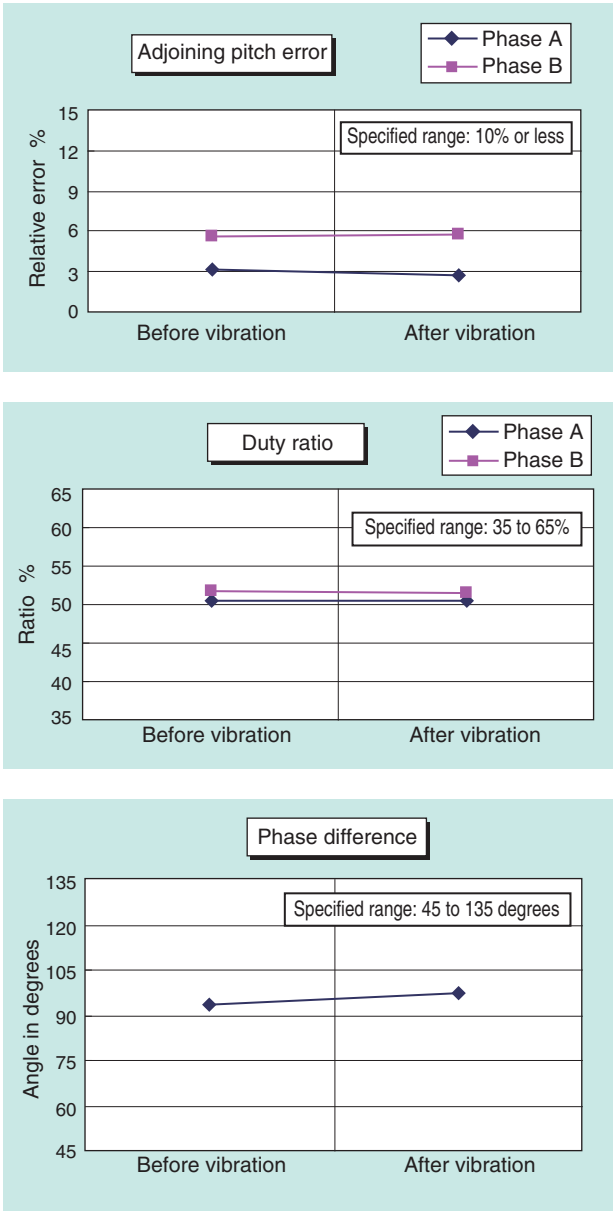

Fig. 11 Result of vibration test

6.5 Results of evaluation

These results show that:

(1) The initial accuracy of the sensor output is within the specified range, allowing one to judge the initial performance to be without problems. The sensor output accuracies remained within the specified range after the sensors had undergone the high temperature, low temperature, thermal shock, and vibration tests, allowing one to ascertain product durability;

(2) The difference observed in adjoining pitch errors between phase A output and phase B output is estimated to be due to the effect of the magnetic field of the RP track of each phase.

7. Afterward

In this paper, the authors have introduced a newly developed technology for a high resolution sensor bearing with an index signal (built to the specification of phase A and B output pulses of 2,560 pulses/rotation). They will make efforts to advance commercialization development of rotation sensor bearings using this new technology.

They will also continue pushing ahead aggressively to broaden the market reach of high resolution rotation sensor bearings built to the specification of 1,280 pulses per rotation. This product has already completed the commercialization development stage.

References

1) H. Ito and K. Koike, Bearing with Integral Revolution Sensor, NTN Technical Review No. 69.
2) T. Koike, T. Ishikawa, H. Ito and N. Mizutani, Improvement of Leakage Magnetic Flux Resistance of Integrated Sensor Bearings, NTN Technical Review No. 71 (2003) 74-79.
3) P. Desbiolles and A. Friz, Development of High Resolution Sensor Element MPS40S and Dual Track Magnetic Encoder for Rotational Speed and Position Measurement, NTN Technical Review No. 75 (2007) 36-41.

Photo of authors

Hiriyoshi ITO
Industrial Business HQ
Industrial Engineering Dept.

Toru TAKAHASHI
Industrial Business HQ
Industrial Engineering Dept.

Pascal DESBIOLLES
NTN-SNR ROULEMENTS
New product and
Mechatronics R&D

Cyril PETERSCHMITT
NTN-SNR ROULEMENTS
New product and
Mechatronics R&D

Shintarou UENO
NTN-SNR ROULEMENTS
New product and
Mechatronics R&D

[Technical Paper]

Improved Method of Rolling Bearing Fatigue Life Prediction Under Edge Loading Conditions

Haruo NAGATANI*

Various types of life prediction methods have been proposed that calculate total lifespans by synthesizing the lives of subdivided stressed volumes. These methods seem to be devised to deal with any stress distribution. However from this study, it has been found that the life prediction accuracy of these methods decrease when stress concentration occurs. In response to this, an improved method is proposed. This method calculates the total life by synthesizing the lives at the locations where stress concentrations occur.

1. Foreword

More than half a century has passed since Lundberg and Palmgren (referred to as LP in the following) established a theory on the life of rolling bearings [1) 2)], and problems with the theory such as its lack of capability of considering shear force (tangential force) on the surface caused by slip or the initial or residual stress due to fit have been pointed out, with correction to these problems having been reported in many ways. [3)-6)] However, these problems occur only when the theory is used under special conditions, and in most cases, the subjects above do not pose problems. For this reason, designing and examination based on the LP theory is still in practice now from the viewpoint of respecting past track records also.

On the other hand, the design of crowning is important in designing roller bearings. When an imbalance in sharing of load exists between the edge section and the middle section or when misalignment exists, that region will be damaged in a short time should a greater load is exerted on either of both. To avoid a problem of this kind, it is necessary to provide a suitable crowning.

The method of Ito and Sugiura [7)] is well-known as a method of determining a crowning profile. On the basis of results of various life tests conducted with the amount of crowning of full-crowning rollers being varied, they used the method of Harris [8)] and Moyer et al. [9)], proposing an optimum crowning design method. However, this method cannot be applied to **(a)** the edge load problem occurring in the necking section for grinding on a rolling surface and to **(b)** the one occurring in the joint between the cylinder section and the crowning section in cut crowning as shown in **Fig. 1**. Other methods [10) 11)] of determining a crowning profile have been suggested; however, those methods are intended to determine crowning profiles to reduce contact pressure and stress, not intended to calculate the bearing life.

Recently, as is seen in the theory of Ionnides and Harris (referred to as IH in the following) [12)], various methods have been suggested that determine the life of the entire bearing by dividing the surface loaded by stress into finite pieces, calculating the life of each, and then combining them. These methods are considered to be applicable to any stress distribution condition and should be applicable to the life projection for cases where edge load occurs; however, this has not been ascertained adequately.

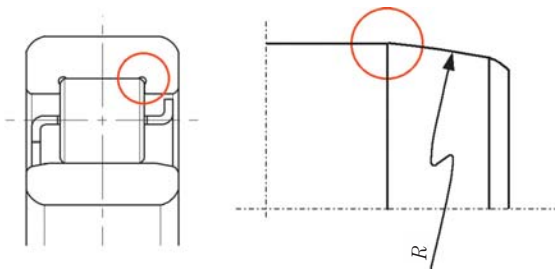

(a) Undercut part for grindings **(b)** Connecting part of cut crowning

Fig. 1 Examples that Ito and Sugiura's method cannot be applied

*Automotive Business HQ. Automotive Engineering Dept.

In actual designing, machining restrictions and cost problems often prevent one from defining an optimum crowning shape, forcing one to determine a crowning shape within the performance limit of the current processing machine. It is necessary to determine whether the life of the bearing designed in this way can meet the requirement; in doing so, if one can obtain a tool to predict the bearing life accurately, such tools are extremely useful. This paper discusses a method of predicting the life under the effects edge loading that can handle such problem.

2. Rolling fatigue test conducted by Ito and Sugiura

Table 1 shows the result of the rolling fatigue test conducted by Ito and Sugiura [7]. They conducted the rolling fatigue test in which they changed the crowning radius of a full-crowning cylindrical roller with $\phi 12 \times 12$ and the load.

Fig. 2 shows an example of the contour of the amplitude of subsurface shearing stress that occurred this test. The figure shows the half of the contour in the axial direction for the reason of the symmetry. **Fig. 3** shows the coordinate system used in the calculation of the shearing stress amplitude. The horizontal axis in **Fig. 2** denotes the direction of the axis of the roller and the vertical axis the direction of the depth, with the contour lines of stress amplitude plotted in the figure. **Photo (a)** shows a state of contact without edge load, exhibiting a stress concentration in the middle of the axial direction (at x = 6). **Photo (b)** shows a concentration of stress both at the edge (x = 0.5) and in the middle. **Photo (c)** shows the result of calculation of stress on a roller without a crowning, exhibiting a remarkable concentration of stress at the edge. **Photo (b)** shows a weaker concentration of stress in the middle than that in **Photo (a)**, exhibiting a relatively uniform stress distribution.

Table 1 Rolling fatigue test results [7]

Test No.	V1	V2	V3	V4	V5	V6	V7	V8
Load (kN)	13.72					17.35	11.76	9.8
Crowning radius (mm)	300	480	890	1200	∞	480	890	1200
$L_{10} \times 10^4$	560	1240	930	900	400	410	2200	4010
$L_{50} \times 10^4$	2160	4640	2360	1640	745	1330	5100	7250
Weibull slope	1.4	1.4	2.0	3.2	3.0	1.6	2.2	3.2
Edge failure/ test frequency	0/14	0/15	7/15	12/15	13/15	3/15	6/15	8/15

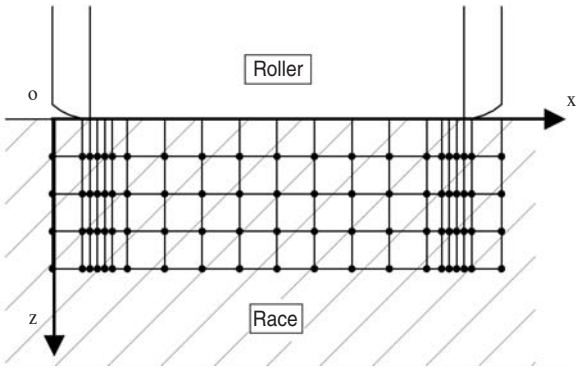

Fig. 3 Contour plots of orthogonal shear stress amplitude

3. Prediction based on the current life model

The current life prediction model is applied to the results of the experiment described above to ascertain the prediction accuracy of the model. This paper discusses the four life models shown below. In the following analysis, indexes e, c, and h are coefficients, being 9/8, 31/3, and 7/3 for a roller bearing, respectively.

Model-A

This is a model based on the concept of the LP theory, but it does not use the method of stress calculation in the LP theory; it calculates the life by

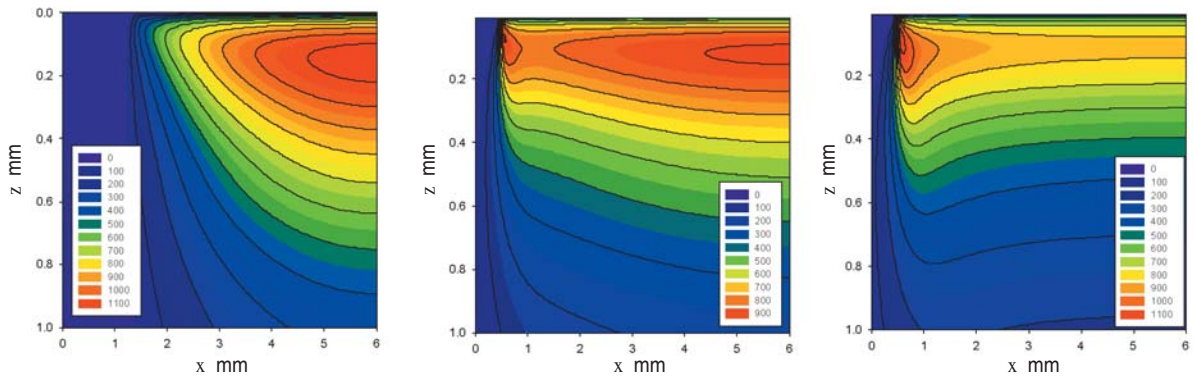

(a) V1　(b) V4　(c) V5

Fig. 2 Contour plots of orthogonal shear stress amplitude

means of equation (1) on the basis of the maximum value among the entire shearing stress distribution determined by numerical calculation and the depth of that maximum value. S denotes the survival probability, τ_0 the maximum amplitude of shearing stress, z_0 the depth of τ_0, V the stress volume, a the contact width, ℓ the perimeter length of the rolling surface, and N the number of times of loading.

$$\log\frac{1}{S} \propto \frac{{\tau_0}^c}{{z_0}^h} \cdot N^e \cdot V = \frac{{\tau_0}^c}{{z_0}^{h-1}} \cdot N^e \cdot a\ell \cdots\cdots\cdots\cdots (1)$$

Model-B, and -C

These are methods based on the IH theory, in which the subsurface portion is divided (see **Fig. 4**.), and the life in the domain V_R in which the roller undergoes stress greater than the fatigue limit is calculated to determine the life as a whole. The calculation equation is given by equation (2). τ_u denotes the stress value of each slice, tu the fatigue limit, and ΔV_i the volume of each slice. With model B, it is assumed that the fatigue limit τ_u is 350 MPa, and with model C, it is assumed that the fatigue limit does not exist. The stress volume V_R of model C is assumed to be the same as the stress volume at a fatigue limit of 350 MPa. Although the IH theory does not explicitly show the stress that provides the reference for life calculation, the shearing stress amplitude is used in this paper as in the LP theory. z' is the depth weighted with stress, taking the same value common to all slices.

$$\log\frac{1}{S} \propto \sum_{V_R} \frac{(\tau_i - \tau_u)^c}{{z'}^h} \cdot \Delta V_i \cdot N^e \cdots\cdots\cdots\cdots\cdots (2)$$

$$z' = \frac{\int_{V_R} z(\tau - \tau_u)dV}{\int_{V_R} (\tau - \tau_u)dV} = \frac{\sum_{V_R} z_i(\tau_i - \tau_u)\Delta V_i}{\sum_{V_R} (\tau_i - \tau_u)\Delta V_i} \cdots\cdots (3)$$

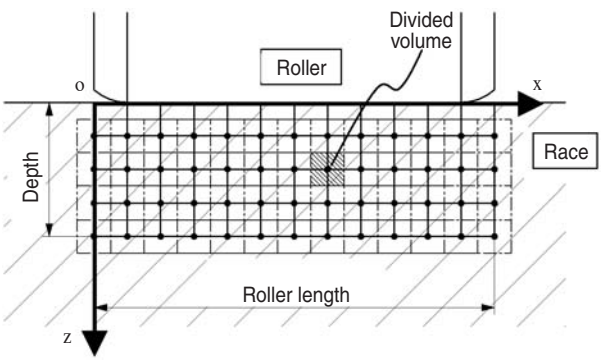

Fig. 4 Subdivide volumes in Model-B and -C

Model-D

This model is worked out to allow one to consider stress distribution on the basis of the LP theory [13]. (See **Fig. 5.**) The portion below the surface is not divided in the direction of depth but in the direction of axis only, with disk-shaped slices formed after division. The life of a slice is calculated using the maximum amplitude of stress to which a slice is subjected τ_{0j} and its depth z_{0j}, and combining the life of each slice. In this way, the significance of the progress of cracking in the LP theory as it is can be brought into each slice. a_j denotes the width of each slice.

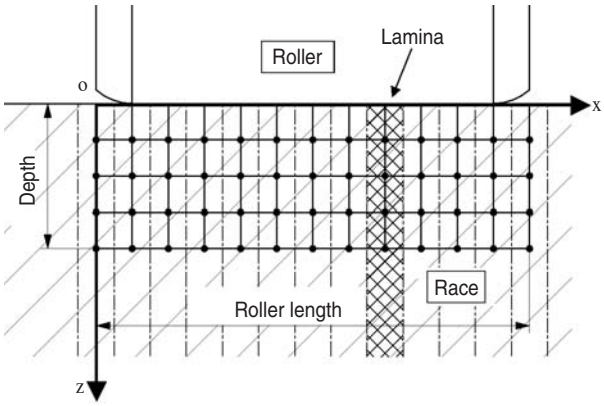

Fig. 5 Laminas in Model-D

$$\log\frac{1}{S} \propto \sum_{\ell_{eff}} \frac{{\tau_{0j}}^c}{{z_{0j}}^h} \Delta V_j \cdot N^e = \sum_{\ell_{eff}} \frac{{\tau_{0j}}^c}{{z_{0j}}^{h-1}} a_j \ell \cdot N^e \cdots\cdots (4)$$

Fig. 6 shows the results of the life calculation according to the four models described above. **Fig. 6** shows the ratios of life with reference to V1. The scale graduations are provided up to 20; the scale is exceeded depending on the model.

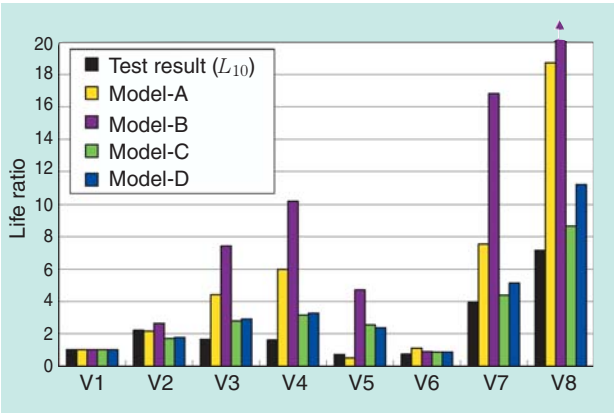

Fig. 6 Comparison of life predictions and test results

In the results of life tests shown in **Fig. 6**, model A capture overall trends in samples V2 and V5, while the agreement deteriorates in samples V3, V4, V7, and V8. Model B shows a similar trend, with the agreement becoming poorer in samples V3, V4, V5, V7, and V8. By contrast, model C in which the fatigue limit is not specified shows a better agreement than model B. When the fatigue limit is taken into consideration as in model B, the value of the stress term of equation (2), $(\tau_i - \tau_u)^c$, decreases as a result of subtracting the fatigue limit component τ_u from the actual stress; accordingly, it is considered that the agreement with the experimental values becomes poor. Model D shows a trend similar to that of model C for which the fatigue limit is not considered.

Table 2 brings together the evaluations of the results of calculation based on the four models described above.

Of the results of calculation using the four life models above, those obtained from model A, model C, and model D show a relatively satisfactory agreement with experimental values, but the agreement in all cases cannot be said to be enough. Models C and D are ones that combine the life values of divided slices; in a case in which the edge load is strict as in sample V5, however, the calculated life becomes larger than the life obtained through experiments. On the other hand, model A, which does not combine life values of divided slices, captures the results of experiments on sample V5 best. This suggests that the method model A follows is effective in making it easier to reflect the effect of the edge on the life. The reason for a poorer agreement with experiments in models C and D with severe edge load is considered in the following.

Table 2 Validation of the 4 models

	V2	V3	V4	V5	V6	V7	V8
Model-A	○	×	×	△	△	△	×
Model-B	○	×	×	×	○	×	×
Model-C	△	△	△	×	○	○	○
Model-D	○	△	△	×	○	○	△

○ : Errors from experimental values up to about 30%
△ : Errors from experimental values from 30% to twice
× : Errors from experimental values above twice

4. Discussion

The distribution in the axial direction of the life of each slice in model D is investigated on sample V5. Life values represented by LIFE Parameter shown in equation (5) are shown in **Fig. 7**. As shown in the comparison with equation (4), this value is perfectly proportional to the life. In equation (5), the stress is expressed in MPa and the length in mm.

$$LIFE\ Parameter = \tau_{0j}^{-\frac{c}{e}} \cdot z_{0j}^{\frac{h-1}{e}} \cdot a_j^{-\frac{1}{e}} \quad \cdots\cdots\cdots\cdots\cdots\cdots \quad (5)$$

In **Fig. 7**, intervals between calculation points (slice widths) are shortened, as shown in **Fig. 3**, to express the abrupt change in stress at the edge.

In **Fig. 7**, discontinuity appears in the section near the edge in which the slice width is small (x = 0.49–0.65 mm) and stress is concentrated; however, the life is not shortened so much as in the middle section. The reason for this is as follows: the slice width is reduced to one tenth of that in the middle in order to express stress concentration; as a result the value in equation (5) is lowered, and taking the reciprocal causes the life to be lengthened. In this way, the effect of the volume on the life is very great, with a slice with a smaller volume having a longer life. The life of the edge load section must become short basically; however, it has already become equal to that of the middle section at the stage shown in **Fig. 7**. However, combining them to determine the life as a whole further weakens the effect of the edge load. In other words, with the volume in the middle far greater than that of the edge, the effect of a decrease in the life in the edge is thinned out in the process of combining life values.

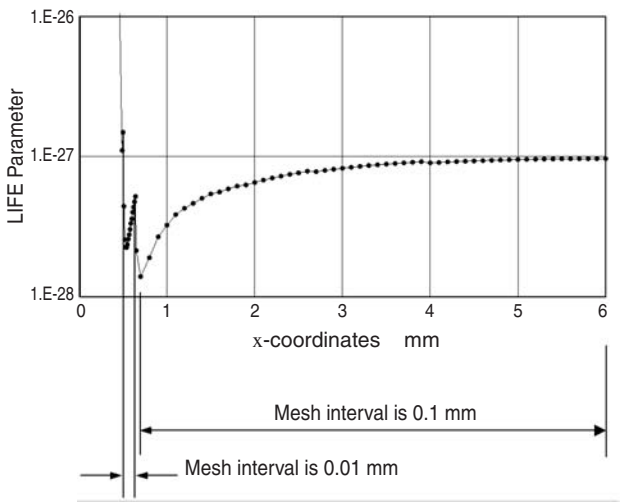

Fig. 7 Life distribution of V5

To express the detail mentioned above numerically, combining LIFE Parameter for the range x = 0.5–0.64 mm (in the edge) yields 2.95E-29, while doing the same operation for the range x = 0.8–11.2 mm yields 1.08E-29 (in the middle). This means that the life of the middle section is reduced to one third of that in the edge section in terms of calculation.

As seen in **Table 1**, however, sample V5 shows that 13 of 15 actual breakages have occurred in the edge section; therefore, the life of the edge section should be shorter than that in the middle section. As shown above, the method shown above does not agree with the real phenomenon at all. This is considered to be an adverse effect of combining life values of slices. This mechanism is common to methods of using stress distribution to combine life values. It is considered that a similar mechanism works when the calculated life is longer than the experimental life of sample V5 in model C based on the IH theory.

By the way, when a notched flat sheet undergoes the fatigue test, rupture starts at the notch section on which stress concentrates; for this reason, only the stress exerted on that section is considered and not combined with the life value calculated from the stress exerted on other parts. Assuming that most of cracks occur at the location at which the maximum amplitude of shearing stress occurs, the LP theory makes calculation using the stress and its depth at that location only. In other words, the LP theory practices the very calculating method just mentioned above. It is considered that the stress volume V in the LP theory is intended for the consideration of the effect of the length of the race, not for the consideration of stress distribution.

As described above, the method of model A that uses the value at the part in which stress is concentrated is effective in making it easier to reflect the effect of the edge on the life. However, model A needs to be improved because of the disagreement of the result of calculation with the result of experiments in other T.P.s such as samples V3, V4, and V8.

5. Improved model (Multi-point LP method)

On the basis of the consideration described above, an improved model was worked out. Following the concept of the LP theory, the improved model gives consideration only to the stress amplitude τ_{0peak} and its depth z_{0peak} at several parts in which stress is concentrated, expressing the life of one of those parts in the following equation:

$$\ln\frac{1}{S_{peak}} \propto \frac{{\tau_{0\,peak}}^{c}}{{z_{0\,peak}}^{h-1}} \cdot \phi_v \cdot {N_{peak}}^{e} \cdot a\ell \quad \cdots\cdots\cdots\cdots \quad (6)$$

In the full-crowning in which the experiment was conducted, the parts in which stress is concentrated are two in the edge and one in the middle, with equation (6) applied to these three parts to calculate the life of different parts. Since the life is determined by the stress in the middle only when edge load is absent, this model is quite identical to the LP theory. The value of the life as a whole L is determined by combining the life values of these parts in which stress is concentrated. The life value combining the life value of each of the three parts in which stress is concentrated under the full-crowning condition is given by equation (7). The three sum values for i are associated with two locations in the edge and with one in the middle.

$$(1/L)^e = \sum_{i=1}^{3} (1/L_i)^e \cdots\cdots\cdots\cdots\cdots\cdots\cdots\cdots\cdots\cdots \quad (7)$$

ϕ_v in equation (6) is a coefficient to correct the life value depending on how uniform the stress is, being called the “stress uniformity coefficient.” The three parts in which stress is concentrated are identified on the assumption that the peak of stress amplitude is distinct; depending on conditions, however, the degree of stress concentration in the middle becomes lower, making a peak not distinct. To clarify this condition, **Fig. 8** shows the axial distribution of the maximum values of shearing stress observed on samples V1, V4, and V5. **Fig. 8** is equivalent to a

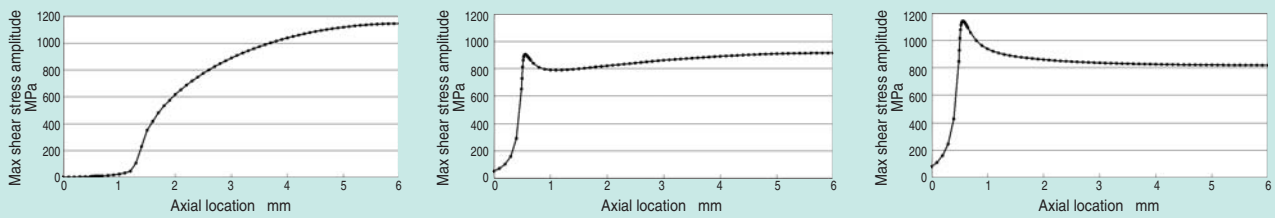

(a) V1 **(b)** V4 **(c)** V5

Fig. 8 Distributions of max orthogonal shear stress amplitudes

diagram that plots the values obtained by searching the maximum values of shearing stress amplitude in the direction of depth on the contour diagram shown in **Fig. 2**. **Fig. 8** shows how the maximum stress amplitude that determines the life of each slice in model D is distributed in the axial direction.

Fig. 8 shows that sample V4 exhibits a considerably lower stress concentration in the middle than sample V1 and the stress distribution has been made considerably uniform. It is estimated that such state appears when the crowning profile comes close to the optimum shape. This corresponds to a case in which the radius of the notch is very large in the fatigue test on the notched flat sheet described earlier. The maximum stress values are about the same at any position in the axial direction, and it becomes impossible to predict where a crack starts depending on the unevenness in strength of the material. It is considered, in such a case, that a mechanism similar to the dimensional effect may cause the life to be shortened, with some kind of correction being necessitated. However, what this means is simply an increase in the odds of the occurrence of cracks due to the unevenness of materials, not affecting the life substantially. Determining this value needs to conduct detailed experiments; however, ϕ_v is calculated under a certain supposition here. For this reason, the following idea of calculation is intended merely to show guidance in considering the decrease in life in the middle.

Stress uniformity coefficient ϕ_v

As seen from equation (6), a ϕ_v value greater unity shortens the life. In the following, the approach to determine the value of this coefficient is described. In a stress distribution such as that observed in a normal Hertz contact, it is considered that a sufficient stress concentration occurs and a stress uniformity coefficient needs not considering; therefore, it is assumed that ϕ_v = 1 holds. Since the degree of stress concentration on the edge is more intense than in the middle, ϕ_v is always equal to unity. What matters is the stress in the middle, and as this becomes increasingly uniform, the value of ϕ_v increases.

Fig. 9 shows diagrammatically the axial distributions of stress amplitude shown in **Fig. 8** into four types. Sample V1 provides a Hertz contact without edge load, corresponding to a quadratic stress distribution shown in **Fig. 9 (a)**. As described above, the ϕ_v value in this case is unity. As edge load is intensified, the stress distribution changes to those shown in **Figs. 9 (b)** and **(c)** and finally to that shown in **(d)**; in **Fig. 9 (d)**, stress concentration is not regarded as existing in the middle, and for this reason, the stress in the middle is neglected. However, since the edge exhibits a remarkable decrease in the life than the middle, combining life values including that in the middle yields about the same result. Sample V4 shows a characteristic relatively close to that shown in **Fig. 9 (c)**. Sample V5 shows a characteristic similar to that shown in **Fig. 9 (d)**. It may be better to express the degree of stress concentration by means of the curvature in the middle of the stress distribution shown in **Fig. 8**. However, this needing complex calculation, the degree of stress concentration is expressed by the area occupied by the stress in **Fig. 8**. This area is given by equation (8).

$$S=\sum \tau_{yzj\max}\Delta a_j \quad \cdots\cdots\cdots\cdots\cdots\cdots\cdots\cdots\cdots\cdots \quad (8)$$

The extent for which area S is calculated is determined with the edge domain excluded in order to avoid being affected by the stress peak in the edge. Although the roller chamfer of T.P. is 0.5 mm, the part extending 1 mm from the roller end face was excluded in the present discussion.

In general, area S is between area S_a shown in **Fig. 9 (a)** and area S_c shown in **Fig. 9 (c)**, with areas S_a and S_c being expressed by equations (9) and (10), respectively. ϕ_v is set at unity in **Fig. 9 (a)** and at 2 in **Fig. 9 (c)**, and ϕ_v values between unity and 2 are determined depending on area S. Therefore, ϕ_v can be expressed as shown in equation (11):

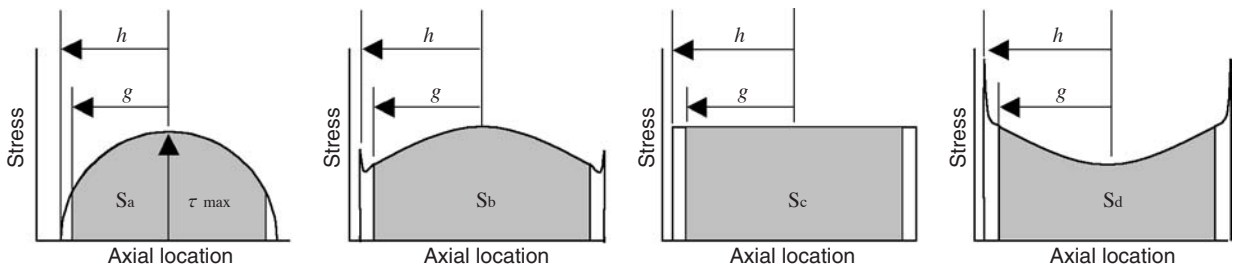

(a) Hertzian contact　**(b)** Slightly edge loading　**(c)** Uniform stress　**(d)** Severe edge loading

Fig. 9 Type of max. shear stress distribution at center part

$$S_a=\frac{\tau_{max}}{2h}\left\{g\sqrt{h^2-g^2}+h^2\sin^{-1}\left(\frac{g}{h}\right)\right\} \quad \cdots\cdots (9)$$

$$S_c=2g\,\tau_{max} \quad \cdots\cdots (10)$$

$$\phi_v=1+\frac{(S-S_a)}{(S_c-S_a)} \qquad 1\leq\phi_v\leq 2 \quad \cdots\cdots (11)$$

6. Results of calculation using the improved model

Fig. 10 shows the result of calculation using the improved model. The illustration shows the result of calculation not using the stress uniformity coefficient (ϕ_v = 1) and that of calculation using model D. **Table 3** shows the stress uniformity factors used in calculation.

It is clearly seen that the improved method exhibits a far better agreement with experimental results than the results obtained on four models (**Fig. 6**). In particular, the improved model excels other four models in that it can be used to determine the optimum crowning radius. In other words, the optimum crowning radius under a load of 13.72 kN can be determined using the results of the life test on samples V1 to V5. Ito and Sugiura consider that the optimum crowning radius is 830 mm, slightly closer to the result from sample V2 than to that from sample V3, while the result from sample V4 shows a peak with models A, B, C. and D. On the other hand, the peak life value appears between samples V2 and V3, capturing the life value peak in the experimental results successfully. **Table 4** shows the result of evaluation of the improved method in comparison with the result obtained using model D.

A shortcoming with the improved method is the estimation of the calculated life value at a lower value compared with the experimental value under severe edge load condition as in sample V5. This is due to the fact that despite a change in the stress value due to the plastic deformation caused by the high contact pressure exerted by edge load, the calculation of stress values on the basis of the theory of elasticity has yielded an estimation of a higher stress value than an actual one. For this reason, the estimation is on the safe side from the design viewpoint, and this will pose no practical problem.

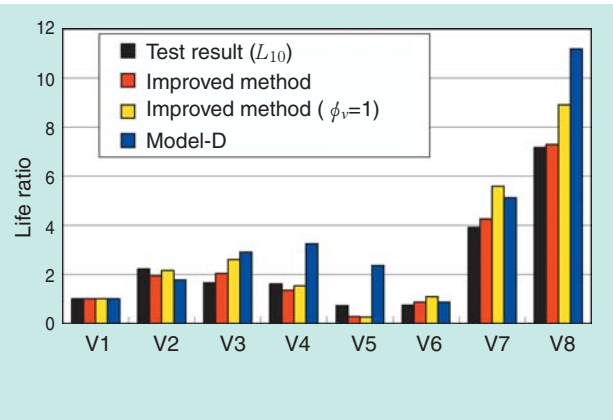

Fig. 10 Life ratio of improved model

Table 3 Stress uniformity factors for center part

	V1	V2	V3	V4	V5	V6	V7	V8
Stress uniformity factor	1.000	1.128	1.582	1.731	—	1.302	1.498	1.586

Table 4 Validation of the improved method

	V2	V3	V4	V5	V6	V7	V8
Improved method	○	○	○	△	○	○	○
Improved method (ϕ_v=1)	○	△	○	△	△	△	○
Model-D	○	△	△	×	○	○	△

○ : Errors from experimental values up to about 30%
△ : Errors from experimental values from 30% to three times
× : Errors from experimental values above three times

7. Afterword

Methods of predicting the life under the effect of edge load occurring in the roller bearing were discussed.

It was clarified that the commonly-used life calculation method of dividing subsurface volume into slices and calculating and combining the life values of individual divided slices does not yield a correct life prediction due to a great effect exerted by the stress volume.

As an improved method, the “multi-point LP method” was proposed in which, on the basis of an idea that each of several parts where stress is concentrated forms the starting point leading to bearing damage, the life value at each starting point to damage is calculated by the LP theory and the values thus calculated are combined. This method introduces the “stress uniformity factor” to take into consideration the phenomenon of fatigue-based life shortening similar to the dimension effect occurring when the stress distribution becomes uniform. To determine the stress uniformity factor, the method of determining it using the area formed by the axial distribution of the maximum values of shearing stress was employed temporarily. To determine this value, it will be necessary to accumulate experimental data as in the process in which the dimension factor was determined in the field of strength of materials in the past.

This paper has been prepared with additions and modifications on the basis of a paper titled “Improved Method of Roller Bearing Fatigue Life Prediction Under Edge Loading Conditions” (Tribology Transactions, Vol. 53, issue 5, pp. 695–702).

References

1) Lundberg, G., and Palmgren, A., Dynamic Capacity of Rolling Bearing, Act a Polytechnica, Mechnical Engineering Series, Vol. 1, No. 3 (1947).
2) Lundberg, G., and Palmgren, A., Dynamic Capacity of Rolling Bearings, Act a Polytechnica, Mechnical Engineering Series, Vol. 2, No. 4 (1952).
3) Harris, T., A., and Ragen, M., A., Spitzer, R., F., The Effect of Hoop and Material Residual Stresses on the Fatigue Life of High Speed, Rolling Bearings, Tribology Transactions, Vol. 35, No. 1 (1992) 194-198.
4) Yu, W., K., and Harris, T., A., A New Stress-Based Fatigue Life Model for Ball Bearings, Tribology Transactions, Vol. 44, No. 1 (2001) 11-18.
5) Kudish, I., A New Statistical Model of Contact Fatigue, Tribology Transactions, Vol. 43, No. 4 (2000) 711-721.
6) Kotzalas, M., A Theoretical Study of Residual Stress Effects on Fatigue Life Prediction, Tribology Transactions, Vol. 44, No. 4 (2001) 609- 614.
7) S. Ito and I. Sugiura, Investigation into the optimal amount of crowning in linear contact turning fatigue tests, NTN Bearing Engineer, No. 48 (1982) pp. 18-26.
8) Harris, T. A., The Effect of Misalignment on the Fatigue Life of Cylindrical Roller Bearings Having Crowned Rolling Members, Transaction of the ASME, Journal of Lubrication Technology, Vol. 91, Series F, No. 2 (1969) 294-300.
9) Moyer, C. A., and Neifert, H. R., A First Order Solution for the Stress Concentration Present at the End of Roller Contract, Transaction of the ASLE, Vol.6 (1963) 324-336.
10) H. Fujiwara and T. Kawase, Logarithmic Profile of Rollers in Roller Bearings and Optimization of their Profiles, Transactions of the Japan Society of Mechanical Engineers C, Vol. 72, No. 721 (2006) 338-345.
11) M. Harada, S. Kamamoto, Y. Fujiwara, Roller Bearing Crowning Form Designed in Consideration of Internal Stress, Conference on Tribology 2000-5 proceedings (2000), C6, pp. 171-172.
12) Ioannides, E., and Harris, T. A., A New Fatigue Life Model for Rolling Bearings, Transaction of the ASME, Journal of Tribology, Vol. 107, July (1985) 367-378.
13) H. Hasegawa, Fatigue Life Estimation for Roller Bearings Under Edge Load Occurrence, Transactions of the Japan Society of Mechanical Engineers C, Vol. 74, No. 742 (2008) 1609-1616.

hoto of author

Haruo NAGATANI
Automotive Business HQ.
Automotive Engineering Dept.

[Technical Paper]

Long Life Grease Added Naturally Derived Antioxidants

Yosuke TAGUCHI*
Hidenobu MIKAMI*

It is generally known that preventing the oxidation degradation of oil is necessary to develop long-life grease. The evaporation of oil has been controlled by having used the best antioxidant up to now. In attempting to make long-life grease, an additive with a function that is superior to conventional antioxidants is needed. Therefore, we adopted naturally-derived antioxidants of plant origin as additives and aimed to develop long-life grease while maintaining low noise and low torque.

1. Introduction

Rolling bearings are used in rotary components on various machines to help improve efficiency of the machines and reliability of the rotary components. Generally, any rolling bearing requires a lubricant, and the most commonly used lubricant type for this purpose is lubricating grease.

When used for an extended time at a higher operating temperature, a lubricating grease will be deteriorated by oxidation: therefore, an antioxidant will need be added into the grease to help inhibit deterioration in its lubricating performance. Various antioxidants have been commercially used for this purpose. In particular, phenolic antioxidants boast greater benefits when added into grease, since they themselves make stable radicals that help terminate chain reactions while they donate hydrogen atoms. Most phenolic antioxidants used in lubricating greases are phenolic derivatives having a tertiary butyl group [1, 2].

Recently, bearings have been increasingly used in applications where high temperature environments are present. Therefore, lubricating greases used for these bearings need to be more durable in high temperature environments, and very effective antioxidants have to be added to these greases.

We have recently researched naturally derived antioxidants, which have not been used as antioxidants for industrial lubricating oils, and have studied their oxidation inhibition capability as additives for lubricants. Also, we have determined influences of these antioxidants as additives in lubricating greases onto various lubricant characteristics including life of the lubricating grease.

2. Mechanism of oxidative deterioration

Generally, researchers believe a lubricating oil will undergo oxidative deterioration in the following sequence [3)–5)].

<Step 1> Owing to factors including high temperature, a lubricating oil will be decomposed into alkyl radicals.

<Step 2> An alkyl radical will react with one oxygen molecule; thereby a peroxide and alkyl radical will be generated.

<Step 1> The peroxide generated in Step 2 will react with two normal lubricating oil molecules, producing alkyl radical.

<Step 1> RH→R ·
<Step 2> R · +O2→ROO ·
ROO · +RH→ROOH+R ·
<Step 3> ROOH+ 2RH→
ROH+H2O+2R ·

RH: hydrocarbon (lubricating oil)
R · : alkyl radical
ROO · : peroxy radical
ROOH: peroxide

To be able to withstand use for an extended period at a higher temperature, lubricating oils usually contain antioxidant additives. Antioxidants used for this purpose can be categorized into two types—(1) chain stoppers (primary antioxidants), and (2) peroxide decomposers (secondary antioxidants). These types differ in oxidation inhibition mechanism. The known examples of the chain stopper include phenolic stoppers and amine stoppers, and those of

*Elemental Technology R&D Center

the peroxide decomposer include phosphites, phosphates, thio ethers, and thio esters.

Being chain stoppers, phenolic antioxidants each donate a hydrogen atom derive from a hydroxyl group to a peroxy radical that occurs during the growth phase in oxidative deterioration mechanism of a lubricating grease (Formula 1) to turn the radical into a harmless radical. The resultant phenoxy radical is then resonance-stabilized (Formula 2), and then reacts with another peroxy radical to make a non-radical compound [6] (Formula 3), thereby oxidative deterioration of the target lubricating oil is inhibited.

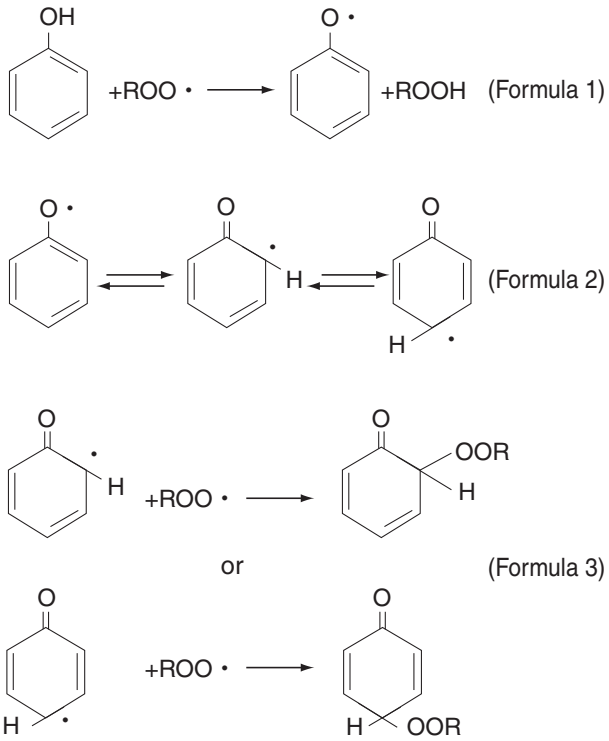

3. Natural antioxides

"Natural antioxide" is the generic name for plant or vegetable derived constituents whose molecules each have a plurality of phenolic hydroxyl groups (hydroxyl groups linked to aromatic rings such as benzene ring, and naphthalene ring). Natural antioxidants are contained in a diversity of plants or vegetables. Well known plant- or vegetable-derived antioxidants include curcumin, flavonol, isoflavone, tannin, catechin, quercetin, and anthocyanin. These antioxidants have been proven to efficiently function as antioxidants when taken into human body [7].

In the present study, we, in expectation of oxidation inhibition effects of natural antioxidants for bearing grease, have focused our study efforts onto curcumin that is extracted from turmeric and quercetin that is extracted from onion: we have added these substances into greases in an attempt to extend grease life. Structural formulas of curcumin and quercetin are shown in **Table 1**, and appearances of these substances are shown in **Fig. 1**. These substances are generally used as health foods or food antiseptics.

Table 1 Naturally derived antioxidants

Description	Structural formula
Curcumin (turmeric)	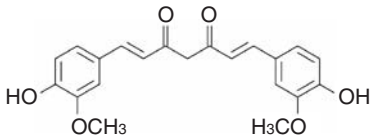
Quercetin (onion)	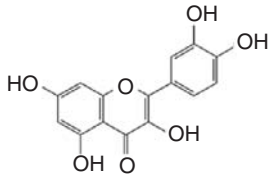

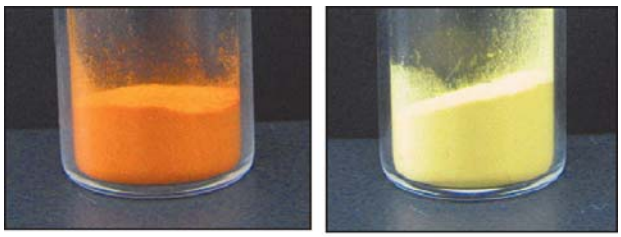

10mm

Curcumin　　Quercetin

Fig. 1 Appearance of naturally derived antioxidants

4. Weight decrease of greases at higher temperature

To be able to achieve longer life for lubricating greases, it is necessary to inhibit oxidative deterioration of base oil (lubricating oil). Examples of weight decrease with lubricating oils having been allowed to stand at a higher temperature are graphically plotted in **Fig. 2**. When a given lubricating oil is allowed to stand at a higher temperature, its weight decreases as time elapses. Once a period to initiation of oxidation of lubricating oil (induction period) ends, its weight begins to drop suddenly. It appears that when oxidized, lubricating oil is decomposed, and the decomposition products readily evaporate, leading to weight decrease of the lubricating oil [2]. Consequently, the induction period of

lubricating oil lacking antioxidant is shorter while the similar period of lubricating oil having antioxidant is longer. Note that the addition of less effective antioxidant will result in shorter induction period with the lubricating oil.

We have added natural antioxidants and conventional antioxidants into lubricating oils, and determined the magnitude of oxidative deterioration inhibition effects of these antioxidants. The conventional antioxidants used were phenolic antioxidant having a tertiary butyl group (AO-1) and amine antioxidant (AO-2) (**Table 2**). The lubricating oil used was ester oil (33 mm^2/s, at 40˚C). 1wt% of antioxidant was added to the ester oil and the specimen was then allowed to stand at 150˚C, thereby the weight decrease rate of the specimen was determined [8]. The results are graphically plotted in **Fig. 3.**

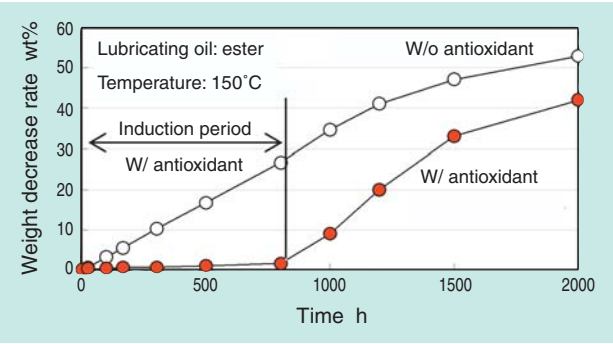

Fig. 2 Typical weight decrease of lubricating oil

Table 2 Conventional antioxidants

Description	Structural formula
Phenolic antioxidant (AO-1)	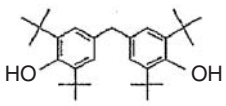
Amine antioxidant (AO-2)	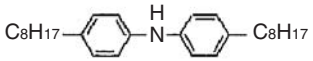

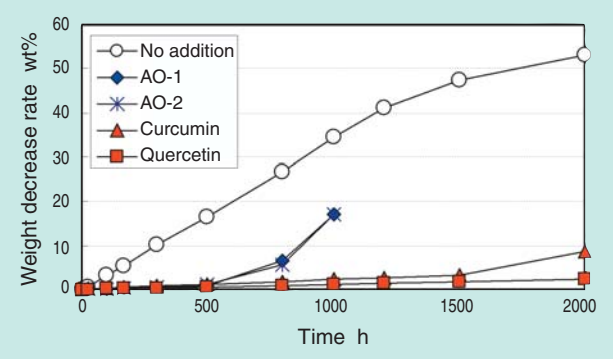

Fig. 3 The weight decrease rate of lubricant

The lubricating oil specimens lacking antioxidant begins oxidative deterioration immediately after start of the test, and the weight decrease rate becomes greater as time elapses. In contrast, the lubricating oil having antioxidant shows inhibition of weight decrease for a certain period. The specimen containing either phenolic antioxidant (AO-1) or amine antioxidant (AO-2) exhibits apparent weight decrease of lubricating oil at around 500 hours after start of the test. In contrast, the specimen having natural antioxidants such as curcumin or quercetin shows little weight decrease of lubricating oil, even after 2,000 hours has elapsed. A longer period before weight decrease of lubricating oil becomes apparent means more positive inhibition of oxidative deterioration of the lubricating oil. Thus, we believe that these natural antioxidants excel in oxidation inhibiting performance and both curcumin and quercetin are positively effective antioxidants for ester oil.

5. Application of natural antioxidants to lubricating grease

Li-soap/ester grease is typically used as motor bearing grease, and boasts excellent reduction in running torque and noise, possibly occurring on motor bearings.

We have added natural antioxidant to Li-soap/ester grease, and evaluated the improvement to high-temperature life of grease and positive influence in reducing noise and torque on the bearing lubricated by the grease.

5.1 High-temperature grease life

Samples of a particular **NTN** rolling bearing type (#6204) were each prefilled with grease containing curcumin or quercetin or conventional antioxidant, and these samples were subjected to a high-temperature grease life test. The compositions of the test greases are summarized in **Table 3.**

The four different greases summarized in **Table 3.** were subjected to high-temperature grease life test (per ASTM D3336). The test rig used is schematically illustrated in **Fig. 4**, and the results are summarized in **Fig. 5**. The amount of lubricating grease used for prefilling is equivalent to 38% (1.8 g) relative to the bearing internal volume. The number of repetitions for each test sequence (number of test runs) was n=3. The grease life of each grease type was calculated by determining the mean for three test runs. The Test Greases C and D, each having natural antioxidant, boasts longer life—approximately 10 times as long as that of the Test Grease D that lacks antioxidant and approximately three times as long as that of the Test

Grease B that contains amine antioxidant (AO-2). When considering the result of this test, together with the result of weight decrease test in the previous section (see **Fig. 3**), we think that an antioxidant additive that more positively helps inhibit weight decrease of lubricating oil also contributes to longer life for the associated lubricating grease.

Table 3 Test grease

	A	B	C	D
Thickener	Li-soap			
Base oil	Ester			
Base oil viscosity mm²/s 40˚C	26			
Additive	—	AO-2	Curcumin	Quercetin
Amount added wt%	—	2	2	2
Worked penetration 60W 25˚C	250	245	245	245

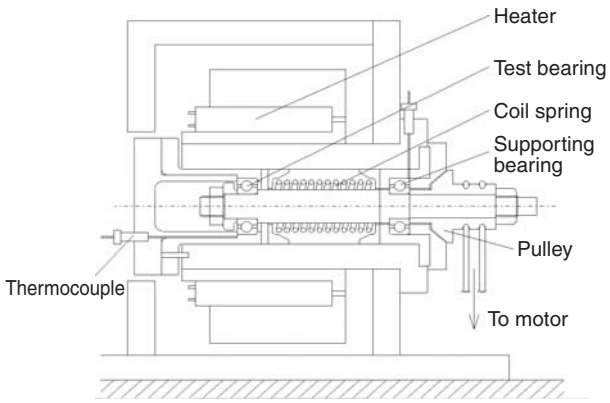

Fig. 4 High temperature bearing endurance test machine

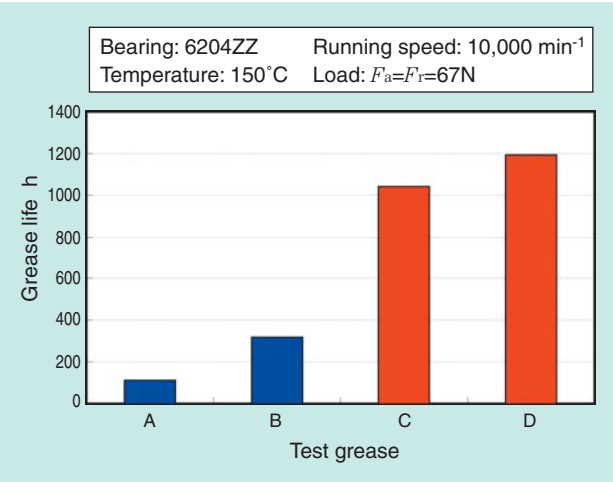

Fig. 5 Result of high-temperature bearing durability test (1.8 g prefill)

5.2 Difference in effect with varied amount of addition

We have attempted to determine an optimal amount of addition of natural antioxidant. For this purpose, we chose curcumin as the natural additive tested and added in Li-soap/ester grease. Curcumin was added in six levels of amount, in a range of 0 to 10wt% concentration relative to the amount of grease. The resultant grease specimens were each prefilled into a rolling bearing, and thereby their high-temperature lives have been determined. The test results are shown in **Fig. 6**. The grease specimen containing 2wt% of curcumin boasts longest grease life, while addition of 5wt% or greater results in shorter grease life. To sum up, there appears an optimal amount of addition about curcumin. Note, that, a much greater amount of curcumin added resulted in reduced effect in extending grease life. The most probable cause for this problem is: when the amount of curcumin added exceeds 2wt%, a certain portion of addition remains non-solved in the grease, and the insoluble matter promotes vibration of the bearing, causing lubricity of the grease to deteriorate.

Based on these findings, we believe that curcumin and quercetin are efficient antioxidants for lubricating greases and positively extend grease life.

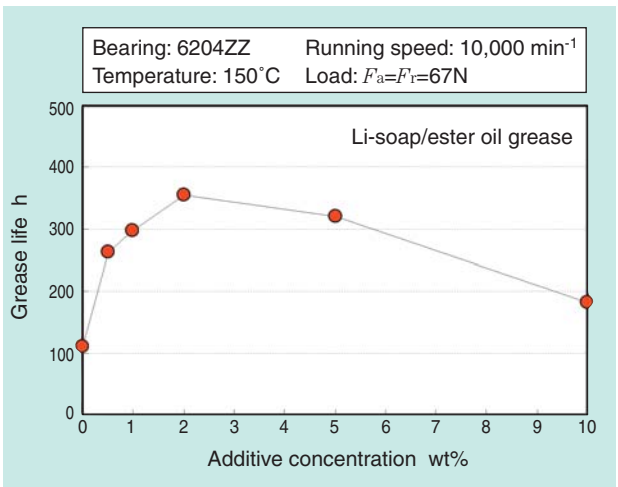

Fig. 6 Varying influence of amount of curcumin added (0.7 g prefill)

5.3 Noise reduction characteristics

The noise level needs to be as low as possible with bearings, in particular for motor bearings. Being solid at an ordinary temperature, a natural antioxidant needs to be dissolved in grease in order to help maintain low noise levels on bearings. **Fig. 7** shows photomicrographs of curcumin added in amount of 2wt% to commercially available Li-soap/ester grease. **Fig. 7(a)** shows a state where curcumin remains

simply mixed with the grease and curcumin particles are apparently present. In contrast, **Fig. 7(b)** illustrates a state where curcumin has been fully dissolved in the grease thanks to an improved grease manufacturing process.

The noise levels of greases either containing or not containing dissolved curcumin were measured with an Anderon meter. The resultant measurements are summarized in **Fig. 8**. The noise level of the grease specimen containing dissolved curcumin was approximately equivalent to that of the specimen not containing curcumin. Because curcumin can be dissolved in Li-soap/ester oil grease, the grease can help the bearing run without developing higher running noise.

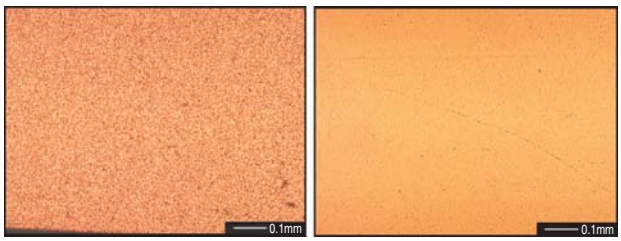

(a) Insoluble state **(b)** Fully dissolved state

Fig. 7 Photomicrograph of curcumin addition grease

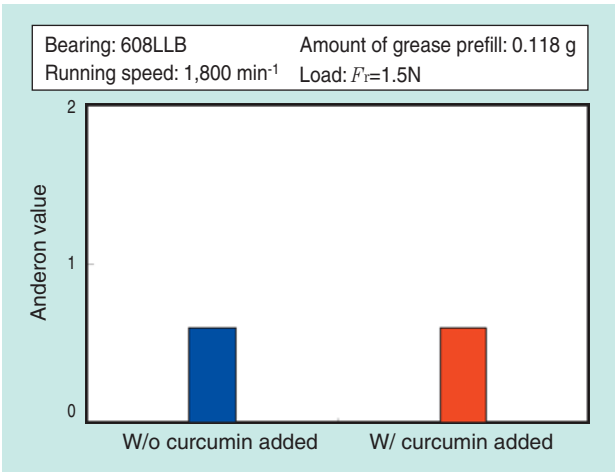

Fig. 8 Noise levels of various greases

5.4 Running torque

The running torque needs to be as low as possible with bearings, in particular for motor bearings in order to minimize power consumption of the electric motors. We have determined the effect of addition of curcumin onto bearing running toque. **Fig. 9** schematically illustrates the test rig used, and **Fig. 10** graphically plots the result of the running torque measurement.

The measuring operation was performed while increasing the bearing running speed from 1,800 min^{-1} up to 10,000 min^{-1} in several steps, and the test bearing was allowed to run for 1 hour at each speed setting, thereby the mean running torque at each running speed was measured.

We have learned that the grease consisting of commercially available Li-soap/ester oil grease and 2wt% curcumin additive provides bearing running torque equivalent to that obtained from a lubricating grease not containing curcumin, at any bearing running speed. We may judge that addition of curcumin does not lead to increased bearing running torque.

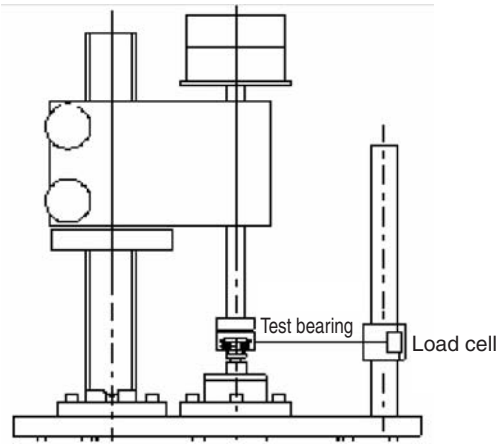

Fig. 9 Vertical torque examination machine

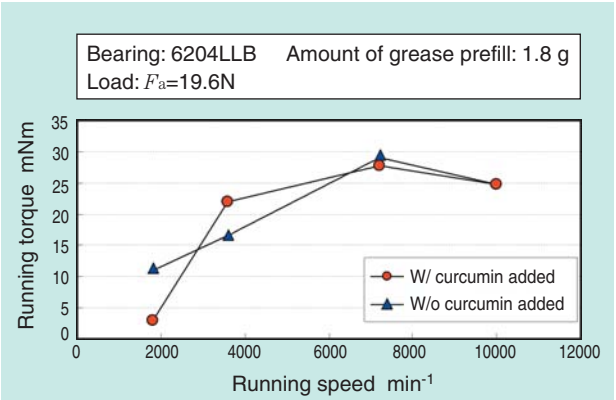

Fig. 10 Rotational torque of various greases

6. Decreased bearing running torque by reduction in amount of grease prefill

High-temperature durability of any rolling bearing can be governed by the amount of grease prefill in the bearing. Life of a given rolling bearing at higher temperatures is longer with a greater amount of prefilled grease, while the running torque of a rolling bearing is lower when the amount of prefilled grease is smaller. Thus, smaller amount of prefilled grease will help realize lower running torque of the bearing, at a cost of shorter bearing life.

Addition of a natural antioxidant in grease will positively extend life of the grease. In other words, a grease containing natural antioxidant will help reduce the amount of grease prefilled in a bearing without decreasing grease life in the bearing when compared with a conventional grease.

For the purpose of this section, we have added a natural antioxidant in varying amounts into Li-soap/ester oil grease to prepare specimens, and by testing the specimens attempted to determine the relation between the amount of lubricating grease prefill and grease life, and the amount of grease prefill and bearing running torque. **Fig. 11** graphically plots the relation between the amount of grease prefill and grease life, while **Fig. 12** shows the relation between the amount of grease prefill and bearing running torque. Compared with grease not containing curcumin, the useful life of grease containing 25wt% of curcumin is about three times as long. Thus, use of curcumin-containing grease leads to a unique benefit—the percentage of grease prefill in bearing internal space volume can be reduced from 38% to 25% (reduction ratio: 30%) without causing decrease in grease life (**Fig. 11**).

Also, the bearing running torque with the curcumin-containing grease is 35% smaller, compared with the running torque with bearings prefilled with standard grease not containing curcumin (**Fig. 12**).

It is also possible that reduction in amount of grease prefill helps prevent grease leakage and contamination around the bearings.

7. Conclusion

From the currently available test results, we have verified that use of lubricating oil or Li-soap/ester oil grease containing natural antioxidant used to lubricate a bearing will help realize not only low running noise and low running torque on the bearing but also longer effective life for either lubricating oil or grease.

A natural antioxidant may be added to a lubricating grease in order to inhibit oxidation of the lubricant in the grease and help extend high temperature life of the lubricating grease. This type of grease, even if prefilled in a smaller amount, can maintain useful life of the bearing. At the same time, smaller amount of prefill means lower stirring resistance of the grease; thereby the running torque of the bearing will be decreased.

It appears highly possible that natural antioxidants can be applied to those lubricants having compositions other than the Li-soap/ester oil

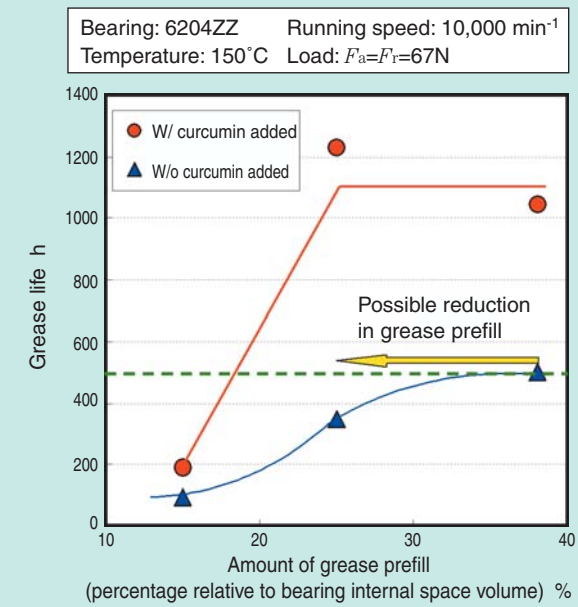

Fig. 11 Relation between amount of grease and longevity

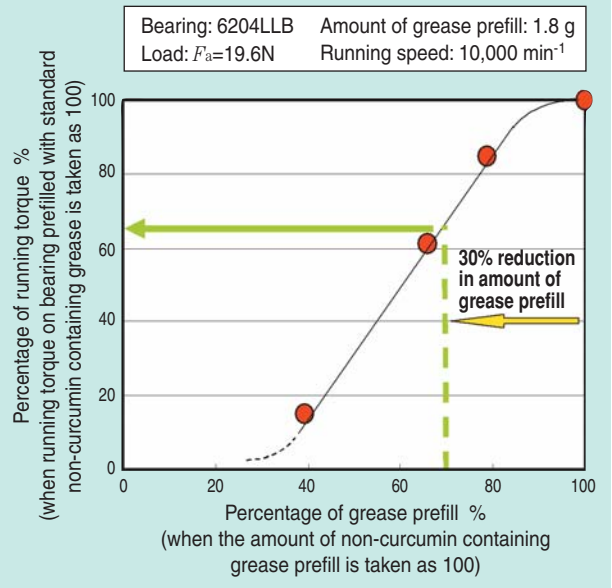

Fig. 12 Influence of amount of grease on rotating torque

combination described above. We expect their applicability in a diversity of lubricants. We believe that longer grease life together with decreased amount of grease prefill in bearings will positively contribute to reduction in environmental impacts through decreased energy consumption, lower cost, and prevention of contamination of the environment around the bearing resulting from possible grease leakage.

References

1) H. Mikami, Book of Synopses ITC Kobe (2005) 145.
2) H. Mikami, Development of Long Life Grease for High Speed Application—ME-1 Grease for Motor Bearings, NTN Technical Review No. 72 (2004) 20-25.
3) Y. Ohkatsu, T. Aoshima and K. Yamaguchi, Molecular Design of New Phenolic Antioxidants, Chemical Society of Japan, No.11 (1998) 711-721.
4) J.L. Reyes-Gavilan, Paul Odorisio, NLGI Spokesman, 64, 11 (2001) 22.
5) J. Igarashi, Nisseki Technical Review, 32, 3 (1990) 5
6) T. Watanabe, Functions and Applications of Antioxidants, Junkatsu Keizai, pp. 6-3 (2003).
7) H. Nishino , Development of Free Radical Theory and Food Products for Ageing Prevention, CMC Technical Library, pp. 14-21 (1999).
8) Y. Taguchi, H. Mikami, Effectiveness of Natural Antioxidants on the Oxidation and Deterioration of Lubrication Grease, Proceedings of Tribology Conference, pp. 283-284 (2010).

hoto of author

Yosuke TAGUCHI
Elemental Technology
R&D Center

Hidenobu MIKAMI
Elemental Technology
R&D Center

[Technical Paper]

Improvement of Grease Leakage Prevention for Ball Bearings Due to Geometrical Change of Ribbon Cages

Norihide SATO*
Tomoya SAKAGUCHI*

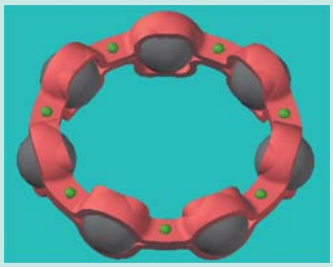

Grease leakage from sealed grease bearings shortens bearing life and pollutes nearby parts. Therefore, the seal shape was changed and the included grease amount was decreased. However, these changes reduce performance, such as causing higher torque, and shorten bearing life.

Generally, grease leaks from between the inner seal groove and the seal, which rotate relative to each other. In this report, in order to improve the prevention of grease leakage from sealed deep groove ball bearings, new geometrical cage designs were developed. These cages were confirmed experimentally to have excellent performance in grease leakage prevention.

1. Introduction

To avoid grease purge from a greased and sealed bearing a number of measures can be taken. The pressure the seal lip exerts on the inner ring can be increased[1)], the shape of the seal lip can be changed to help keep the grease in[2)], or the amount of grease in the bearing can be decreased. Unfortunately these changes can increase the shaft torque, the cost of the bearing, or shorten the life respectively.

Grease purge occurs between the seal and the inner ring seal groove that rotate against each other. It has been found that grease purge occurs when the grease can adhere to a surface close to an opening. For this reason, it is postulated that if the adhesion of grease to certain bearing components can be suppressed, grease purge can be reduced. On the basis of this concept, a cage with a new shape was developed in an attempt to improve the resistance to grease purge.

2. Mechanism of grease purge and the state of adhesion of grease to the ribbon steel cage

A ball bearing with a full contact-seal and filled with a lithium/ester based grease (6203 LLU, ribbon steel-sheet cage containing 870 mg of grease) was run at a speed of 3,600 min^{-1} under a radial loading. The test was conducted under both inner ring and outer ring rotation. Following the test, the post test bearing mass was measured and the results from inner ring rotation were compared to the results for outer ring rotation. It was found that the bearings run under outer ring rotation saw five times the mass decrease compared to inner ring rotation. All mass decreased were found to e the result of grease purge.

Fig. 1 shows the results of running a bearing at 3600 min^{-1} for five seconds in either inner ring or outer ring rotation with no seal. Grease does not adhere to the inner ring seal groove with the inner ring rotating, while a large amount of grease is seen adhering there with the outer ring rotating. This allows one to estimate that the adherence of grease to the inner ring seal groove is one of the prerequisite for the large amount of grease purge under outer ring rotation.

It is theorized that grease purge in a bearing with full contact seal occurs by the mechanism shown in **Fig. 2**:

*Elemental Technology R&D Center

(1) Outer ring rotation causes the grease to move to the inner ring seal groove
(2) The heat from bearing operation raised the temperature of the air inside the bearing resulting in an increase in pressure
(3) The increased pressure pushes the seal lip outward opening a path for grease purge to occur

The above progression suggested that if the amount of grease adhering to the inner ring seal groove can be reduced grease purge in a sealed bearing can be reduced. To achieve this, the shape of the cage was examined.

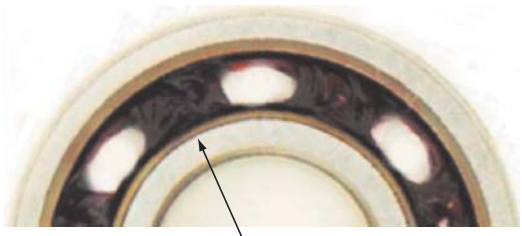

a) Inner ring rotation

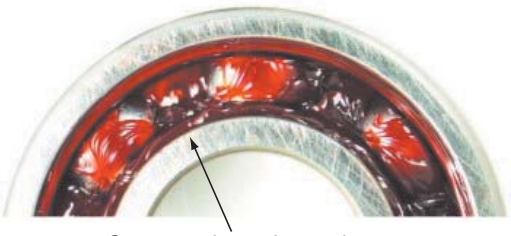

b) Outer ring rotation

Fig. 1 Location of grease in a ball bearing with a ribbon cage after operation

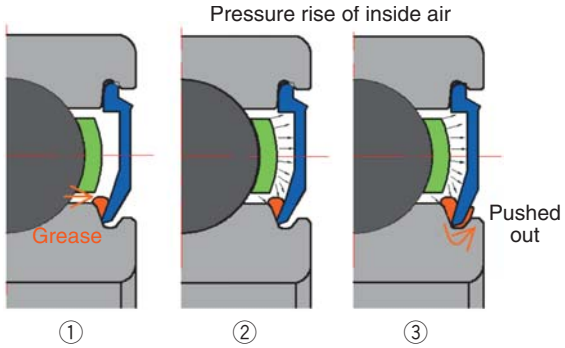

Fig. 2 Grease purge mechanism from a sealed ball bearing

3. Behavior of grease adhering to the inner ring seal groove

In order to observe how grease moves under outer ring rotation a test was conducted where a bearing with a minute amount of grease was rotated for five seconds.

A 6203 type bearing was filled with 60 mg of grease. The grease was located between the outer ring raceway and the cage. After the bearing was rotated it was found that the grease had migrated to the leading edge, with respect to rotation, of the cage pocket (**Fig. 3**). It was theorized that grease adhering to the rolling element was scratched off by the inner diameter of the cage after which the greases collected at the leading edge of the cage pocket. **Fig. 4** shows the grease state when 320 mg of grease is placed in the bearing. The amount of grease on the leading edge of the cage pocket increases. Additionally grease is found to adhere to the middle of the cage pocket and to the outer diameter of the inner ring.

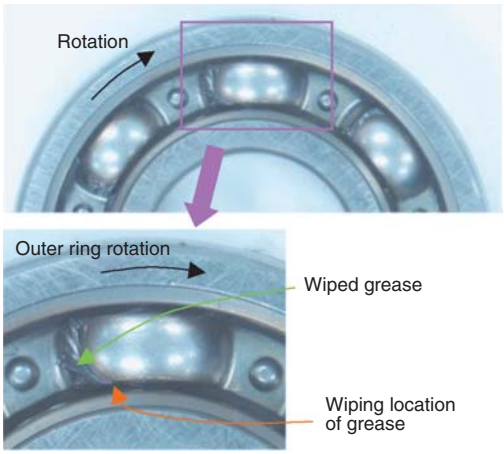

Fig. 3 Grease dispersal in a ball bearing with 60 mg of grease after outer ring rotation

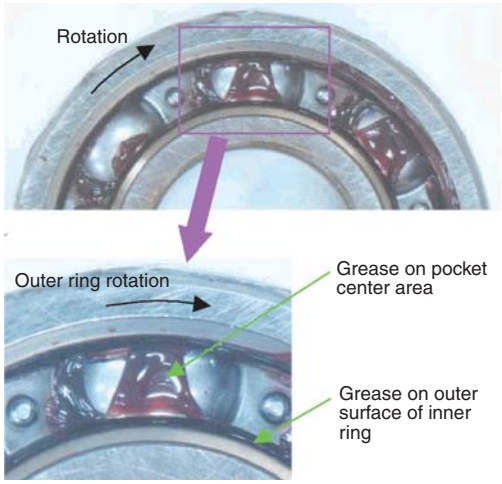

Fig. 4 Grease dispersal in a ball bearing with 320 mg of grease after outer ring rotation

These test results suggests the grease follows the a specific route to the inner ring seal groove, assuming outer ring rotation and a ribbon steel cage.

I) Grease adhering to the rotating rolling element is scraped off by the inner diameter of the cage pocket and attaches to location G_w in **Fig. 5 a**).
II) An increase in the accumulated amount of grease at G_w on the edge of the pocket causes grease to also attach to the outer diameter of the inner ring at G_O in **Fig. 5 b**).
III) An increase in grease at G_O causes grease to attach to the inner diameter surface of the cage at G_t. This only occurs at the middle part of the cage pocket
IV) As the amount of grease at G_t increases, part of that grease is pushed out into the inner ring seal groove at G_g in **Fig. 5 d**). As the bearing continues to rotate more grease is deposited into the inner ring seal groove. Under inner ring rotation the grease at G_O in **Fig. 5 b**) is scattered back into the bearing by centrifugal force, helping to prevent grease purge. However, under slower inner ring rotational speeds the centrifugal force is reduced leading to the same behavior as that observed in outer ring rotation.

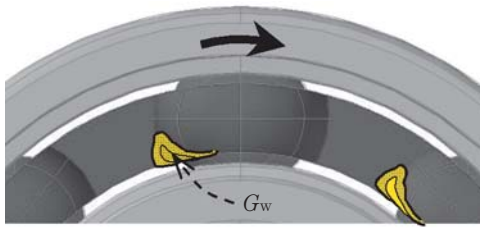

a) Wiping step

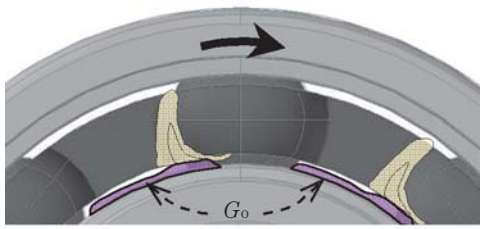

b) Grease transfer step to outer surface of inner ring

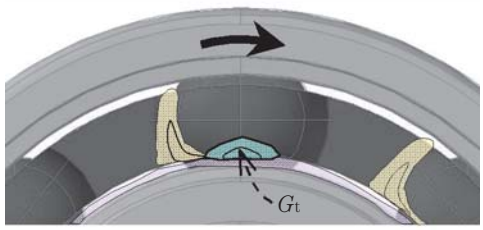

c) Grease transfer step to pocket center area

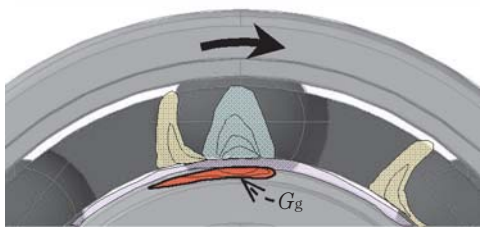

d) Grease shift step to inner seal groove

Fig. 5 Grease movement from ball surface to inner ring seal groove

4. Development of a cage that reduces grease buildup to the inner ring seal groove

4.1 Working out an improved cage

The discussion in Section 3 suggests three concepts would be effective in suppressing the adherence of grease to the inner ring seal groove:

(1) Reducing the ability of the inner diameter of the cage pocket to scratch off grease off the outer diameter of the inner ring (position G_O), thereby reducing grease accumulating on the pocket edge;
(2) Preventing grease from moving from the leading edge of the cage pocket and attaching to the outer diameter part of the inner ring; and
(3) Preventing the movement of grease to the inner ring seal groove from the edge of the cage pocket.

On the basis of these concepts, three prototype cages were made to confirm the effect of cage design of grease on the behavior of grease. All of these cages were fabricated from common ribbon steel sheet cages with minor alterations (referred to as reference cages in the following).

The cage shown in **Fig. 6** has a larger chamfer to a wide area in the middle part of the cage pocket (dotted zone). This cage aims at suppressing the scratching action of the edge on the inner diameter side of the cage pocket (concept (1)) and at suppressing the movement of grease to the inner ring seal groove (concept (3)). This cage was called the ‘widely recessed cage’.

The cage shown in **Fig. 7** is an example of realization of concept (1), in which only the area of the cage that scratches the grease is chamfered. This cage is called the ‘diagonally recessed cage’. Its effect is considered smaller than that of the widely recessed cage described above.

Fig. 8 shows a cage with an cut-out where the cage pocket would contact the outer diameter of the inner ring. This aims to avoid the effects of concepts (2) and (3) by increasing the gap between the edge of the cage pocket and the outer diameter of the inner ring. This cage is called a narrow pocket width cage.

4.2 Effect of preventing grease from adhering to the inner ring seal groove

Figs. 9 to **11** show results of the outer ring rotation test for each of the new cage designs. Compare this with the results for the standard cage shown in **Fig. 1** (the amount of sealed-in grease: 870 mg).

Fig. 9 shows the result obtained with the widely recessed cage. No attachment of grease to the inner ring seal groove observed. Additionally grease was not found in the outer diameter part of the inner ring and at the center of the outer surface of the pocket, with the anticipated effect obtained.

Fig. 10 shows the result obtained with the diagonally recessed cage, with no attachment of grease to the inner ring seal groove observed. While this was a satisfactory result this was a realization of only concept (1) for grease purge reduction.

Fig. 11 shows the result obtained from the narrow pocket width cage. While the amount of grease scratched off by the edge of the pocket (G_w in **Fig. 5**) is large, the adherence of grease to the inner ring seal groove was not observed.

In short all three cage designs worked at suppressing the adherence of grease to the inner ring seal groove.

Fig. 6 Design for the widely recessed cage with large chamfer

Fig. 9 Grease deposition in bearing using the widely recessed cage (**Fig. 6**)

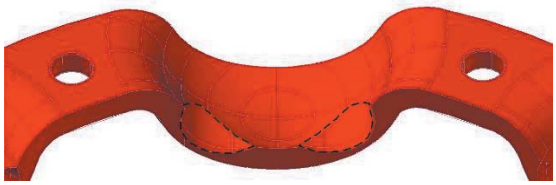

Fig. 7 Design for the diagonally recessed cage with two small chamfers

Fig. 10 Grease deposition in bearing using diagonally recessed cage (**Fig. 7**)

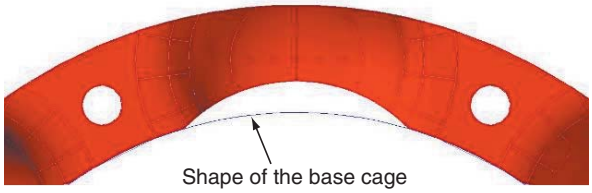

Fig. 8 Design for the narrow pocket cage

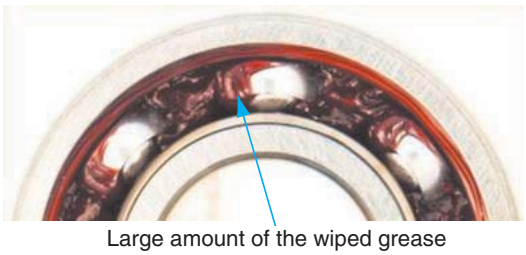

Fig. 11 Grease deposition in bearing using narrow pocket cage (**Fig. 8**)

5. Effect of the improved cages on the resistance to grease leakage

The cages used for testing in Section 4 were standard cages that had been modified by additional cutting steps. For additional testing cages made using the standard die stamping, as in volume production, were examined.

It was found that a widely recessed cage made using the die stamping process caused the outer surface of the cage to swell outward into where the bearing seal is located. This would necessitate a change in the design of the bearing inside. For this reason, the evaluation of production cages was limited to two types, the diagonally recessed cage and the narrow pocket width cage.

Fig. 12 Standard cage with ball

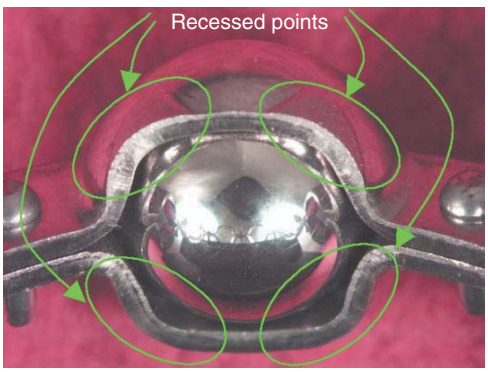

Fig. 13 Diagonally recessed cage with ball

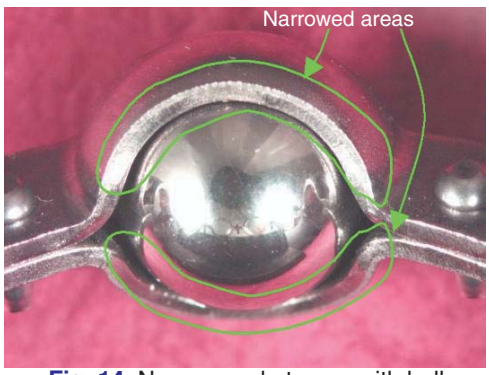

Fig. 14 Narrow pocket cage with ball

Figs. 12 to **14** show the effects of the cage changes (the standard cage for comparison, diagonally recessed cage, and narrow pocket width cage).

These three cage types were built into bearings and grease leakage tests were performed under outer ring rotation conditions (**Table 1**) in which grease leakage would normally easily occur. The test criterion was based on a visual check for purged grease to the outside of the bearing.

Table 2 shows the results of the grease leakage test. Six base cages out of 15 showed grease leakage. However, the improved cages showed satisfactory results of one diagonally recessed cage and no narrow pocket width cage showing leakage.

Figs. 15 to **16** show the amount of grease attached to the inside of the seal in a bearing with the standard cage and the narrow pocket cage respectively. A large

Table 1 Test conditions

Bearing	6203LLU (Sealed ball bearing)
Outer ring rotation speed, min^{-1}	3600
Operation time, min	15
Grease	870 mg, Lithium soap-Ester, Penetration 255
Leakage detection	Visual inspection

Table 2 Test results

Cage shape	Leakages / Total
Base cage (**Fig.12**)	6 / 15
Press cage of diagonally recessed pocket (**Fig.13**)	1 / 15
Press cage of narrow pocket width (**Fig.14**)	0 / 15

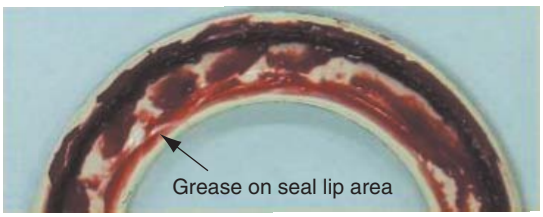

Fig. 15 Adhered grease on the inside of seal with the standard cage (**Fig. 12**)

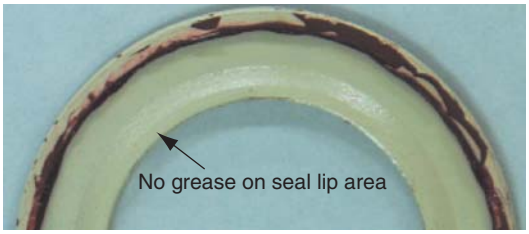

Fig. 16 Adhered grease on the inside of seal with the narrow pocket width cage **Fig. 14**)

amount of grease is observed in the seal lip of the bearing with the standard cage, but no grease is observed in the seal lip of the bearing with the narrow pocket cage. It was concluded that the improvement in the shape of the cage has made it possible to suppress the flow of grease to the inner ring seal groove, thereby reducing grease purge from the bearing.

This test demonstrated that a cage capable of reducing the adherence of grease to the inner ring seal groove also reduced the amount of grease purge.

6. Examination of the strength of improved cages

The new cages differ in shape from that of the standard cage. It was anticipated that this will change how much stress occurs in the cage and where the stress is concentrated. The cage strength was examined by means of a static structural analysis based on the finite element method.

For this analysis the following assumptions were made; the rolling element moves relatively to the direction of revolution and gives contact load and frictional force to the pocket plane.

Fig. 17 shows for the results for the standard production cage. To speed the analysis only a section of cage was examined. This section consisted of an area between rivet holes. Circumferential displacement lock was given to the cross-section of division, and axial displacement lock to the mating face side of the rivet presser. When a bearing is run under moment load, cracks often occur on the boundaries between the plane with rivet holes and the pocket (referred to as a pocket end in the following). Also the analysis illustrated in **Fig. 17** shows that the maximum principal stress occurs at the same position in the modified cage.

Figs. 18 and **19** show the distributions of principal stress in the two improved cages. The upper and lower limit values of the stress contour are similar between the three cage designs. In the diagonally recessed cage shown in **Fig. 18**, the maximum principal stress occurs at the pocket end as with the standard production cage, while in the narrow pocket width cage shown in **Fig. 19,** the maximum principal stress occurs in the middle of the pocket.

Fig. 20 shows the ratios of the principal stress values at the pocket end and at the middle of the pocket of the different cage designs to the maximum principal stress value of the standard production cage. A standard cage and a diagonally recessed cage, both with the same width in the radial direction, exhibit the same stress value. By contrast, a narrow pocket width cage is narrow in width in the radial direction in the pocket and for this reason has low rigidity. As a result, the stress in the middle of the pocket inside increases relatively, being 6% greater than the maximum value with the base cage.

Due to the higher stresses in narrow pocket width cage care should be taken to ensure that the strength of the cage is sufficient under operating conditions.

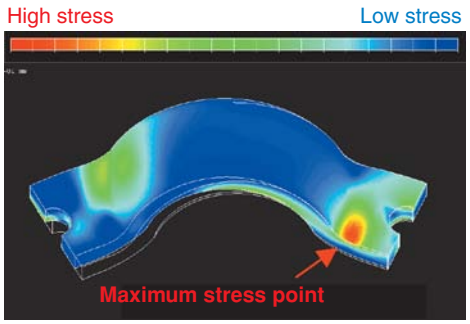

a) Pocket-back side

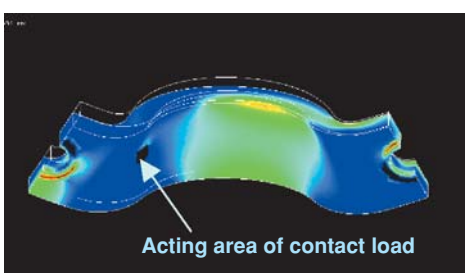

b) Pocket side

Fig. 17 Principal stress distribution in standard production cage (**Fig. 12**)

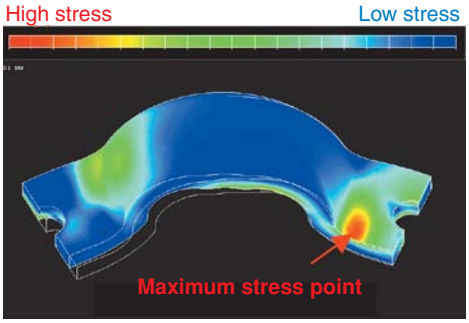

a) Pocket-back side

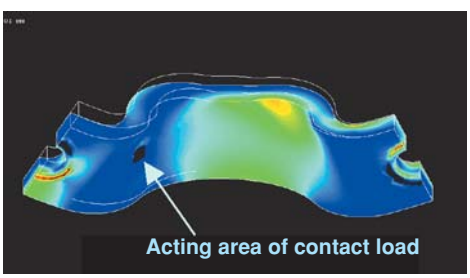

b) Pocket side

Fig. 18 Principal stress distribution in diagonally recessed pocket cage (**Fig. 13**)

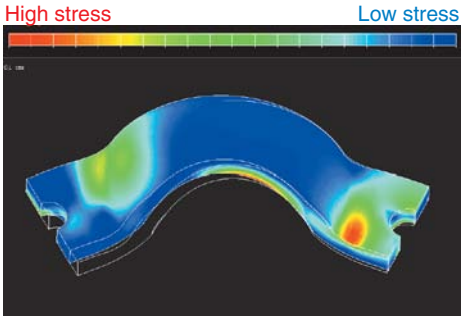

a) Pocket-back side

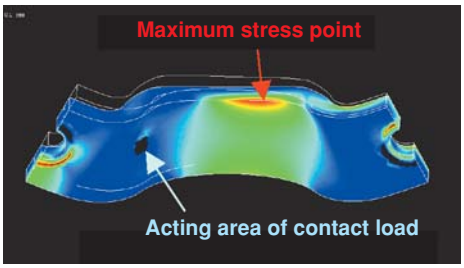

b) Pocket side

Fig. 19 Principal stress distribution in narrow pocket width cage (**Fig. 14**)

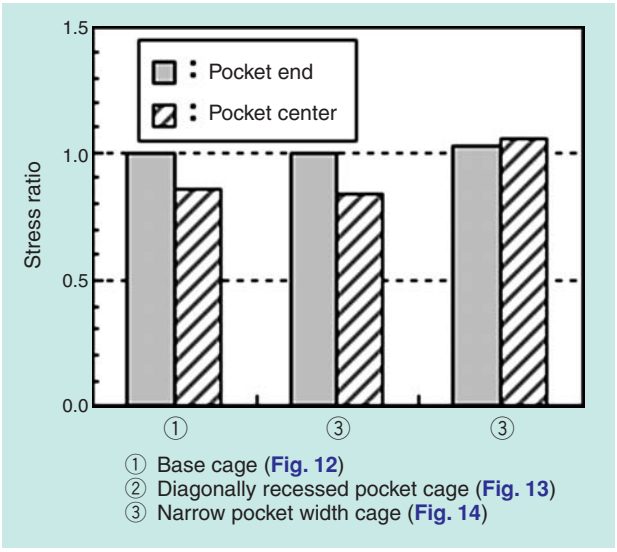

Fig. 20 Stress ratios of cages at pocket end and center using structure strength analysis

7. Conclusion

With the aim of reducing grease purge from a greased and sealed ball bearing, the behavior of grease adhering to the inner ring seal groove was studied. As a result an improved cage capable of reducing the leakage was designed and evaluated. The conclusions of this evaluation are as follows:

1) It was theorized that an increase in the internal temperature of a sealed bearing causes a pressure on grease located on the inner ring seal groove resulting in grease purge. It was also theorized that the adherence of grease to the inner ring seal groove is caused by (1) scratching off of grease adhering to the rolling element at the edge on the inner diameter side of the cage pocket, (2) migration of grease from there to the outer diameter part of the inner ring, and (3) pushing out of grease to the inner ring seal groove.
2) Changing the shape of the cage made it possible to suppress the adherence of grease to the inner ring seal groove. Any of the following changes will result in lowered grease purge: (1) it reduces the action of scratching off grease adhering to the rolling element by the edge on the inner diameter side of the cage pocket, thereby reducing the amount of accumulated grease, and (2) it increases the gap between the cage and the outer diameter of the inner ring.
3) Building a cage capable of suppressing the adherence of grease to the inner ring seal groove into the bearing improves the resistance to grease purge substantially.
4) Regarding the strength of the cage, the maximum stress of the narrow pocket width cage is 6% greater than that of a standard production cage. For this reason, it is necessary, before applying the improved cage, to conduct a cage strength evaluation under the operating condition to ensure that the cage has sufficient strength.

Previously grease purge had been addressed by means of improvements in the seal or an adjustment of the amount of sealed-in grease; however, the present study has made it clear that an improvement in the cage shape enables grease purge to be mitigated substantially.

Furthermore, since using the improved cage described above allows for higher grease fills, compared to a standard cage, improvements in life can be expected.

References

1) NTN, Ball and Roller Bearings Cat. No. 2202/E (1997).
2) S. Nozaki, M. Okasaka, Y. Kubota and S. Akabe, Trends in Automotive Instrument and Auxiliary Bearing Technologies, NTN Technical Review No. 65 (1996) 65-72.
3) N. Sato & Sakaguchi, The Influence of the Retainer Form on Grease Adhesion to the Inner Ring Seal Groove, Proceedings of Tribology Conference Tokyo, 2008-5 (2008) 135.
4) N. Sato, T. Sakaguchi and M. Kawamura, Development of a Corrugated Iron Retainer for Ball Bearings that Prevents Grease Leakage, Proceedings of Tribology Conference Nagoya, 2008-9 (2008) 323.
5) T. Sakaguchi and Y. Akamatsu, Simulation for Ball Bearing Vibration, Proc. Int. Trib. Cont., Nagasaki 2000, 3 (2000) 1795.

Photo of authors

Norihide SATO
Elemental Technology
R&D Center

Tomoya SAKAGUCHI
Elemental Technology
R&D Center

NTN-SNR High Performance Oil-lubricated Plummer Blocks SNOE Ⅱ

Ulrich GIMPEL*
Martin SOMMER*
Jens ULBRICH*

Oil-lubricated plummer blocks are used for large plant industrial machinery. **NTN-SNR** has developed the new SNOE Ⅱ series of plummer blocks. Compared to the previous SNOE plummer blocks, these were redesigned with greater housing rigidity and a labyrinth sealing system, and they have improved performance and reliability.

1. Introduction

Oil-lubricated plummer blocks are used extensively in plant-related facilities using industrial machinery. For example, plummer blocks are used in air blowers for ventilation or drying installed in steel and petrochemical plants and thermal power stations or in crushers in mining facilities as shown in **Fig. 1**. Plummer blocks used in these facilities must meet the requirements of higher speed and shortened maintenance work to improve operational efficiency. They must meet the environmental requirement of preventing oil leakage while in use outdoors. In response to these requirements, we have modified existing oil-lubricated plummer blocks (SNOE series) and developed the SNOE Ⅱ series products which are superior in terms of functionality and reliability while being designed to use common parts.

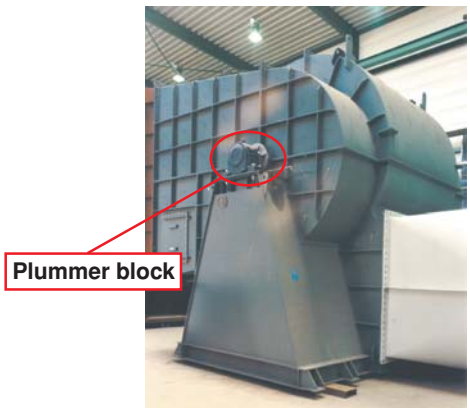

Fig. 1 Application example of oil-lubricated plummer block (large size air blower)

2. Oil-lubricated Plummer Block SNOE II

2.1. Construction

Fig. 2 shows the construction of the newly developed product. This product consists of a two-part housing using a series 222 or 223 self-aligning roller bearing (cylindrical hole). To lubricate the system efficiently, this product is mounted with the splash ring hanging from the slinger on the axis side; the ring

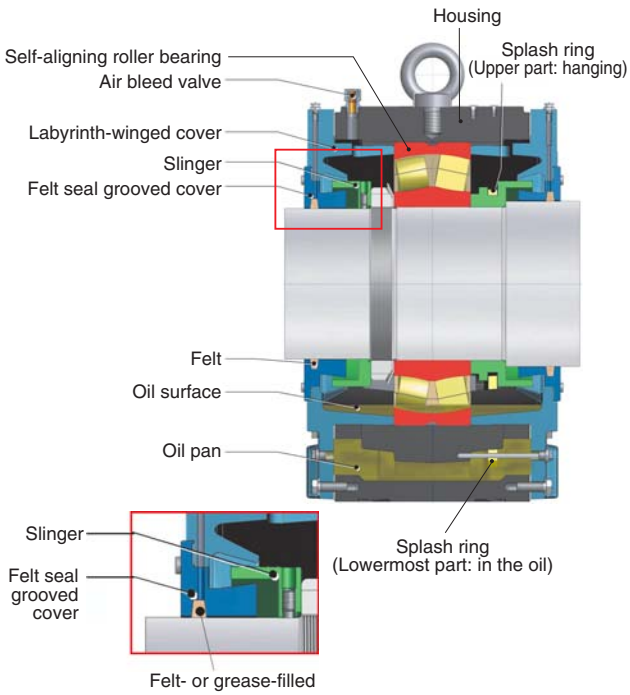

Fig. 2 Oil-lubricated plummer block SNOE Ⅱ (fixed side)

*SNR Wälzlager GmbH Engineering Bielefeld

feeds lubricant from the oil pan to the bearing during operation.

The product adopts the optimum labyrinth construction, using a felt seal compatible with high speed rotation. The housing must be supported securely to allow the bearing inside to rotate stably under severe environmental and load conditions. Installing the product on a common machine, two plummer blocks made up of the fixed side and the free side bearing are used. In particular, in response to the large axial displacement of a large-sized facility in operation, the housing of the plummer block used on the free side is designed to accommodate a large displacement of the bearing.

2.2 Functions

2.2.1 Lubrication

The self-aligning roller bearing inside the housing is lubricated with the oil stored in the lower part of the housing. In addition to ordinary oil-bath lubrication, lubricant is fed into the bearing by the splash ring, placed off-center with the axis, in the groove provided on the labyrinth spacer as shown in **Fig. 3**. In other words, the splash ring rotating with the shaft draws up lubricant from the ring immersed in the oil pan in the lower part of the housing, splashing the lubricant to the upper part of the bearing.

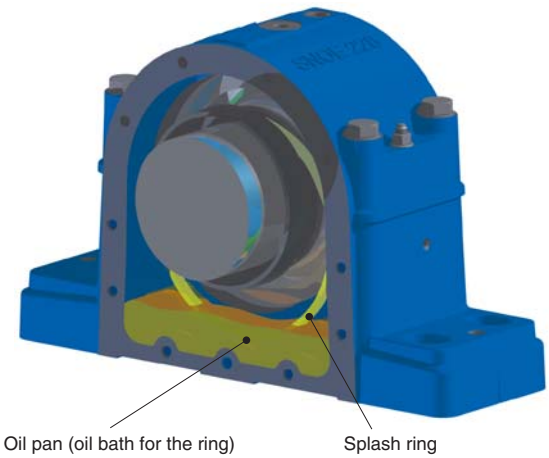

Fig. 3 Location oil pick up ring

2.2.2 Sealing performance

This product is provided with a non-contact labyrinth seal on both sides of the bearing. By optimizing the design of the labyrinth ring (labyrinth spacer) on the rotating side and the labyrinth ring (cover with labyrinth) on the fixed side, the lubricant splashed onto the bearing is collected reliably to the oil pan inside the housing without leaking out of the plummer block.

The felt seal grooved cover shown in **Fig. 2**, added to the labyrinth seal, enables one to add felt depending on the surrounding environmental conditions such as the shaft rotational speed, temperature, humidity, and presence of dust. Furthermore, with this cover provided with a hole to feed grease to the felt seal groove, the grease seal scheme (grease-filled) may be adopted.

2.3 Features of plummer block SNOE Ⅱ

2.3.1 Housing material

As shown in **Table 1**, gray cast iron (EN-GJL-250 (DIN GG25; JIS FC250)) characterized by large attenuation was used as SNOE housing material in the past.

In response to the recent increase in load and speed, however, nodular graphite cast iron (EN-GJS-600-3 (DIN GGG60; JIS FCD600) that excels in shock resistance and vibration characteristics is adopted.

Table 1 Specification of ductile materials

		Existing material	Material used in the newly developed product
EN standard		GJL-250	GJS-600-3
DIN		GG25	GGG60
JIS		FC250	FCD600
Tensile strength	N/mm^2	250	600
Young's modulus	N/mm^2	103,000	174,000
Hardness (HB 30)	—	180 - 250	190 - 270

2.3.2 Optimum design of the housing body

In order to minimize the effect on the strength of plummer blocks and on the bearing and bearing fitting face, the rigidity was increased without changing the outside dimensions and the tying method for the two-part housing, as shown in **Fig. 4**. In addition, the housing was designed, while considering the heat dissipation of the bearing while rotating, to improve lubrication and the bearing life.

The features of optimized housing design are shown below.

(1) Two-part housing clamping section
(2) Bearing fitting face
(3) Housing
(4) Fastening bolt area

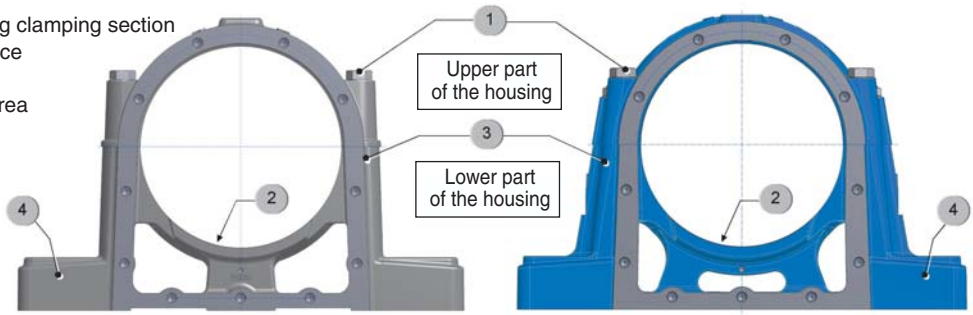

Existing product: SNOE　　**Newly developed product: SNOE Ⅱ**

Fig.4 Design of housings

(Features)

- **Adoption of the two-pillar construction system in the bearing support in the lower part of the housing**
- **Reinforcement between clamping bolts over the part from the lower part to the upper part of the housing**
- **Reinforcement of areas surrounding mounting bolts**
- **Change in the distance between the clamping bolts (both ends)**
- **Improvement of heat dissipation from the clamping face**

(1) Pillar construction

In changing over from the conventional product to the one with two pillars, the construction was designed to maintain the volume of the oil pan. The finite element analysis method (FEM) shown in **Fig. 5** was used to determine the pillar installation angle at which the deformation of the bearing fitting face is minimized.

As shown in **Fig. 6,** it was confirmed that the deformation of the bearing fitting face is smaller at the pillar angle of 25 degrees. The analysis of deformation in the upper and the lower part of the housing under this condition was conducted as shown in **Figs. 7** and **8**.

(2) Construction of the area around the clamping of the two-part housing

The two-part housing of the newly developed product is provided with a reinforcement rib between the fastening bolts shown in **Fig. 9** for improved rigidity. The upper and the lower housing are held by the tapered securing pins to provide accurate positioning in maintenance and inspection.

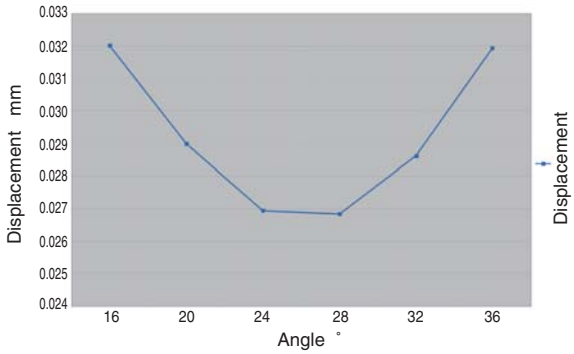

Fig. 6 Relationship between rib angle and deformation of fitting area

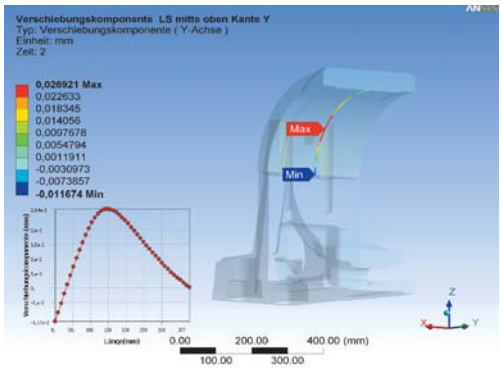

Fig. 7 Deformation of bearing fitting area (upper part)

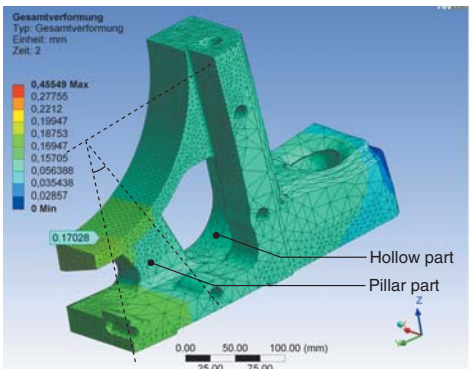

Fig. 5 FEM-analysis model

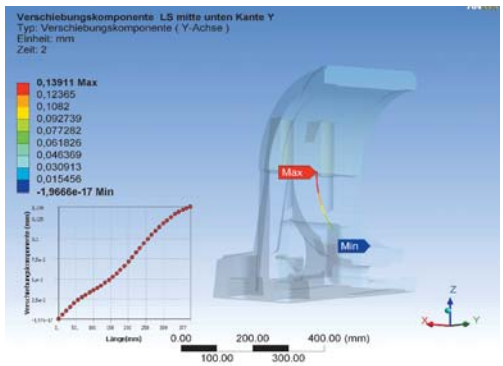

Fig. 8 Deformation of bearing fitting area (bottom part)

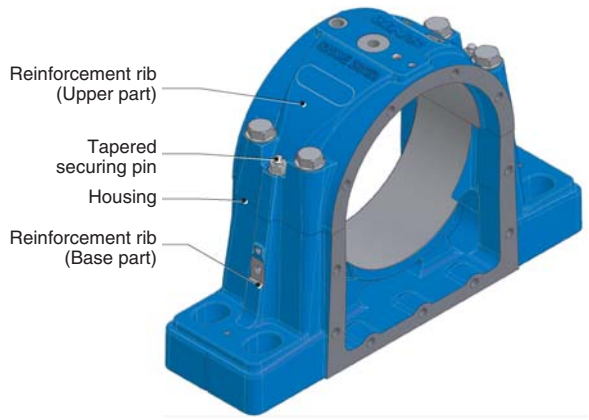

Fig. 9 Fastened area of sprit type housing

(3) Position of clamping bolts

The clamping bolts fastening the upper and the lower housing are placed closer to each other on each side, as shown in **Fig. 10**, to prevent them from separating from each other and to suppress the shift of the bearing fitting surfaces (sections).

(4) Housing fastening face

As shown in **Fig. 11**, the ground contact face of the housing is stabilized against load by not providing the boring in the lower part of the bearing fitting part, with the heat from the bearing being radiated sufficiently.

The area surrounding the spot at which fastening bolts are connected is kept solid to allow the tension due to bolt clamping to be absorbed; this contributes to suppressing the effect on the deformation of the housing as a whole.

(5) Other examples of fastening

Installing sensors capturing vibration, temperature, and other physical quantities on this housing makes it possible to control the rotational state of plummer blocks. For this reason, holes for placing a sensor are provided in different parts of the housing. The oil level of the lubricant can be checked constantly with an oil gauge.

When a high temperature is expected during operation, installing a cooling pipe in the oil pan space as shown in **Fig. 12** allows heat to be removed from the oil and transferred to the heat exchanger installed outdoors.

On the other hand, when the bearing is used in a cold region, preheating the lubricant is necessary before starting machines; for this purpose, consideration has been given to installing a heater and a thermostat as shown in **Fig. 13**.

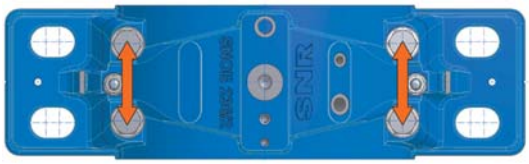

Fig. 10 Position of fastened bolts

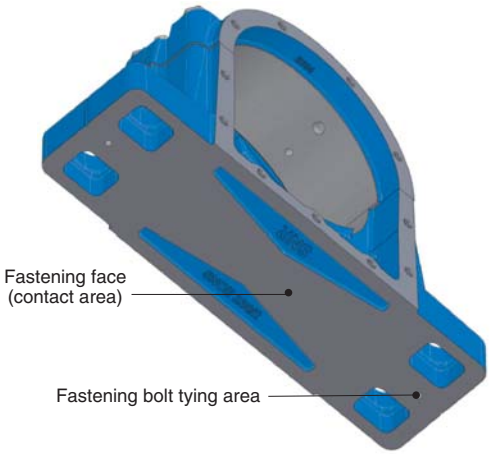

Fig. 11 Contact area of housing

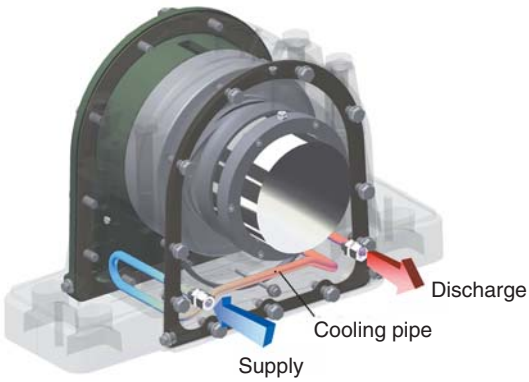

Fig. 12 Housing with integrated cooling pipe

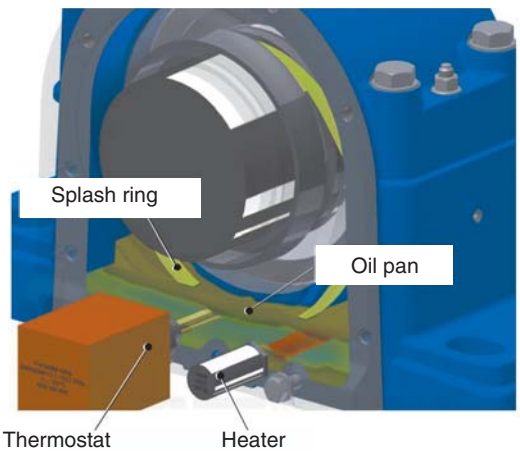

Fig. 13 Preheating device of lubricant oil

2.3.3 Seal construction

The labyrinth seal is used as a common seal construction of plummer blocks. With the existing SNOE series product, the free side and the fixed side labyrinth alike are designed so that each cover (both through and non-through (for use at the shaft end)) may meet individual customer specifications. To address this situation, a unified design specification was used for labyrinths while accounting for different processing methods to reduce the number of parts and simplify specifications.

In SNOE Ⅱ series products, as shown in **Fig. 14**, the slinger and felt seal grooved cover for the fixed side and those for the free side, to be used in combination with the labyrinth winged cover for the fixed side bearing and the one for the free side bearing, are constructed in the same design.

This measure eliminated the necessity of substantial design changes to address special applications (reinforcement of sealing performance such as grease seal and resistance to desert environments).

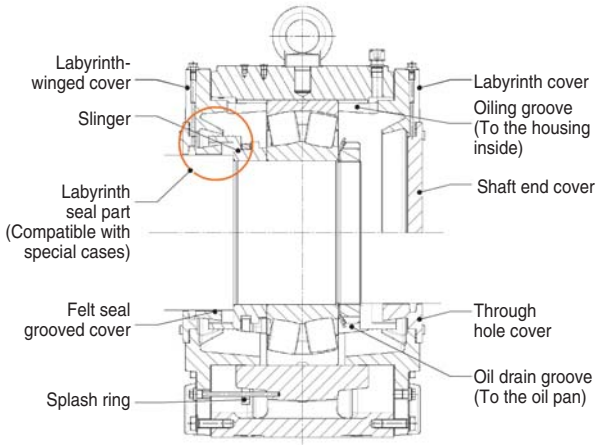

Fig. 14 Labyrinth sealing design of SNOE Ⅱ (fixed side)

(1) Labyrinth seal function of the fixed side bearing

Fig. 15 shows the construction of the labyrinth. Lubricant is splashed, inside the housing, from the oil pan (3) by the splash ring to lubricate the upper part of the bearing. At the same time, lubricant attaches to the inclined surface of the labyrinth winged cover (1) or the outside diameter face (4) of the slinger (2) and is collected into the oil pan (3).

When splashed lubricant does not fall onto the lower part of the housing but flows into the labyrinth inside (the area around the inside diameter of the labyrinth winged cover (5)), lubricant attaches to the felt grooved cover (6) and is then collected via the route from the opening (7) of the lower part of the labyrinth winged cover to the oil pan (3).

When lubricant further penetrates into the labyrinth (8), it is returned from the labyrinth (8) due to the conical form of the slinger outside diameter part of the felt seal grooved cover (6), being collected via the path from the opening (7) of the lower part of the labyrinth winged cover to the oil pan (3).

Besides the action of the labyrinth seal function, providing a felt seal in the felt groove enables lubricant outflow to be prevented more efficiently.

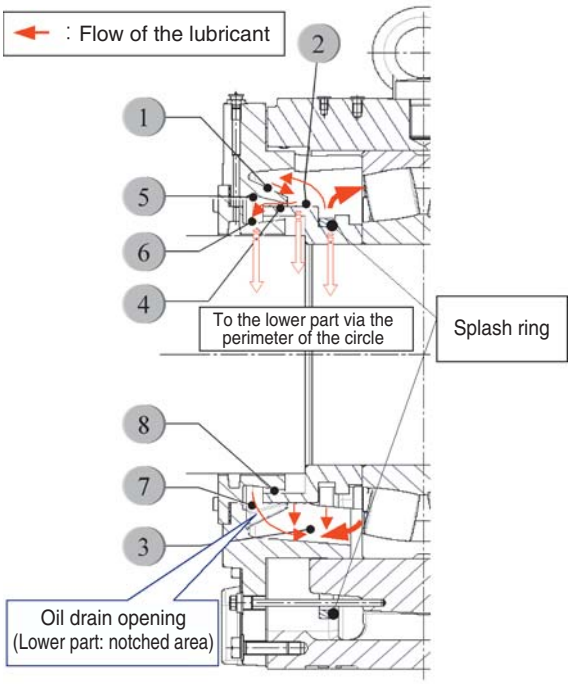

Fig. 15 Labyrinth sealing design of fixed side

(2) Labyrinth seal function of the free side bearing

As shown in **Fig. 16**, the construction of the labyrinth on the free side is basically identical to that on the fixed side. However, when the axial displacement (distance) of the bearing is the greatest with reference to the labyrinth winged cover, the labyrinth passage is secured, though the slinger position becomes shallow. On the other hand, the slinger position is determined so as to avoid the interference of the slinger with the labyrinth cover should the slinger position become the least remote; this assures the function of the labyrinth seal adequately.

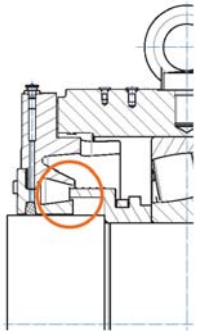

Fig. 16 Labyrinth sealing design of floating side

2.4 Evaluation

Since the sealing performance is referred to as an important function of an oil-lubricated plummer block in an operating facility, the oil leakage evaluation test was conducted.

(1) Test conditions

Table 2 shows typical test conditions for evaluating the sealing performance of a labyrinth seal. This evaluation was not applied to the felt seal and grease, but the gap between the shaft and the felt seal grooved cover (the exit from the labyrinth) was monitored continuously as shown in **Fig. 17**.

Table 2 Test condition of lubricant leak (example)

Basic scheme of a plummer block	**SNOE Ⅱ 218**	
Type of bearing used (self-aligning roller bearing)	22218 (ϕ90×ϕ160×40)	
Test atmosphere temperature	20˚C (RT)	
Lubricant viscosity	40 mm^2/s	
Bearing rotational speed	3,000 min^{-1} (max)	
Shaft inclination (misalignment)	0˚	0.25˚
Test duration	Four hours for each test item	
Criteria	Visual inspection; measurement of the oil level (oil gauge)	

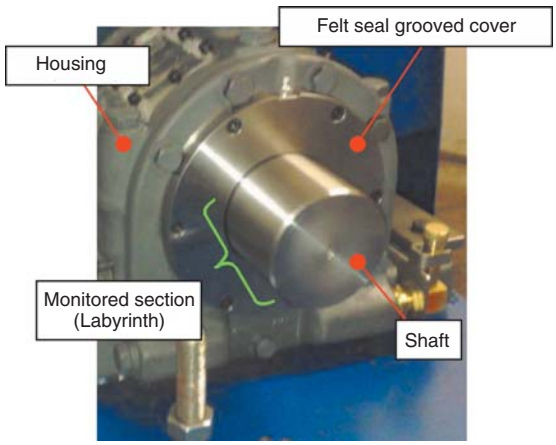

Fig. 17 Test plummer block (monitoring oil leak)

(2) Test results

As shown in **Fig. 18** no oil leakage was observed in all of the tests, and abnormalities in the bearing and interference in the labyrinth were not observed, with these satisfactory results proving high sealing performance.

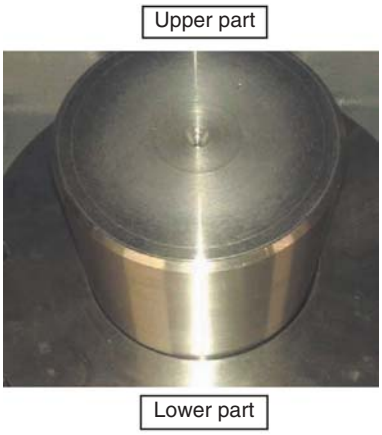

Fig. 18 Gap area after lubricant leak test (no leakage)

3. Conclusion

This paper introduces **NTN-SNR** oil-lubricated plummer blocks.

In addition to addressing an increase in efficiency arising from the improvement of performance of industrial plant facilities and from the reduction in maintenance work, the authors will give constant consideration to the environment under severe working conditions such as the outdoor environment and push ahead with a further improvement in performance.

Photo of authors


Ulrich GIMPEL
NTN Wälzlager GmbH
Engineering Bielefeld


Martin SOMMER
NTN Wälzlager GmbH
Engineering Bielefeld


Jens ULBRICH
NTN Wälzlager GmbH
Engineering Bielefeld

Development of Oil-impregnated Sintered Bearing of Low Wear and Corrosion Resistance

Kazuhiro KIMURA*

Recently, oil-impregnated sintered bearings, which are slipping bearings, are used for a variety of applications because their steady sliding performance can be demonstrated over a long period of time without adding oil.

In this text, we added manganese sulphide (MnS) as a solid lubricant because MnS has sliding characteristics equal to oil-impregnated sintered bearings made of steel, and we introduce an oil-impregnated sintered bearing made of stainless steel that has excellent resistance to corrosion.

1. Introduction

Generally speaking, sintered oil-retaining bearings made of bronze or iron as a base material often use graphite (C) or molybdenum disulfide (MoS_2) as solid lubricant [1]. However, bronze- and iron-based materials were found inferior in corrosion resistance in special environments (in a gasoline atmosphere, for example) causing deterioration of sliding performance.

To solve this problem, we have developed, jointly with the Nagoya Municipal Industrial Research Institute, stainless steel sintered oil-retaining bearings, made of austenite-based stainless steel which are excellent in corrosion resistance. They have a sliding characteristic equivalent to that of iron-based sintered oil-retaining bearings as a result of the selection and quality of an adequate solid lubricant.

This paper presents the materials, basic characteristics, and performance of the newly developed product.

2. Materials of the newly developed product

For bearings using stainless steel as the base metal to achieve an excellent sliding characteristic, the selection of a solid lubricant plays an important role. The solid lubricants selected to evaluate the base metal and their sliding characteristic were bismuth (Bi), boron nitride (BN), graphite (C), molybdenum disulfide (MoS_2), antimony (Sb), and manganese sulfide (MnS). **Table 1** shows how the solid lubricants react with the base metal under heated conditions.

Solid lubricants are required not to react below the sintering temperature (1,200˚C) of the base metal. However, C, MoS_2, and Sb produce compounds under this condition which tend to exhibit increased hardness; for this reason, C, MoS_2, and Sb cannot be used as solid lubricants for sintered bearings.

Bi, BN, and MnS do not produce reactants below 1,200˚C, the sintering temperature of stainless steel, and the wear and friction tests showed that MnS exhibits the best sliding characteristic; for this reason, manganese sulfide (MnS) was selected as the solid lubricant. **Fig. 1** shows an enlarged picture of manganese sulfide (MnS) powder.

Table 1 Reaction by temperature with stainless steel

Solid lubricant	Temperature	Reaction
Graphite (C)	1100	Deposition of $(Cr, Fe)_7C_3$
	1200	Fusion
Molybdenum disulfide (MoS_2)	800	Production of compounds after decomposition
Antimony (Sb)	700	Production of compounds
Bismuth (Bi)	1200	No reaction
Boron nitride (BN)		
Manganese sulfide (MnS)		

***NTN** Powder Metal Corp. Engineering Dept.

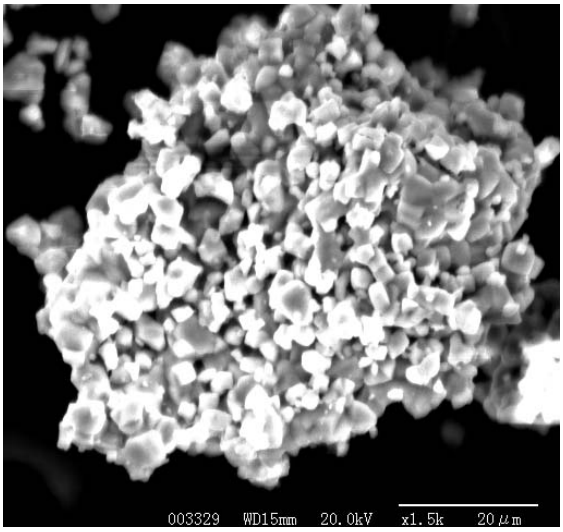

Fig. 1 Manganese sulfide (MnS)

3. Basic characteristics of the newly developed product

3.1 Features of the newly developed product <Features>

(1) The newly developed product excels in seizure resistance and wear resistance as a result of using manganese sulfide (MnS) as solid lubricant;
(2) It excels in corrosion resistance because manganese sulfide (MnS) does not hinder the formation of passive state membrane by chromium oxide in stainless steel; and
(3) Its sliding characteristics excel even in special environments (gasoline atmosphere).

3.2 Corrosion resistance

Table 2 shows the chemical composition of the newly developed product. Its base metal is austenite-based stainless steel, a material excellent in corrosion resistance.

A humidity cabinet test was conducted to ascertain the corrosion resistance of the newly developed product and iron-based sintered bearings.

(Test method)

The newly developed product and iron-based sintered bearings were left alone in a thermostatic bath for 200 hours under the following conditions to observe how rust occurred:

Table 2 Chemical composition

Chemical composition (%)				
Fe	Cr	Ni	MnS	Others
Residue	15–20	10–15	1–3	1 or less

• Temperature: 50±5˚C
• Humidity: 95±5%RH
• No protective layer of lubrication

Fig. 2 shows the appearance of the bearing after the test.

Rust was observed on the surface of the iron-based sintered bearings 24 hours after the start of the test, while it was not observed on the surface of the newly developed product 200 hours after the start of the test.

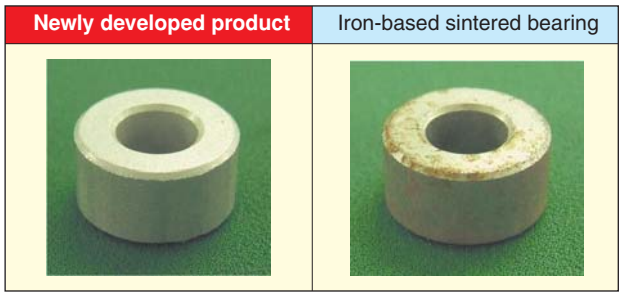

Fig. 2 Result of humidity cabinet test

3.3 Evaluation of corrosion resistance in a special environment

Excellent corrosion resistance is required of fuel pump bearings as they are used in gasoline or bio-fuel, which have been found to be highly corrosive when used around past products.

For this reason, bronze-based bearings, widely used as sintered oil-retaining bearings, and the newly developed product, both without a protect oil coating, were immersed in a sulfur-containing solution for comparison.

(Test method)

• Solution: Liquid mixture of regular gasoline, ethanol, and sulfur
• Solution temperature: 60˚C
• Test duration: 100 h
• Bearing size: Inside diameter: 6 mm; outside diameter: 12 mm; width of 6 mm

Fig. 3 shows the appearance after the test and **Fig. 4** the change in dimensions due to corrosion.

After the test, discoloration was observed on the bronze-based sintered bearings, and the inside diameter, outside diameter, and width all showed changes of at least 0.1 mm, evidence of corrosion. By contrast, the newly developed product showed no change in appearance, with change in dimension being one-tenth or less than that found in bronze-based bearings.

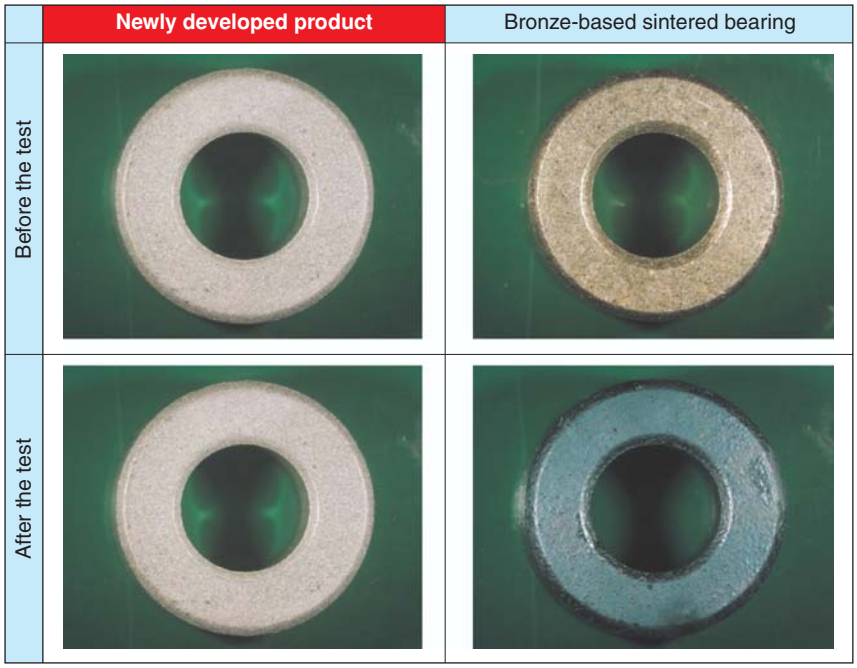

Fig. 3 Result of corrosion test

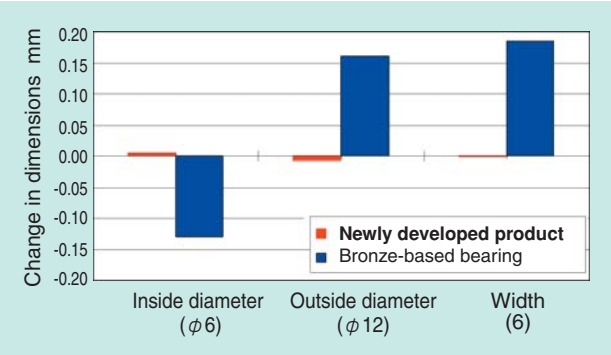

Fig. 4 Dimensional change of after test

3.4 Evaluation of the corrosion resistance of solid lubricant, manganese sulfide (MnS)

The humidity cabinet test was conducted to see how sulfur-containing manganese sulfide (MnS) affects the base metal, stainless steel, when the newly developed product undergoes corrosion positively.

(Test method)
- Temperature: 60˚C
- Humidity: 90%Rh
- Test duration: Observation was conducted at intervals of 168 hours, and the test was to be ended when a change was observed on the surface.

After 1,176 hours of testing, the surface of the newly developed product exhibited discoloration. The test was ended in order to perform SEM/EDX-EPMA analysis on the areas of the part showing the most discoloration. **Fig. 5** shows the surface state and **Fig. 6** the result of analysis.

The manganese sulfide (MnS) surface is blackened by oxidation, while the stainless steel surface near the manganese sulfide (MnS) area does not exhibit changes. The results of the analysis before and after the test show that oxygen (O), which was not observed in the sample before the test, was detected in the sample after the test. Also, a slight amount of oxygen (O) was observed on the surface of manganese sulfide (MnS). That being said, the stainless steel surface exhibited no change, which shows that manganese sulfide (MnS) did not affect the corrosion resistance of the base metal.

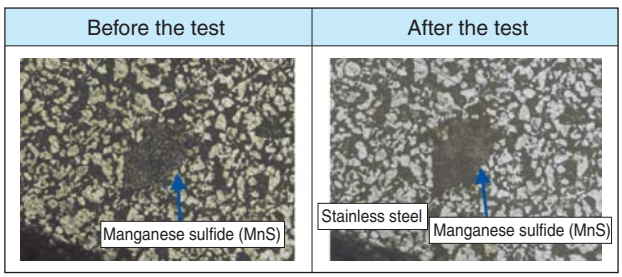

Fig. 5 Surface before and after corrosion test

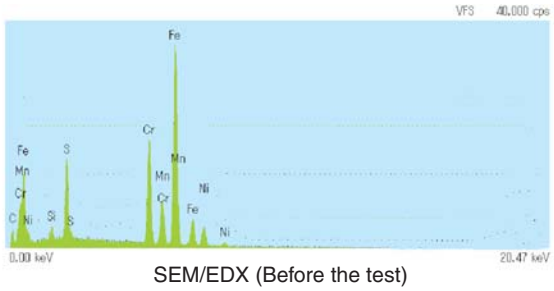

SEM/EDX (Before the test)

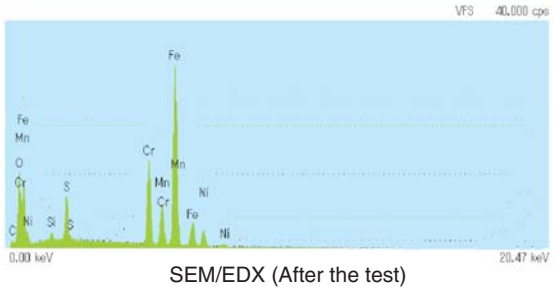

SEM/EDX (After the test)

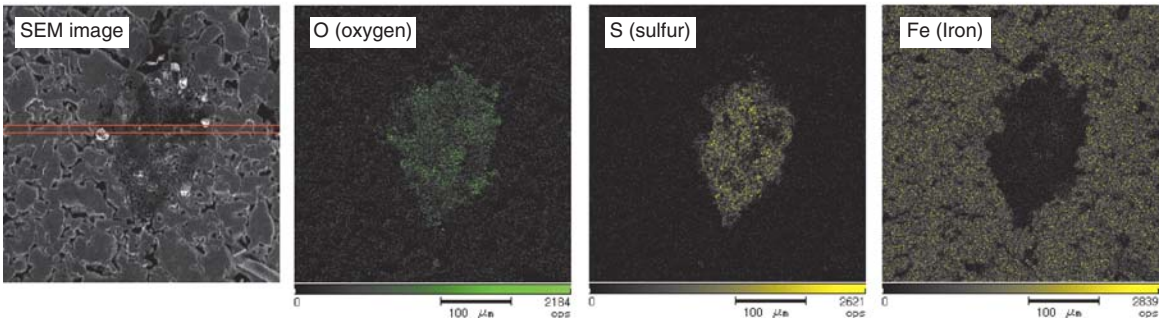

SEM/EPMA (After the test)

Fig. 6 Analysis result

3.5 Sliding performance of the stainless steel sintered bearing

To compare the coefficient of friction between the newly developed product and the iron-based sintered bearing, the testing machine shown in **Fig. 7** was used to measure the coefficient of friction. **Table 3** shows the physical property values of the newly developed product and iron-based sintered bearing.

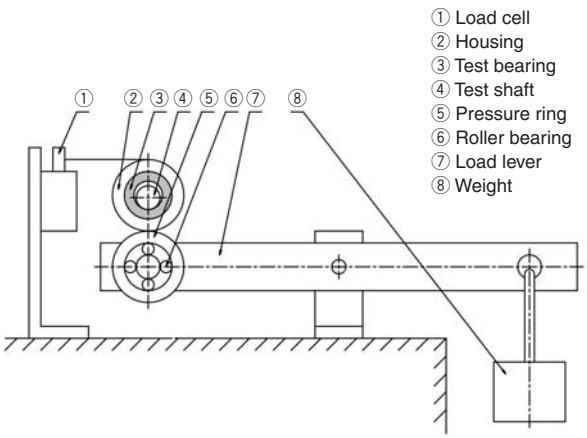

Fig. 7 Test rig

Table 3 Basic characteristics

	Density g/cm^3	Pressure ring strength MPa	Surface hardness HRF	Oil content Vol.%
Newly developed product	6.5–7.0	150 or more	70 or more	8 or more
Iron-based sintered bearing	5.9–6.3	200 or more	40 or more	18 or more

※Physical property values are typical ones.

(Test method)

- Peripheral speed (V): 37.7 m/min
- Contact pressure (P): 0.2–1.5 MPa
- Lubricant: Mineral oil
- Atmosphere: Room temperature

* With the peripheral speed kept constant, the PV value was varied by varying the contact pressure.

Fig. 8 shows the relationship between the PV value and the coefficient of friction. Both materials show their coefficients of friction at about 0.1, which is about the same as that of an iron-based sintered bearing.

Fig. 9 shows the initial adaptive characteristic at a peripheral speed of 37.7 m/min and a contact pressure of 1.0 MPa and the change in the coefficient of friction over a 500-hour period of time.

Like iron-based sintered bearings, the newly developed product exhibits a high coefficient of friction immediately after the start of the test, but the value of the coefficient of friction begins to decrease gradually and shows about the same value as that of iron-based sintered bearings at the end.

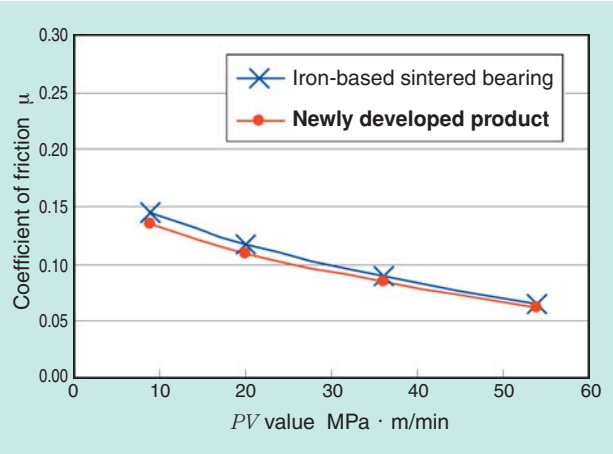

Fig. 8 Comparison of frictional properties

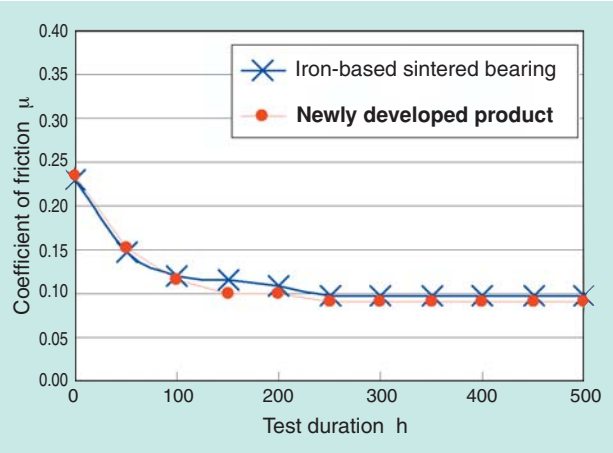

Fig. 9 Measurement result of frictional properties

4. Points to notice in using stainless steel sintered bearings

In sintered bearings, generally speaking, lubricant retained in the bearing by means of impregnation seeps to the bearing surface to form oil film with the effect of preventing the contact between the shaft and bearing surfaces. For this reason, the presence of lubricant is indispensable to maintaining a good sliding characteristic; the same characteristic is true of the newly developed product[2]. Accordingly, the sliding performance deteriorates remarkably without lubrication or under high temperature conditions in which the lubricant cannot perform its role sufficiently. A solid lubricant (MnS) works to prevent abnormal friction, however, since there is a danger that the lubricant will lead to abnormal heating of the sliding part and abnormal wearing of the shaft and bearings, it is necessary to select a lubricant compatible with the temperature of the atmosphere.

5. Conclusion

A new sintered oil-retaining bearing with excellent corrosion resistance and low friction has been developed by means of adopting stainless steel as the base metal and manganese sulfide (MnS) as the solid lubricant. The newly developed product has a sliding characteristic equivalent to that of a conventional iron-based sintered bearing, with its corrosion resistance improved substantially. The result of this development work will contribute to further lengthening of the service life of sintered bearings under special environments.

References

1) Teruhisa Watanabe , Powder Metallurgy New Edition, Gijutsu Shoin, 65, 1995.
2) Teruhisa Watanabe, Powder Metallurgy New Edition, Gijutsu Shoin, 63, 1995.

Photo of author

Kazuhiro KIMURA
NTN Powder Metal Corp.
Engineering Dept.

Fluid Dynamic Bearing Unit for the Home Ventilation Fan

Masaharu HORI*

As a rule, the installation of the ventilation equipment has come to be required for all buildings that have rooms where people live since the revision of the Building Standard Law. Therefore, the demand for home ventilation fans has increased for ordinary families and the demand for high reliability and low noise for home ventilation fans has also increased.

NTN has developed a fluid dynamic bearing unit with excellent reliability and quietness that is easily used to replace rolling bearings. This fluid dynamic bearing unit can be applied not only for use in home ventilation fans, but also in other applications where rolling bearings are used and quietness is demanded.

This report introduces this fluid dynamic bearing unit for home ventilation fans.

1. Introduction

With the aim of reducing the room concentration of chemical substances causing sick house syndrome, the revised Building Standard Law took effect on July 1, 2003 that regulates building materials and ventilation facilities used in buildings.

This has made it obligatory, as a rule, to install mechanical ventilation facilities in all buildings because of emissions from furniture even if building materials do not diffuse formaldehyde.

Obligatory installation of ventilators in living rooms, bedrooms, and other rooms as a result of the law revision has increased the need for freedom from noise in particular, bringing about requests of replacing roller bearings with sliding bearings. In response to these requests, we have developed a fluid dynamic bearing that has the same dimension as that of a roller bearing and that can replace it easily; the new bearing is presented below.

2. Construction and features of the new bearing

Currently, roller bearing 695 (a deep-grooved ball bearing with dimensions of $\phi 5 \times \phi 13 \times 4$ mm) is used mainly, and the major dimensions of the newly developed product was adapted to those of bearing 695 as shown in **Fig. 2.**

In addition, in response to the strong request of a ventilator manufacturer having production lines using roller bearings, we decided to develop a new product that can be handled in a similar way as current roller bearings.

Fig. 1 shows how the rotor and the fluid dynamic bearing are assembled and **Fig. 2** the bearing as a unit. With the aim of reducing costs, we adopted mold-produced products in all component parts of a fluid dynamic bearing. Press-machined products were adopted in both of two housings and sintered oil-retaining bearings were used for the rotating bodies.

Two housings are fastened by means of bonding as shown in **Fig. 2**; forming the cross-section of each of the two housings in an L shape enlarged the overlapping of the bonded parts of the housings, resulting in increased joint strength.

Figs. 3 and **4** show the shapes of fluid dynamic grooves.

The thrust grooves were provided on the inside end surface of both housings. The radial grooves were provided on the outside diameter surface of the rotating body.

The oil membrane formed by these fluid dynamic grooves supports the rotating body in perfect non-contact state in both radial and thrust directions.

*Fluid Dynamic Bearing Unit Division Engineering Dept.

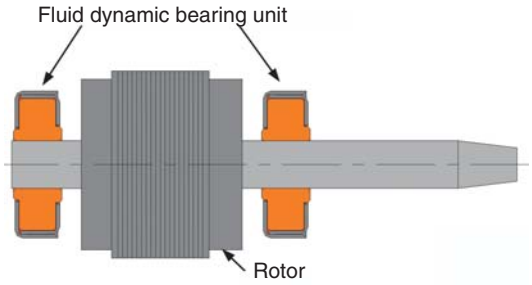

Fig. 1 Schematic layout of rotor and fluid dynamic bearing unit

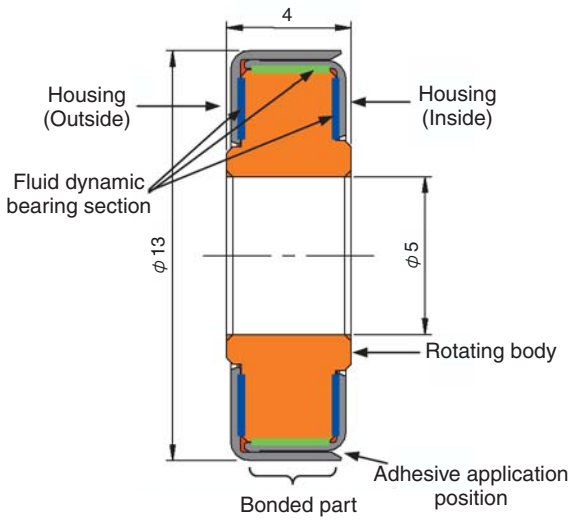

Fig. 2 Cross-section shape of fluid dynamic bearing unit

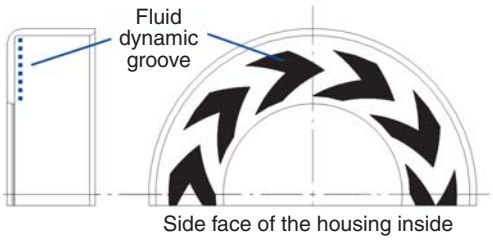

Fig. 3 Thrust groove

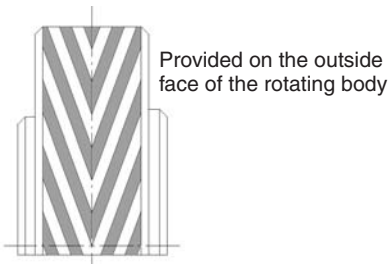

Fig. 4 Radial groove

2.1 Method of processing thrust grooves

The housing was a stamped product, and incorporating the fluid dynamic groove processing into the stamping process prevented an increase in the total number of processes.

To fabricate groove processing molds, the mold design technology was used that had been cultivated in the production of fluid dynamic Bearphite, currently mass-produced for use in support bearings for hard disk drives (referred to as HDDs in the following). This allowed high-accuracy fluid dynamic grooves to be produced. **Fig. 5** shows the picture of the appearance of the thrust groove section.

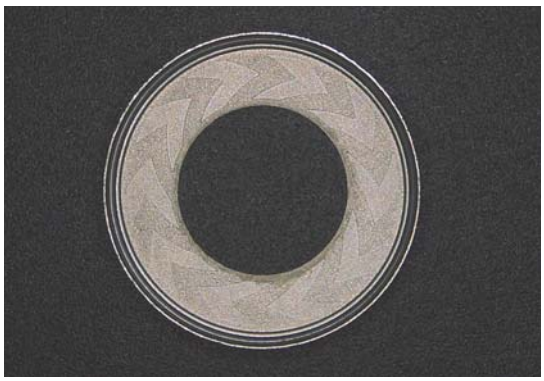

Fig. 5 Photo of thrust groove

2.2 Method of processing radial grooves

Unlike fluid dynamic Bearphite currently in mass production, radial grooves must be provided on the outside diameter surface of a rotating body; therefore, a groove processing method based on strong sizing, which is a conventional means of processing on the Bearphite inside diameter surface, cannot be adopted.

To solve this problem, the porosity of sintered oil-retaining bearings was used to adopt the component rolling scheme; this allowed satisfactory bearing surfaces to be obtained. **Fig. 6** shows the picture of the appearance.

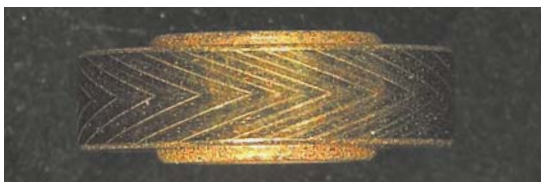

Fig. 6 Photo of radial groove

2.3 Assembling method

A method of assembling proven in mass-producing HDD-use fluid dynamic bearings was applied.

Three members were brought into intimate contact with one another first, and then one housing was moved by the distance equal to the axial gap, and adhesive was applied to the housing to bond and fasten other two housings, and after this, the bearing was impregnated with lubricant.

2.4 Load capacity

The rotating body weight of the actual device requires a radial load capacity in the horizontal condition of 1 N or more.

To meet this requirement, we calculated the load capacity using the program for analyzing the characteristics of a porous oil-retaining bearing unit developed by us to determine the bearing specification.

Table 1 shows the conditions for analysis and **Fig. 7** the results of analysis. As shown in **Fig. 7**, it was ascertained that a radial gap of 20 mm allows a load capacity of 1.44 N to be secured.

Table 1 Analysis condition

Rotational speed	2000 min^{-1}
Temperature of atmosphere	25˚C

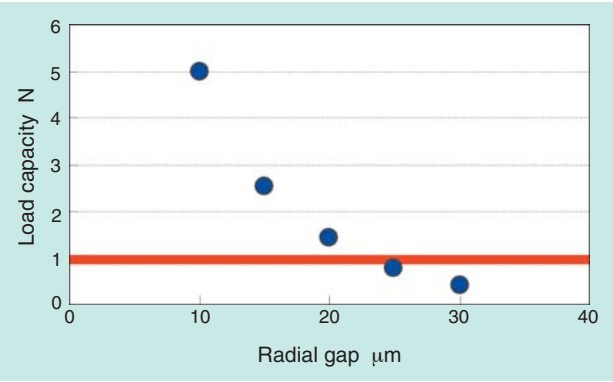

Fig. 7 Analysis result

3. Evaluation of performance

3.1 Working conditions of a ventilator bearing

Table 2 shows common functional requirements for ventilator bearings.

Since a fluid dynamic bearing rotates on oil film without coming into contact, the service life of a bearing depends on the evaporation of lubricant. The lubricant used this time is identical to the one used in mass-produced HDD fluid dynamic bearings, with an extremely low evaporation rate of less than 1 wt% at 80˚C after 50,000 hours in service.

It is ascertained experimentally that the evaporation speed roughly doubles due to a temperature rise of 10˚C. Accordingly, the service life of the bearing extends over 22 years when converted into the working condition of a ventilator (60˚C), satisfying the service life requirement of 15 years shown in **Table 2**. The durability is being tested on an actual device described in subsection 3.5.

Table 2 Functional requirements

Service life	15 years
Ambient temperature	-10–60˚C
Ambient humidity	0–100%
Rotational speed	2000 min^{-1}

3.2 Oil membrane formation test

To make sure that oil membrane is formed during operation, the **NTN** fluid dynamic bearing test unit shown in **Fig. 8** was used to measure the oil membrane formation rate.

1) Evaluation conditions

- Test machine: **NTN**-made fluid dynamic bearing unit test machine
- Measuring item: Oil membrane formation rate; torque
- Rotational speed: 2,000 min^{-1}
- Lubricant: Lubricant for fluid dynamic bearing unit (Used in mass production of HDD fluid dynamic bearings)
- The oil membrane formation rate is measured by means of the electric conduction between the main shaft and the housing.

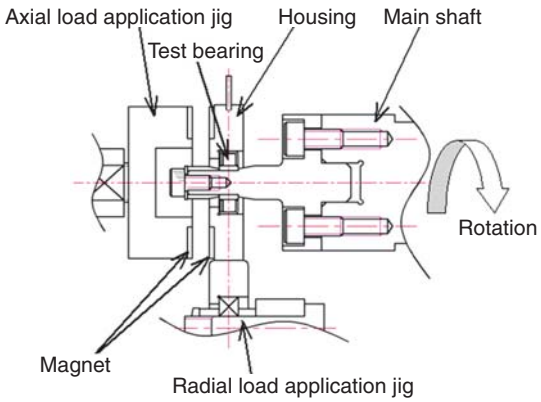

Fig. 8 Schematic view of test rig

2) Results of evaluation

Fig. 9 shows that the oil membrane formation rate reaches 100% at an early stage of rotation with oil membrane formed completely and that the bearing rotates without contact.

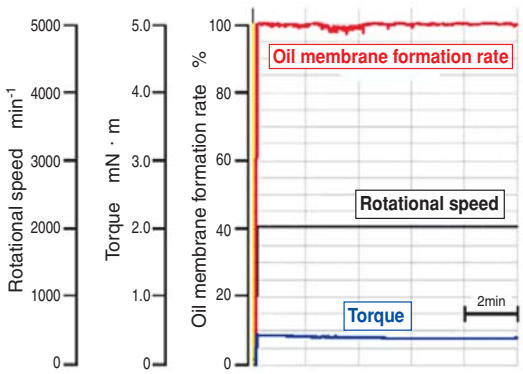

Fig. 9 Evaluation result of fluid dynamic bearing unit

3.3 Temperature characteristic test

The variation of rotational speed resulting from temperature variation was investigated.

1) Evaluation conditions

- Test machine: Motor installed on the actual device
- Applied voltage: AC 100 V
- Measuring item: Rotational speed
- Temperature of atmosphere: -10–60˚C
- Lubricant: Lubricant for fluid dynamic bearing unit

2) Results of evaluation

In a fluid dynamic bearing, as shown in **Fig. 10**, the increase in lubricant viscosity in the low temperature range causes the rotational speed to lower; however, the customer requirement of 2,000 min^{-1} was achieved.

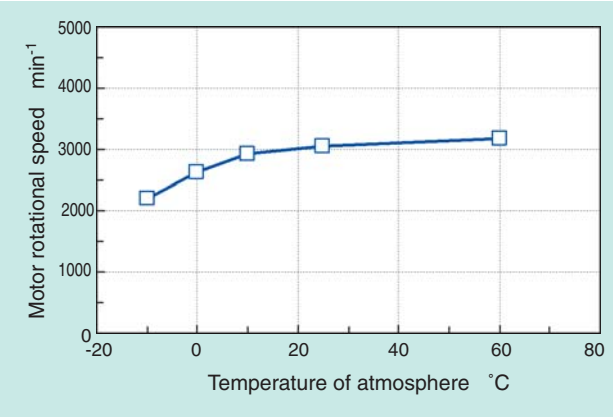

Fig. 10 Evaluation result as electric motor

3.4 Sound measurement on the actual device

Noise produced by the newly developed product was compared with that produced by roller bearings.

Fig. 11 shows the method of measuring noise. The method of measuring noise from a ventilator is specified by JIS (Noise test: JIS C9603); the measurement is conducted using the noise meter specified by JIS C1502 (normal noise meter).

For the reason of comparing noise between the roller bearing and the fluid dynamic bearing unit, the measurement was conducted with the fan removed and hence without the effect of wind noise. In addition, since noise values were small, the measurement was conducted with the distance to the microphone shortened to 100 mm, one tenth of the specified value.

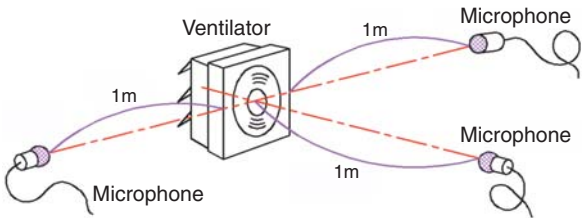

Fig. 11 Method of noise measurement

1) Measuring conditions

- Test machine: Motor installed on the actual device (not equipped with a fan)
- Rotational speed: About 3,000 min^{-1}

(Applied voltage: AC 100 V)

- Temperature of atmosphere: 25˚C
- Motor position: Shaft horizontal
- Lubricant: Lubricant for fluid dynamic bearing unit
- Distance to the microphone: 100 mm
- Measuring environment: Anechoic room (Ground noise: 13.5 dBA)

2) Results of evaluation

As shown in **Fig. 12,** the fluid dynamic bearing unit produces less noise than the current roller bearing.

The audible frequency range is commonly said to be from 20 Hz to 20 kHz, and the frequencies that are uncomfortable to human ears are said to be near 3 kHz. The fluid dynamic bearing exhibited lower values in the entire range of interest. A difference in noise value of 14.5 dBA shows that the fluid dynamic bearing produces about one fifth of the noise the current bearing does. Since the fluid dynamic bearing unit is driven without contact, the sound produced by the bearing is extremely small.

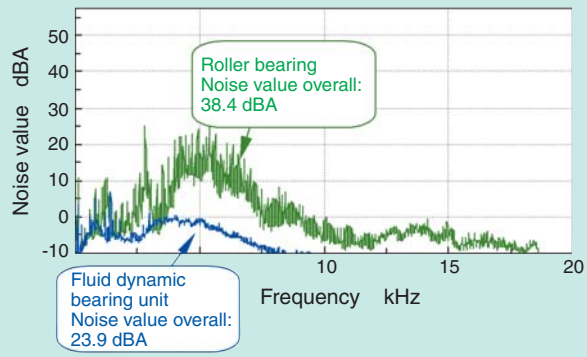

Fig. 12 Result of noise measurement

3.5 Endurance test on the actual device

An endurance test was conducted using the motor on the actual device. This test was conducted to make an evaluation at 80˚C in contrast to 60˚C, the upper limit of the required temperature of the atmosphere. Accordingly, this test is one with a four-time acceleration compared with the experimental result with a double evaporation rate for an increase in temperature of 10˚C, described in subsection 3.1.

1) Endurance test conditions

- Test machine: Motor installed on the actual device (not equipped with a fan)
- Rotational speed: About 3,000 min^{-1} (Applied voltage: AC 100 V)
- Temperature of atmosphere: 80˚C

• Motor position: Shaft horizontal
• Lubricant: Lubricant for fluid dynamic bearing unit

2) Results of evaluation

As shown in **Figs. 13** and **14**, both the rotational speed and the vibration value do not exhibit significant changes after 1,000 hours in operation, showing a satisfactory result. The test will continue for two years to check functional aspects and to determine the evaporation of the lubricant on the basis of the decrease in the weight.

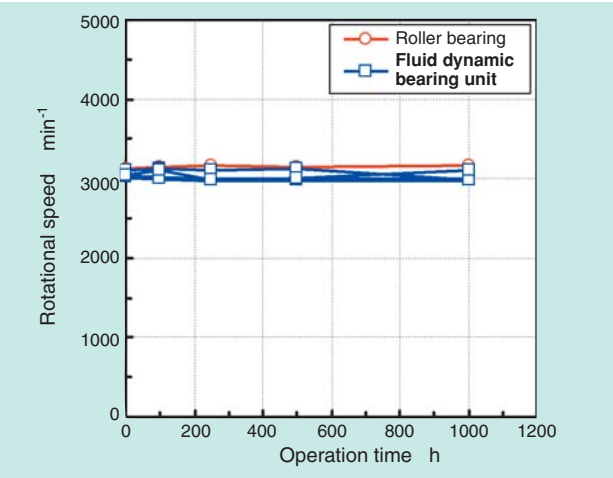

Fig. 13 Result of rotational stability

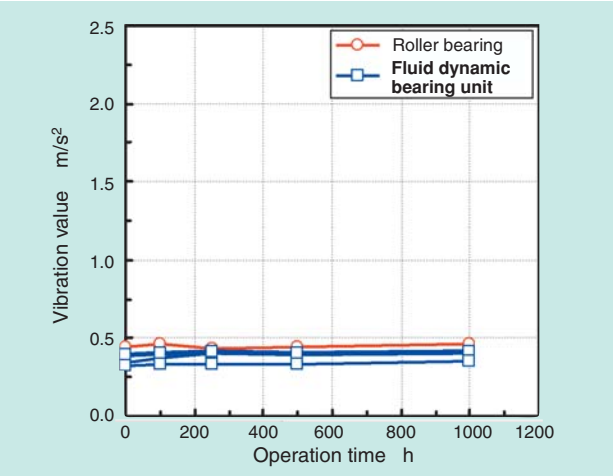

Fig. 14 Result of vibration stability (Radial direction)

3.6 Hydrolysis test on lubricant

Unlike HDDs, ventilators are expected to be used in high-humidity environments. In consideration of these circumstances, a comparative test on hydrolysis was conducted between the base oil of ester-based grease for roller bearings, used in ventilators, and lubricant for fluid dynamic bearing units.

The test method was based on ASTM D 2619: the test oil and water were mixed, and the mixture was stirred at a high temperature and in the presence of catalyst to observe the change in the acid value in the oil layer and that in the water layer.

1) Test conditions

• Mixing ratio: Test oil: 75 g; water: 25 g
• Test temperature: 93˚C
• Catalyst material: Copper
• Stirring speed: 6 min^{-1}
• Test duration: 48 hours

2) Test results

As shown in **Table 3**, the lubricant for the fluid dynamic bearing unit exhibits a smaller acid value increment and a smaller water layer acid value than those the base oil for ester-based grease for roller bearings does, being resistant to hydrolysis and excelling in humidity resistance in terms of the characteristics of the lubricant itself.

Table 3 Result of hydrolytic reactivity

	Item to be studied	Base oil for ester-based grease	Lubricant for fluid dynamic bearing unit
Before test	Dynamic viscosity 40˚C [mm^2/s]	25.44	12.3
	Acid value [mgKOH/g]	0.71	0.05
After test	Dynamic viscosity 40˚C [mm^2/s]	25.51	12.24
	Acid value [mgKOH/g]	1.06	0.09
	Acid value increment [mgKOH/g]	0.35	0.04
	Water layer acid value [mgKOH/g]	6.23	2.72

4. Conclusion

We have developed a fluid dynamic bearing unit for home-use ventilators that capitalizes on the freedom from noise and high reliability, features of a fluid dynamic bearing, and that has the same dimensions as those of the current roller bearings and can be used in the same manner as those current roller bearings.

The newly developed product can be extended to other applications needing freedom from noise and high reliability than ventilators; we will extend it into various series to apply it to other product models and applications.

Photo of author

Masaharu HORI
Fluid Dynamic Bearing Unit Division
Engineering Dept.

[Technical Paper]

Surgical Support System for Cerebral Aneurysm Coil Embolization

Yoshitaka NAGANO*
Yukihiro NISHIO*
Noriaki MATSUBARA**
Shigeru MIYACHI**
Hideo FUJIMOTO***

Endovascular coil embolization is becoming a standard treatment option for people with cerebral aneurysms. The embolization method is the filling of an aneurysm with embolization coils by the combined manipulation of a microcatheter and a coil delivery wire. The manipulation requires the skilled collaboration of two surgeons. Thus, we have developed a new surgical support system that can be operated by only one surgeon. Basic verification for this system was conducted using a silicone dummy aneurysm. The results confirmed that the delivery of the wire at a constant velocity is an effective method for decreasing coil insertion force, and that only one surgeon can perform the same coil embolization procedure. In this paper, we report on the system features and the results of verification.

1. Introduction

In the medical field, treatments with minimized size of surgery scars to reduce the physical demands of patients are widespread. A typical example of such treatments is a therapy using a catheter. This procedure involves inserting a thin tube called a catheter into a duct of the human body and treating an affected part from inside the duct. Recently, the catheter therapy is also used in the field of treating thin and tortuous cerebral blood vessels, and has been applied to treatments for preventing the rupture of cerebral aneurysm, which is a cause of subarachnoid hemorrhage. Coil embolization shown in **Fig. 1** is a procedure that involves blocking the blood flow within the aneurysm by filling the cerebral aneurysm with platinum coils at a predetermined density to purposely form a blood clot and prevent the rupture of the aneurysm [1), 2)].

A microcatheter is inserted from the femoral artery in the groin to the cerebral aneurysm, and then a delivery wire with detachable Note [1)] coils connected at its tip is inserted and maneuvered through the microcatheter from outside the body. Since the aneurysm has thin blood vessel walls and is easily ruptured, a maneuver which can insert the coils with as little force as possible is required. The doctor moves the tip of the microcatheter to a site into which the coils can be easily inserted while carefully monitoring the insertion force of the wire. Positioning of the tip of the microcatheter is influenced by pushing and pulling of the coils, and therefore fine adjustment of the force depending on the movement of the coils is required to operate the microcatheter. On the other hand, a guiding catheter is used to guide a microcatheter, which has a soft tip, near an arterial aneurysm.

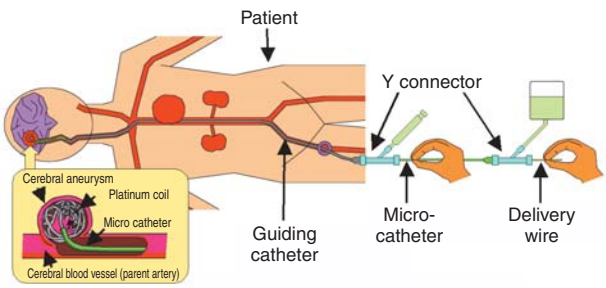

Fig. 1 Endovascular coil embolization of cerebral aneurysm

Note 1) Electric systems which detach the coils from the wire by energizing the delivery wire are widely used.

* New Product Development R&D Center Mechatronics Research Dept.
** Department of Neurosurgery Nagoya university, Graduate School of Medicine.
*** Department of Engineering, Nagoya Institute of Technology Graduate School

The procedures of coil embolization are divided into two types: one in which two doctors operate the microcatheter and the wire, respectively, with both of their hands; and the other in which one doctor operates the microcatheter by the left hand and the delivery wire with the right hand [3), 4)]. In the latter case, a highly skilled maneuver for simultaneously operating both the catheter and the wire with the left and right hands, respectively, is required. It is therefore often the case that two doctors are involved in the treatment. Mutual understanding between the doctors about "the sense of the wire insertion force felt by the hand" and "pushing and pulling operation of the catheter" is necessary.

In the past, **NTN** has developed a sensing system for cerebral aneurysm therapy which measures and displays the manual insertion force of the delivery wire working in collaboration with Nagoya Institute of Technology and Nagoya University [5), 6)]. As shown in **Fig. 2**, the sensing system consists of an optical force sensor integrated into a medical device called a Y connector for passing the delivery wire through the catheter. Converting the manual insertion force of the wire into sound pitch and presenting the force audibly provides the circumstance that allows all the medical staff in the operating room to share the same understanding of the provided insertion force [7) to 9)].

By extending the function of this sensing system, we developed a cerebral aneurysm coil embolization support device which allows a single doctor to simultaneously and coordinately operate the catheter and the wire as in the two-doctor procedure [10)]. In this report, we will discuss the coordinated manipulation of the catheter and the coil, the construction of the developed support device, and the verification results confirming the advantages of this device.

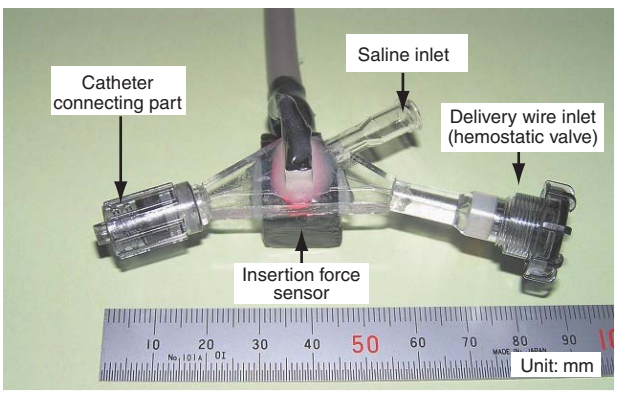

Fig. 2 Sensing system for cerebral aneurysm treatment

2. Coordinated manipulation of catheter and coils

If the contraction of the volume of a coil lump, called coil compaction [2)], occurs after coil embolization, blood flows back into the aneurysm and the effect in preventing a rupture is lost. In order to prevent coil compaction, the coils need to be inserted into the aneurysm uniformly and densely [11)]. The doctor inserts the coils into a site which is estimated not to be densely filled with the coils so that an excessive force is not exerted on the aneurysm.

2.1 Painting phenomenon

Coil embolization is performed by visually observing the state of the aneurysm and the coils with a fluoroscope. To estimate the sites which are not densely filled with the coils, a head-swinging phenomenon [9)] called "painting" [Note 2)] generated at the tip of the microcatheter shown in **Fig. 3 (a)** is used. This phenomenon is generated by the interaction between the coils inserted and the inner walls of the aneurysm, in the following manner:

(1) Parts of the coils are restrained by the friction between the inner walls of the aneurysm and the coils which have been already inserted.
(2) When the coils are inserted further in this state, they start to undergo pressure deformation with the restrained parts as the fulcrums, and the tip of the microcatheter starts to swing (painting).
(3) The coils then buckle, and the tip of the microcatheter is released from the restraint by the coils and returns to its original position in the painting movement.

In a space which is densely packed with the coils, the tip of the microcatheter is restrained by the coils, and painting does not occur. In this state, an excessive force is required to insert the coils, and forced insertion may lead to the rupture of the aneurysm.

2.2 Maneuver by two doctors

Two doctors who operate the microcatheter and the delivery wire, respectively, communicate through conversations while checking the fluoroscopic images, and as shown in **Fig. 3 (b)**, insert the coils by the following procedure:

(1) During the coil insertion, when no painting is observed and resistance is felt during insertion, the doctor who operates the wire temporarily stops the insertion of the delivery wire.

Note 2) Named so since the movement of the catheter resembles brush strokes.

(2) The doctor who operates the catheter retracts the tip of the microcatheter to such a degree that it is not completely removed from the aneurysm, and then inserts the catheter back into the aneurysm.
(3) When the tip of the catheter moves to a site which is not densely packed with the coils, the doctor who operates the wire can insert the wire (coils) with a small insertion force.

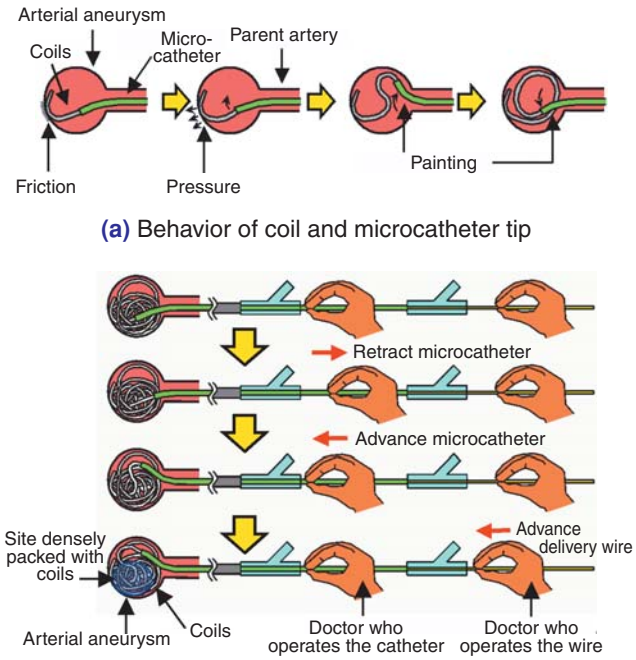

(a) Behavior of coil and microcatheter tip

(b) Collaborative manipulation of microcatheter and delivery wire

Fig. 3 Coil insertion by two surgeon

2.3 Operation of microcatheter

The doctor who operates the microcatheter conducts fine positioning operation of the microcatheter by predicting the degree of bending of the microcatheter in the blood vessel, so that the tip of the microcatheter is not removed from the aneurysm during insertion of the coils. Even in the case where the tip is not moved, the pushing and pulling operations of the microcatheter are necessary. For example, the microcatheter is kept pushed so that the microcatheter is not pushed back during insertion of the coils.

Since the insertion and removal of the microcatheter involve opening and closing of the hemostatic valve (see **Fig. 2**) of the Y connector, it can be smoothly performed if the hemostatic valve is operated by the left hand while retaining the Y connector, and the microcatheter is operated by the right hand.

3. Developed support device

3.1 Overall construction

Fig. 4 shows the overall construction of this device. In this construction, as in a conventional system, the doctor operates the microcatheter with both hands and operates the delivery wire by a foot switch. The wire is delivered at a constant speed by the wire delivery device. The insertion force of the wire is detected by the cerebral aneurysm sensing system, converted into sound pitch information, and is transmitted to the doctor. The delivery speed is adjusted by a switch. This construction allows performance of coil embolization without a doctor who operates the wire.

Fig. 5 shows the appearance of the sensing system and the wire delivery device. To allow the doctor to check the state of the patient at all times, this mechanism is small in size for use on the surgery table. It also has the function to allow the operator to open the top cover and operate the wire directly by the hand. This function characterizes the system in that it can be used not only to move the delivery wire before insertion of the coils and recover the delivery wire after the coils are detached, but can be also switched to a conventional treatment mode during the operation [12].

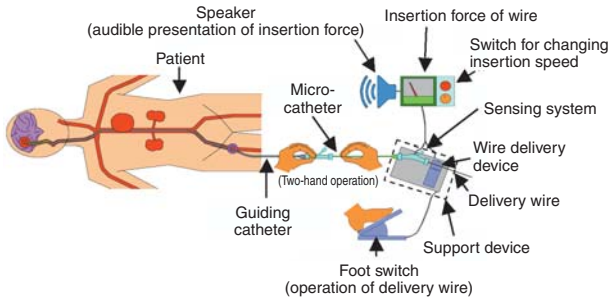

Fig. 4 Structure of the surgical support system

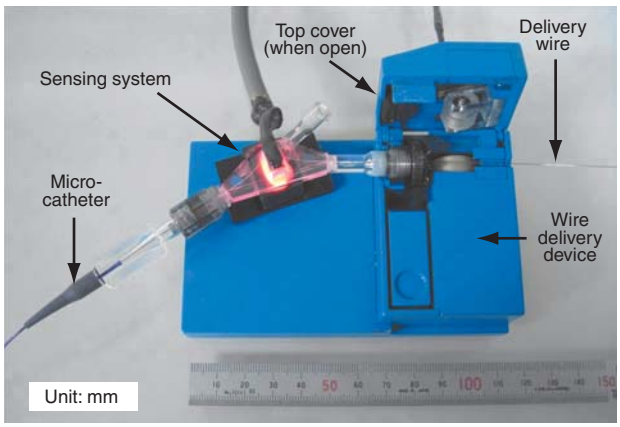

Fig. 5 Photo of the sensing system and the delivery wire driving unit

3.2 Wire delivery device

Fig. 6 shows the construction of the developed wire delivery device. A direct-current motor is connected to a driving roller via reduction gears, and drives the delivery wire in the longitudinal direction. To prevent slipping and horizontal shift of a super-thin delivery wire (diameter: about 0.3 mm), a guide rail is provided at the center of the driving roller. A follower roller is attached to the top cover via a thrust spring, and the delivery wire is held between the driving roller and the follower roller by fixing the top cover onto the body part. The maximum insertion speed of the delivery wire is 2.0 mm/s based on measurement results of the insertion speed of manual wire delivery by a doctor.

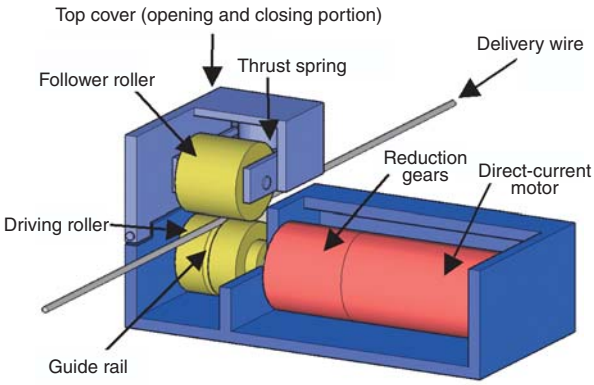

Fig. 6 Structure of the delivery wire driving unit

4. Evaluation of continuous insertion

Fig. 7 shows an experimental evaluation system. A simulated aneurysm was placed in water, and water was injected into a guiding catheter, a microcatheter, a Y connector, and a sensing system. A delivery wire inserted into the catheter was then advanced, and the state of the coil embolus was evaluated by observing it with a microscope. The overall length of the catheter is 1.5 m, and while overall length of the delivery wire is 1.75 m (excluding the coil portions). The simulated aneurysm was formed in the shape of a terminal with a diameter of 4 mm, using a transparent silicone to impart appropriate plasticity and enable observation of the coils inside the aneurysm. The number of the coils inserted was two so that the packing fraction was 20% or higher [13], which does not cause coil compaction.

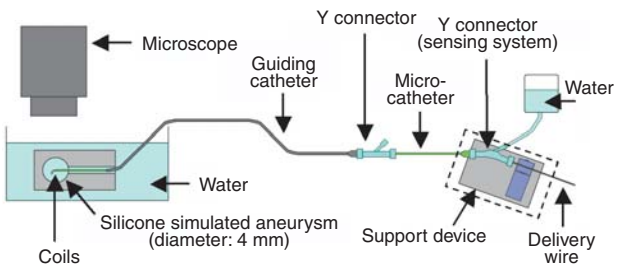

Fig. 7 Evaluation system for the surgical support system

4.1 Speed and insertion force

Table 1 shows the results of coil insertion when inserting the delivery wire at a constant speed. The insertion was conducted with the microcatheter fixed. The coil used was a two-dimensional type which develops into a screw-like shape when it comes out of the catheter tip. The first coil has a development diameter Note 3) of 4 mm, the same as the diameter of the simulated aneurysm, and the second coil has a smaller diameter of 3 mm. The overall length of the first coil was 80 mm, while two different lengths of 60 mm (packing fraction: 21%) and 80 mm (24%) were selected for the second coil for comparison of packing fraction.

The coils were inserted at different speeds varied by 0.5 mm/s. As a result, insertion of the first coil, due to a packing fraction as low as 12%, was successful at the maximum speed evaluated, i.e., 2.0 mm/s. On the other hand, the second coil was not inserted into the aneurysm and pushed out to the parent artery side when driven at a high speed from 1.0 mm/s to 1.5 mm/s or higher. The higher the packing fraction, the lower the upper limit of the speed which allows successful insertion.

Fig. 8 (a) shows the insertion force trend of the delivery wire when the first coil was used. Insertion force is clearly less for the insertion at a constant speed of 1.0 mm/s shown in red than for the intermittent insertion by the manual operation of the doctor shown in blue, the former being about half the latter. The maximum force of the former is also 1/2 or

Table 1 The delivery wire speeds for completed filling coil insertion

Number of coils inserted [Coil No.]	Coil specification Shape-Diameter-Length [mm]	Volume packing fraction of coils [%]	Wire speed for completed filling coil insertion [mm/s]
1	2D-4-80	12	0.5～2.0
2	2D-3-60	21	0.5～1.0
2	2D-3-80	24	0.5

Note 3) The coils return (develop) to their original two-dimensional (spiral) or three-dimensional (basket-like) shapes once they are out of the catheter tip. The coil diameter at this time is referred to as the development diameter, and the development diameter of the coils inserted is selected depending on the diameter of the aneurysm.

less compared with the latter. A decrease in the insertion force directly leads to a decrease in the risk of a rupture of the aneurysm during insertion of the coils. Therefore, continuous insertion at a constant speed is considered useful.

4.2 Insertion force and developed state

Fig. 8 (b) shows the developed states of the coils after being inserted by the manual operation of a doctor (intermittent insertion) and by the wire delivery device (continuous insertion). The development by the intermittent insertion of the doctor resembles the state of the insertion at a low speed of 0.5 mm/s, in which the coil is twisted. In contrast, when the speed is1.0 mm/s or higher, in which the insertion force became less, the coil was not twisted, and developed into a desirable spiral (cylinder) shape. Such developments can hardly be achieved by human operation. In order to examine the relationship between the insertion force and the developed state in more detail, photographs of the developed states of the coils were taken at one second intervals as shown in **Fig. 9**. The coil used was a three-dimensional coil which develops into a basket shape (development diameter: 4 mm, overall length: 40 mm). Photographing was started when about half of the overall length of the coil was inserted.

In case of 0.5 mm/s, as shown in **Fig. 9 (a)**, sawtooth wave patterns are frequently found in the insertion force trend over time. It can be confirmed from **Fig. 9 (c)** that the developed states of the coils have not changed. This is presumably because static friction force is exerted due to low speed insertion,

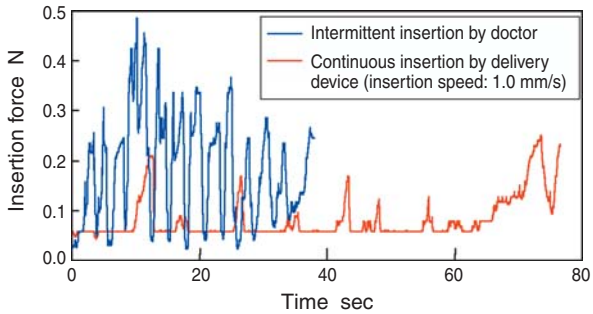

(a) Comparison of coil insertion forces

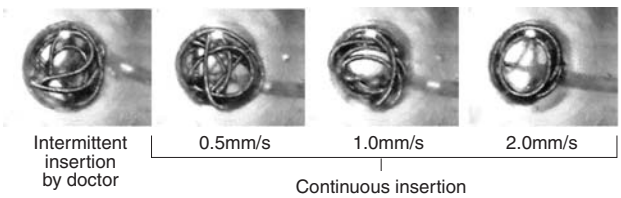

(b) The photos of the deployed 2D coil

Fig. 8 Intermittent and continuous insertion

and the coil is restrained by the wall of the aneurysm. In this rigid state, the insertion force increases in correspondence with the insertion of the coils, and the painting phenomenon occurs at the tip of the catheter. As shown in **Fig. 8 (a)**, sawtooth wave patterns as in **Fig. 9 (a)** are frequently found with the intermittent insertion by a doctor. This is presumably because static friction is exerted when the insertion is paused, and the coil is restrained by the wall of the aneurysm.

In contrast, in case of 1.0 mm/s, the development state of the coils often changes as shown in **Fig. 9 (d)**, indicating that the coil is sliding and moving on the wall of the aneurysm. In case of wire insertion at a high speed, it is thought that the frictional force is little so that the coil cannot be restrained by the wall of the aneurysm. In **Fig. 9 (b)**, although a sawtooth wave increase of the insertion force, which possibly results

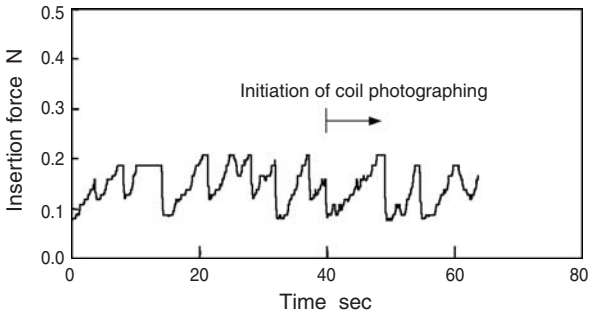

(a) Low speed continuous insertion (0.5 mm/s)

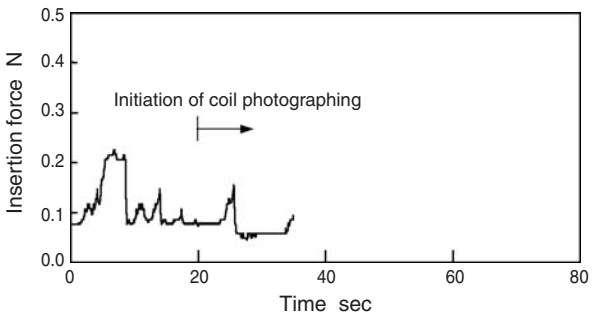

(b) High speed continuous insertion (1.0 mm/s)

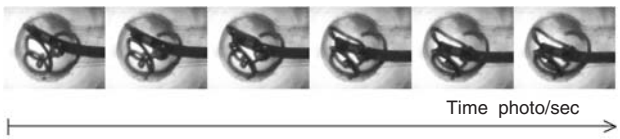

(c) Photos of the deployed 3D coil by low speed coil insertion (0.5mm/s)

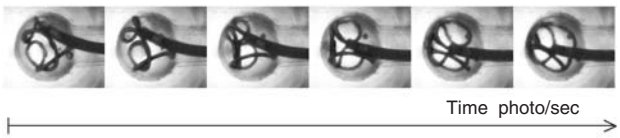

(d) Photos of the deployed 3D coil by high speed coil insertion (1.0mm/s)

Fig. 9 Comparison of insertion speed using 3D coil

from the exertion of static friction, is found in part, the insertion force is almost constant at slightly lower than 0.1 N.

5. Evaluation of coordinated manipulation by hand and foot

5.1 Results of coordinated manipulation

Since the second coil cannot be inserted simply by feeding the wire at a constant speed, “manual operation of the catheter” and “foot operation of the delivery wire” by the doctor were added. The results of such insertions are shown in **Table 2**.

When the overall length of the coil was 60 mm, insertion of the coil was successful at all insertion speeds used in the evaluation (0.5 mm/s to 2.0 mm/s) by additionally employing the manual operation of the catheter. On the other hand, when the overall length of the coil was 80 mm, the gaps between coils were difficult to find even when the doctor moved the tip of the catheter as appropriate since the packing fraction was high, and the coils could not be inserted simply by operating the catheter in some cases.

When there is an indication that the coils are pushed out from the entrance of the arterial aneurysm, stopping of the delivery wire by the foot switch and pulling back operation were additionally performed, and gaps between the coils were carefully searched to complete the insertion.

As mentioned above, it was confirmed that in a state when the packing fraction of the coils is high, a single doctor could manipulate the catheter and the delivery wire coordinately and simultaneously using this system to insert the coils.

Table 2 Delivery wire insertion speeds with collaborative manipulation

Coil specification Shape-Diameter-Length [mm]	Manual operation of microcatheter	Foot operation of delivery wire	Wire speed for completed filling coil insertion [mm/s]
2D-3-60	No	Advance only	0.5～1.0
	Yes	Advance only	0.5～2.0
2D-3-80	No	Advance only	0.5
	Yes	Advance only	0.5
	Yes	Advance and Retraction	0.5～2.0

5.2 Evaluation of operability

We had four doctors (very skilled to 3 to 4 years of experience) subjectively evaluate the operability of this system. The results are shown below.

(1) Since the insertion force of the coils is audibly presented by a change in sound pitch, the delivery wire can be operated while always checking the state of the coil insertion by fluoroscopic images. The coils are inserted at a constant speed, and it is therefore easy to predict the development movement in the aneurysm.
(2) Compared to wire operation, fine insertion and retraction operations of the catheter based on the observation of painting are comfortable since it is a two-hand operation as in a conventional system.

6. Conclusion

In cerebral aneurysm coil embolization, which has been conventionally performed by two doctors collaboratively, a new support device which can be performed only by a single doctor was developed. This device is small in size for use on the surgery table, and can switch to a normal operation mode performed by the hand of the doctor at any time. The results of the verification conducted using a silicone simulated aneurysm are shown below.

(1) It was confirmed that the continuous insertion at a constant speed requires 1/2 or less the maximum force for inserting the wire than the intermittent insertion by a doctor.
(2) Since the insertion force of the coils is audibly presented, the doctor can operate the catheter by hand and the delivery wire by foot simultaneously while checking the state of coil development by fluoroscopic images as in a conventional system.
(3) Since the delivery wire is inserted at a constant speed, it is easy to predict the coil development in the aneurysm.

In the future, the operability of the system in cases where the shapes of the aneurysms are difficult for coil insertion and the advantages of this system will be verified in further detail in simulated surgery using blood vessel models and animals.

References

1) S. Miyachi, Neuroendovascular Treatments, Gendai Igaku, 52-1 (2004) 73-84.
2) A. Hyodo, the Ordinary Method of Cauterization Inside Cerebral Aneurysms and GDC Treatment Techniques, in A. Hyodo and S. Nemoto, eds., Endovascular Surgery for Cerebral Aneurysms using GDCs, Igaku Shoin, Ltd. (1999) 30-34.
3) S. Miyachi, Setup and Angiography Practitioners and Assistants, J. Yoshida and S. Miyachi, eds., Neuroendovascular Treatment Do's & Don'ts 2nd Edition, Igaku Shoin, Ltd. (2006) 16-20.
4) Y. Ito, Fundamental Techniques for Intraaneurysmal Embolization of Cerebral Aneurysms, in H. Kikuchi, ed., Collection of Recent Cases of Endovascular Treatment of Cerebral Aneurysms, Pioneering Medical Techniques Laboratory , (2005) 49.
5) Y. Nagano, A. Sano, M. Sakaguchi and H. Fujimoto, Development of a Super Fine and Long Linear Sensor for Physiological Applications—Application for Cerebral Aneurysm Coil Embolization, Transactions of the Society of Instrument and Control Engineers, Vol. 44, No. 3 (2008) 278-284.
6) Y. Nagano and H. Fujimoto, Development of a Sensing System for Cerebral Aneurysm Treatment, NTN Technical Review No. 76 (2008) 63-67.
7) Y. Nagano, A. Sano, M. Sakaguchi, H. Fujimoto, S. Miyachi, T. Ohshima, N. Matsubara, O. Hososhima and J. Yoshida, Development of a Sensing System for Cerebral Aneurysm Coil Embolization: Evaluation of Insertion Force Using Simulated Aneurysms Using Arterial Models and In Vivo Imitations, Journal of Japan Society of Computer Aided Surgery, Vol. 10, No. 2 (2008) 147-153.
8) N. Matsubara, S. Miyachi, Y. Nagano, T. Ohshima et al., A novel pressure sensor with an optical system for coil embolization of intracranial aneurysms, Journal of Neurosurgery, 111-1 (2009) 41-47.
9) N. Matsubara, S. Miyachi, T. Ohshima, O. Hososhima, T. Izumi, A. Tsurumi, T. Nishikori, J. Yoshida, Y. Nagano, A. Sano, M. Sakaguchi and H. Fujimoto, Development of an optical force sensor system for cerebral aneurysm coil embolization, Journal of Neuroendovascular Therapy, Vol. 2, No. 2 (25th Annual Meeting of the Japanese Society for Neuroendovascular Therapy).
10) Y. Nagano, A. Sano, N. Matsubara, S. Miyachi, Y. Nishio, O. Hososhima, T. Ohshima, T. Wakabayashi and H. Fujimoto, Development of a Single Surgeon Surgery System for Cerebral Aneurysm Coil Embolization, Journal of Japan Society of Computer Aided Surgery, Vol. 12, No. 2 (2010) 101-107.
11) N. Sakai, Endovascular Treatment of Unruptured Cerebral Aneurysms, in H. Kikuchi, ed., Pioneering Medicine Series 9: Endovascular Treatment for Neurological Surgeons—Practice and Prospects, Pioneering Medical Techniques Laboratory , 2001, 173-180.
12) http://www.jscas.org/guideline.htm
13) Y. Kawanabe, A. Sadato, W. Taki and N. Hashimoto, Endo vascular Occlusion of Intracranial Aneurysms with Guglielmi Detachable Coils, Correlation Between Coil Packing Density and Coil Compaction, Acta Neurochir (Wien), 143-5 (2001) 451-455.

Photo of authors

Yoshitaka NAGANO
New Product Development R&D Center Mechatronics Research Dept.

Yukihiko NISHIO
New Product Development R&D Center Mechatronics Research Dept.

Noriaki MATSUBARA
Department of Neurosurgery Nagoya university, Graduate School of Medicine.

Shigeru MIYACHI
Department of Neurosurgery Nagoya university, Graduate School of Medicine.

Hideo FUJIMOTO
Department of Engineering, Nagoya Institute of Technology Graduate School

Automatic Repair Technology of Fine Pattern in LCD Manufacturing Process

Hiroaki OBA*

NTN has been working on the development of repair technologies to boost the yield of color filters (CF) and thin film transistors (TFT), which are components of liquid crystal displays (LCD). Recently, customer demand for greater productivity in the repair process has increased, and we have developed automatic repair technologies in response.

This paper presents an overview of the automatic repair function used in an LCD repair system. As automatic repair functions, automatic defect detection, repair position calculation, ink color selection and detection of abnormal repairs, for example, are realized by applying image-processing technologies. These functions improve the efficiency of repair processes and meet customer demands for high productivity.

1. Introduction

As the demand for LCD television sets increase, the upsizing of substrates as characterized by the adoption by panel manufacturers of the 10th generation glass substrate with a side over three meters is in progress, while the need for defect repair devices contributing to the improvement of production yield is increasing. **NTN** has developed and is selling repair devices for color filters that apply ink to defects with a repair needle, while other repair devices cut circuits on TFT substrates with YAG laser to remove defects. They are implemented in a vast number of liquid crystal manufacturing processes.

Of these repair devices, the shortening of tact time and the improvement of repair quality are required. In addition, requirements for efficiency improvement in manufacturing processes and labor saving have increased recently to reduce panel cost. In response to these requirements, **NTN** has engaged in the development of automatic repair functions that will provide effective labor saving tools.

In the past, the operator who observed the defect state displayed on the monitor chose the machining repair conditions and specified the repair position. **NTN** developed an image processing algorithm of our own suitable to defects to be repaired, and by using the outcome of this development, **NTN** realized the automation of defects detection, calculation of repair positions, selection of ink color for the repair, and repair abnormalities detection.

In this paper, after a brief description of the liquid crystal display repair device, the automatic repair function **NTN** developed will be presented.

2. Liquid crystal display repair device

Fig. 1 shows the appearance of the liquid crystal display repair device. This device consists of a chuck mechanism that fastens the substrate, a repair head that is equipped with a repair function, and an XYZ stage that moves the repair head to the defect position.

Fig. 1 Appearance of LCD repair system

* Precision Equipment Division Product Engineering Department

The repair head is equipped with an optical system to observe defects on substrates, a laser with which patterns are cut and defects are removed, and an ink applying mechanism that applies ink to spots where defects were removed.

Special hardware is not necessary to implement the automatic repair function. Images fit for image processing are captured with a CCD camera by controlling the reflecting light source and the transmission light source, taken into the computer of the repair device and processed arithmetically, and the repair device is controlled in accordance with the results of the image processing; these processes make it possible to allow the automatic repair function to work.

Fig. 2 shows the general flow of automatic repair processes. When a substrate to be repaired is brought into the device, the substrate is chucked and aligned, and the repair head moves to the defect position. The information on the defect position is acquired from the inspection device while the substrate is being carried in position.

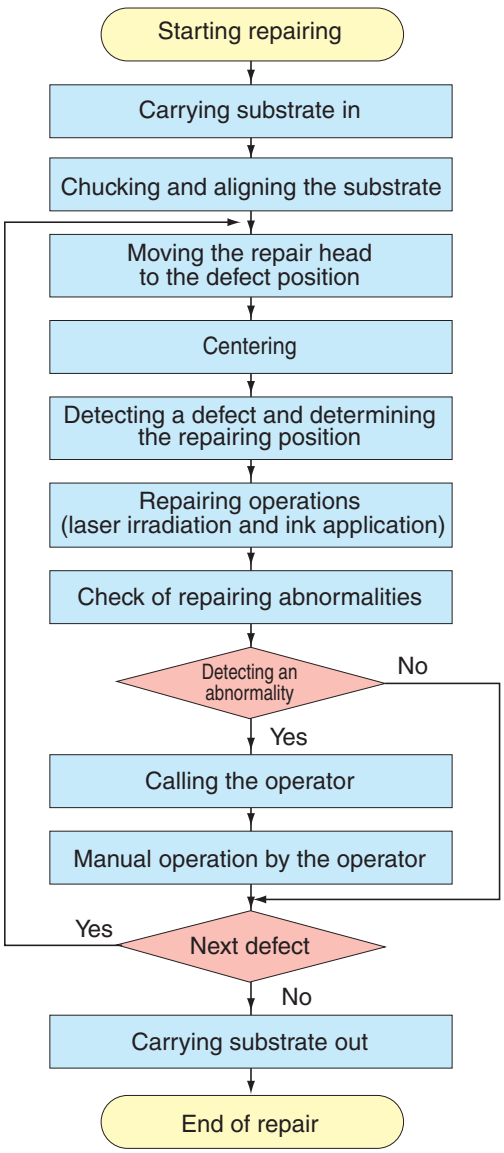

Fig. 2 Flow chart of repair

After the repair head has been moved to the defect position, the substrate surface is focused on for the defect to be centered. After this, the defect is detected to identify the kind of defect (black defects, white defects, and so forth), and depending on the kind of defect, the repair measure (laser irradiation or ink application) is chosen and implemented.

Furthermore, whether repair abnormalities remain after the repair is checked. When an abnormality is detected such as a remaining defect in a laser-irradiated area or a white defect in an ink-applied area, the buzzer is sounded with the automatic repair work interrupted and the operation is changed over to manual operation by the operator.

When a substrate is judged to be repaired correctly, the repair head is moved to the next defect to repeat identical automatic repair operations, carrying out repair operations on all defects on the substrate.

Processes needing repair operations in liquid crystal manufacturing processes are either so-called upstream ones such as TFT substrates and color filter substrates or downstream processes in which liquid crystals sealed into cells or modules are processed.

Depending on the process introduced, the defect kind and the repair methods vary. In the following, the function of automatically repairing color filter substrates and TFT substrates is described.

3. Function of automatically repairing color filter substrates

For this function, a dedicated image processing algorithm was developed that allows (1) the defect detection, (2) the repair position calculation, (3) the correction ink color determination, and (4) the detection of abnormal repair to be processed automatically.

Defects occurring in the color filter are white defects and black defects shown in **Fig. 3 (a).** A white defect is a result of a missing part of the membrane formed on the substrate and the original RGB colors are missing. A black defect is one characterized by the mixture of colors as a result of the black matrixes membranes swelling out or RGB colors due to defective shapes and other causes. In repairing these defects, the defect is removed by means of laser in the first place regardless of the defect kind, and after this, the part that the defect has been removed is repaired by applying ink on it. In addition, the

hardening treatment of ink by means of an UV light source or the drying treatment by means of an IR light source is conducted as an after-treatment.

The above automated treatment not only allows a series of operations to be carried out as a batch treatment automatically in sequence, but also allows one to expect that the finish and quality of operations are equivalent to those of operations carried out by an operator. In other words, this means that it is required to automatically perform the defects recognition and the indication of repair positions, and the repair ink color selection that have been done visually by the operator, and that it is also required to detect abnormalities occurring during the course of automatic repairing to assure that repair has been done properly.

3.1 Detection of defects

Defects are detected by comparing an image containing a defect with a normal image condition registered in advance and extracting parts that do not match the latter image.

With **Fig. 3 (a)** showing an image containing a defect and **Fig. 3 (b)** one showing the normal condition, they are compared with each other with regard to density; the result of the comparison is shown in **Fig. 3 (c)**. In **Fig. 3 (c)**, areas in which the density agrees between two images are shown in gray, and of areas in which the agreement of density is not seen, areas darker than the normal image is shown in black and areas lighter than the normal image are in white. This function recognizes areas in black as black defects (candidates) and areas in white as white defects (candidates), and area with the difference between black and white larger than the threshold value are detected as defects in the end.

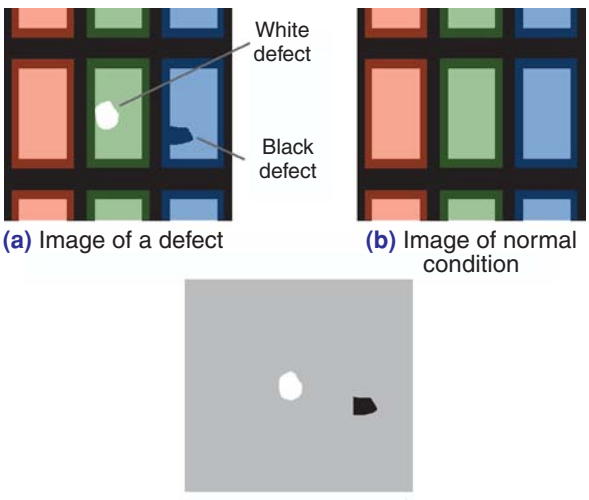

(a) Image of a defect **(b)** Image of normal condition

(c) Result of density comparison

Fig. 3 Example of defects on color filter panel and defect detection

3.2 Method of determining repair positions

As described above, in repairing the color filter, a defect is irradiated with laser to remove it first, and then the area that a defect is removed is covered with ink for repairing. For this purpose, it is necessary to determine the laser irradiation position and the ink application position automatically. This function uses the information on the position and size of the defect obtained through the processing of defect detection to determine these positions.

Fig. 4 shows an example of determining the repair position. When the defect is smaller than the circle on which ink is applied as shown in **Fig. 4 (a)**, the repair position is determined so that the ink application center aligns with the defect center. When the defect is larger as shown in **Fig. 4 (b)**, repairing work is divided into several operations to be conducted. The number of repairing operations is determined by the defect size and the size of the circle on which ink is applied.

Actual automatic repair requires a treatment that is equivalent to the repair quality achieved by an operator and is more efficient. For this reason, the algorithm contains ordered steps to minimize damage to the normal region near a defect and the number of times of repair.

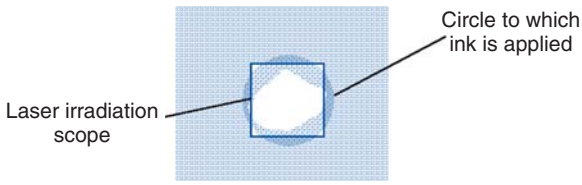

(a) When the defect is smaller than the diameter of the circle to which ink is applied

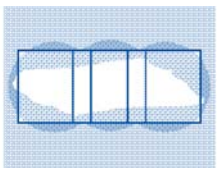

(b) When the defect is larger than the diameter of the circle to which ink is applied

Fig. 4 Calculation example of repair positions

3.3 Determination of the repair ink color

In repairing a defect, ink with the normal color area must be applied to the defect; this requires determining the ink color to be applied.

In this treatment, the color information on the same region in the normal image as that in the extracted defect is obtained by means of image processing, and the color information obtained is compared with that which is associated with each ink beforehand to choose an ink having the closest color information.

Using the example of the defect image and the normal image, how to determine the repair ink color is explained below. Suppose, for example, that pieces of color information cR, cG, cB, and cBlk are assigned to four kinds of repair ink R, G, B, and Black (abbreviated as Blk in the following). If, in **Fig. 5**, the piece of color information on position (b) in the normal image, which corresponds to position (a) in the defect image, is judged as the closest to the color information piece cG, ink G that has the color information piece cG is chosen as the repair ink.

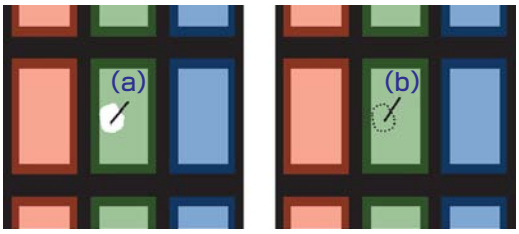

Fig. 5 Ink color selection for repair

3.4 Detection of repair abnormalities

In repair operations carried out by an operator manually, he or she inspects images visually from time to time in the course of operation to check to see if repair operations are carried out properly. For instance, he or she proceeds with his or her operations visually checking to see if defects remain not removed after laser irradiation and how a defect has been filled with ink after ink application.

This function carries out inspection based on image processing after each automatic laser irradiation and ink application to ensure that repair treatment has been performed properly.

3.4.1 Inspection after laser irradiation

After laser irradiation, the irradiated domain is inspected to make sure that defects are not remaining. **Fig. 6 (a)** shows an example of remaining defects. Defects such as foreign objects with an elevation may not be removed with single laser irradiation, needing repeated laser irradiation for removal as shown in **Fig. 6 (b)**. However, when laser is used for a long time, a decrease in power may prevent removing defects; therefore, if a defect cannot be removed after a predetermined number of removal operations, it is judged as abnormal.

3.4.2 Inspection after ink application

After the application of ink, the presence of white patches that are not filled with ink, as shown in **Fig. 7 (a)**, and that of areas on which a large quantity of ink is dropped, as shown in **Fig. (b)**, are detected. When the viscosity of ink changes or when the needle cleaning is not enough, such phenomena occur rarely. As in the defects removal by means of laser irradiation, the possibility is high that a desired result is not obtained after the repetition of operations, and such phenomena are judged as abnormal.

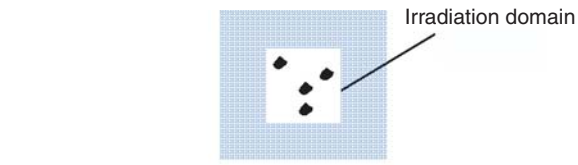

(a) Remaining defects after laser irradiation

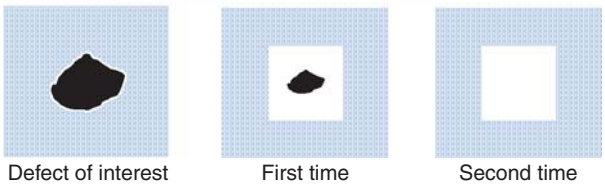

(b) Case in which laser irradiation is repeated

Fig. 6 Check after laser cutting

(a) Presence of white patches after application

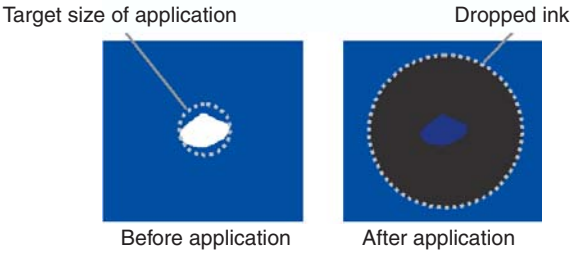

(b) Dropped ink

Fig. 7 Check after ink pasting

4. Function of automatically repairing TFT substrates

Major repair operations on TFT substrates include removing defects by means of laser and cutting part of electrical circuits formed on the substrate. Repair operations include finding breaks in continuous electrical wires on a substrate and also applying metal paste on them with an application needle to restore continuity. Repair operations using laser are divided roughly into the two kinds that follow:

(1) Carrying out repair operations predetermined as needed by defects, such as removing a defect and cutting part of a pattern; and
(2) The operator confirms a defect visually and determines the detail of the repair operation.

Operations falling under category (1) can be automated by combining them with image processing. The repair head is moved to the defect position, and the accurate defect position is detected by image processing, and then the defect is moved to the center of the laser irradiation scope. After this, the result of the repair operation by laser irradiation is checked using image processing.

Operations falling under category (2) are considerably complex. Even if the defect position can be identified by using image processing, repair is not always carried out at that position. For this reason, the operator makes an assessment of the defect state visually and selects the repair method. To address an increase in the time needed for repair operations, a function is needed for the device to carry out automatic repair operations on a defect separately from the operator while he or she is defining the repair details operations for another defect.

In repair operations using an application needle to restore breaks in a group of continuous electrical wires, on the other hand, the inspection device on the previous process is not capable of identifying where on continuous wiring a break has occurred. To address this problem, the repair device is required to be equipped with a function to identify where a break has occurred.

For this function, too, the algorithm has been developed with the aim of minimizing operations carried out by the operator so that this function may contribute to reducing repair operation time and labor. In addition to flat panel displays, this inspection algorithm can be applied to uses aiming at trimming.

4.1 Automatic removal of defects by means of laser

The following are automatic repair steps to remove defects such as foreign objects adhering to a pattern.

(1) The head is moved to the defect position detected by the inspection device on the previous process;
(2) The defect position displayed on the monitor is detected by a method suitable for the defect in question such as the method described in Subsection 3.1 and the comparison of repeated adjoining patterns, and is moved to the center of the screen again (**Fig. 8**).
(3) The scope of laser irradiation is changed to the specified size or the one equivalent to the defect and the defect is irradiated by laser. The machining conditions such as laser power and oscillation frequency are registered in the device in advance.
(4) The result of repair is checked by the method equivalent to that described in Subsection 3.4.1 or comparing images before irradiation with ones after irradiation; if no defects are left, the workpiece is judged as normal. If part of defects is found remaining, they are irradiated by laser again. If defects remain after the repetition of the specified times of laser irradiation, the workpiece is judged as abnormal.

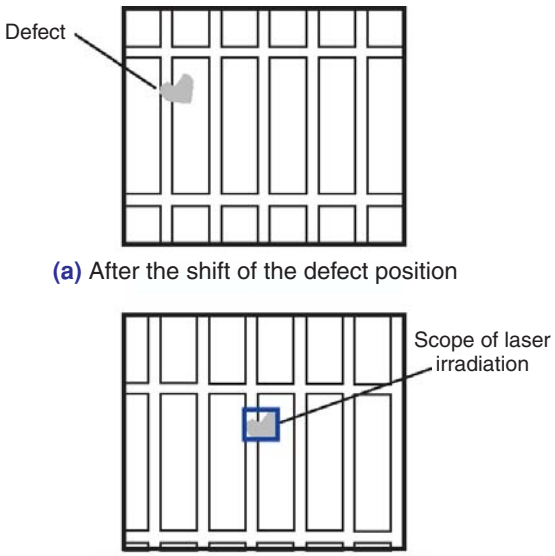

(a) After the shift of the defect position

(b) The defect is moved to the center of the monitor

Fig. 8 Centering of defect

4.2 Automatic cutting of a specified position

The steps of automatic repair operations by which a specified position on a pattern is irradiated with laser to form a redundant circuit and similar purposes are shown below:

(1) The head is moved to the defect position detected by the inspection device on the previous process;
(2) The region to be cut by means of laser irradiation is detected from among the patterns displayed on the monitor by image processing such as pattern matching, and moved to the center of the screen

as shown in **Fig.9**.

(3) The scope of laser irradiation is changed to the specified size and the workpiece is irradiated with laser, the machining conditions such as laser power and oscillation frequency are registered in the device in advance.

(4) The result of repair is checked by the method equivalent to that described in Subsection 3.4.1 or comparing images before irradiation with ones after irradiation; if no defects are left, the workpiece is judged as normal. If part of defects is found remaining, they are irradiated by laser again. If defects remain after the repetition of the specified times of laser irradiation, the workpiece is judged as abnormal.

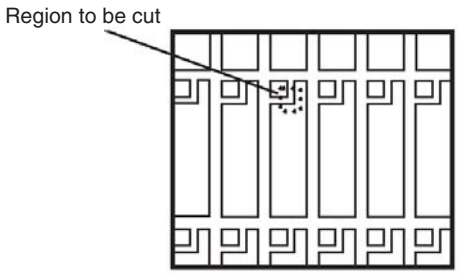

(a) After the shift of the defect position

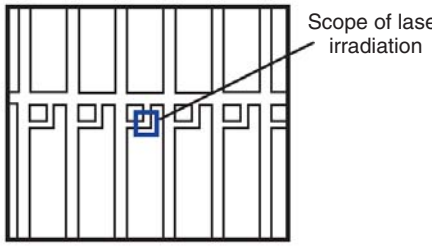

(b) The defect is moved to the center of the monitor

Fig. 9 Centering of cutting target

4.3 Automatic defect tracking and repair of continuous wiring

Automatic repair operations are applicable also to a break and a short-circuited part of continuous wiring shown in **Fig. 10**.

These defects are detected by electric inspection, but the inspection device in the previous process gives the information on the number of the wire in which a defect exists, not the information on the abnormal point coordinates.

For this reason, in manual repair operations by the operator, the repair head was moved to the start of the wiring, from which the operator moved the repair head along the wiring with a tool such as a joystick while following the head visually to identify a default. However, this method took a great many hours to identify a defect, which necessitated the development of an automatic repair function.

Fig. 11 shows how this automatic repair function follows a defect. Tracking starts from screen A. The repair device acquires the number of the line marked with a black circle in screen A. The coordinates of the black circle are calculated from the pieces of design information such as the line number and line-to-line pitches. The design information is registered in the device in advance.

With the head starting from A and moving from stage to stage in order of A, B, and C, image data is captured in sequence, and the defect is detected after the binarization processing and comparison with the adjoining patterns. When a defect is detected, the stage is stopped there and repair operations suitable to the defect are conducted automatically. **Fig. 11** shows a straight-line-like pattern; however, tracking can also be performed on a pattern that twists midway.

When a defect is a break in wiring, metal paste is applied to the broken part with an application needle to recover continuity. When a defect is a short circuit, it is irradiated with laser to be removed for repair.

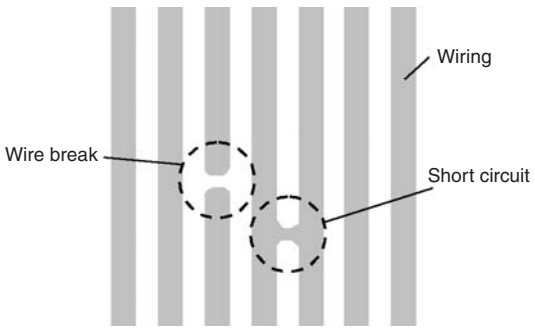

Fig. 10 Defect example of line pattern

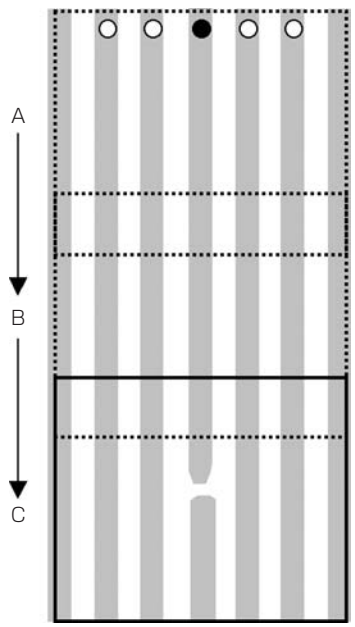

Fig. 11 Defect search

5. Conclusion

This paper presented the automatic function of the liquid crystal display repair device.

The flat panel display market will continue widening, with the screen becoming larger and finer. This will, it is anticipated, require repair devices to be capable of repairing more defects efficiently and with good quality, while requirements for shorter tact times and labor saving becoming still stronger.

Aiming at the development of repair devices capable of responding to new requirements from manufacturing processes and contributing to the improvement of the yield of flat panel displays, we will continue making an effort to enhance functions of the repair device.

References

- M. Saruta, Sagasaka , High Performance Repair Equipment and its Underlying Technologies, NTN Technical Review No. 64.
- S. Shimizu and H. Ohba, Technology for the Detection and Repair of Micro-Defects Occurring in Transparent Thin-Film on LCD Panels, NTN Technical Review No. 68 (2000) 81-85.
- M. Saruta, Multi-Repair System for Color Filters, NTN Technical Review No. 72 (2004) 52-55.
- A. Yamanaka and A. Matsushima, Development of a Linear Changer with a Built-in Pasting Unit for a Flat Panel Defect Repair System, NTN Technical Review No. 76 (2008) 138-143.

Photo of author

Hiroaki OBA

Precision Equipment Division
Product Engineering
Department

Presentation of award-winning articles

Awarded: Fiscal 2010 Minister of Education, Culture, Sports, Science and Technology Prize in the Science and Technology Fields

The Commendation for Science and Technology by the Minister of Education, Culture, Sports, Science and Technology in Development Category

Chikara OHKI

1. Introduction

A Fiscal 2010 Minister of Education, Culture, Sports, Science and Technology Prize was awarded to us for the Development of High-performance Bearings Reinforced by means of Grain Refinement (Product name: FA-processed bearing[1)]). FA-processed bearings are made of steel material consisting of crystal grains whose size is reduced by means of special heat treatment. The size of the crystal grains is now less than half the size of conventional crystal grains used in bearing steel. These bearings have been in full-scale mass production for five years, currently used mainly in valve gears of automotive engines.

2. Background

In response to the current trend in machine facilities of weight reduction, downsizing, cost reduction, and resources-saving construction, technology that will allow roller bearings, made with general-purpose steel, to achieve a long service life under severe working conditions has been desired. This technology uses high-carbon chromium bearing steel (a general-purpose bearing steel) undergoing a specific heat treatment technology; however the performance is equivalent to high-performance steel containing rare earth metals. We developed a heat treatment method by which crystal grains are made finer while they are kept in granulated state. The result obtained by this method of heat treatment was used to develop high-strength, long-life bearing materials based on the enhancement of solid solubility through the use of nitrogen, enhancement through the refinement of crystal grains, and enhancement through the precipitation of carbides and nitrides.

3. Performance

The development of FA treatment has enabled us to positively increase the bearing life when the bearing is operating with contaminated lubrication. the failure life under the condition of lubrication with foreign bodies mixed in the bearing The life of bearings which undergo the FA treatment and operate with contaminated lubrication go beyond that of conventional standard products (bearing steel of the second class subjected to standard heat treatment). It also enabled us to raise the static rated load, which is theresistance to plastic deformation . The FA treatment has also enabled us to reduce the dimensional change rate over time below that of conventional long-life products (carbonitriding-processed bearing steel of the second class).

Fig. 1 shows crystal grains of an FA-treated bearing and those of a standard bearing, while **Fig. 2** shows the result of the life test under the condition of lubrication with foreign bodies mixed.

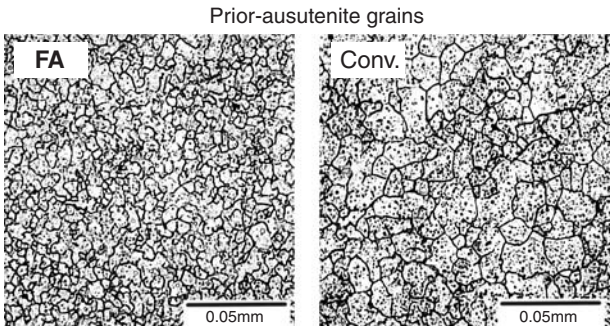

Fig. 1 Grain sizes of FA treated and conventional

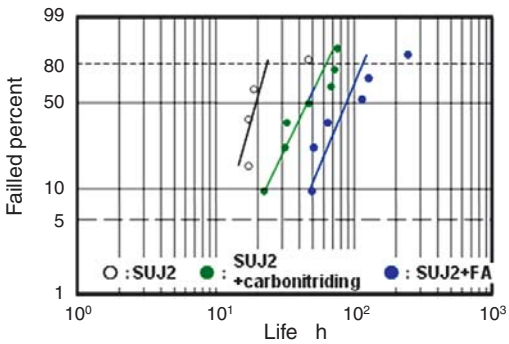

Fig. 2 RCF life under contaminated lubrication condition

References

1) C. Ohki, Improving Rolling Contact Fatigue Life of Bearing Steels through Grain Refinement, SAE Technical Paper Series (2004) 2004-01-0634.

Photo of author

Chikara OHKI
Elemental Technology R&D Center

Presentation of award-winning articles

The 25th Annual Meeting of The Japanese Society for Neuroendovascular Therapy JNET Gold Award-winning paper

Development of Optical Force Sensor System for Cerebral Aneurysm Coil Embolization*

Noriaki MATSUBARA**, Shigeru MIYACHI**, Yoshitaka NAGANO***, Hideo FUJIMOTO**** et al.

1. Introduction

Recently, cerebral endovascular treatments using catheters have been rapidly developing. Such treatments typically include coil embolization for preventing a cerebral aneurysm rupture, which is a cause of subarachnoid hemorrhage. In embolization, inserting coils with an excessive force may cause a rupture of the aneurysm,resulting in severe complications, Removal of the tip of the catheter from the aneurysm may result in insufficient embolus formation. We will report the development of a device which measures the insertion force of the coils using an optical system, present a device overview and the results of its basic experiments.

2. Procedure

The coils are connected to the tip of the delivery wire, and then inserted into the aneurysm by operating the wire. A Y connector and an optical sensor are incorporated into the catheter (**Fig. 1**) which improves the ability of the device to insert the delivery wire. The wire passing through the catheter is “bent” by the insertion force. A LED light[1)] shines on the wire which then creates a shadow; the amount of bending in the shadow is used to determine the insertion force. The coils were inserted into silicone simulating the insertion into an aneurysm, and the insertion force was measured by this device.

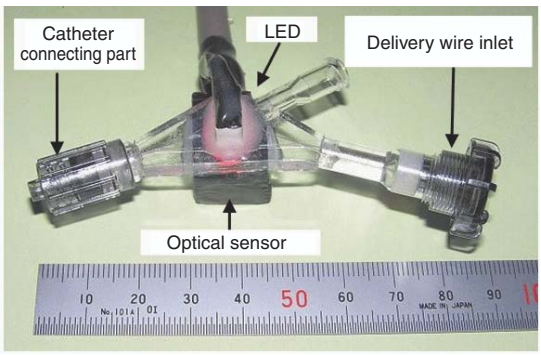

Fig. 1 Force sensor

3. Results

As shown in **Fig. 2**, the maximum insertion force when the coils were inserted into the simulated aneurysm did not exceed 0.3 [N], and a bimodal distribution of the force was observed, indicating that an accurate measurement of the insertion force of the coils was possible.

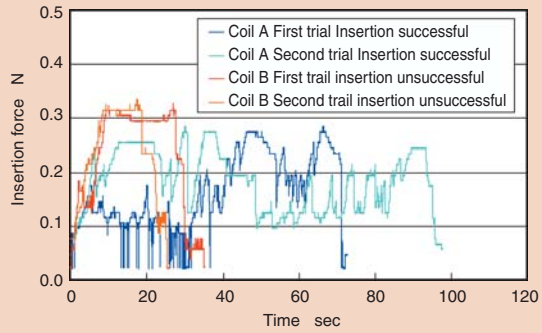

Fig. 2 Measurement results of insertion force

4. Conclusion

A device for measuring the insertion force of coils by an optical sensor was developed. Wider clinical application of this device will allow safer and more reliable performance of embolization.

References

1) Y. Nagano, A. Sano, M. Sakaguchi and H. Fujimoto, Development of a Super Fine and Long Linear Sensor for Physiological Applications, Vol. 44, No. 3 (2008) 278-284.

*Abstract from JNET (Neuroendovascular Therapy), 2-2 (2008), 113-118
**Department of Neurosurgery Nagoya university, Graduate School of Medicine.
***New Product Development R&D Center Mechatronics Research Dept.
****Department of Engineering, Nagoya Institute of Technology Graduate School

Photo of authors (Representative)

Noriaki MATSUBARA
Department of Neurosurgery
Nagoya university,
Graduate School of Medicine.

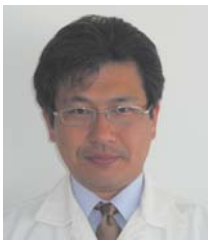

Yoshitaka NAGANO
New Product Development
R&D Center
Mechatronics Research Dept.

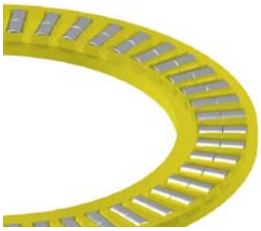

Awarded: 2009 Japanese Society of Tribologists Prize of Promotion

Study of a Long-Life Thrust Needle Roller Bearing Lubricated with Low -Viscosity Lubricant [1)]

Hiroki FUJIWARA

1. Introduction

Thrust needle roller bearings are used in compressors of automotive air conditioners; the mixture fluid of refrigerant and refrigerating machine oil is used as lubrication. Recently the viscosity of this mixed fluid has been lowered to increase compressor efficiencies, unfortunately this causes the lubrication performance to dramatically decline. To address this situation, the extension of service life under the use of low viscosity oil is required. In this study, experiments and theoretical considerations were conducted on the mechanism by which thrust needle roller bearings lubricated with low-viscosity oil are damaged. The results of the study were used to extend the life of thrust needle roller bearings. The results of the study were presented at the World Tribology Congress 2009, and for the reason of an outstanding contribution to the improvement of reliability and energy efficiency of rotary machines, the 2009 Japanese Society of Tribologists Prize of Promotion was given to this study.

2. Elucidation of the damaging mechanism

A standard thrust needle roller bearing operating under low lubricant viscosity causes flaking to occur in the drive sprocket raceway surface in a short time. Elements of the drive sprocket such as the heat treatment method, shape accuracy, and materials were not found to effect the flaking. Investigation of the flaked raceway surface revealed that flaking originating in the surface had occurred on the edge on the inside diameter side of the roller trace. Based on this observation, we estimated that heating and accompanying plastic flow had caused the damage. This theory was confirmed by a surface analysis. In order to identify the heating quantitatively; we introduced the theory of mixed lubrication to theoretically analyze friction torque due to spin, rolling viscous resistance, and elastic hysteresis loss. This revealed that the dominant factor governing friction torque under the l lubrication using low viscosity oil is slip due to spin as shown in **Fig. 1**.

3. Extension of bearing life

Heating depends on frictional force and sliding velocity. In order to decrease frictional force; crowning was provided to decrease contact pressure on the roller edge part in which slip is large. In addition, rollers were put in double rows to decrease the slip velocity. The motion of a roller turns into pure rolling on its pitch circle; therefore, arranging rollers in a double-row configuration causes the slip velocity on the edge section to be reduced. Using these technologies, we obtained a service life of about eight times that of a conventional single-row straight bearing as shown in **Fig. 2**.

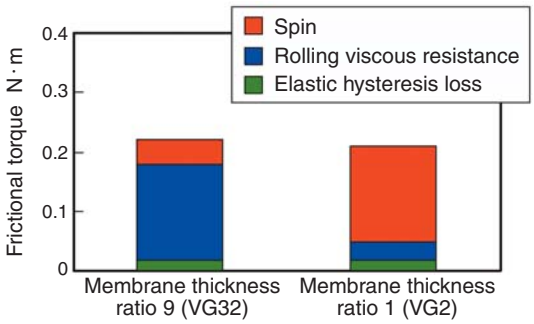

Fig. 1 Analysis of frictional torque factor

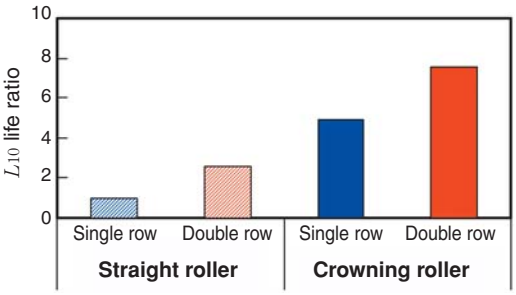

Fig. 2 Results of life test

References

1) H. Fujiwara and K. Tamada, Study of a long-life thrust needle roller bearing lubricated with low viscous lubricant, Proceedings of WTC 2009 (Kyoto, Japan), F-232, p.350.

Photo of author

Hiroki FUJIWARA
Elemental Technology R&D Center

Intelligent In-wheel Unit

Axle Unit*that NTN proposes for next-generation electric vehicles (*consists of an in-wheel motor, an electric brake and a multi-axis load sensor)

Features

(1) Compact, lightweight in-wheel motor that combines a high-speed, high-efficiency, high-output motor and the world's fastest cycloid decelerator with large load capacity;

(2) Increased fuel efficiency and driving safety.

Applications

- Electric vehicles, Hybrid vehicles, fuel cell vehicles

Construction

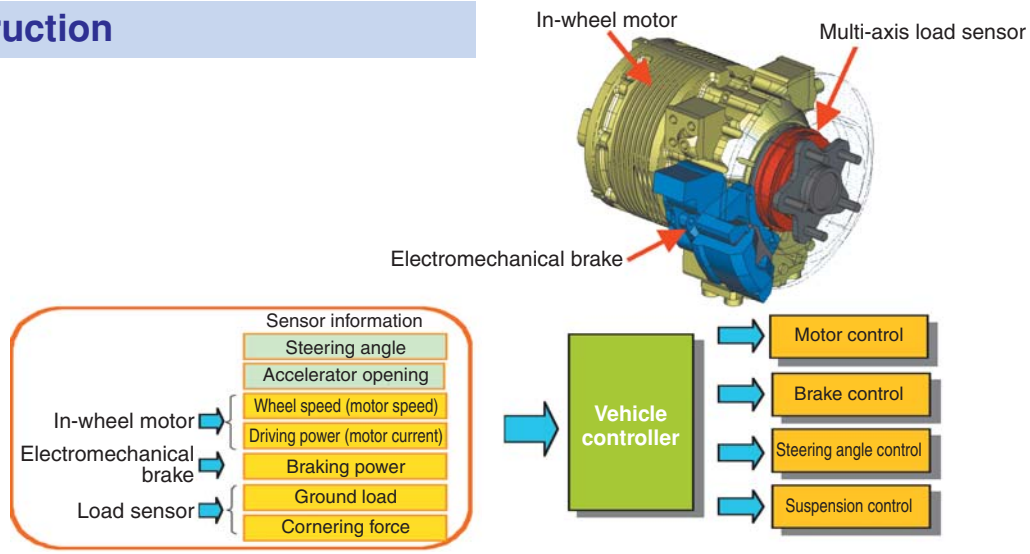

Low Friction Hub Bearing

Improves vehicle fuel efficiency by reducing straight-line driving friction!

Features

(1) Use of a combined-groove curvature for the raceway
Reduction of rolling friction while maintaining the same bearing durability as conventional type

(2) A reduced initial preload range
Reduction of rolling friction

(3) Use of a low friction seal

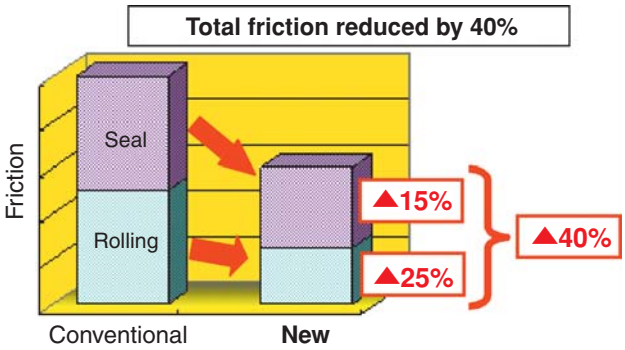

Construction

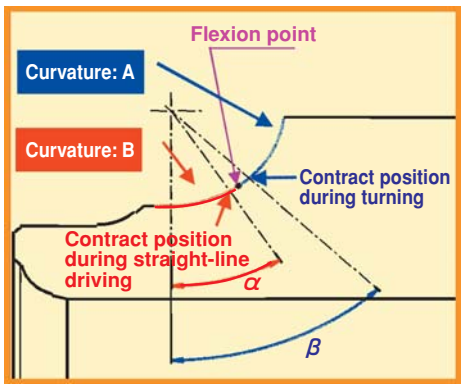

Depending on contact position with steel ball, a different curvature radius is applied.
• During turning: Curvature radius A
(Same as conventional type)
↓
Same durability as conventional type
• During straight driving: Curvature radius B
↓
Torque reduction
Curvature radius B > Curvature radius A

Applications

- Wheel hub bearings for passenger cars

NTN SNR Multi Axis Load Sensor Integrated Hub Bearing

Improves advanced-vehicle safety control
with the world's most precise load measuring technology!

Features

(1) Able to detect ground-contact loads for the four wheels separately.

(2) Loads detectable at any time from the vehicle being stopped to traveling at a high speed.

(3) Three-axis (Fx, Fy, Fz) loads detectable with high accuracy (±5% FS).
⇒Precise vehicle control through very accurate assessment of road conditions

(4) Loads measured close to the tires (hub bearings).
⇒Road condition changes detected in a response time of 0.05 sec. (conventionally, 0.2 sec.), which represents a difference of 4.2 m distance traveled at 100 km/hour.

Construction

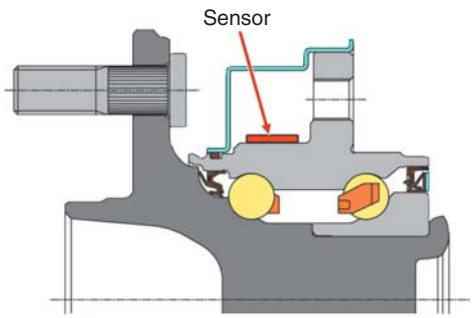

Fx：Driving force, controlling force
Fy：Cornering force
Fz：Vertical force

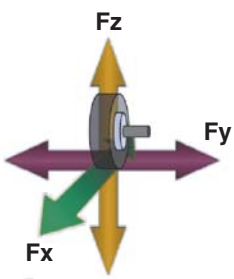

Applications

Wheel hub bearings for passenger cars
- Vehicle stability control

Light and High Drive Shaft for Rear Wheel Drive Cars

Reduced weight and torque increase
the fuel efficiency and ride comfort of luxury cars!

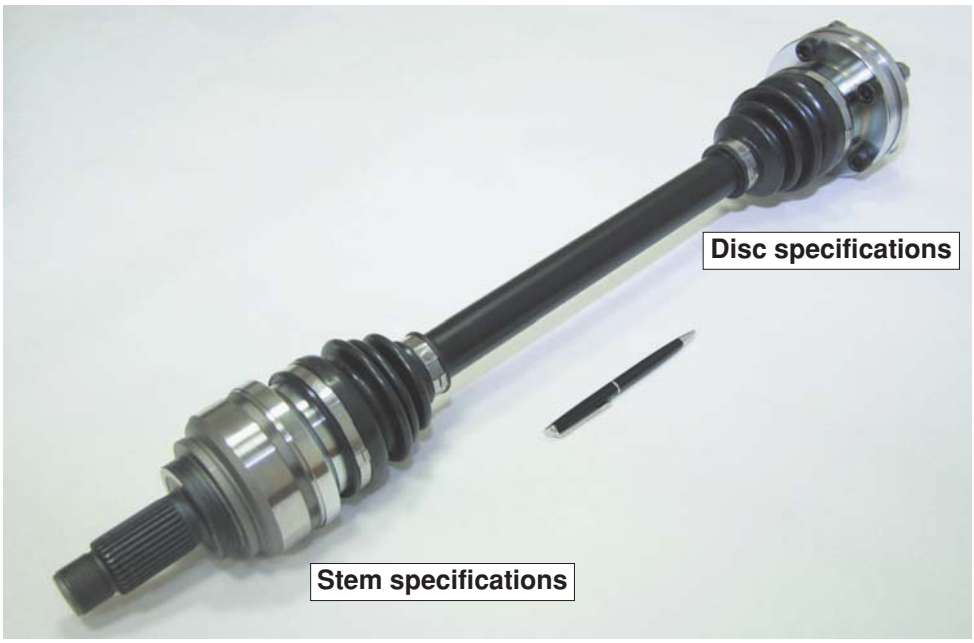

Features (compared to conventional products)

(1) Lightweight: weight reduced by 16%.

(2) Highly efficient: torque loss reduced by 40%.

Applications

- Automotive drive shaft
  For use in the rear wheels of RWD and 4WD automobiles

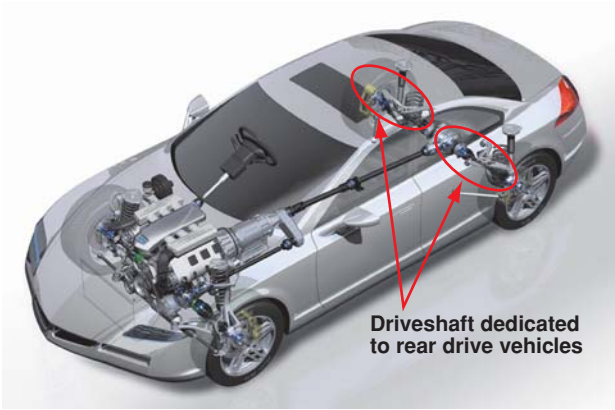

Construction (comparison with conventional products)

- Balls with reduced diameter and a smaller and lighter inner ring, outer ring and cage;
- Lighter shaft with a thin-walled, hollow body;
- Optimally angled ball slots helps reduce frictional resistance occurring on balls in axially shifting motion, reducing heat generation.

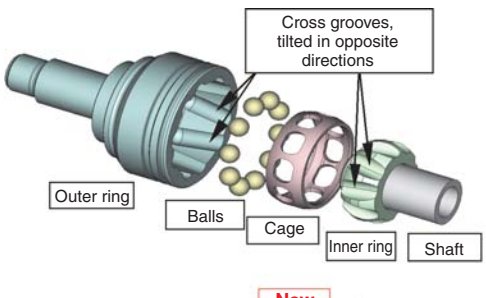

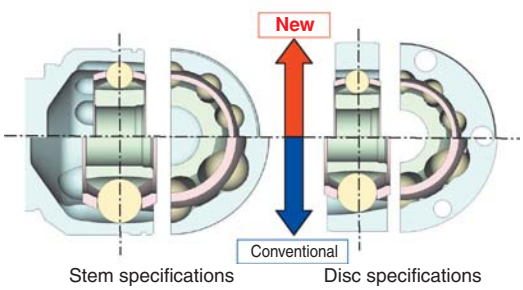

Low Torque Thrust Needle Roller Bearing

Greater fuel economy, 50% less rotational torque than conventional products!

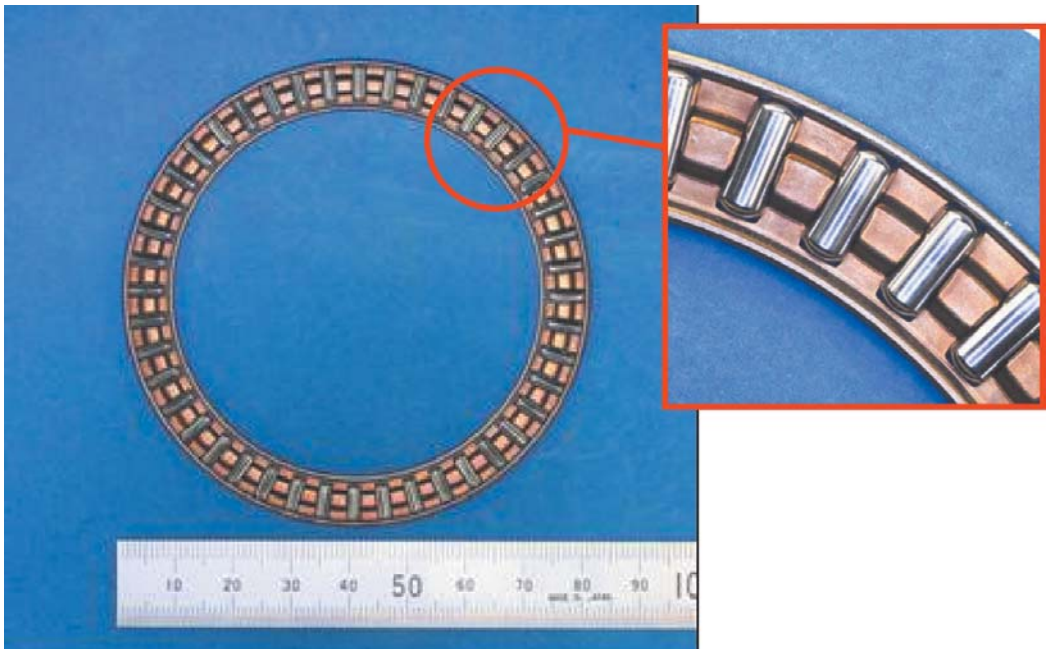

Features (comparison with conventional products)

(1) 50% reduction in bearing rotational torque

(2) Limited bearing temperature rise

Applications

- **Transmission for gasoline-fuelled vehicles and hybrids**

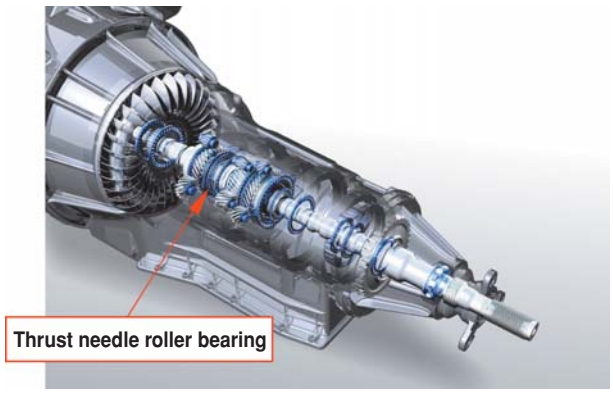

Construction

'Fully crowned rollers', arc-shaped in axial direction at outside cylindrical surface, are used.

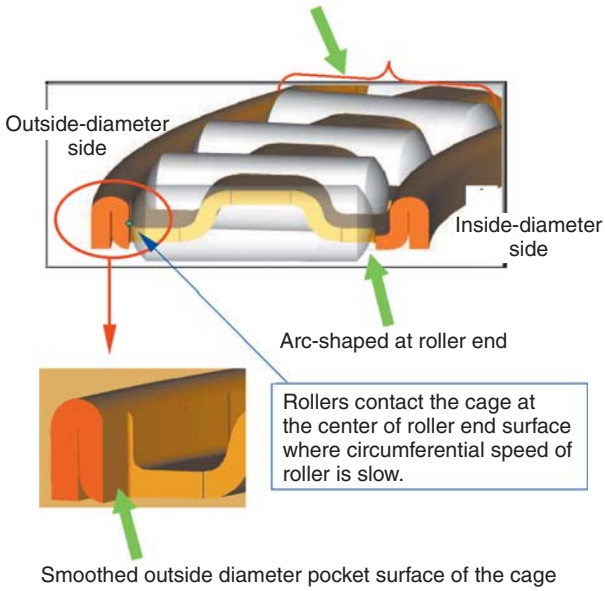

World's Smallest Bore Hydrodynamic Bearing

Achieving the world's smallest bore in a hydrodynamic bearing, thanks to a special grooving technique !

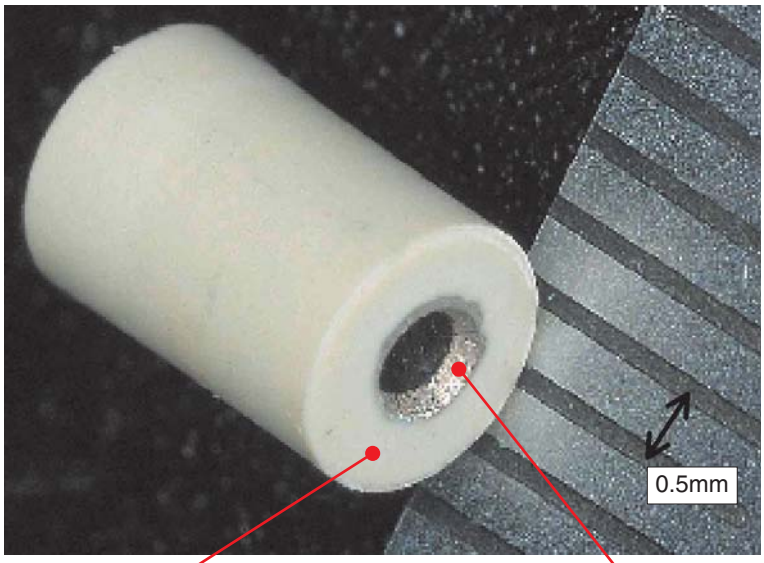

Features

(1) World's smallest bore hydrodynamic bearing:
0.6 mm shaft diameter using precision repeatable performance of electrocasting

(2) Integration with plastic parts is possible:
Integral molding is made possible by plastic injection molding

(3) Quieter sound level and high reliability:
Rotational shaft is supported by hydrodynamic effect

Applications

- **Fan motor for mobile equipment**

Construction

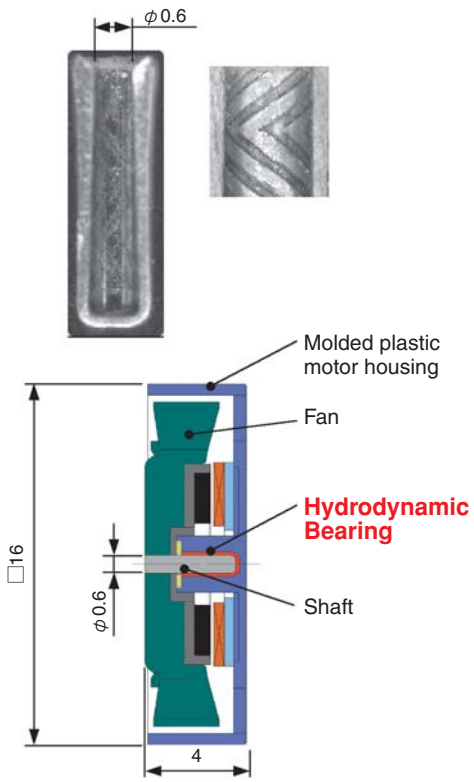

Desktop Type Microscopic Coating Applicator

Ideal for the R&D or production of
prototype/small-volume liquid crystal

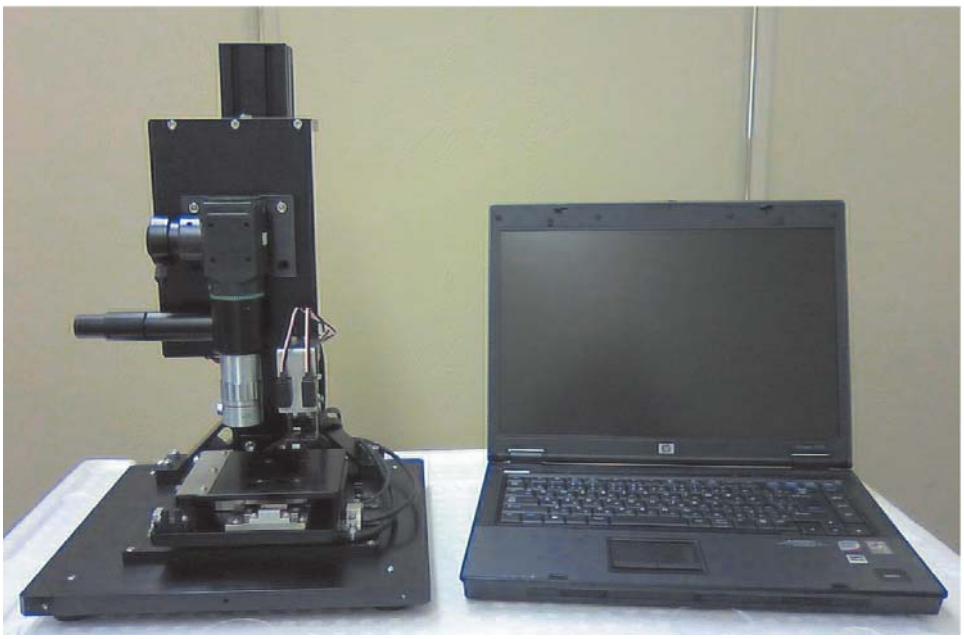

Features

(1) Repair ink coating function
1) Able to apply liquids such as a drug on the order of picoliters.
2) Unique coating method using a needle eliminates nozzle clogging.

(2) Compact desktop size for easy operation
1) Footprint occupied by the applicator is about a 30 cm square.
2) Powered by 100 V AC.
3) Easily operated with a mouse.

Applications

R&D or small-volume production of:
- **Biological products and new drugs,**
- **Prototype electronic circuits (ICs), or**
- **Liquid materials such as conductive paste,**
- **Assembly of micro-machines and other microscopic components.**

Construction

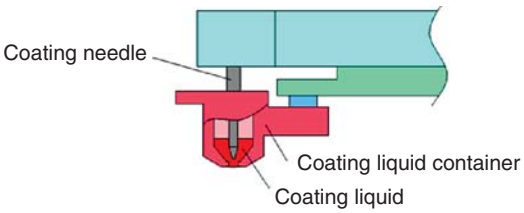

<Construction of the coating unit>

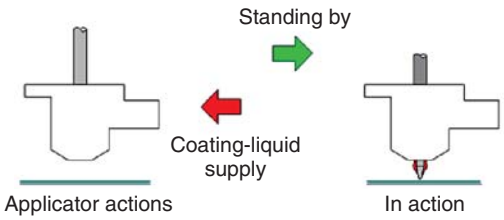

<Flow of coating actions>

High Performance Large Type Gantry XY Table

Large type precision positioning drive unit attains light weight, high rigidity, and low cost

Helps shorten setup time and reduce drive motor output !

Features

Function and performance responding to production equipment and inspection equipment for large type glass substrates etc. are realized.

- **Light weight:**
  60% compared with conventional type (Upper-axis beam)
- **High rigidity:**
  120% compared with conventional type (Upper-axis beam)
- **Table traveling speed:**
  120% compared with conventional type (Max. speed: 2,000 mm/s)

Construction

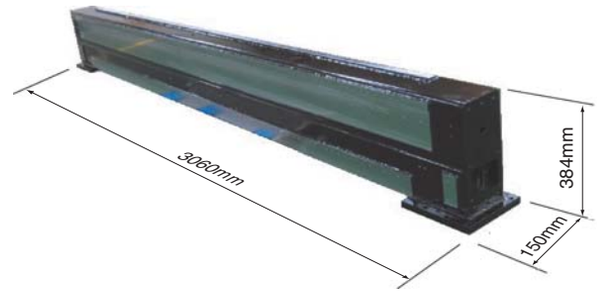

Appearance of the gantry-type upper-axis steel tube beam

Applications

- **Making and inspecting flat panels;**
- **Making solar panels.**